Integration of online partial discharge monitoring and defect location in medium-voltage cable networks

Please check the document version of this publication:

Integration of
Online Partial Discharge Monitoring
and Defect Location
in Medium-Voltage Cable Networks

Paul Wagenaars

Integration of Online Partial Discharge Monitoring and
Defect Location in Medium-Voltage Cable Networks

PROEFSCHRIFT

ter verkrijging van de graad van doctor aan de
Technische Universiteit Eindhoven, op gezag van de
rector magnificus, prof.dr.ir. C.J. van Duijn, voor een
commissie aangewezen door het College voor
Promoties in het openbaar te verdedigen
op donderdag 4 maart 2010 om 16.00 uur

door

Paul Wagenaars

geboren te Schaijk

Dit proefschrift is goedgekeurd door de promotor:

prof.dr.ir. E.F. Steennis

Copromotor:
dr. P.A.A.F. Wouters

Summary

Partial discharge (PD) diagnostics is a proven method to assess the condition of underground power cables. PDs are symptomatic for a defect (weak spot) that may evolve into a complete breakdown. A PD induces a small pulse in the conductor(s) and earth screen that propagates through the cable in both directions. In previous research an online PD detection and location system was developed for medium-voltage cables. This system is currently introduced by utilities on an increasingly large scale. This thesis deals with several new challenges that are related to the integration of online PD monitoring in different medium-voltage power cable network configurations.

A transmission line model of the power cable is required to enable optimal PD detection. A three-core power cable with common earth screen has multiple coupled propagation modes. The propagation modes are decoupled into a modal solution. A practical method to measure and analyze the cable parameters is developed and validated by measurements on a cable sample. Detailed prediction of multiple reflections was achieved, including the mixing of propagation modes having distinct propagation velocities, validating both the model and the measurement method for three-core cables with common earth screen.

The semiconducting layers in a cable with cross-linked polyethylene (XLPE) insulation have a significant influence on the transmission line parameters. Unfortunately, the dielectric properties of these layers are usually unknown and can differ between similar cable types. It is shown that nonetheless the characteristic impedance and propagation velocity of single-core and three-core XLPE cables can be calculated using information available from the cable specifications. The calculated values are validated using pulse response measurements on several cable samples. The accuracy of the calculated characteristic impedance and propagation velocity is 5–10%, which is sufficient for estimating PD pulse shape and amplitude in a cable circuit.

The online PD monitoring system was initially developed to be installed on a single cable connection between two consecutive ring-main-units (RMUs). It is more efficient to monitor two or more consecutive cables, with one or more RMUs or substations in

between, using a single monitoring system. Models for RMUs and substations are proposed and verified by measurements. The influence of RMUs and substations along the cable under test on the PD detection sensitivity and location accuracy is studied using these models and measurements. The influence of a compact RMU with two connected cables is neglectable if the total cable length is longer than approximately 1 km. The longer the total cable length, the smaller the influence of an RMU along the cable under test. An RMU or substation along the cable under test with more than two connected cables introduces a significant signal loss, decreasing the detection sensitivity significantly. The higher the number of connected cables, the higher the signal loss.

In the equipment found in some substations and RMUs it is not possible to install a PD measurement unit at a desired location. The models and measurements are used to study the feasibility of a single-sided PD measurement, including PD location, with the problematic RMU/substation at the far end. The study shows that a major part of an incoming pulse reflects on a large RMU/substation with many connected cables. This reflection enables a single-sided PD measurement from the other cable end. A single-sided measurement has the disadvantage that the maximum cable length that can be monitored is halved and that it is sensitive to reflections on joints in the cable under test and other connected cables.

Accurate location of PDs in cables, based on arrival times, is imperative for the identification and assessment of defects. Five algorithms that determine the time-of-arrival of pulses are evaluated to investigate which method yields the most accurate location under different circumstances. The methods are evaluated analytically, by simulations, and by measurements on a cable system. From the results the energy criterion method and the phase method show the best performance. The energy criterion is a robust method that achieves location accuracy of 0.5% of the cable length or better. The phase method has a good performance only if the phase shift introduced at the transmission from the cable under test to the RMU is known accurately.

For maximum detection sensitivity the PD monitoring system uses matched filters. These filters are constructed using predicted PD waveforms. These predictions are based on a series of online system identification measurements and a standard cable model. Due to signal distortions that are not taken in account in the model, e.g. an RMU along the cable under test, the predictions can be inaccurate, resulting in a sub-optimal PD detection. An automated procedure that creates new signal templates, based on measured PD signals, is proposed and tested on signals measured during online PD measurements on multiple cable systems. The algorithm generated new templates for PD signals and for disturbing pulses. New PD pulse templates for may be used to improve the cable system model. Disturbing pulse templates may be used to improve disturbance rejection by the measurement unit.

Samenvatting

Partiële-ontladingsdiagnostiek is een bewezen methode om de conditie van ondergrondse energiekabels te bepalen. Partiële ontladingen zijn symptomatisch voor defecten (zwakke plekken) die een complete doorslag kunnen veroorzaken. Een partiële ontlading induceert een kleine puls in de geleider(s) en aardscherm. Deze puls propageert door de kabel in beide richtingen. In voorgaand onderzoek is een systeem ontwikkeld om online partiële ontladingen te detecteren en te lokaliseren in middenspanningskabels. Dit systeem wordt op dit moment op steeds grotere schaal geïntroduceerd bij netbeheerders. Dit proefschrift behandelt nieuwe uitdagingen die te maken hebben met de integratie van online partiële-ontladingsdiagnostiek in verschillende netwerkconfiguraties van middenspanningskabels.

Voor optimale detectie van partiële ontladingen is een transmissielijnmodel van de kabel vereist. Een drie-aderige kabel met gemeenschappelijk aardscherm heeft meerdere gekoppelde propagatiemodi. De propagatiemodi worden ontkoppeld in een modale oplossing. Een praktische methode om de kabelparameters van een drie-aderige kabel met gemeenschappelijk aardscherm te meten en te analyseren is ontwikkeld en gevalideerd door middel van metingen aan een testkabel. Het complete gemeten signaal wordt correct voorspeld door het model, inclusief het mengen van signalen uit propagatiemodi met verschillende loopsnelheden. Deze meting valideert zowel het model als de meetmethode.

De halfgeleidende lagen in een kabel met vernet polyethyleen (XLPE) isolatie hebben een significante invloed op de transmissielijnparameters. De hoogfrequente diëlektrische eigenschappen van deze lagen zijn meestal onbekend en kunnen significant verschillen tussen vergelijkbare kabeltypen. De karakteristieke impedantie en propagatiesnelheid van enkel-aderige en drie-aderige kabels kunnen desondanks worden berekend aan de hand van informatie uit de kabelspecificaties. De berekende waarden zijn gevalideerd met pulsresponsie-metingen op verschillende testkabels. De nauwkeurigheid van de berekende karakteristieke impedantie en propagatiesnelheid is 5–10%. Dit is voldoende om de pulsvorm en amplitude van partiële ontladingen af te schatten.

Het systeem om online partiële ontladingen te meten is oorspronkelijk ontwikkeld om

een enkele kabelverbinding tussen twee opeenvolgende middenspanningsruimtes (MSR's) te bewaken. Het is efficiënter om meerdere opeenvolgende kabelverbindingen, met een of meer MSR's ertussen, te bewaken met één enkel meetsysteem. Modellen voor MSR's en onderstations zijn opgesteld en geverifieerd door middel van metingen. De invloed van een compacte MSR in de bewaakte kabelverbinding is verwaarloosbaar als de totale kabellengte groter is dan ongeveer 1 km. Hoe groter de totale kabellengte, hoe kleiner de invloed van een MSR in de bewaakte kabelverbinding. Als een MSR of onderstation in een bewaakte kabelverbinding meer dan twee aangesloten kabels heeft, veroorzaakt deze een significant signaalverlies, zodat de detectiegevoeligheid afneemt. Hoe meer aangesloten kabels een MSR of onderstation heeft, hoe groter het signaalverlies is.

Bij de installatie in sommige MSR's of onderstations is het niet mogelijk om de meetapparatuur te installeren op een correcte plaats. De haalbaarheid van enkelzijdige ontladingsmetingen, inclusief lokalisatie, met het problematische MSR /onderstation aan het verre kabeluiteinde is bestudeerd met behulp van de modellen en metingen. Het grootste deel van een puls reflecteert op een MSR /onderstation met veel aangesloten kabels. Deze goede reflectie maakt een enkelzijdige ontladingsmeting mogelijk vanaf het andere kabeluiteinde. Een enkelzijdige meting heeft het nadeel dat de maximale kabellengte die kan worden bewaakt wordt gehalveerd. Ook is de meting gevoelig voor reflecties op moffen in de bewaakte en andere aangesloten kabels.

Nauwkeurige lokalisatie van partiële ontladingen in kabels, gebaseerd op aankomsttijden, is cruciaal voor de identificatie en beoordeling van defecten. Vijf algoritmes om de aankomsttijd van pulsen te bepalen zijn geëvalueerd om te bepalen welke methode de beste resultaten geeft onder verschillende omstandigheden. De methoden zijn analytisch bestudeerd, door middel van simulaties en door middel van metingen aan een kabelverbinding. De resultaten tonen aan dat de energie-criterium-methode en de fase-methode het beste presteren. De energie-criterium-methode is robuust en heeft een lokalisatienauwkeurigheid beter dan 0.5% van de kabellengte. De fase-methode heeft alleen een goede nauwkeurigheid als de fasedraaiing die optreedt bij de overgang van de kabel naar de MSR nauwkeurig bekend is.

Voor een maximale detectiegevoeligheid gebruikt het partiële-ontladingsmeetsysteem zogenaamde "matched filters". Deze filters worden geconstrueerd met behulp van voorspelde signaalvormen (sjablonen) van partiële ontladingen. Deze voorspellingen zijn gebaseerd op systeem-identificatiemetingen en een standaard kabelmodel. Als gevolg van signaalvervormingen die niet in het model zijn opgenomen, bijvoorbeeld een MSR in de bewaakte kabelverbinding, zijn de voorspellingen niet altijd optimaal. Dit heeft een verslechterde detectiegevoeligheid tot gevolg. Een geautomatiseerde procedure om nieuwe signaalsjablonen te maken op basis van gemeten signalen is beschreven en getest op signalen die zijn gemeten tijdens online ontladingsmetingen aan verschillende kabelverbindingen. Het algoritme maakt nieuwe sjablonen voor zowel ontladingspulsen als storpulsen. Nieuwe sjablonen voor ontladingspulsen kunnen worden gebruikt om het model van de kabelverbinding te verbeteren. Sjablonen voor storpulsen kunnen worden gebruikt om deze storingen te herkennen en te verwerpen.

CONTENTS

INTRODUCTION

1.1 Medium-voltage cable networks

Underground power cables are a crucial component of the electricity distribution network in many parts of the world. In most densely-populated areas in developed countries the electricity distribution at medium-voltage (MV) level relies on underground power cables. In the Netherlands for example virtually 100% of the MV grid consists of underground power cables. Overhead lines are cheaper but have significant disadvantages, such as being visually intrusive and more vulnerable to damage caused by external factors, such as storms, ice formation, and vehicles hitting the lines.

The electricity network usually has a top-down structure and is organized by voltage level. At the power station the voltage is transformed to high-voltage level (HV: $> 36\,$kV). The transportation of energy over large distance takes place mainly over HV overhead lines. In large substations the voltage is transformed down to MV level ($1\,$kV - $36\,$kV). A number of MV feeders (typically $10 - 30$) are leaving the substation to distribute the power to customers in the region. In densely-populated areas, such as the Netherlands, these feeders usually consist of underground cables. A feeder is not a single cable, but is divided into a number of shorter sections that are interconnected by ring-main-units (RMUs) above ground. Depending on the situation, the length of a cable between two RMUs can vary from $100\,$m to $4\,$km. Most of the cables between two RMUs consist of multiple shorter cables that are connected together by underground joints. In most countries every RMU contains a busbar that connects multiple, usually two, incoming MV cables. The cables can be switched on and off the busbar. A transformer that transforms the medium voltage to low voltage (LV: $< 1\,$kV) is also connected to the busbar. LV cables or overhead lines leave the RMU to deliver power to customers in the neighborhood.

The MV cables are often laid out in a ring structure. The term ring-main-unit refers to the fact that RMUs are nodes in this ring. The ring structure has the advantage that
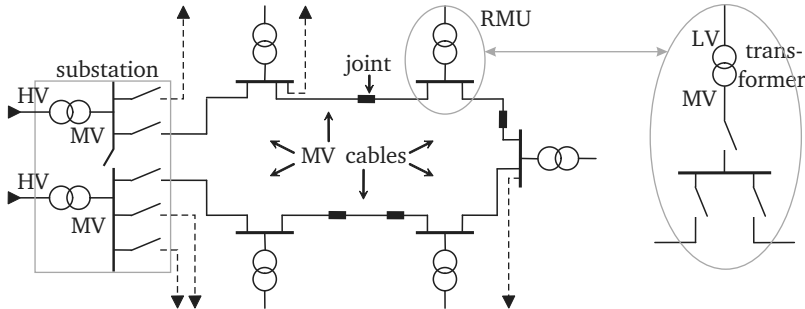
Figure 1.1 Example of a ring structure in an MV grid. The dashed lines represent MV cables that are not part of this ring.

the RMUs can be fed from both ends, so that if a cable between two RMUs breaks down power can be restored by a few switching operations in nearby RMUs. Therefore, the power delivery to customers can be restored before the cable is repaired. If a cable needs maintenance, the ring structure allows it to be isolated from the grid without interrupting power delivery to the customers. In practice there are many variations to this ring structure, such as connections between two different rings or a feeder going from one substation to another. In Figure 1.1 an example of a ring structure is depicted.

In many countries a huge expansion took place in the MV cable networks in the 60's and 70's. The cables installed in that period are nearing their designed end-of-life. Replacing all these cables in a relatively small time span would be a very costly operation. Instead, utilities prefer to repair or replace only the weak spots in the network so that it can operated with high reliability much longer than originally designed for. Condition based maintenance (CBM), as this strategy is called, requires knowledge on the current condition of the network. Also for newer cable networks it can be cost efficient to use CBM.

1.2 Online partial discharge diagnostics

A number of different techniques are available to estimate the current condition of components in the network. One of the proven methods to detect different types of defects in HV and MV components is diagnostics based on partial discharge (PD) measurement [3]. A partial discharge is a small charge displacement in the insulation of a component. A PD does not completely bridge the insulation between conductors, but is restricted to a small part, e.g. a cavity within the insulation. This cavity has a lower breakdown strength than the surrounding insulation. A PD does not directly lead to a complete insulation breakdown. Depending on the insulation type and defect location the time between the occurrence of the first PD and complete breakdown can vary from a couple of minutes to many years, in certain cases even decades. A PD measurement can therefore be

used to detect defects before they evolve into a complete breakdown and cause a power outage. Owing to the broad time range in which PDs may lead to insulation failure the interpretation of PD activity is crucial. Trends in PD behavior are indicative for changing insulation integrity, hence the arise of regular or even continuous PD diagnosis.

Advantages of online PD diagnosis

Until a couple of years ago only offline methods to detect and locate PDs in MV power cables were available [14, 26, 29, 45]. Offline means that the cable under test is isolated from the grid and an external power source is used to energize the cable. Online PD measurements have a number of advantages compared to offline PD measurements.

- There is no need to disconnect the cable under test. Every switching operation brings a small chance of equipment failure and can result in damage to the equipment and personal injury. Furthermore, depending on the network configuration, switching is not always possible without loss of power to some customers. Inductive sensors can be installed safely while the cable under test is live.

- The cable is not subjected to extra stress. Because offline measurement are applied only once in a while, e.g. once every year, it is necessary "to look far into the future" to predict an upcoming cable failure. This is done by increasing the applied voltage far above the nominal voltage. Tiny defects start discharging that would not yet be discharging under normal operation conditions. Even though they are small, PDs might degrade the insulation. Additionally, the increased voltage may lead directly to a complete breakdown somewhere along the cable that would not have happened under nominal voltage. Although such a cable is defective, it may operate for many years if no over-voltage is applied.

- An external high voltage source is not required.

- The PD measurement can be continuous because the cable remains in normal operation. The measurement equipment is installed on the cable under test for longer periods of time or even permanently. This brings a few huge advantages:

  - Monitoring the trend in PD activity gives important information on the severity of a defect. For example, a fast rising PD level is more dangerous than a sustained PD level of the same magnitude.
  - Depending on the type of defect and the environmental conditions, such as loading, the PD activity is not always constant. There can be periods during which there is no PD activity. An offline test conducted in that period will fail to detect the defect. Most defects in the joints in cross-linked polyethylene (XLPE) cables lead to a rapid breakdown within a few days or weeks of PD activity [10, 60]. The chance of detecting such a defect with a periodic offline measurement is small. Continuous online PD monitoring detects every period of PD activity.
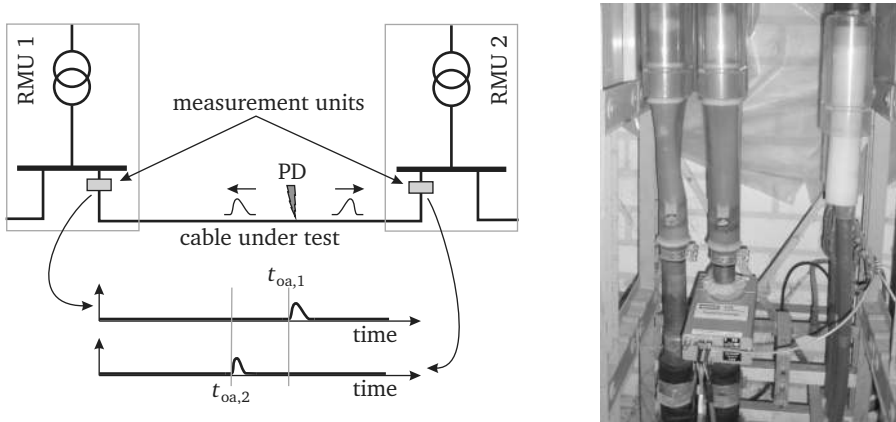
Figure 1.2 Left: Schematic drawing of online PD detection and location in an MV cable between two RMUs. The PD signals recorded by both sensors are also shown. Right: photo of measurement unit installed around cable.

Development of PD-OL

Since several years online PD monitoring systems that employ a separate sensor for each accessory are applied to HV cable systems [1, 17]. This type of system is relatively expensive. They can be applied cost-effectively to HV cable connections because the cost of a cable failure is high. For MV cable systems, where the cost of a failure is much lower, these systems are not cost effective. A cost-effective online PD detection and location system for MV cable circuits was investigated during the period 2001 – 2005 [50, 59]. The developed concept uses two inductive sensors, placed in the RMU at each cable end, that can be clamped around the cable under test or its earth connection. The research resulted in a proof-of-concept system that was tested on a setup consisting of two RMUs connected by a 300 m belted paper-insulated lead-covered (PILC) cable. In 2005 the system was introduced to the industry [64] and the development of a commercial system, named PD-OL (Partial Discharge monitoring, Online with Location), started. In Figure 1.2 an impression of a PD-OL system installed on an MV cable system is shown.

Basics of PD location

A power cable is a long homogeneous structure. A PD occurring somewhere in a cable will induce a voltage/current pulse with a duration in the order of magnitude of 1 ns. Because the cable is much longer that the wavelengths of a pulse this short the cable must be treated as high-frequency transmission line to predict the behavior. The pulse will travel along the cable in both directions. As it propagates through the cable its shape and amplitude will change due to attenuation and dispersion. At the end of the cable the pulse is detected by the measurement unit. The origin of the PD is determined by the difference

in time-of-arrival (t_{oa}) of the PD pulse at each end of the cable (see Figure 1.2) [59]:

$$z_{PD} = \tfrac{1}{2} l_c \left(1 - \frac{t_{oa,2} - t_{oa,1}}{t_c} \right) \tag{1.1}$$

where z_{PD} is the distance from RMU 1 to the PD origin, l_c is the total length of the cable, and t_c is the total propagation time of a pulse traveling from RMU 1 to RMU 2 (or vice versa). The time bases of both measurement units must aligned to establish an accurate difference in time-of-arrival ($t_{oa,2} - t_{oa,1}$). This is achieved by the injection of synchronization pulses by one measurement unit and the detection of these pulses by the unit at the other cable end, and vice versa. For this purpose each measurement unit contains an injection coil besides the current detection probe. Injection of a pulse and detection of the same pulse at the far end is also used to measure the total propagation time t_c of the cable.

The goal of PD location is to determine the physical location of a defect, allowing the utility the replace the defective component. Furthermore, if circuit data is available, the location gives the type of the component. Knowledge of the type of the defective component improves the reliability of the interpretation of PD measurements to a large extend. The PD location accuracy must be sufficient to be able to easily locate the physical location of the defect. A PD detection system locates the defect as a percentage of the total cable length. In order to convert this location to a physical location the exact cable length and cable route needs to be known. Depending on the utility, the accuracy of this information can vary from 5–10 m to being completely unknown for a few cases. A PD detection system should have at least the accuracy of the lower limit to make sure that it is not the limiting factor in locating the physical defect. Due to the attenuation and dispersion this accuracy is not achievable for cables longer than approximately 1 km. Due to the frequency-dependent attenuation it is more convenient to specify the location accuracy relative to the cable length. A relative PD location accuracy is generally valid for a large range of cable lengths. Practical experience shows that a location accuracy of 1% of the cable length is both achievable during field measurements and acceptable for locating the physical defect location [45, 64].

Noise reduction

PD measurements are impeded with noise and disturbances. During online PD measurements the noise and disturbance levels are higher than during an offline measurement because the cable under test remains connected to the rest of the grid. For the suppression of noise and disturbances the PD-OL system applies matched filters [50, 51] to the measured signals. Matched filtering is a technique to detect known signals in the presence of noise. It is optimal in the sense that it maximizes the signal-to-noise (SNR) ratio at the output of the filter, provided that the signal, the PD waveform, and noise spectrum are known. The measurement unit estimates the PD waveform and noise spectrum using a number of system identification measurements and a model of the power cable.

1.3 Research goals

Simultaneously to the development of the commercial PD-OL, scientific research continued to further improve the system and its applicability. The scientific research was split into two projects. The first project focuses on the technical challenges related to the large scale application of the system in various cable networks. The second project aims to develop knowledge rules for the automated interpretation of detected PD patterns to estimate the condition of the components in the cable circuit. This thesis addresses the first project. It deals with a number of different aspects of online PD monitoring. The challenges in this project are to extend the applicability of the system and to address issues encountered during the deployment of the commercial PD-OL system.

The scientific research conducted in the 2001 – 2005 period focused on PD monitoring of belted PILC cables because this is currently the most common cable type in use in MV networks in the Netherlands. Nowadays, virtually all the new MV cables being installed are cables with cross-linked polyethylene (XLPE) insulation. Therefore, XLPE cables will become increasingly prominent in the Dutch network. Outside the Netherlands most MV cable networks already have a majority of XLPE cables; many networks even are 100% XLPE insulated. *Research goal:* investigate the propagation of PD signals through, both single-core and three-core, XLPE cables.

The original proof-of-principle system was designed to monitor a single cable between two consecutive RMUs. It would be more efficient in terms of cost and effort if two or more consecutive cables could be monitored with a single system. This means that the PD pulses and the injected pulses have to travel through the RMU(s) that are in between. *Research goal:* investigate the influence of an RMU on the propagation of a pulse and its consequences for PD detection sensitivity and location accuracy. Not only the influence of RMUs on the propagation of (PD) pulses is important, but also that of large substations. The equipment found in some substations and RMUs does not allow installation of a measurement unit at the correct location. *Research goal:* find alternatives for monitoring the cables connected to substations and RMUs that do not allow installation of a measurement unit.

Currently, approximately 120 PD-OL systems are installed on cable circuits. During the installation of these systems in the networks of several utilities a couple of problematic circuits where encountered. For a variety of reasons the PD-OL equipment could not monitor those particular circuits. *Research goal:* evaluate these circuits and find appropriate solutions.

Accurate location of PDs is imperative for the identification and assessment of defects in cable circuits. The location of PDs is based on the estimation of the time-of-arrival of the PD pulse at each cable end. Previously, the arrival time was defined as the time instant that the measured pulse signal crossed a certain threshold. There are other methods to estimate time-of-arrival of a pulse. *Research goal:* determine which method yields the best results, i.e. the most accurate location of the PD origin, under the various circumstances that are encountered in practice.

Extraction of PD signals from a noisy measured signal is achieved by matched filters

[49–51]. For the construction of a matched filter a prediction of the PD waveform is required. This prediction is based on a local impedance measurement and a cable model. It does not take into account the characteristics of the particular cable under test or the influence of joints or RMUs along the cable under test. The predicted PD waveforms can therefore be sub-optimal and consequently the detection sensitivity and location accuracy degrade. Even if a filter is not optimal, it will still detect the larger PDs. The performance can be improved using detected PDs as PD waveform predictions for the construction of matched filters. *Research goal:* investigate how an adaptive matched filter bank can be achieved in a reliable and stable manner.

1.4   Thesis outline

Chapter 2 focuses on the power cable itself. It analyzes the propagation of PD signals through power cables with an emphasis on three-core cables with common earth screen. A measurement method to fully determine the properties of the multiple propagation channels of such a cable is presented. This method is applied to a three-core XLPE cable with common earth screen. A method to estimate the characteristic impedance and propagation velocity of XLPE cables, both single-core and three-core, using only information that is easily available is described.

In Chapter 3 other components of a cable network that are relevant for online PD diagnostics are discussed. This includes RMUs, substations and circuits with cross-bonding joints. In later chapters these models are used to analyze their effect on online PD monitoring. This chapter also analyzes some of the issues encountered during the large scale implementation of online PD monitoring in MV cable networks.

Different methods to determine the arrival time of PD pulses are described and compared in Chapter 4. Criteria for the comparison include the sensitivity to noise level, noise spectrum, PD pulse shape, reflections in the signal and the PD location accuracy. The methods are tested to these criteria analytically, using simulations, and using an experiment on a test setup consisting of a belted PILC cable between two RMUs.

The predictions of PD waveforms that are used to construct matched filters can be improved by using detected PD waveforms. Chapter 5 presents a method that achieves this. The method is tested on measurement data that was acquired during online PD measurements in three different cable circuits.

In the chapters mentioned above several aspects involved in online PD monitoring are analyzed in detail. In Chapter 6 these aspects are combined to analyze the options for online PD monitoring in different cable network configurations and installations. It discusses the implications of different configurations and installations on the PD detection sensitivity and location accuracy.

Chapter 7 summarizes the conclusions of the work presented in the thesis and contains a few recommendations for future work.

POWER CABLE MODEL

2.1 Introduction

The power cable needs to be modeled for understanding and analysis of the propagation of partial discharges through cable networks. If the propagation characteristics are known the PD magnitude and waveform of the measured signal at the cable ends can be predicted. This allows estimation of the PD charge at its origin from a measured PD signal and construction of matched filters for sensitive PD detection [51]. For high-frequency phenomena, such as PDs, a long homogeneous structure such as an underground power cable can be modeled as a transmission line. A transmission line is characterized by two parameters: the characteristic impedance Z_c and the propagation coefficient γ. The propagation coefficient incorporates both the attenuation coefficient α and the propagation velocity v_p.

A single-core power cable can be modeled as a coaxial two-conductor transmission line with a single propagation mode. For this type of cable accurate models to predict the transmission line parameters have been developed, e.g. [7, 48]. Literature on the modeling of three-core power cables, on the other hand, is scarce. There are many designs of three-core cables. They differ in applied insulation material, additional layers for electric field control, and protection against water ingress. Most designs apply a metallic earth screen around each individual core. For such a design the cores can be modeled as three uncoupled two-conductor transmission lines. A belted PILC cable, however, has a single metallic earth screen around the assembly of the cores. Some three-core XLPE cable designs also apply only a single metallic earth screen around the assembly of the three cores. This type of cable is widely used in the Netherlands. A three-core cable with common earth screen has multiple propagation modes and must be analyzed as a

---

Parts of this chapter have been accepted for publication [55, 56]

multiconductor transmission line. A PD occurring in the insulation will, depending on its location, induce a current in multiple modes. Therefore it is important to know the characteristics of all modes.

Much work has been done to develop accurate models to predict the transmission line parameters of single-core XLPE cables, e.g. [31, 33, 48, 57]. These models require detailed information on the cable construction and material properties. Unfortunately, not all required parameters are readily available, especially the dielectric properties of the semiconducting layers are hard to obtain. Even though the exact dielectric properties of the semiconducting layers are unknown it is possible to estimate Z_c and v_p using only parameters that are available from the cable manufacturer's specifications. This estimation is based on the assumption that the semiconducting layers have a much lower impedance than the XLPE insulation. The estimation method does not only apply to single-core XLPE cables, but can also be used to estimate the parameters of the multiple propagation channels in a three-core XLPE cables with common earth screen.

For single-core cables methods to measure Z_c and γ of a cable sample have been described, e.g. [34, 35, 52, 59]. It is impossible to use these methods to couple signals to and from all the individual (uncoupled) modes of a three-core cable with common earth screen without coupling to another mode as well. Therefore, these methods can not be applied directly to measure the parameters of each mode independently. It is possible, however, to combine the results of different measurements to determine the transmission line parameters of all propagation channels in such a cable.

In §2.2 the cable constructions studied in this chapter are described in detail. The (multiconductor) transmission line model is analyzed in §2.3 for both single-core and three-core power cables. This includes decoupling the multiple modes in three-core

Figure 2.1 Picture and schematic drawing of a typical single core XLPE cable. The drawing shows only the parts most relevant for estimating the propagation characteristics. Light gray: metallic parts (i.e. conductor and earth screen), dark gray: semiconducting layers (i.e. conductor screen, insulation screen and swelling tapes).

cables with common earth screen into three independent propagation modes and the interpretation of these modes. In §2.4 a method to estimate Z_c and v_p of single-core and three-core XLPE cables is discussed. A practical method to measure the transmission line parameters of single-core and three-core cables is presented in §2.5. This method is applied to several cable samples in §2.6. In this section the measured parameters are also compared to the parameters estimated using the method from §2.4. Finally, conclusions are drawn in §2.7.

2.2 Power cable constructions

The cable constructions considered in this chapter are summarized in this section. These constructions include the single-core XLPE cable, the belted PILC cable and the three-core XLPE cable with common earth screen. The cable layers and their properties relevant for the analysis as transmission line and for the estimation of Z_c and v_p are also indicated. More in-depth information on power cables can be found in books such as [4, 5].

2.2.1 Single-core XLPE cables

The cross-section of a typical single-core XLPE cable is depicted in Figure 2.1. The cable consists of the following layers:

- Conductor of aluminum or copper with radius r_c.

- Conductor screen, semiconducting layer extruded around conductor with thickness t_{cs} and complex permittivity $\epsilon_{r,cs}$ ($= \epsilon'_{r,cs} - j\epsilon''_{r,cs}$). For convenience the conductivity is incorporated in $\epsilon''_{r,cs}$.

- Insulation, most modern MV and HV cables use XLPE with complex relative permittivity $\epsilon_{r,insu}$ ($= \epsilon'_{r,insu} - j\epsilon''_{r,insu}$). For convenience the conductivity is incorporated in $\epsilon''_{r,insu}$.

- Insulation screen, semiconducting layer around insulation with thickness t_{is} and complex relative permittivity $\epsilon_{r,is}$ ($= \epsilon'_{r,is} - j\epsilon''_{r,is}$). For convenience the conductivity is incorporated in $\epsilon''_{r,is}$.

- Swelling tapes, many modern cables have semiconducting swelling tapes wrapped around the insulation screen. Because the electrical properties of this layer are assumed to be similar to the insulation screen [31], we consider these layers as one.

- Earth screen with inner radius r_s. Construction of this metallic screen depends on cable type. A widely used configuration consists of copper wires wrapped helically around the cable. These wires are held in place by a counter-wound copper tape. Some configuration also include an aluminum foil earth screen. Other configurations only apply an aluminum earth screen, without the copper wires. This chapter deals with all these constructions.
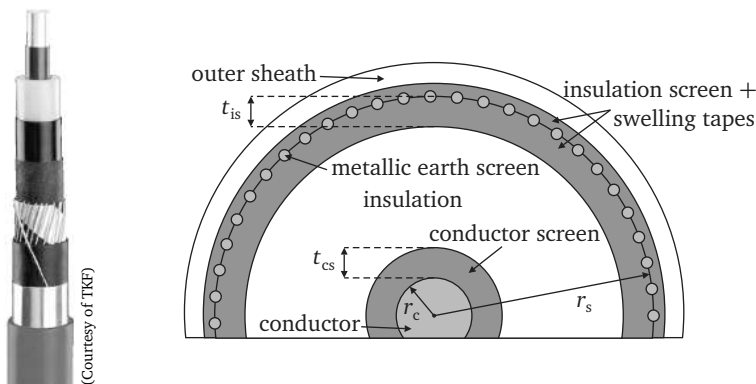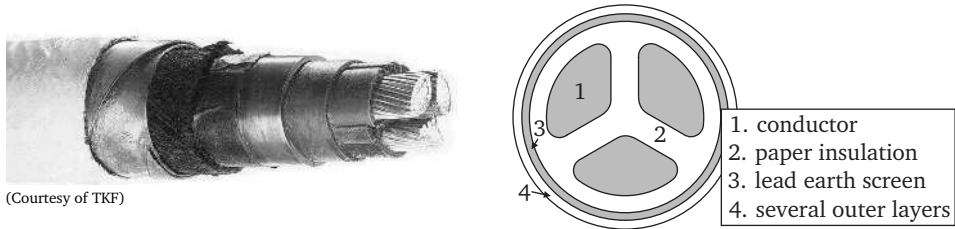
Figure 2.2 Picture and schematic drawing of a typical belted PILC cable. The drawing shows only the parts most relevant for estimating the propagation characteristics. Light gray: metallic parts (i.e. conductor and earth screen).

- Outer sheath, usually polyethylene (PE) or polyvinyl chloride (PVC). Layers outside the wire earth screen have virtually no influence on the characteristic impedance and propagation coefficient for the frequency range of interest [36].

2.2.2 Three-core belted PILC cables

One of the oldest designs of a three-core power cable with common earth screen is the belted paper-insulated lead-covered (PILC) cable. Even though nowadays they are rarely used in new cable circuits, in many countries the majority of the currently installed distribution-class cables are still PILC cables. A schematic drawing of the relevant parts is depicted in Figure 2.2. It consists of the following parts:

- Each core has:

  - Conductor of copper or aluminum.
  - Insulation of paper tape impregnated with a compound of oil, wax and resin.

- Belt of insulation around the assembly of the cores. The insulation consists of paper tape impregnated with a compound of oil, wax and resin.

- Solid lead sheath serving as earth screen and ensuring water-tightness.

- Several layers, such as bituminized paper, jute, steel armor, bituminized jute and chalk. Due to the good electrical screening of the lead sheath these layers have no influence on the propagation of signals through the cable.

2.2.3 Three-core XLPE cables

There are various constructions of three-core XLPE cables. Each core can be equipped with a metallic earth screen. From a transmission-line-modeling point-of-view each core in this type of cable behaves effectively as a separate single-core cable due to the electrical
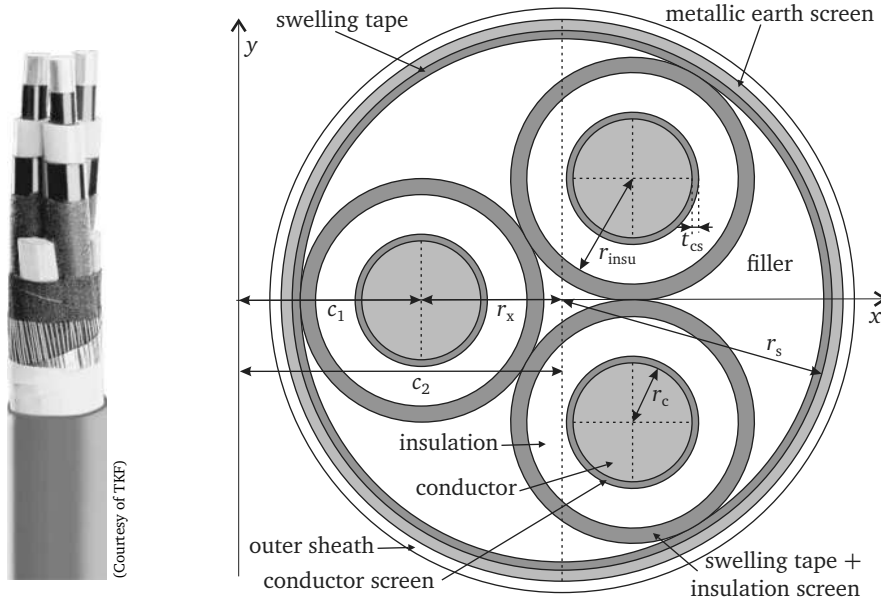
Figure 2.3 Picture and schematic drawing of a three core XLPE cable with common earth screen. The drawing shows only the parts most relevant for estimating the propagation characteristics. Light gray: metallic parts (i.e. conductor and earth screen), dark gray: semiconducting layers (i.e. conductor screen, insulation screen and swelling tapes)

screening of the metallic earth screen. Some designs, however, do not apply a metallic earth screen around individual cores. Instead, each separate core is only equipped with a semiconducting insulation screen and swelling tapes and a single earth screen is applied around the composition of all three cores. A schematic drawing is depicted in Figure 2.3. It consists of the following parts:

- Each core has:

  - Conductor with radius r_c.

  - Conductor screen, a semiconducting layer extruded around conductor with thickness t_{cs} and complex relative permittivity $\epsilon_{r,cs}$ $(= \epsilon'_{r,cs} - j\epsilon''_{r,cs})$. For convenience the conductivity is incorporated in $\epsilon''_{r,cs}$.

  - Insulation, usually XLPE, with outer radius r_{insu} and complex permittivity $\epsilon_{r,insu}$ $(= \epsilon'_{r,insu} - j\epsilon''_{r,insu})$. For convenience the conductivity is incorporated in $\epsilon''_{r,insu}$.

  - Insulation screen, a semiconducting layer around insulation with thickness t_{is} and complex relative permittivity $\epsilon_{r,is}$ $(= \epsilon'_{r,is} - j\epsilon''_{r,is})$. For convenience the conductivity is incorporated in $\epsilon''_{r,is}$.

   – Swelling tapes, in this paper considered to be part of the insulation screen.

- Filler, the space between the cores is filled with a filling material. This material has virtually no influence on the transmission line parameters of the cable.

- Swelling tapes, semiconducting swelling tapes cover all three cores and the filler.

- Metallic earth screen with inner radius r_s. This screen usually consists of helically wound copper wires.

- Outer sheath, usually PE, has no influence on the transmission line parameters due to the electrical screening of the the earth screen.

2.3   Transmission line model

A power cable is a long homogenous coaxial structure. For high frequencies (i.e. corresponding wavelength much shorter than the cable length) a coaxial structure such as a power cable can be modeled as a transmission line. A transmission line is usually characterized by two parameters: its characteristic impedance Z_c and propagation coefficient γ. If a transmission line is terminated by a load impedance (e.g. the impedance of an RMU) a pulse traveling through the transmission line and arriving at the load impedance will partially reflect on and partially transmit to the load impedance. These fractions are given by the reflection and transmission coefficients. This section discusses the basics of transmission lines and the definitions and derivations of the characteristic impedance, propagation coefficient and reflection and transmission coefficients for both single-core and three-core power cables.

2.3.1   Single-core cables

General transmission line theory for two-conductor transmission lines can be found in textbooks such as [39, 42]. Since transmission line theory is well established this section only summarizes the transmission line analysis and the parameters required later in this thesis.

Telegrapher's equations

The relation between the frequency-domain voltage $V(z)$ on the conductor with respect to the earth screen and the current $I(z)$ through the conductor at position z is described by the differential equations known as the Telegrapher's equations:

$$\begin{aligned}
\frac{\partial V(z)}{\partial z} &= -Z\, I(z) \\
\frac{\partial I(z)}{\partial z} &= -Y\, V(z)
\end{aligned} \tag{2.1}$$

where Z is the distributed series impedance Z and Y the distributed shunt admittance. These parameters can be expressed in terms of the resistance R, inductance L, conductance G and capacitance C:

$$
\begin{aligned}
Z &= R + j\omega L \\
Y &= G + j\omega C
\end{aligned}
\tag{2.2}
$$

All these parameters can be frequency-dependent.

Characteristic impedance and propagation coefficient

The solution of Eq. 2.1 consists of forward and backward traveling waves:

$$
\begin{aligned}
V(z) &= V^+(0)\,e^{-\gamma z} + V^-(0)\,e^{+\gamma z} \\
I(z) &= I^+(0)\,e^{-\gamma z} - I^-(0)\,e^{+\gamma z}
\end{aligned}
\tag{2.3}
$$

where V^+ and I^+ describe the forward traveling wave, V^- and I^- the backward traveling wave, and γ is the frequency-dependent propagation coefficient. The propagation coefficient is given by:

$$
\gamma = \sqrt{ZY} \stackrel{\text{def}}{=} \alpha + j\beta
\tag{2.4}
$$

The real part of γ is the attenuation coefficient α in Nepers/m (Np/m). This frequency-dependent parameter describes the attenuation due to losses as waves propagate through the transmission line. The imaginary part β of γ is the phase coefficient in radians per meter (rad/m). It can be converted to the frequency-dependent propagation velocity v_{p} (also called phase velocity and wave velocity) in meters per second (m/s):

$$
v_{\mathrm{p}} = \frac{\omega}{\beta}
\tag{2.5}
$$

The ratio between voltage and current of a traveling wave at any point on the cable is the characteristic impedance Z_{c} in ohm (Ω):

$$
Z_{\mathrm{c}} = \frac{V^+(z)}{I^+(z)} = \frac{V^-(z)}{I^-(z)} = \sqrt{\frac{Z}{Y}}
\tag{2.6}
$$

Reflection and transmission coefficients

Consider a transmission line terminated by load impedance Z_{L}. This load impedance is not necessarily a discrete impedance. It can also be the characteristic impedance of another transmission line. If Z_{L} is not equal to Z_{c} an incoming wave will partially reflect on and partially transmit to Z_{L}. The ratio between the voltage of the incident wave and the reflected wave is called the voltage reflection coefficient (Γ_V). Similarly, the ratio between the current of the incident and reflected wave is the current reflection coefficient (Γ_I). The voltage and current transmission coefficients (τ_V and τ_I) are defined as the ratio of

the transmitted voltage or current and the incident voltage or current. The reflection and transmission coefficients can be calculated using the continuity of the voltage and current at the interface:

$$V^{\mathrm{i}} + V^{\mathrm{r}} = V^{\mathrm{t}}$$
$$I^{\mathrm{i}} - I^{\mathrm{r}} = I^{\mathrm{t}} \tag{2.7}$$

where V^{i}, V^{r} and V^{t} are the voltages and I^{i}, I^{r} and I^{t} are the currents of the incident, reflected and transmitted waves. The polarity of the currents is taken positive in the traveling direction of the corresponding wave. Combining these equations with

$$V^{\mathrm{i}} = Z_{\mathrm{c}} I^{\mathrm{i}}, \qquad V^{\mathrm{r}} = Z_{\mathrm{c}} I^{\mathrm{r}} \qquad \text{and} \qquad V^{\mathrm{t}} = Z_{\mathrm{L}} I^{\mathrm{t}}$$

results in the following expressions for the voltage (Γ_V) and current (Γ_I) reflection coefficients:

$$\Gamma_V \stackrel{\text{def}}{=} \frac{V^{\mathrm{r}}}{V^{\mathrm{i}}} = \frac{Z_{\mathrm{L}} - Z_{\mathrm{c}}}{Z_{\mathrm{L}} + Z_{\mathrm{c}}} \qquad \text{and} \qquad \Gamma_I \stackrel{\text{def}}{=} \frac{I^{\mathrm{r}}}{I^{\mathrm{i}}} = \frac{Z_{\mathrm{L}} - Z_{\mathrm{c}}}{Z_{\mathrm{L}} + Z_{\mathrm{c}}} \tag{2.8}$$

and the voltage (τ_V) and current (τ_I) transmission coefficients:

$$\tau_V \stackrel{\text{def}}{=} \frac{V^{\mathrm{t}}}{V^{\mathrm{i}}} = \frac{2Z_{\mathrm{L}}}{Z_{\mathrm{L}} + Z_{\mathrm{c}}} \qquad \text{and} \qquad \tau_I \stackrel{\text{def}}{=} \frac{I^{\mathrm{t}}}{I^{\mathrm{i}}} = \frac{2Z_{\mathrm{c}}}{Z_{\mathrm{L}} + Z_{\mathrm{c}}} \tag{2.9}$$

.

2.3.2 Three-core cables

General multiconductor transmission line theory can be found in many textbooks, e.g. [37]. This section summarizes the multiconductor transmission line analysis specific for a three-core power cable with common earth screen, such as depicted in Figure 2.2 or Figure 2.3. A three-core cables with a metallic earth screen around each core can be considered as three independent single-conductor transmission lines (see §2.3.1). A three-core cable has three identical conductors which have cyclic symmetry with respect to the common earth screen. The earth screen serves as the reference conductor. Due to the rotational symmetry of the three conductors the impedance matrix **Z** has only two distinct values. The self impedances Z_{s} on the diagonal are equal and all mutual impedances Z_{m}, the off-diagonal elements, are equal. For the admittance matrix **Y** the same considerations apply. The self and mutual impedances and admittances are a function of the cable geometry and material properties. They are frequency-dependent and incorporate effects such as skin and proximity effect, increased inductance due to the helical lay of the wire earth screen and dielectric losses in the insulation and semiconducting layers.

Telegrapher's equations

A three-core power cable has three conductors and a metallic earth screen, which serves as the reference/ground conductor. The frequency-domain voltages on and currents through

the three core conductors at position z along the transmission line can be defined as column vectors $\mathbf{V}$ and $\mathbf{I}$:

$$
\begin{aligned}
\mathbf{V} &= \begin{pmatrix} V_1 & V_2 & V_3 \end{pmatrix}^T \\
\mathbf{I} &= \begin{pmatrix} I_1 & I_2 & I_3 \end{pmatrix}^T
\end{aligned}
\tag{2.10}
$$

where V_i is the voltage of the ith conductor (with respect to the earth screen) and I_i is the current through the ith conductor. The Telegrapher's equations relating the voltages and currents at position z become:

$$
\begin{aligned}
\frac{\partial}{\partial z}\mathbf{V}(z) &= -\mathbf{Z}\,\mathbf{I}(z) \\
\frac{\partial}{\partial z}\mathbf{I}(z) &= -\mathbf{Y}\mathbf{V}(z)
\end{aligned}
\tag{2.11}
$$

where $\mathbf{Z}$ is the (3×3) per-unit-length impedance matrix, and $\mathbf{Y}$ the (3×3) per-unit-length admittance matrix:

$$
\mathbf{Z} = \begin{pmatrix} Z_s & Z_m & Z_m \\ Z_m & Z_s & Z_m \\ Z_m & Z_m & Z_s \end{pmatrix}
\quad \text{and} \quad
\mathbf{Y} = \begin{pmatrix} Y_s & Y_m & Y_m \\ Y_m & Y_s & Y_m \\ Y_m & Y_m & Y_s \end{pmatrix}
\tag{2.12}
$$

Modal analysis

Eq. 2.11 can be decoupled by applying a transformation matrix. Let the modal voltages $\mathbf{V}_{\text{m}}$ and currents $\mathbf{I}_{\text{m}}$ be defined as:

$$
\begin{aligned}
\mathbf{V} &\overset{\text{def}}{=} \mathbf{T}_V \mathbf{V}_{\text{m}} \\
\mathbf{I} &\overset{\text{def}}{=} \mathbf{T}_I \mathbf{I}_{\text{m}}
\end{aligned}
\tag{2.13}
$$

where $\mathbf{T}_I$ and $\mathbf{T}_V$ are transformation matrices that define the transformation between the voltages and currents of the individual conductors to the modal quantities. From Eq. 2.11 and Eq. 2.13 the wave equations for the modal voltages and currents are obtained:

$$
\begin{aligned}
\frac{\partial^2}{\partial z^2}\mathbf{V}_{\text{m}}(z) &= \mathbf{T}_V^{-1}\mathbf{Z}\mathbf{Y}\mathbf{T}_V\mathbf{V}_{\text{m}}(z) = \mathbf{Z}_{\text{m}}\mathbf{Y}_{\text{m}}\mathbf{V}_{\text{m}}(z) \\
\frac{\partial^2}{\partial z^2}\mathbf{I}_{\text{m}}(z) &= \mathbf{T}_I^{-1}\mathbf{Y}\mathbf{Z}\mathbf{T}_I\mathbf{I}_{\text{m}}(z) = \mathbf{Y}_{\text{m}}\mathbf{Z}_{\text{m}}\mathbf{I}_{\text{m}}(z)
\end{aligned}
\tag{2.14}
$$

where $\mathbf{Z}_{\text{m}} = \mathbf{T}_V^{-1}\mathbf{Z}\mathbf{T}_I$ and $\mathbf{Y}_{\text{m}} = \mathbf{T}_I^{-1}\mathbf{Y}\mathbf{T}_V$. The transformation matrices $\mathbf{T}_V$ and $\mathbf{T}_I$ must be chosen such that the equations become decoupled, i.e. the matrices $\mathbf{T}_V^{-1}\mathbf{Z}\mathbf{Y}\mathbf{T}_V$ and $\mathbf{T}_I^{-1}\mathbf{Y}\mathbf{Z}\mathbf{T}_I$ are diagonal. The columns of $\mathbf{T}_V$ are the eigenvectors of $\mathbf{Z}\mathbf{Y}$ and the columns of $\mathbf{T}_I$ the eigenvectors of $\mathbf{Y}\mathbf{Z}$ [37, 38]. We choose a set of eigenvectors corresponding to two

distinct eigenvalues, of which one is two-fold degenerate, such that we obtain convenient propagation modes. The transformations matrices are given by:

$$\mathbf{T}_V = \begin{pmatrix} 1 & \frac{1}{3} & \frac{1}{3} \\ 1 & -\frac{2}{3} & \frac{1}{3} \\ 1 & \frac{1}{3} & -\frac{2}{3} \end{pmatrix} \qquad \mathbf{T}_I = \begin{pmatrix} \frac{1}{3} & \frac{2}{3} & \frac{2}{3} \\ \frac{1}{3} & -\frac{4}{3} & \frac{2}{3} \\ \frac{1}{3} & \frac{2}{3} & -\frac{4}{3} \end{pmatrix} \tag{2.15}$$

These transformation matrices decompose the propagation modes in a three-core power cable with common earth screen into three uncoupled modes: the shield-to-phase (SP) mode and two phase-to-phase (PP) modes. The SP mode travels in the propagation channel between shield and the three phases together. The voltage V_{sp} and current I_{sp} of this mode are defined as:

$$\begin{aligned} V_{sp} &\overset{\text{def}}{=} \tfrac{1}{3}(V_1 + V_2 + V_3) \\ I_{sp} &\overset{\text{def}}{=} I_1 + I_2 + I_3 \end{aligned} \tag{2.16}$$

The voltage $V_{pp,1}$ and current $I_{pp,1}$ of the first PP channel is defined as:

$$\begin{aligned} V_{pp,1} &\overset{\text{def}}{=} V_1 - V_2 \\ I_{pp,1} &\overset{\text{def}}{=} \tfrac{1}{2}\left(I_1 - I_2\right) \end{aligned} \tag{2.17}$$

The voltage $V_{pp,2}$ and current $I_{pp,2}$ of the second PP channel are similar except that V_2 and I_2 are replaced by respectively V_3 and I_3. Applying $\mathbf{T}_V$ and $\mathbf{T}_I$ to Eq. 2.13 verifies that the modal voltages and current are equal to the defined SP and PP channels:

$$\begin{aligned} \mathbf{V}_{\mathrm{m}} &= \begin{pmatrix} V_{sp} & V_{pp,1} & V_{pp,2} \end{pmatrix}^T \\ \mathbf{I}_{\mathrm{m}} &= \begin{pmatrix} I_{sp} & I_{pp,1} & I_{pp,2} \end{pmatrix}^T \end{aligned} \tag{2.18}$$

.

Characteristic impedance and propagation coefficient

The solution of the differential equations in Eq. 2.14 is a superposition of forward and backward traveling waves:

$$\begin{aligned} \mathbf{V}_{\mathrm{m}}(z) &= e^{-\gamma_{\mathrm{m}} z}\mathbf{V}_{\mathrm{m}}^+(0) + e^{\gamma_{\mathrm{m}} z}\mathbf{V}_{\mathrm{m}}^-(0) \\ \mathbf{I}_{\mathrm{m}}(z) &= e^{-\gamma_{\mathrm{m}} z}\mathbf{I}_{\mathrm{m}}^+(0) - e^{\gamma_{\mathrm{m}} z}\mathbf{I}_{\mathrm{m}}^-(0) \end{aligned} \tag{2.19}$$

where the diagonal transmission coefficient matrix $\boldsymbol{\gamma}_{\mathrm{m}}$ is given by:

$$\boldsymbol{\gamma}_{\mathrm{m}} = \sqrt{\mathbf{Y}_{\mathrm{m}}\mathbf{Z}_{\mathrm{m}}} = \sqrt{\mathbf{Z}_{\mathrm{m}}\mathbf{Y}_{\mathrm{m}}} \tag{2.20}$$

The relation between voltage and current for the forward or backward traveling waves is given by the characteristic impedance matrix $\mathbf{Z}_c$:

$$\mathbf{V} = \mathbf{Z}_c\mathbf{I} \tag{2.21}$$

Similarly, a diagonal modal characteristic impedance matrix $\mathbf{Z}_{c,m}$ can be defined:

$$\mathbf{V}_m = \mathbf{Z}_{c,m}\mathbf{I}_m \tag{2.22}$$

which is related to $\mathbf{Z}_c$ according:

$$\mathbf{Z}_{c,m} = \mathbf{T}_V^{-1}\mathbf{Z}_c\mathbf{T}_I = \begin{pmatrix} Z_{sp} & 0 & 0 \\ 0 & Z_{pp} & 0 \\ 0 & 0 & Z_{pp} \end{pmatrix} \tag{2.23}$$

The expressions for the SP and PP mode characteristic impedances and propagation coefficients can be obtained from the diagonal components of Eq. 2.19 and Eq. 2.22:

$$Z_{sp} = \frac{V_{sp}}{I_{sp}} \qquad \text{with} \qquad \begin{aligned} V_{sp}(z) &= e^{-\gamma_{sp}z}V_{sp}^+(0) + e^{\gamma_{sp}z}V_{sp}^-(0) \\ I_{sp}(z) &= e^{-\gamma_{sp}z}I_{sp}^+(0) - e^{\gamma_{sp}z}I_{sp}^-(0) \end{aligned} \tag{2.24}$$

and

$$Z_{pp} = \frac{V_{pp,k}}{I_{pp,k}} \qquad \text{with} \qquad \begin{aligned} V_{pp,k}(z) &= e^{-\gamma_{pp}z}V_{pp,k}^+(0) + e^{\gamma_{pp}z}V_{pp,k}^-(0) \\ I_{pp,k}(z) &= e^{-\gamma_{pp}z}I_{pp,k}^+(0) - e^{\gamma_{pp}z}I_{pp,k}^-(0) \end{aligned} \tag{2.25}$$

where k is either 1 or 2. Owing to the rotational symmetry both PP channels have equal transmission line parameters.

The characteristic impedance matrix $\mathbf{Z}_c$ in terms of the SP and PP impedances is obtained from Eq. 2.23:

$$\mathbf{Z}_c = \begin{pmatrix} Z_{sp} + \frac{1}{3}Z_{pp} & Z_{sp} - \frac{1}{6}Z_{pp} & Z_{sp} - \frac{1}{6}Z_{pp} \\ Z_{sp} - \frac{1}{6}Z_{pp} & Z_{sp} + \frac{1}{3}Z_{pp} & Z_{sp} - \frac{1}{6}Z_{pp} \\ Z_{sp} - \frac{1}{6}Z_{pp} & Z_{sp} - \frac{1}{6}Z_{pp} & Z_{sp} + \frac{1}{3}Z_{pp} \end{pmatrix} \tag{2.26}$$

The parameters of the SP and PP channel (Eq. 2.24 and Eq. 2.25) can be expressed in terms of the self and mutual impedances (Z_s and Z_m) and admittances (Y_s and Y_m):

$$\begin{aligned} Z_{sp} &= \frac{1}{3}\sqrt{\frac{Z_s + 2Z_m}{Y_s + 2Y_m}} \\ Z_{pp} &= 2\sqrt{\frac{Z_s - Z_m}{Y_s - Y_m}} \\ \gamma_{sp} &= \sqrt{(Z_s + 2Z_m)(Y_s + 2Y_m)} \\ \gamma_{pp} &= \sqrt{(Z_s - Z_m)(Y_s - Y_m)} \end{aligned} \tag{2.27}$$

Reflection and transmission coefficients

Reflection and transmission coefficients can be defined for a multiconductor transmission line similar to those of a two-conductor transmission line. Again the reflection and transmission coefficients can be calculated using the knowledge that the voltages and currents at the interface are continuous:

$$\mathbf{V}^{\text{i}} + \mathbf{V}^{\text{r}} = \mathbf{V}^{\text{t}}$$
$$\mathbf{I}^{\text{i}} - \mathbf{I}^{\text{r}} = \mathbf{I}^{\text{t}}$$

(2.28)

where $\mathbf{V}^{\text{i}}$, $\mathbf{V}^{\text{r}}$, $\mathbf{V}^{\text{t}}$ are the voltages and $\mathbf{I}^{\text{i}}$, $\mathbf{I}^{\text{r}}$, $\mathbf{I}^{\text{t}}$ are the currents of the incident, reflected and transmitted waves, respectively. The polarity of the currents is again taken positive in the traveling direction of the corresponding wave.

The voltage reflection and transmission coefficient matrices $\mathbf{\Gamma}_V$ and $\mathbf{\tau}_V$ and the current reflection and transmission coefficient matrices $\mathbf{\Gamma}_I$ and $\mathbf{\tau}_I$ are defined as:

$$\mathbf{V}^{\text{r}} \stackrel{\text{def}}{=} \mathbf{\Gamma}_V \mathbf{V}^{\text{i}} \quad \text{and} \quad \mathbf{V}^{\text{t}} \stackrel{\text{def}}{=} \mathbf{\tau}_V \mathbf{V}^{\text{i}}$$
$$\mathbf{I}^{\text{r}} \stackrel{\text{def}}{=} \mathbf{\Gamma}_I \mathbf{I}^{\text{i}} \quad \text{and} \quad \mathbf{I}^{\text{t}} \stackrel{\text{def}}{=} \mathbf{\tau}_I \mathbf{I}^{\text{i}}$$

(2.29)

Applying Eq. 2.28 and Eq. 2.29 yields the reflection and transmission coefficient matrices:

$$\mathbf{\Gamma}_V = \left(\mathbf{Z}_{\text{L}} - \mathbf{Z}_{\text{c}} \right) \left(\mathbf{Z}_{\text{L}} + \mathbf{Z}_{\text{c}} \right)^{-1} \quad \text{and} \quad \mathbf{\tau}_V = \mathbf{1} + \mathbf{\Gamma}_V$$
$$\mathbf{\Gamma}_I = \mathbf{Z}_{\text{c}}^{-1} \mathbf{\Gamma}_V \mathbf{Z}_{\text{c}} \quad \text{and} \quad \mathbf{\tau}_I = \mathbf{1} - \mathbf{\Gamma}_I$$

(2.30)

where $\mathbf{1}$ is the identity matrix.

2.4   Parameter estimation for XLPE cables

Theoretical models of the transmission line parameters of power cables, e.g. [31, 33, 48, 57], require detailed knowledge of the cable parameters. Generally, the cable manufacturer can supply most of them, but not all. Especially, the frequency-dependent complex relative permittivity ϵ_{r} of the semiconducting layers at high frequencies is usually not available. Accurate measurement of ϵ_{r} is possible, but complicated [31, 68]. Estimation of the transmission line parameters, using only information that is readily available from the cable manufacturer, is described in this section.

2.4.1   Single-core cables

Characteristic impedance

For the frequency range of interest the series impedance Z is primarily determined by the inductance L and the shunt admittance Y by C. Assuming $Z = j\omega L$ and $Y = j\omega C$ reduces Eq. 2.6 to:

$$Z_{\text{c}} = \sqrt{\frac{L}{C}}$$

(2.31)
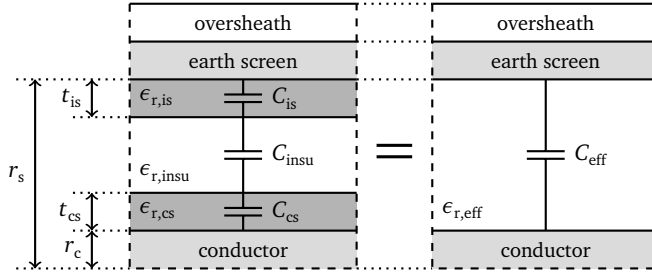
Figure 2.4 Relation between the complex capacitances C_{cs} – C_{insu} – C_{is} and C_{eff}.

Substitution of L and C with their equations for a coaxial structure yields:

$$Z_c = \frac{1}{2\pi} \sqrt{\frac{\mu_0 \mu_r}{\epsilon_0 \epsilon_r}} \ln\left(\frac{r_s}{r_c}\right) \qquad (2.32)$$

The relative permeability μ_r of the insulation and semiconducting layers is equal to one. The complex relative permittivity of the insulation $\epsilon_{r,insu}$ differs from the relative permittivity of the conductor screen $\epsilon_{r,cs}$ and the insulation screen $\epsilon_{r,is}$. Therefore, ϵ_r in equation Eq. 2.32 is replaced by an effective permittivity $\epsilon_{r,eff}$. This is the relative permittivity of the homogeneous insulation material of a fictive coaxial capacitor with the same total capacitance and inner and outer radius (respectively r_c and r_s). The capacitance of a single-core XLPE cable with semiconducting screens is a series of three (complex) capacitances: C_{cs} for the conductor screen, C_{insu} for the XLPE insulation, and C_{is} for the insulation screen. Figure 2.4 depicts the capacitances of the insulation and semiconducting layers and their relation to the effective capacitance C_{eff}.

For frequencies up to at least several tens of MHz C_{insu} is much smaller than C_{cs} and C_{is} because (i) the relative permittivity (both ϵ_r' and ϵ_r'') of the semiconducting layers is much larger than for XLPE [6, 31, 68], and (ii) the insulation is much thicker. Therefore, $C_{cs} \gg C_{insu}$ and $C_{is} \gg C_{insu}$, and thus $C_{eff} \approx C_{insu}$. Because XLPE has extremely low losses $\epsilon_{r,insu} \approx \epsilon_{r,insu}'$. The effective relative permittivity can therefore be expressed in terms of $\epsilon_{r,insu}'$ and the cable dimensions:

$$C_{eff} = \frac{2\pi\epsilon_0 \epsilon_{r,eff}}{\ln\left(\frac{r_s}{r_c}\right)} \approx \frac{2\pi\epsilon_0 \epsilon_{r,insu}'}{\ln\left(\frac{r_s - t_{is}}{r_c + t_{cs}}\right)}$$

$$\epsilon_{r,eff} \approx \epsilon_{r,insu}' \frac{\ln\left(\frac{r_s}{r_c}\right)}{\ln\left(\frac{r_s - t_{is}}{r_c + t_{cs}}\right)} \qquad (2.33)$$

This equation shows that $\epsilon_{r,eff}$ is always larger than $\epsilon_{r,insu}'$. For a typical $240\,\text{mm}^2$ $6/10\,\text{kV}$ cable where $r_c = 9.0\,\text{mm}$, $t_{cs} = 0.7\,\text{mm}$, $t_{is} = 0.7\,\text{mm}$ and $r_s = 13.8\,\text{mm}$ $\epsilon_{r,eff}$ is $1.4\times$

larger than $\epsilon'_{\text{r,insu}}$. Note that for XLPE insulation $\epsilon'_{\text{r,insu}}$ is frequency-independent for the frequency range up to several tens of MHz, the range required for most diagnostic tools applied on power cables [32].

Combining Eq. 2.32 and Eq. 2.33 yields:

$$
\begin{aligned}
Z_c &\approx \frac{1}{2\pi} \sqrt{\frac{\mu_0}{\epsilon_0 \epsilon_{\text{r,eff}}}} \ln\left(\frac{r_s}{r_c}\right) \\
&\approx \frac{1}{2\pi} \sqrt{\frac{\mu_0}{\epsilon_0 \epsilon'_{\text{r,insu}}}} \ln\left(\frac{r_s}{r_c}\right) \ln\left(\frac{r_s - t_{\text{is}}}{r_c + t_{\text{cs}}}\right)
\end{aligned}
\tag{2.34}
$$

Propagation velocity

The propagation velocity is determined by the imaginary part β of the propagation coefficient. The β is predominantly determined by the inductance and capacitance. Therefore, we assume $Z = j\omega L$ and $Y = j\omega C$. This reduces Eq. 2.4 to:

$$
\gamma = \sqrt{j\omega L\, j\omega C} = j\omega \sqrt{L\,C}
\tag{2.35}
$$

The propagation velocity can be approximated by:

$$
v_p = \frac{1}{\sqrt{L\,C}}
\tag{2.36}
$$

For homogeneous media $LC = \epsilon_0 \epsilon_r \mu_0 \mu_r$ [37]. However, the material between conductor and (wire) screen is not homogeneous. Therefore, ϵ_r has to be replaced $\epsilon_{\text{r,eff}}$ as derived in equation Eq. 2.33.

If the cable has a helical wire screen the velocity v_p is also affected by the helical lay of the wire screen. The conductive current over the individual wires of the screen can hardly cross over. The charges of a pulse in the wire tend to follow the helical lay [19, 36, 67]. Therefore, the pulse must travel a longer distance, resulting in a lowered velocity along the cable axis. Assuming a helical wire screen with a "large" number of wires (> 10), sufficiently low frequencies (below several tens of MHz), and a straight conductor the correction factor F_{hl} for the velocity is given by [19]:

$$
F_{\text{hl}} = \frac{1}{\sqrt{1 + \frac{1 - \left(\frac{r_c}{r_s}\right)^2}{2\ln\left(\frac{r_s}{r_c}\right)} \left(\frac{2\pi r_s}{l_l}\right)^2}}
\tag{2.37}
$$

with l_l the lay length, this is the longitudinal distance along the cable required for one complete helical wrap of one wire. Note that F_{hl} is always larger (i.e. closer to 1) than the extra length of the helical lay relative to the axial length would result in directly. This is in agreement with the simulation in [36]. From this observation, it is apparent that the pulses do not completely follow the helical lay of the wire screen.

Note that Eq. 2.37 does not take into account the following aspects:

- Semiconducting layers. The presence of semiconducting layers may have an influence on the factor F_{hl} because charges can transfer from one wire to another more easily.

- Stranded core conductors. These strands also have a helical lay. Usually, the helical lay length of the conductor strands is much shorter than the lay length of the wire screen, but the capacitive/conductive coupling between these wires is much stronger than between the earth screen wires. Therefore, the helical lay of conductor strands has negligible influence on the propagation velocity.

- Some wire screens with a helical lay do not have a constant angle between wire and cable axis. Instead, the lay angle goes back and forth. In this situation correction factor is expected to be between the value for a helical screen given by Eq. 2.37 and the value 1 if no helical screen is present.

Combining Eq. 2.33, Eq. 2.36 and Eq. 2.37 the velocity can be approximated with:

$$v_p \approx \frac{c \cdot F_{hl}}{\sqrt{\epsilon_{r,eff}}} = \frac{c \cdot F_{hl}}{\sqrt{\epsilon'_{r,insu}}} \sqrt{\frac{\ln\left(\frac{r_s - t_{is}}{r_c + t_{cs}}\right)}{\ln\left(\frac{r_s}{r_c}\right)}} \tag{2.38}$$

where c is the speed of light in vacuum ($c = 1/\sqrt{\epsilon_0 \mu_0}$). For cables with an aluminum foil earth screen the factor F_{hl} must be omitted. Note that the approximated v_p is independent of the frequency if $\epsilon'_{r,insu}$ is frequency-independent, which is true over a wide frequency range for XLPE. In reality the propagation velocity of most XLPE cables has a small frequency dependency, especially for frequencies below 1 MHz. This is shown in the experiments presented in §2.6.

Attenuation

For convenience, the dielectric losses (described by ϵ''_r) are incorporated into G, making C real-valued. The attenuation is determined by the real part of the propagation coefficient. Therefore, R and G must be taken into account for the calculation of the attenuation. Assuming $R \ll \omega L$ and $G \ll \omega C$, with Eq. 2.4, the attenuation becomes:

$$\alpha \approx \tfrac{1}{2} R \sqrt{\frac{C}{L}} + \tfrac{1}{2} G \sqrt{\frac{L}{C}} \stackrel{def}{=} \alpha_R + \alpha_G \tag{2.39}$$

The attenuation can be split in two parts: α_R and α_G. The first part, α_R, is the attenuation caused by losses in the conductor and earth screen. Due to the skin effect, the conductor and earth screen resistances are proportional to the square root of the frequency, i.e. $\alpha_R \propto \sqrt{\omega}$. The second part, α_G, is caused by the losses in the insulation and semi-conducting layers. Since XLPE has a very small loss tangent the losses in the semi-conducting screens are dominant. Due to the large variation in the properties of

the semiconducting layers [31, 68] it is not possible to estimate the attenuation with reasonable accuracy without knowledge of the exact properties of the semiconducting layers of the cable under test. For most cables however, the dielectric losses increase approximately linearly with frequency: $\alpha_G \propto \omega$. In [33, 67] it is shown that for lower frequencies α_R is dominant while for higher frequencies α_G becomes dominant. The cut-off frequency where α_G starts having a significant influence on the total attenuation can be as low as 1 MHz.

Being unable to accurately estimate the attenuation α does not have a significant influence on PD detection and location. If the charge of a PD is estimated by the time-integral of the current, a different attenuation does not significantly change estimated charge. The attenuation also does not have a significant influence on PD location.

2.4.2   Three-core cables

In order to calculate the characteristic impedance and propagation coefficient of the SP and PP channel, the self-impedance/admittance (Z_s and Y_s) of each phase and the mutual-impedance/admittance between phases (Z_m and Y_m) are required. These impedances and admittances can be converted to Z_{sp}, Z_{pp}, γ_{sp} and γ_{pp} using Eq. 2.27. Again we assume that the impedances are dominated by the inductances: $Z_s = j\omega L_s$ and $Z_m = j\omega L_m$. And that the admittances are dominated by the capacitances: $Y_s = j\omega C_s$ and $Y_m = j\omega C_m$. Next, the values for L_s, L_m, C_s and C_m have to be determined. These parameters can be estimated using numerical methods, such as the boundary element method (BEM) [70]. The main disadvantage of this method is that it requires dedicated software. Another option is to estimate the parameters analytically using conformal mapping [40, 41].

BEM estimation

In order to determine the self and mutual capacitances, conductor i is set to 1 V, while the other conductors are set to 0 V. From the electric field distribution the associated charge on each conductor j is determined, which is equal to the capacitance c_{ij}. The inductances can be determined in a similar fashion by sending a current of 1 A through the ith conductor, 0 A through the other conductors. From the simulated magnetic flux the inductance matrix can be constructed. Alternatively, if the cable does not contain any components with a $\mu_r \neq 1$ the inductance matrix $\mathbf{L}$ can be directly obtained from the free-space capacitance matrix $\mathbf{C}_0$ (capacitance matrix when ϵ_r of all materials is set to 1). The relation $\mathbf{L} = \mu_0 \epsilon_0 \mathbf{C}_0^{-1}$ can be applied to calculate the inductance matrix. The resulting $\mathbf{L}$ and $\mathbf{C}$ can be converted to the characteristic impedance and propagation velocity for both propagation modes using Eq. 2.27.

Conformal mapping estimation

The analytical method used in [40, 41] uses a conformal transformation to calculate the capacitances and inductances for a metallic pipe with eccentric conductors. The

transformation maps the orthogonal coordinate system to another coordinate system for which a closed form solution is available. The method assumes that the second and third conductor have no influence on the magnetic field lines resulting from a current through the first conductor. If the conductors are small relative to the radius of the metallic screen this assumption holds. For a typical power cable this approximation does not really apply, but nonetheless, the method may provide indicative values with sufficient accuracy for parameter estimation. In [2] a more accurate analytical method derived from Poynting's theorem is described. This method, however, is computationally intensive, and therefore provides little advantage over the BEM estimation.

The conformal mapping is given by:

$$x' + jy' = \frac{x + jy - s}{x + jy + s} \tag{2.40}$$

where x and y are the Cartesian x- and y-coordinates, x' and y' are the coordinates after transformation, and s is a parameter that is chosen such that after transformation the eccentric conductor and earth screen become concentric. The parameter s is calculated using:

$$c_1 = \frac{r_s^2 - r_c^2 - r_x^2}{2r_x} \tag{2.41}$$

$$s^2 = c_1^2 - r_c^2 \tag{2.42}$$

where r_x is the distance from the center of a conductor to the center of the entire cable, and c_1 the x-coordinate of the center of the first conductor. See also Figure 2.3 for the definition of these parameters. The conductor radius, earth screen radius, and distance from cable center to center of the 2nd and 3rd conductor after transformation (respectively R_c, R_s and R_x) are given by:

$$c_2 = \frac{r_s^2 - r_c^2 + r_x^2}{2r_x} = c_1 + r_x \tag{2.43}$$

$$R_c = \frac{r_c}{c_1 + s} \tag{2.44}$$

$$R_s = \frac{r_s}{c_2 + s} \tag{2.45}$$

$$R_x = \sqrt{\frac{\left(c_2 + \frac{1}{2}r_x - s\right)^2 + \frac{3}{4}r_x^2}{\left(c_2 + \frac{1}{2}r_x + s\right)^2 + \frac{3}{4}r_x^2}} \tag{2.46}$$

Compared to the conductors and the earth screen the semiconducting screens and swelling tapes have a negligible conductivity. Their influence on the self and mutual

inductances is negligible. The self- and mutual-inductances are given by:

$$L_s = \frac{\mu_0}{2\pi} \ln\left(\frac{R_s}{R_c}\right) \tag{2.47}$$

$$L_m = \frac{\mu_0}{2\pi} \ln\left(\frac{R_s}{R_x}\right) \tag{2.48}$$

A three-core XLPE cable with common earth screen does not have a metallic screen around each core, but each core is enclosed by a semiconducting insulation screen. The impedance, both the resistance and the capacitance, of the semiconducting screen is low compared to the impedance of the XLPE insulation. The swelling tapes, which are between the insulation screen and the metallic earth screen are also semiconducting. Therefore, the insulation screen around each core has approximately the same potential as the earth screen and the total voltage drops across the XLPE insulation. This results in a straightforward calculation of the admittance matrix $\mathbf{Y}$. The self-capacitance C_s is given by the equation for a single-core coaxial capacitance. The mutual capacitance C_m is equal to zero because of the screening by the semiconducting insulation screens:

$$C_s = \frac{2\pi\epsilon_0\epsilon'_{r,insu}}{\ln\left(\frac{r_{insu}}{r_c + t_{cs}}\right)} \tag{2.49}$$

$$C_m = 0 \tag{2.50}$$

where r_{insu} is the outer radius of the insulation.

2.4.3 Parameter sensitivity

The input parameters of the estimation method all have an uncertainty margin. This uncertainty results in error margins in the transmission line parameters. The sensitivity of the transmission line parameters to these uncertainties is studied in this section. The value of Z_c is required to estimate the fraction of the signal which transmits at the cable end to the load impedance, e.g. for PD signal detection. An accuracy of 10% is usually enough to have a sufficient accurate notion of the PD shape and amplitude. If the estimated propagation velocity v_p is used to determine the PD origin, the relative accuracy should be better than 1%.

Characteristic impedance Z_c

Using Eq. 2.34 the influence of changes in the conductor radius r_c, earth screen radius r_s, conductor screen thickness t_{cs}, insulation screen thickness t_{is} and the insulation permittivity $\epsilon'_{r,insu}$ on the impedance Z_c is calculated and plotted in Figure 2.5. As a nominal situation a typical 12/20 kV single-core XLPE cable is used. All parameters are varied around these nominal values. The figure shows that Z_c is not very sensitive to changes in the thickness of the semiconducting layers. It is much more sensitive to changes
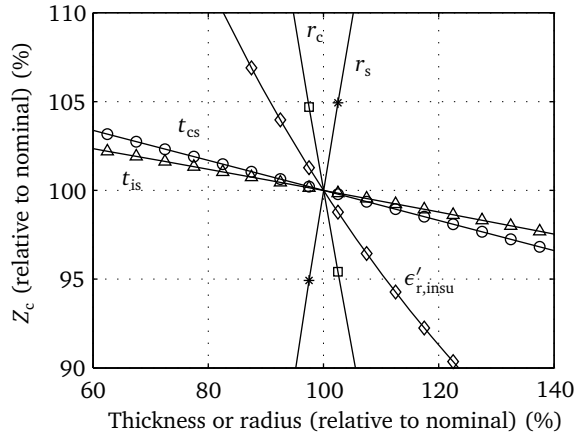
Figure 2.5 Relative change in characteristic impedance Z_c as a function of relative variation in t_{cs}, t_{is}, r_c, r_s and $\epsilon'_{r,insu}$

in the conductor and earth screen radius. The relative uncertainty in the specification of these radii (in the order of 1%) is smaller than the uncertainty in the values given for the layer thicknesses (in the order of 10%).

Propagation velocity v_p

Using Eq. 2.38 the sensitivity of v_p to changes in all five input parameters in plotted in Figure 2.6(a). The sensitivity of the propagation velocity v_p to variations in t_{cs}, t_{is} and $\epsilon'_{r,insu}$ is similar to Z_c. Only the sensitivity to changes in r_c and r_s is different. This shows that v_p is not as sensitive as Z_c to changes in the conductor and earth screen radius.

If the cable has a helical earth screen the propagation velocity is also influenced by the lay length l_l. In Figure 2.6(b) the factor F_{hl} is plotted as a function of the lay length using Eq. 2.37. If the lay length is short F_{hl}, and consequently v_p, is very sensitive to small changes in the lay length. For a larger lay length, on the other hand, the factor F_{hl} is virtually insensitive to changes in the lay length. For distribution cables a typical lay length is ten times the earth screen diameter, and a 10% error results in only about 0.5% error for the propagation velocity.

2.5 Measurement method

There are several methods to measure the transmission line parameters of a cable. A practical method that can easily be applied during field measurements is the pulse response measurement. It is based on the pulse response of pulses injected in the cable [34]. The method is described in §2.5.1. In order to measure the parameters of both the

(a) Relative change in propagation velocity v_{p} as a function of relative variation in t_{cs}, t_{is}, r_{c}, r_{s} and $\epsilon'_{\mathrm{r,insu}}$

(b) Helical lay factor F_{hl} as a function of the lay length l_l (when $r_{\mathrm{s}}/r_{\mathrm{c}} = 1.8$)
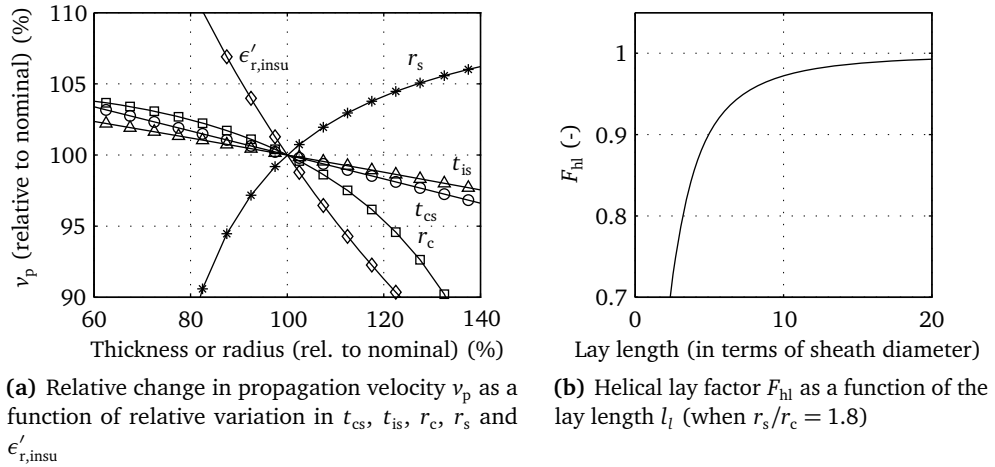
Figure 2.6   Sensitivity of propagation velocity to different input parameters

SP and the PP channel of a three-core cable with common earth screen two pulse response measurements are performed and the results are combined. The method is described in §2.5.2.

2.5.1   Single-core cables

A pulse response measurement can be used to determine the (input) impedance of a device under test. For a cable this includes both the characteristic impedance and the propagation coefficient. For a pulse response measurement, a pulse source is attached to a matching cable (e.g. 50 Ω). The signals are recorded with an oscilloscope using the 1 MΩ input impedance at a short distance from the pulse source. This configuration ensures that the input impedance of the combination of the pulse source and the oscilloscope matches the impedance of the injection cable. Furthermore, their connection is sufficiently short to prevent signal distortion due to reflections between the pulse source and oscilloscope. The cable under test (CBLUT) is connected to the far end of the injection cable. The injection cable is chosen longer than the pulse width so that injected and reflected pulses can be separated in time domain. The setup is depicted in Figure 2.7(a).

Upon an injected pulse the following pulses are recorded by the oscilloscope: v^{i} injected pulse, v^{r1} reflection on transfer from injection cable to CBLUT, v^{r2} reflection on far end of the CBLUT. These pulses are isolated from the recorded signal and converted to the frequency domain. Two transfer function are extracted from these pulses:

$$H_1 = \frac{V^{\mathrm{r1}}}{V^{\mathrm{i}}} \qquad \text{and} \qquad H_2 = \frac{V^{\mathrm{r2}}}{V^{\mathrm{i}}} \tag{2.51}$$

(a) Single-core cable

(b) SP channel of three-core cable with common earth screen

(c) Combination of SP and PP channel of three-core cable with common earth screen
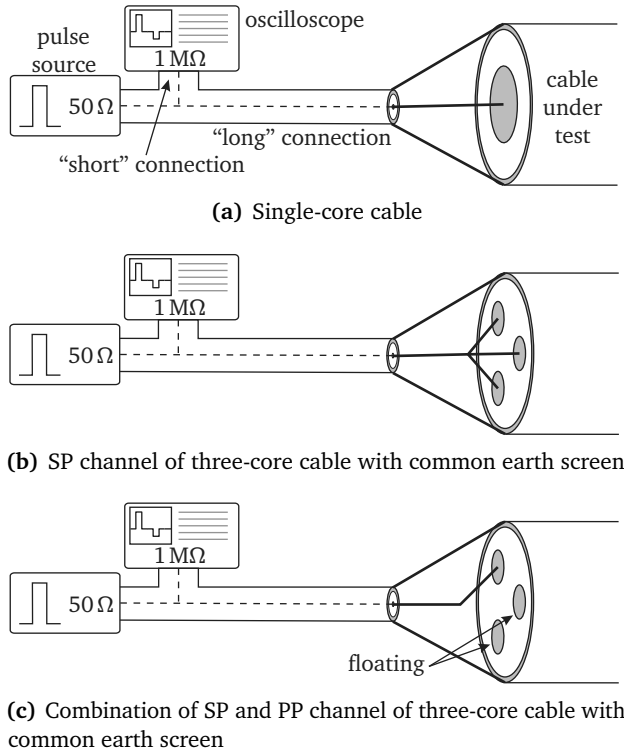
Figure 2.7   Pulse response measurement setups

The transfer functions are not only affected by the CBLUT, but also by the injection cable and the adapter that connects the injection cable to the CBLUT. Therefore, two calibration measurements are conducted to determine their influence. First, the injection cable is short-circuited at the far end. A pulse is injected and the transfer function $H_{\text{cal1}} = {V^{\text{r1}}}/{V^{\text{i}}}$ from injected to reflected pulse is calculated. The voltage reflection coefficient on the short is -1. The transfer function H_{cal1} is corrected for this reflection coefficient yielding the transfer function representing the influence of the injection cable H_{inj}:

$$H_{\text{inj}} = -H_{\text{cal1}} \tag{2.52}$$

Next, the adapter series impedance Z_{adpt} (mostly inductive) is determined by connecting the injection cable to the power cable using the adapter and short-circuiting the conductor and shield at the interface between adapter and CBLUT. The adapter's parallel impedance (mostly capacitive) is neglectable for the frequency range of interest. The transfer function

from injected to reflected pulse of this calibration measurement is:

$$H_{\text{cal2}} = \frac{V^{\text{r1}}}{V^{\text{i}}} = H_{\text{inj}} \Gamma_V = H_{\text{inj}} \frac{Z_{\text{adpt}} - Z_{\text{c,inj}}}{Z_{\text{adpt}} + Z_{\text{c,inj}}} \tag{2.53}$$

The value of the adapter impedance Z_{adpt} is given by:

$$Z_{\text{adpt}} = Z_{\text{c,inj}} \frac{H_{\text{inj}} + H_{\text{cal2}}}{H_{\text{inj}} - H_{\text{cal2}}} \tag{2.54}$$

where $Z_{\text{c,inj}}$ is the characteristic impedance of the injection cable. As an indication for typical Z_{adpt} values: during the SP measurement of the experiment in §2.6.2 the adapter impedance Z_{adpt} behaved approximately as an inductance of 60 nH.

For the actual pulse response measurement the short-circuit from the previous measurement is removed. Now, the injection cable is connected to the CBLUT via the adapter and Z_{adpt} acts as a series impedance in the circuit. Injecting a pulse results in a signal with multiple reflections. The first reflection is required to determine the characteristic impedance $Z_{\text{c,meas}}$ of the CBLUT, and the second reflection is required to determine the propagation coefficient γ_{meas} of the CBLUT. The characteristic impedance of the CBLUT is derived from the transfer function $H_1 = {}^{V^{\text{r1}}}/_{V^{\text{i}}}$ and the earlier calibrated H_{inj} and Z_{adpt}:

$$Z_{\text{c,meas}} = Z_{\text{c,inj}} \frac{H_{\text{inj}} + H_1}{H_{\text{inj}} - H_1} - Z_{\text{adpt}} \tag{2.55}$$

The second reflection V^{r2} is the pulse that was injected, transmitted to the power cable, reflected on the open far end of the power cable, and transmitted back to the injection cable. The transfer function of the injected pulse to the second reflection is given by:

$$H_2 = \frac{V^{\text{r2}}}{V^{\text{i}}} = H_{\text{inj}} \, \tau_V^+ \, \mathrm{e}^{-\gamma 2 l_c} \, \tau_V^- \tag{2.56}$$

where l_c is the length of the CBLUT, τ_V^+ the voltage transmission coefficient from injection cable to CBLUT, and τ_V^- the voltage transmission coefficient from CBLUT to injection cable. The voltage transmission coefficients are given by:

$$\tau_V^+ = \frac{2 Z_{\text{c,meas}}}{Z_{\text{c,inj}} + Z_{\text{adpt}} + Z_{\text{c,meas}}} \tag{2.57a}$$

$$\tau_V^- = \frac{2 Z_{\text{c,inj}}}{Z_{\text{c,inj}} + Z_{\text{adpt}} + Z_{\text{c,meas}}} \tag{2.57b}$$

The propagation coefficient γ_{meas} can be calculated from the measurements:

$$\mathrm{e}^{-\gamma_{\text{meas}} 2 l_c} = \frac{H_2}{H_{\text{inj}} \, \tau_V^+ \, \tau_V^-} \tag{2.58}$$

2.5.2 Three-core cables with common earth screen

In order to determine the parameters of the SP and PP channel of a three-core cable with common earth screen two pulse response measurements are required. Both measurements are analyzed as if it would concern a single-core cable, as described in the previous section, yielding a measured characteristic impedance $Z_{c,meas}$ and a measured propagation coefficient γ_{meas}. Since the pulse injection may simultaneously excite several modes the measured $Z_{c,meas}$ and γ_{meas} must be converted to the desired transmission line parameters of the SP and PP channel.

SP mode measurement

The first measurement yields the parameters of the SP channel. During the SP measurement the three conductors of the three-core cable are interconnected making the voltages on all three conductors equal ($V_1 = V_2 = V_3$) at the injection point. The central conductor of the (single-core) injection cable is connected to the three conductors of the three-core cable, while the outer shield of the injection cable is connected to the common earth screen of the three-core cable. The far end of the three-core cable remains open. The test setup is shown in Figure 2.7(b).

The first step is to perform the measurement procedure as described in §2.5.1, including calibration of injection cable and adapter. This measurement results in a measured characteristic impedance $Z_{c,meas}$ and propagation coefficient γ_{meas}. These parameters are related to SP channel parameters Z_{sp} and γ_{sp}. In order to determine this relationship the injection cable is most conveniently described as if it is a three-core cable. The central conductor of the single-core injection cable can be interpreted as three separate conductors in direct contact. A current through either conductor results in an equal voltage on all three conductors. Therefore, all values of the characteristic impedance matrix must be equal. Additionally, the shield-to-phase impedance Z_{sp} Eq. 2.24 is equal to the characteristic impedance of the injection cable $Z_{c,inj}$. This results in following characteristic impedance matrix for the injection cable during this measurement:

$$\mathbf{Z}_{c,inj} = \begin{pmatrix} Z_{c,inj} & Z_{c,inj} & Z_{c,inj} \\ Z_{c,inj} & Z_{c,inj} & Z_{c,inj} \\ Z_{c,inj} & Z_{c,inj} & Z_{c,inj} \end{pmatrix} \tag{2.59}$$

where $Z_{c,inj}$ is the characteristic impedance of the injection cable, being $50\,\Omega$.

The voltages of the first reflected pulse are given by:

$$\mathbf{V}^{r1} = \boldsymbol{\Gamma}_V \mathbf{V}^i \tag{2.60}$$

where $\mathbf{V}^i$ are incident voltages and $\boldsymbol{\Gamma}_V$ the reflection coefficient matrix Eq. 2.30 with $\mathbf{Z}_c$ the characteristic impedance matrix of the injection cable Eq. 2.59 and $\mathbf{Z}_L$ the characteristic impedance matrix of the three-core cable under test Eq. 2.26. The transfer function from

the injected pulse $\mathbf{V}^i$ to the first reflection $\mathbf{V}^{r1}$ is:

$$H_1 = \frac{\frac{1}{3}\left(V_1^{r1} + V_2^{r1} + V_3^{r1}\right)}{\frac{1}{3}\left(V_1^i + V_2^i + V_3^i\right)} = \frac{Z_{sp} - Z_{c,inj}}{Z_{sp} + Z_{c,inj}} \tag{2.61}$$

where V_k^{r1} is the kth element in $\mathbf{V}^{r1}$ and V_k^i is the kth element in $\mathbf{V}^i$. The injection cable transfer function H_{inj} and adapter impedance Z_{adpt} are not included in this equation because it is assumed that the measurement is already corrected for those as described in §2.5.1. Note that in practice the three voltages of each vector are equal because the three conductors are short-circuited together. Therefore, H_1 is equal to the fraction of any element, i.e. $H_1 = V_k^{r1}/V_k^i$. This transfer function corresponds to the measured H_1 in Eq. 2.55, yielding:

$$Z_{c,meas} = Z_{sp} \tag{2.62}$$

The second reflection $\mathbf{V}^{r2}$ is the pulse that has propagated back and forth once through the three-core cable under test. The voltages of this pulse are given by:

$$\mathbf{V}^{r2} = \boldsymbol{\tau}_V^- \, \mathbf{T}_V \, \mathbf{e}^{-\gamma_m 2l_c} \, \mathbf{T}_V^{-1} \, \boldsymbol{\tau}_V^+ \mathbf{V}^i \tag{2.63}$$

where l_c is the length of the cable under test, $\boldsymbol{\tau}_V^+$ the voltage transmission coefficient matrix from injection cable to three-core cable (i.e. from Eq. 2.59 to Eq. 2.26), and $\boldsymbol{\tau}_V^-$ the voltage transmission coefficient matrix from three-core cable to injection cable (i.e. from Eq. 2.26 to Eq. 2.59). Since the far end is open pulses arriving at the far end reflect unaffected. The transfer function to the second reflection is obtained from Eq. 2.63:

$$H_2 = \frac{\frac{1}{3}\left(V_1^{r2} + V_2^{r2} + V_3^{r2}\right)}{\frac{1}{3}\left(V_1^i + V_2^i + V_3^i\right)} = \frac{4Z_{c,inj}Z_{sp}}{\left(Z_{c,inj} + Z_{sp}\right)^2} \, \mathbf{e}^{-\gamma_{sp} 2l_c} \tag{2.64}$$

where V_k^{r2} is the kth element in $\mathbf{V}^{r2}$. Combining this transfer function with Eq. 2.58 shows that the measured propagation coefficient corresponds to the SP mode:

$$\gamma_{meas} = \gamma_{sp} \tag{2.65}$$

The results for Z_{sp} and γ_{sp} are trivial in the sense that the system can also be considered as a $50\,\Omega$ injection cable connected to a single-core power cable with impedance Z_{sp}. For the PP mode the result is less obvious.

PP mode measurement

A direct measurement of the PP channel requires simultaneous injection of two equal pulses with opposite polarity, along with a differential detection. A more practical option is to connect the central conductor of the injection cable to one conductor of the three-core cable. The other two conductors are floating. In Figure 2.7(c) the test setup is depicted. An incident pulse will couple to both the SP and the PP channel of the three-core cable. As

with the SP measurement a propagation measurement is conducted as if the cable under test is a single-core cable (see §2.5.1) yielding a measured characteristic impedance $Z_{c,meas}$ and propagation coefficient γ_{meas}. These measurements are already corrected for the injection cable transfer H_{inj} and Z_{adpt}. These parameters are converted to the parameters of the PP channel.

Again, the injection circuit, consisting of the single-core injection cable connected to one phase, is interpreted as a three-core cable. The single-core injection cable is connected to one phase of the three-core cable, making $\mathbf{Z}_{c,inj}(1,1)$ equal to the characteristic impedance of the injection cable. The other two phases of the three-core cable are floating, as if they are connected to an infinite impedance Z_{∞}. Therefore, $\mathbf{Z}_{c,inj}(2,2)$ and $\mathbf{Z}_{c,inj}(3,3)$ are Z_{∞}. Since there is no coupling between the injection cable and the infinite impedances the off-diagonal impedances are zero. This results in the following characteristic impedance matrix of the injection cable for this configuration:

$$\mathbf{Z}_{c,inj} = \begin{pmatrix} Z_{c,inj} & 0 & 0 \\ 0 & Z_{\infty} & 0 \\ 0 & 0 & Z_{\infty} \end{pmatrix} \tag{2.66}$$

Similar to the SP measurement the reflection coefficient matrix $\mathbf{\Gamma}_V$ is calculated using Eq. 2.26, Eq. 2.30 and Eq. 2.66. The transfer function of the injected pulse to the first reflection is:

$$H_1 = \lim_{Z_{\infty} \to \infty} \frac{V_1^{r1}}{V_1^i} = \frac{\frac{1}{3}Z_{pp} + Z_{sp} - Z_{c,inj}}{\frac{1}{3}Z_{pp} + Z_{sp} + Z_{c,inj}} \tag{2.67}$$

Combining this transfer function with Eq. 2.55 (remember that $Z_{c,meas}$ is already corrected for H_{inj} and Z_{adpt}) gives:

$$Z_{c,meas} = \frac{1}{3}Z_{pp} + Z_{sp} \tag{2.68}$$

This results in the characteristic impedance of the PP channel:

$$Z_{pp} = 3\left(Z_{c,meas} - Z_{sp}\right) \tag{2.69}$$

The second reflection is calculated using Eq. 2.63 with Eq. 2.66 for the impedance of the injection circuit. The measured transfer function is:

$$\begin{aligned} H_2 &= \lim_{Z_{\infty} \to \infty} \frac{V_1^{r2}}{V_1^i} \\ &= \frac{4Z_{c,inj}}{\left(Z_{c,inj} + \frac{1}{3}Z_{pp} + Z_{sp}\right)^2} \left(\frac{1}{3}Z_{pp}e^{-\gamma_{pp}2l_c} + Z_{sp}e^{-\gamma_{sp}2l_c}\right) \end{aligned} \tag{2.70}$$

Combining this transfer function with Eq. 2.58 gives for the measured propagation coefficient:

$$e^{-\gamma_{meas}2l_c} = \frac{e^{-\gamma_{pp}2l_c}Z_{pp} + 3e^{-\gamma_{sp}2l_c}Z_{sp}}{Z_{pp} + 3Z_{sp}} \tag{2.71}$$

Table 2.1 Parameters of single-core cables used in experiments.

	Cable 1	Cable 2
Conductor radius (r_c)	10.3 mm	10.25 mm
Thickness of conductor screen (t_{cs})	0.7 mm	0.95 mm
Relative permittivity of insulation ($\epsilon'_{r,insu}$) [32, 69]	2.26	2.26
Thickness of insulation screen (t_{is})	1.1 mm	1.25 mm
Inner radius of earth screen (r_s)	15.6 mm	16.05 mm
Lay length (l_l)	N/A (Al tape screen)	257 mm
Cable length	138 m	519.6 m

The propagation coefficient of the PP channel can be calculated from the measured γ_{meas} using:

$$e^{-\gamma_{pp}2l_c} = e^{-\gamma_{\text{meas}}2l_c} \frac{Z_{pp} + 3Z_{sp}}{Z_{pp}} - e^{-\gamma_{sp}2l_c} \frac{3Z_{sp}}{Z_{pp}} \tag{2.72}$$

2.6 Experiments

The estimation in §2.4 of the characteristic impedance and propagation velocity for single-core and three-core cables are validated using pulse response measurements on three cable samples: two single-core cables and a three-core cable with common earth screen. The measured characteristic impedance and propagation velocity are compared with the approximations. The measurement on the three-core cable also serves as validation of the measurement method.

The tested cable samples are new cables on a drum. The measurements are performed using a pulse source that generates a rectangular pulse with a width of 115 ns. The pulse is injected into the power cable via an RG223 50 Ω coaxial cable of 50 m.

2.6.1 Single-core XLPE cable

The dimensions of the two examined single-core MV XLPE cables are summarized in Table 2.1. These values are taken directly from the cable's datasheet or are derived from those values. The value for the lay length for cable 2 was not mentioned in the datasheet. A typical lay length of 8× the shield diameter is assumed. Estimations for the characteristic impedance and propagation velocity are calculated using Eq. 2.34 and Eq. 2.38.

The measured and estimated parameters of cable 1 are plotted in Figure 2.8(a) and Figure 2.8(b). The results of cable 2 are depicted in Figure 2.9(a) and Figure 2.9(b). The "peaks" just below 9 MHz are measurement artifacts caused by the fact that the injected pulse is a square pulse with a width of 115 ns. It has no energy content for that frequency.

The characteristic impedance is estimated within 3% for cable 1 and within about 5% for cable 2. The velocity for cable 1 is approximated within about 1%. A larger deviation

Table 2.2   Parameters of three-core XLPE cable with common earth screen used in experiments.

	Cable 3
Conductor radius (r_c)	8.55 mm
Thickness of conductor screen (t_cs)	0.8 mm
Outer radius of insulation (r_insu)	12.75 mm
Relative permittivity of insulation ($\epsilon'_\text{r,insu}$) [32, 69]	2.26
Distance core center to cable center (r_x)	16.13 mm
Inner radius of earth screen (r_s)	30.5 mm
Cable length	350.9 m

of 4% is found for cable 2. Since both the characteristic impedance and the propagation velocity of cable 2 are slightly off it is likely that one or more input parameters are less accurate. A deviation in the propagation velocity may also be related to the estimated value for the helical lay length of cable 2.

2.6.2   Three-core XLPE cable with common earth screen

The tested cable is a three-core 6/10 kV XLPE cable with common earth screen as depicted in Figure 2.3. The dimensions are listed in Table 2.2. The transmission line parameters of the SP channel and the PP channel are measured using the methods described in §2.5.2.
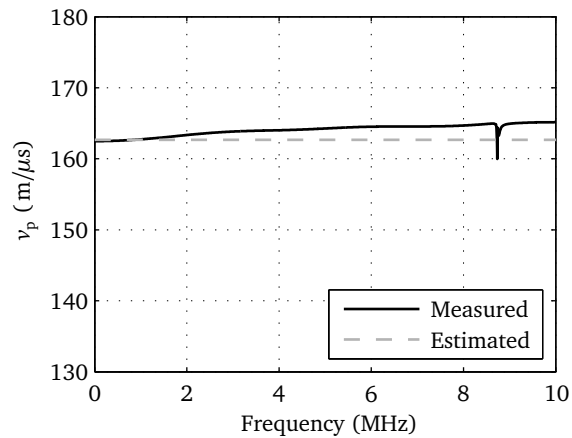
The characteristic impedance and propagation velocity of the measured cable are estimated using the BEM and conformal mapping methods. The estimated Z_c and v_p of the SP and PP channel are plotted in Figure 2.10, along with the measured values. The artifacts around 9 MHz are the same measurement artifacts as in the measurements of the single-core cables. Above 6–8 MHz the measured attenuation and propagation velocity become unreliable due to the lack of energy in the reflected pulses at high frequencies.

The figures show that the estimates of the characteristic impedance of both the SP and the PP channel are less accurate than for the single-core cables. This is probably caused by the relatively higher amount of semiconducting material in a three-core cable. The BEM model is slightly more accurate than the conformal mapping estimation. For the propagation velocity the BEM method deviates approximately 5%, while the conformal mapping shows an accuracy of 5 to 15%. The larger deviation for the conformal mapping estimation is caused by the fact that this method does not take into account the influence of the 2$^\text{nd}$ and 3$^\text{rd}$ conductor on the magnetic field resulting from a current through the first conductor.

As a validation of the measurement method the reflections observed during the PP measurement are simulated using the equations from §2.3.2, the measured injected pulse v^i, the measured calibration parameters H_inj and Z_adpt, the measured characteristic impedances Z_sp and Z_pp and the measured propagation coefficients γ_sp and γ_pp. The simulated response is plotted in Figure 2.11 together with the measured signal. The first and second reflection match perfectly because the transmission line parameters where
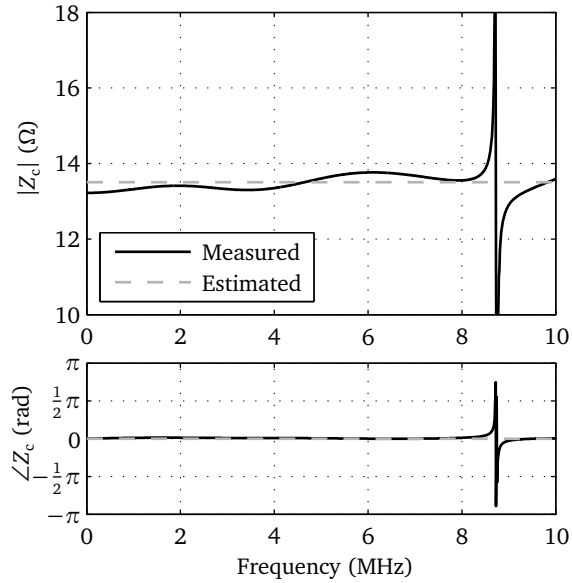
(a) Characteristic impedance

(b) Propagation velocity

Figure 2.8   Measured and estimated characteristic impedance and propagation velocity of cable 1
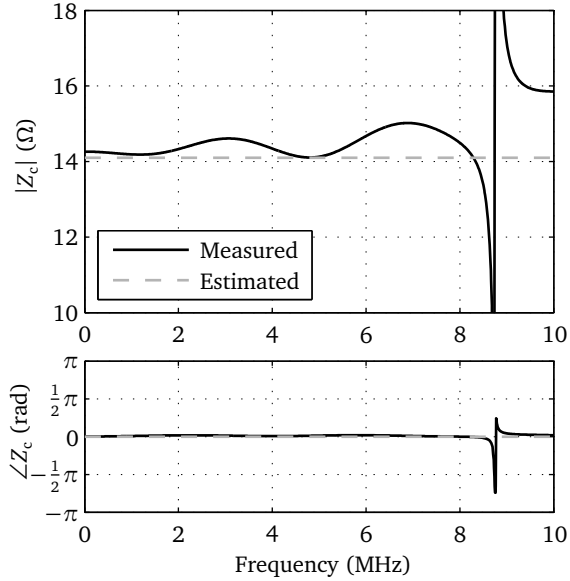
(a) Characteristic impedance

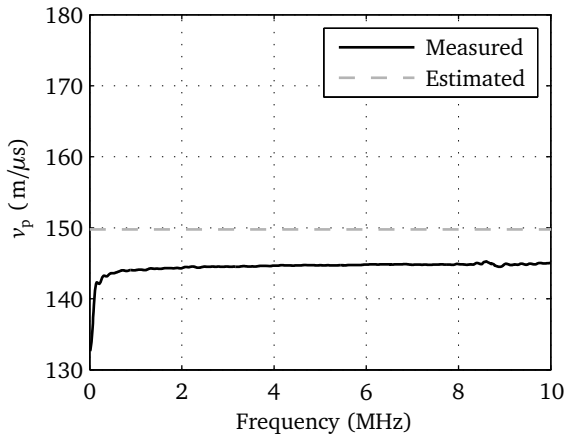**(b)** Propagation velocity

Figure 2.9   Measured and estimated characteristic impedance and propagation velocity of cable 2
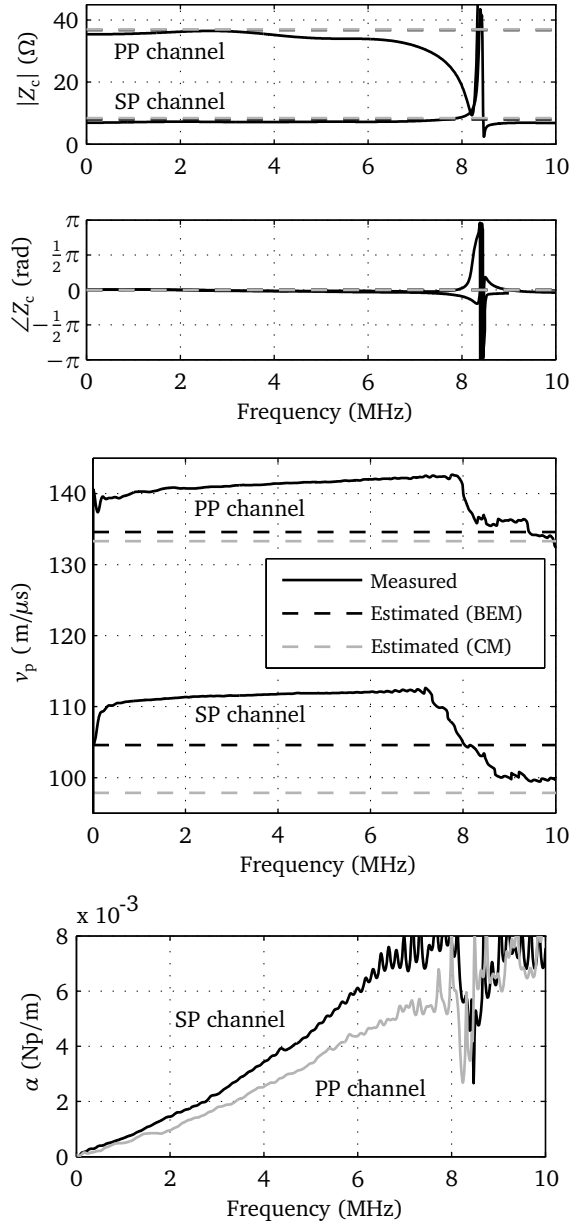
Figure 2.10 Measured characteristic impedance Z_c, propagation velocity v_p and attenuation α of SP and PP channel of cable 3, including estimated Z_c and v_p
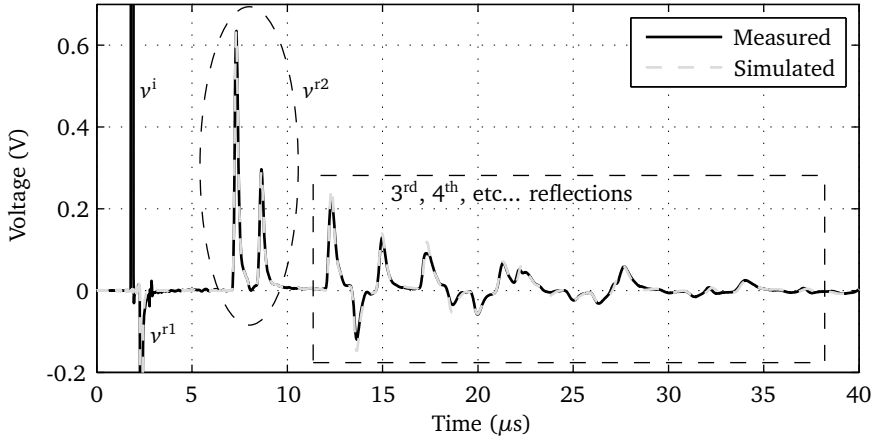
Figure 2.11   Measured and simulated signals of PP measurement. Oval dashed box indicates pulse that has traveled back and forth through the cable under test (through both the SP and the PP channel) once. Rectangular dashed box indicates pulses that have traveled back and forth two or more times.

derived from the part of the measured waveform containing these pulses. The predictions of the 3rd, 4th, and higher order reflections, on the other hand, are a good validation since all aspects of the model and measurement method are involved in the shape of these reflections, including the different propagation velocities of the SP and PP channel. The multiple reflected pulses of the SP and PP modes mix at each reflection from the three-core cable on the injection cable. The measured waveform (incorporating the propagation velocities as well as the amplitudes depending on the impedances) is accurately predicted by the cable model simulation.

2.7   Conclusions

Single-core power cables and three-core power cables that have a metallic earth screen around each core can be interpreted as (uncoupled) two-conductor transmission lines with a single propagation mode. A three-core cable with common earth screen has multiple propagation modes. These modes can be interpreted as an SP mode traveling between the three conductors and earth screen and two PP modes traveling between two conductors.

The characteristic impedance Z_c and propagation velocity v_p of single-core and three-core XLPE cables can be estimated using data that is found in a cable datasheet. For single-core cables Z_c and v_p are estimated with an accuracy within 5%. For three-core cables with common earth screen the accuracy of the estimation of Z_c of both the BEM and the conformal mapping method is 5 to 10%. The accuracy of both the BEM and

the conformal mapping method in the v_p of the PP channel is similar to the accuracy of the estimation for single-core cables. For v_p of the SP channel, however, the conformal mapping estimation is significantly less accurate.

All estimations of Z_c, for both single-core and three-core cables, remain within an accuracy of 10%. That accuracy is sufficient for estimating the shape and amplitude of the transmission coefficient of the transmission from the cable to the load impedance (the RMU). An accuracy of 1% for v_p, required for accurate location of the PD location, is not achieved. Therefore, the estimated velocity can not be used for accurate PD location. But accurate PD location can be achieved nonetheless by measurement of the propagation time of the cable. The accuracy of the estimated v_p is sufficient for other applications, such as judging whether the combination of a measured cable propagation time and the cable length supplied by the utility could be correct. Being unable to estimate the attenuation α accurately does not have a significant influence on PD detection and location.

The sensitivity analysis on single-core cables shows that accurate values for the conductor radius and the shield radius are most crucial for accurate modeling. The transmission line parameters are much less sensitive to variation in the thicknesses of the semiconducting layers.

The transmission line parameters of a single-core cable can be measured by a pulse response measurement. The transmission line parameters of the two different propagation channels of a three-core cable with common earth screen can be assessed by two pulse response measurements. In the first measurement a pulse is injected in all phases with respect to ground and the SP parameters are obtained. In the second measurement a signal is injected in only one phase (and the other two are disconnected). From this measurement and the earlier obtained SP parameters, the PP characteristics can be calculated. The presented method is successfully applied on a cable sample. Detailed prediction of multiple reflections was achieved, including the mixing of propagation modes having distinct propagation velocities, validating both the model and the measurement method for three-core cables with common earth screen.

CABLE SYSTEM MODEL

3.1 Introduction

The power cable itself is not the only component in a distribution cable network. Other components include cable joints, which hardly affect PD pulse propagation, as well as ring-main-units (RMUs) and substations, which have a major effect on PD signals. To analyze and understand the influence of all components on online PD monitoring in cable networks a model of these components is required. When a PD pulse propagates through a power cable higher frequencies are attenuated stronger than lower frequencies (see Chapter 2). Therefore, the usable bandwidth for detecting a PD pulse that has propagated through a cable for several hundreds of meters is limited. In practice the frequency range of interest for PD detection with a sensor installed at the cable end is in the low and sub-MHz range. Sufficient bandwidth for PD detection and analysis is 100 kHz–10 MHz.

The most prominent parts of a cable network, besides the cable itself, are the Ring-Main-Units (RMUs) and substations. A PD measurement unit is installed in the RMU or substation at each end of the CBLUT. In [59] a detailed model for an RMU is proposed. This model is not directly applicable to substations. It is useful to have a simplified model that can still predict the behavior of PD pulses in both RMUs and substations for the relevant frequency range.

Circuits with single-core cables can be equipped with cross-bonding (CB) joints to decrease the current induced in the earth sheaths [5]. Cross-bonding is widely applied in HV cable systems, but some utilities also apply it in long MV cable connections with a relatively high current carrying capacity. These connections are usually strategically important and therefore a good candidate for continuous online PD monitoring. Because cross-bonding joints have an interruption in the earth screen the propagation of PDs through them is not straightforward. Knowledge on the propagation of PD pulses through cross-bonding joints is required to study their influence on PD measurements.
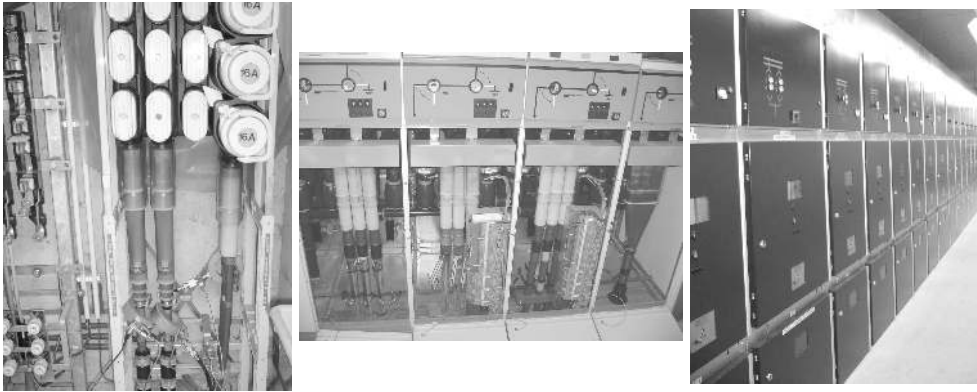
Figure 3.1 Photos of RMUs and substations of different types and sizes.

Currently, online PD monitoring of MV cables is deployed by utilities on an increasingly large scale [61]. During this process several components and issues that were not studied before were encountered. These issues are investigated to determine their influence on the propagation of PD pulses and consequently their effect on online PD monitoring.

In §3.2 a model that is applicable to both RMUs and substations is presented. The propagation of PD pulses in cable circuits with cross-bonding is studied in §3.3. In §3.4 some components and issues encountered during the implementation of online PD monitoring are studied. Finally, §3.5 contains discussion and conclusions.

3.2   RMUs and substations

3.2.1   Overview

There is a large number of different types of installations in RMUs and substations. A few of them are depicted in Figure 3.1. The goal of these installations is to interconnect one or more MV cables and other components such as transformers. The installations also contain switchgear to disconnect individual cables and transformers. In some installations the switchgear also acts as circuit breaker to interrupt the short-circuit current in case of a fault. The distinction between an RMU and a substation is its position in the grid. A substation distributes the energy delivered by an HV/MV transformer over a number of feeders. An RMU is positioned in a feeder and distributes the energy to the customers via an MV/LV transformer and a number of outgoing LV cables.

Even though there is a large variety of installations in RMUs and substations they all have a similar topology. They have one or more incoming MV cables that are connected to a common busbar via a switchgear. The installation is usually modular and consists of a number of compartments. Each compartment connects a single circuit (three single-core cables or a single three-core cable) or transformer to the busbar. There is no clear
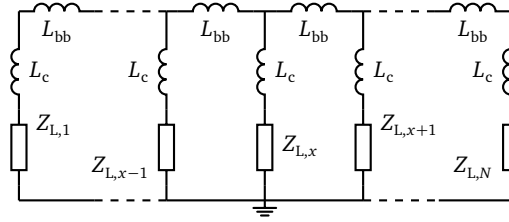
Figure 3.2 Equivalent circuit of RMU or substation with N compartments

distinction between the types of installation employed in an RMU and in a substation. Generally, a substation has more connected MV cables and larger compartments. A typical RMU applied in the Dutch grid has 1–5 connected cables, while a substation can have 5–30 cables. The width of each compartment in an RMU is typically in the range of 10–40 cm, while in a substation the width ranges from 40–150 cm.

3.2.2 RMU and substation model

The model presented in this section is based on a more detailed model presented in [59] and is adjusted so that it can be applied to both RMUs and substations. The model simplification allows to remove elements whose influence is neglectable in the frequency of interest. In Figure 3.2 the proposed generic equivalent circuit of an RMU/substation is depicted. Each compartment has a load impedance Z_L in series with inductance L_c. The impedance Z_L represents the component that is connected to that compartment, usually an MV power cable or a transformer. The inductance L_c is the inductance of the loop from the connected component to the busbar. The inductance L_{bb} is the inductance of the loop between busbar and earth over the distance of the width of one compartment.

In Figure 3.3 the generic model is applied to a small RMU with two MV cables and an MV/LV transformer. The load impedance Z_L in each compartment is replaced by equivalent circuits of the connected components. The MV cables are represented by their characteristic impedance Z_c. The transformer is modeled by the capacitance C_{tr} between transformer windings and grounded core and casing, inductance L_{tr} of the loop inside the transformer and of the connecting cables, and resistance R_{tr} representing losses in the transformer. The transformer connection cables (TCC) that connect the transformer to the busbar are modeled by the capacitance C_{tcc} from cable conductor to earth screen, inductance L_{tcc} of the connecting loop and earth connection, and resistance R_{tcc} representing conductor and insulation losses in those cables.

3.2.3 Measurements

The proposed model is verified by field measurements in RMUs and a substation. The values of the components in the model are fitted to the measurements. Measurements
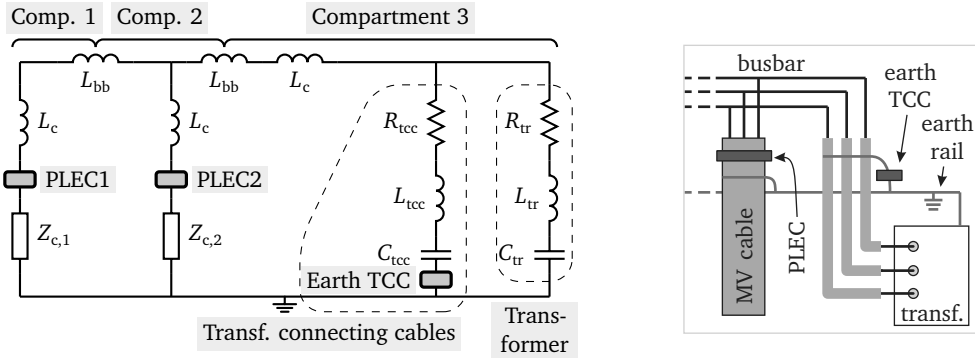
Figure 3.3 Equivalent circuit of RMU with two MV cables and MV/LV transformer. The sensor locations Past Last Earth Connection (PLEC) and the earth of the transformer connecting cables (earth TCC) are indicated in the equivalent circuit and the schematic drawing.

were performed in different types of RMUs to get a feeling for the variation in the different model parameters encountered in practice.

Ring-main-unit measurements

The model parameters for a particular RMU are estimated based on measurements in that RMU. A pulse is injected inductively in the RMU at the far end of one of its cables. In the RMU under test the resulting waveform is measured at three locations: past the last earth connection (PLEC, [59, 62]) around the incoming and outgoing cables (PLEC1 and PLEC2), and around the common earth connection of the transformer connecting cables (earth TCC). These location are indicated in Figure 3.3. Two transfer functions are calculated:

$$H_{c2}(\omega) = \frac{I_{c2}(\omega)}{I_{c1}(\omega)} \quad \text{and} \quad H_{tcc}(\omega) = \frac{I_{tcc}(\omega)}{I_{c1}(\omega)} \tag{3.1}$$

where I_{c1} is the current measured at PLEC1 (incoming cable), I_{c2} the current measured at PLEC2 (outgoing cable), I_{tcc} the current at earth TCC. H_{c2} is the transfer function from the incoming to the outgoing cable, and H_{tcc} the transfer function from the incoming cable to the earth of the transformer connecting cables. An example of the measured H_{c2} and H_{tcc} for one RMU is plotted in Figure 3.4.

The transfer functions H_{c2} and H_{tcc} can be expressed in terms of the model parameters in Figure 3.3. The parameter values for the model are found by a fitting procedure that minimizes an expression for the error between the measured transfer functions and the
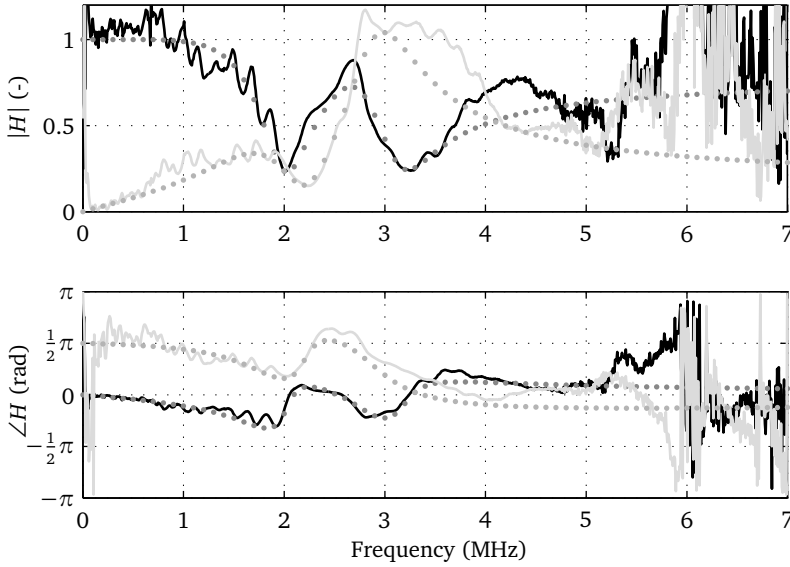
Figure 3.4 Measured (solid) and modeled (dotted) RMU transfer functions H_{c2} (black) and H_{tcc} (gray) of RMU 5.

modeled transfer functions. This expression for the error is chosen as:

$$E_{\text{mean}} = \frac{1}{\omega_{\max} - \omega_{\min}} \frac{1}{2} \int_{\omega_{\min}}^{\omega_{\max}} \frac{\left| H_{c2}^{\text{meas}}(\omega) - H_{c2}^{\text{mod}}(\omega) \right|}{\left| H_{c2}^{\text{meas}}(\omega) \right|} + \frac{\left| H_{tcc}^{\text{meas}}(\omega) - H_{tcc}^{\text{mod}}(\omega) \right|}{\left| H_{tcc}^{\text{meas}}(\omega) \right|} \, d\omega \quad (3.2)$$

where the superscript $^{\text{meas}}$ denotes the measured transfer function, the superscript $^{\text{mod}}$ denotes the transfer function as estimated by the model, and $\omega_{\min}$ and $\omega_{\max}$ are the minimum and maximum frequency of the frequency range used for the fit.

The model has nine parameters and therefore local minima may exist. In order to converge to the global minimum the starting values must be chosen nearby the global minimum. Often, one or two resonances can be observed, as is the case in Figure 3.4 near 2 MHz and 3 MHz. The products $L_{tr}C_{tr}$ and $L_{tcc}C_{tcc}$ are chosen such that they match these frequencies. The capacitance of the transformer connection cables can be estimated by multiplying the length with the capacitance value taken from the cable datasheet (≈ 140 nF/m). The transfer functions are not very sensitive to the absolute values of Z_c, L_c and L_{bb}, they are more sensitive for the ratios between these parameters. To cope with this problem extra constraints are introduced. Earlier measurements on three-core 10 kV PILC cables [59] showed that their Z_c (of the SP channel) is approximately 11 Ω. A value for the combination L_c and L_{bb} is estimated using an online impedance measurement (see
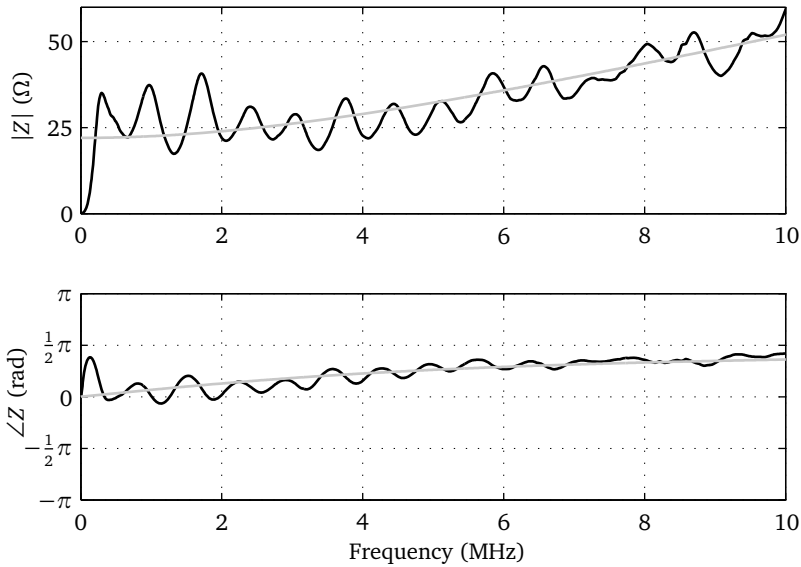
Figure 3.5   Measured RMU impedance (black line); $Z = 2Z_c + j\omega L$ with $Z_c = 11\,\Omega$ and $L = 800\,\text{nH}$ (gray line). The RMU has two connected MV cables and one MV/LV transformer.

Appendix D) at position PLEC1 in an RMU with two connected MV cables and one MV/LV transformer. The results of the impedance measurement are plotted in Figure 3.5. The "oscillation" superimposed on the global trend is caused by a reflection on a nearby joint in one of the connected power cables. If the impedances of the transformer and the cables to the transformer are neglected the measured impedance is according to the model in Figure 3.3 equal to $Z_{\text{meas}} = 2Z_c + j\omega(2L_c + L_{\text{bb}})$. Fitting to the measured impedance yields $(2L_c + L_{\text{bb}}) \approx 800\,\text{nH}$ and $Z_c \approx 11\,\Omega$. Because the field measurements are performed on similar PILC cables and the same type of installation (left photo in Figure 3.1) these values are taken as constraints in the fitting procedure.

The estimated model parameters of six RMUs are listed in Table 3.1. The modeled transfer functions after the fitting procedure of RMU 5 are included in Figure 3.4. The optimal mean absolute error E_{mean} and the frequency range used for fitting are also listed. The frequency range is limited by the energy content of the detected pulse. The frequency range is not the same for all RMUs because the distance the injected pulse had to travel from the injection point to the RMU under test is different for each RMU. Higher frequencies attenuate stronger than lower frequencies and thus the longer the traveled distance the smaller the frequency range. Each parameter value in the table is followed by two percentages. They indicate for which value the mean error is increased by 5% (of the listed optimal mean error), while the values of the other parameters remain the same. This is an indication for the accuracy with which the parameter can be estimated

Table 3.1 Fitted model parameters of six RMUs. The optimal mean absolute error and the frequency range used for fitting are also listed. Each parameter value is followed by two percentages. They indicate for which value the mean error is increased by 5% (of the listed optimal mean error), while the values of the other parameters remain the same.

	RMU 1	RMU 2	RMU 3
L_{tr} (μH)	6.5 (31% – 309%)	1.6 (77% – 128%)	2.3 (86% – 113%)
C_{tr} (nF)	3.2 (48% – 204%)	4.2 (86% – 119%)	1.3 (91% – 114%)
R_{tr} (Ω)	25 (27% – 250%)	13 (87% – 116%)	5.1 (73% – 128%)
L_{tcc} (μH)	1.4 (77% – 129%)	0.34 (10% – 200%)	2.4 (85% – 117%)
C_{tcc} (nF)	1.1 (83% – 115%)	1.1 (94% – 106%)	0.5 (91% – 110%)
R_{tcc} (Ω)	4.4 (42% – 169%)	0 (0% – ∞%)	15 (77% – 131%)
L_{c} (nH)	400 (77% – 156%)	380 (67% – 145%)	377 (69% – 109%)
L_{bb} (nH)	0 (0% – ∞%)	40 (0% – ∞%)	46 (0% – 222%)
Mean error	31%	10%	17%
Frequency range	200 kHz – 5 MHz	200 kHz – 3 MHz	200 kHz – 4 MHz

	RMU 4	RMU 5	RMU 6
L_{tr} (μH)	3.3 (56% – 137%)	3.0 (72% – 142%)	2.9 (0% – ∞%)
C_{tr} (nF)	3.4 (77% – 131%)	1.7 (77% – 133%)	3.0 (40% – ∞%)
R_{tr} (Ω)	22 (82% – 124%)	5.6 (51% – 152%)	61 (61% – 216%)
L_{tcc} (μH)	0 (0% – ∞%)	0.76 (77% – 125%)	0.6 (85% – 123%)
C_{tcc} (nF)	3.1 (94% – 107%)	2.3 (86% – 113%)	3.4 (90% – 110%)
R_{tcc} (Ω)	7.5 (74% – 130%)	2.3 (44% – 161%)	0 (0% – ∞%)
L_{c} (nH)	360 (78% – 181%)	358 (76% – 140%)	324 (88% – 125%)
L_{bb} (nH)	80 (0% – 359%)	84 (0% – 207%)	152 (72% – 143%)
Mean error	10%	22%	29%
Frequency range	200 kHz – 2.5 MHz	200 kHz – 5 MHz	200 kHz – 4 MHz

from the measurement. If both percentages are close to 100% the parameter value can be estimated from the measurement with high accuracy.

The total capacitance C_{tcc} of the transformer connecting cables is determined by their length and capacitance per meter. The cables used in Netherlands for this purpose have a capacitance of approximately 150 pF/m. Depending on the dimensions of the RMU their lengths vary from 1–10 m. During the measurements the lengths of the transformer connecting cables were not measured. Nonetheless, there is a clear trend. RMU 4 and 6 were the largest and RMU 2 and 3 were the most compact units. This corresponds to the C_{tcc} values listed in Table 3.1. The transformer capacitance C_{tr} does not exhibit such a clear correlation with transformer's dimensions or rated power.

The capacitances C_{tr} and C_{tcc} and inductances L_{tr} and L_{tcc} can be determined from
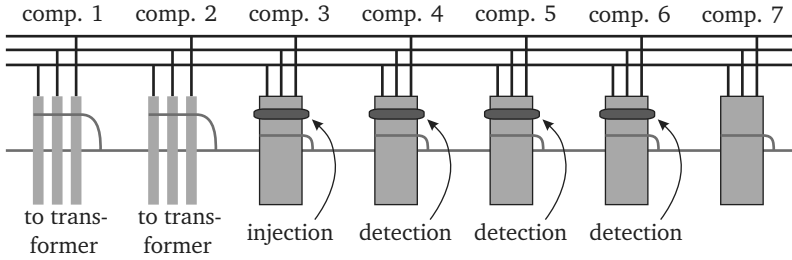
Figure 3.6   Measurement in compact substation with two connected transformers and five MV cables. Locations for pulse injection and detction are indicated.

these measurements with good accuracy, especially when clear resonances are observed in H_{c2} and H_{tcc}. The accuracy of the value for losses R_{tr} and R_{tcc} is much lower, especially if the frequency range is too small and the resonances are not observed clearly. With the impedance measurement the combination of L_c and L_{bb} ($2L_c + L_{bb}$) can be determined with high accuracy. Separating this combined value into a separate L_c and L_{bb} is not accurate for most measurements. This would improve significantly if the RMU contains more than two connected MV cables and the current is measured through more than two MV cables. This is the case for the substation measurement presented in the next section.

For low frequencies most incoming current enters the continuing cable. The transformer and the transformer connecting cables "take" a large portion of the incoming current at their resonance frequencies, reducing the current to the continuing MV cable. This portion is mainly determined by the value of R_{tr} and R_{tcc} relative to the characteristic impedance Z_c of the MV cables. The influence of complete RMUs on the propagation of PD pulses is discussed in detail in Chapter 6.

Substation measurements

A measurement is performed to verify the model of Figure 3.2 in a compact substation with five connected MV cables and two transformers. Each compartment is $42 \times 120 \times 70$ cm (W×H×D). The transformers are connected in compartments 1 and 2, and the cables in compartments 3–7. A drawing of the setup is depicted in Figure 3.6.

For the measurement a pulse was injected inductively around the leftmost MV cable (in compartment 3). The injected current distributes over the components in the other compartments. The injected current ($I_3(\omega)$) and the currents ($I_4(\omega)$ to $I_6(\omega)$) through the cables in compartment 4–6 are measured and the current transfer functions are calculated. For instance, the ratio

$$H_{46} = \frac{I_6}{I_4} \tag{3.3}$$

gives the current through the cable in compartment 6 relative to the cable current in compartment 4. The advantage of calculating $H_{46}(\omega)$ instead of the ratio of a current over the

Table 3.2 Fitted model parameters of compact substation. The optimal mean absolute error and the frequency range used for fitting are also listed. Each parameter value is followed by two percentages. They indicate for which value the mean error is increased by 5% (of the listed optimal mean error), while the values of the other parameters remain the same.

	Substation 1
L_c (nH)	523 (96% – 105%)
L_{bb} (nH)	143 (94% – 107%)
Z_c (Ω)	7.9 (93% – 108%)
Mean error	7.9%
Frequency range	500 kHz – 8 MHz

injected current (e.g. $I_6(\omega)/I_3(\omega)$) is that $H_{46}(\omega)$ is independent of the unknown transformer impedances in compartment 1 and 2. The transfer function $H_{46}(\omega)$ only depends on Z_c, L_c and L_{bb}. Additionally, at each cable an online impedance measurement (see Appendix D) is performed to determine the impedance of that compartment ($j\omega L_c + Z_c$) in series with the rest of the substation. The influence of the unknown transformer impedances on the PLEC impedance in the compartment furthest away from the transformers is neglectable.

At in Figure 3.7 the ratio $H_{46}(\omega)$ is plotted and in Figure 3.8 the impedance measured in compartment 6 is plotted. The model parameters are fitted by minimizing the mean absolute relative error between model and measurement of $H_{46}(\omega)$ and $Z_{tot,6}(\omega)$. The optimal parameter values are listed in Table 3.2. The optimal modeled transfer function $H_{46}(\omega)$ and impedance $Z_{tot,6}(\omega)$ are also plotted in Figure 3.7 and Figure 3.8. The other impedance measurements and transfer functions match the model with similar accuracy with the same acquired parameter values.

At low frequencies the influence of the inductances are negligible and the ratio $H_{46}(\omega)$ is determined by the characteristic cable impedances. Because Z_c is equal for all the connected cables the ratio $H_{46}(\omega)$ plotted in Figure 3.7 starts at 1. This means that the current injected around the cable in compartment 3 distributes equally over the other four cables. At higher frequencies the current distribution is mainly determined by the ratio of L_c and L_{bb}. Above 8 MHz the measurements of the both the transfer function $H_{46}(\omega)$ and the impedance $Z_{tot,6}(\omega)$ start to deviate from the model. This effect can be attributed to transmission line effects along the busbar becoming significant. If the wavelength is much longer than the dimensions of the installation this effect can be neglected. The substation model is used in Chapter 6 to analyze the influence of substations on the propagation of PD pulses and online PD measurements.

3.3 Cross-bonding

Circuits with single-core cables can be equipped with cross-bonding (CB) joints in order to decrease currents induced in the earth sheath [5]. Due to the earth sheath interruption
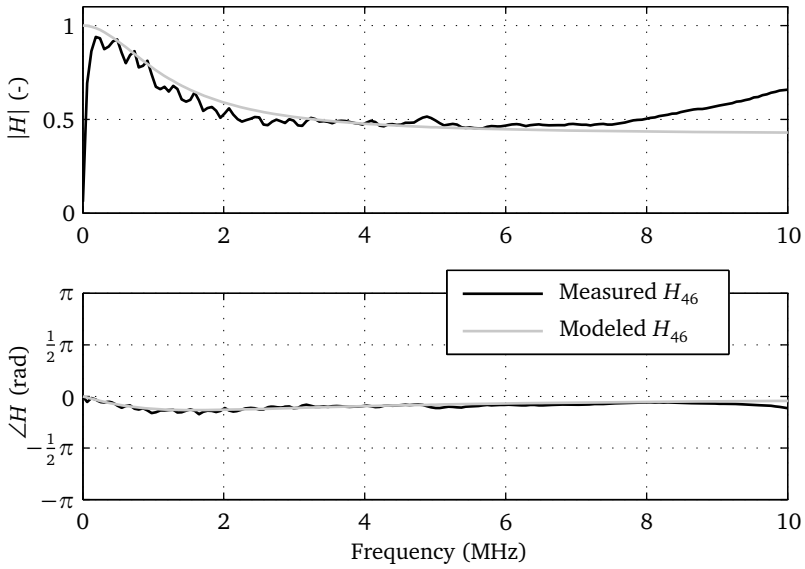
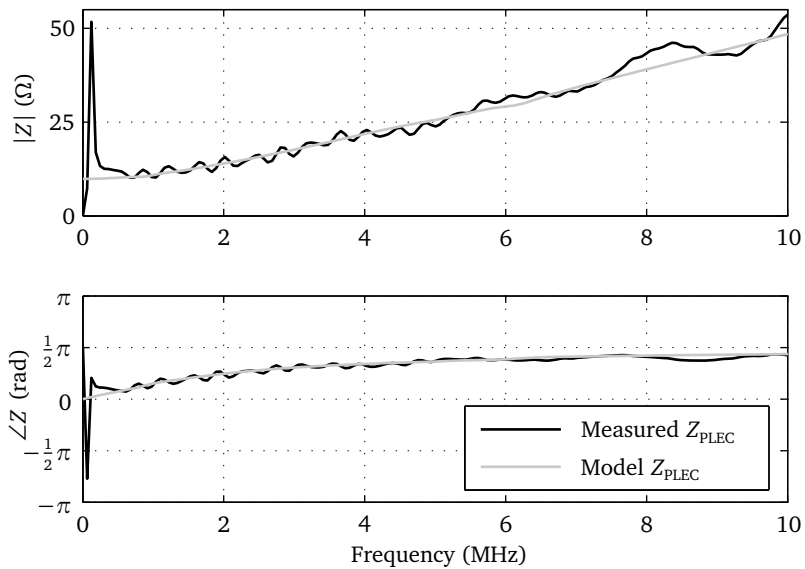**Figure 3.7** Measured and modeled ratio of currents measured in compartment 4 and 6.

Figure 3.8 Measured and modeled PLEC impedance of compartment 6.
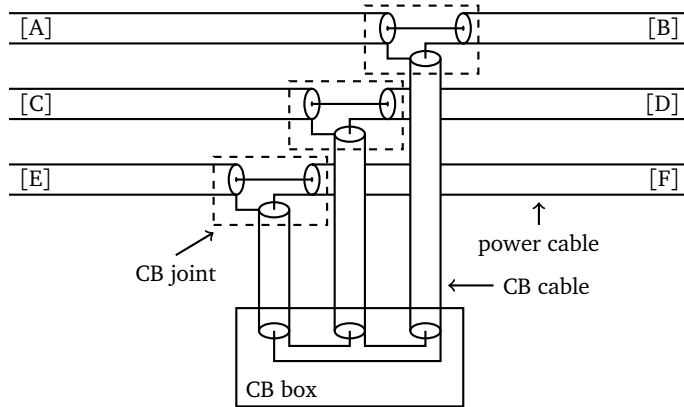
Figure 3.9 Cross-bonding configuration with CB joints, CB cables and CB box.

a PD signal traveling through the cable is distorted by these CB joints. In this section a model is proposed to describe and predict this influence. In [21] an extensive model is described for CB joints. This model requires detailed knowledge about the cable system. Much of this information is not available in practice. The model proposed in this section is a simplified model that requires less input parameters but still predicts the observed effect of CB joints in a test setup on pulse propagation.

3.3.1 Overview of cross-bonded cable system

In a CB joint the earth screen of a single-core cables is interrupted. Both sides of the earth screen are connected to a coaxial cross-bonding cable or to two single-core CB cables. The CB cables of all three phases connect to a CB box where they are interconnected. In some situations there is no CB box, but instead the CB cables are directly connected to the earth screen of another phase. Typically, the CB cables have a length of approximately 10 m. In Figure 3.9 three power cables with CB joints, coaxial CB cables and a CB box are depicted. A complete cable circuit is divided into at least three minor sections connected by CB joints. Depending on the length and configuration cable circuits have several major sections, each consisting of three minor sections.

3.3.2 Cross-bonding model

The power cables are modeled as a transmission line characterized by the characteristic impedance $Z_c(\omega)$ and the propagation coefficient $\gamma(\omega)$ (see Chapter 2). For a PD pulse traveling through the power cable the CB joint acts as an impedance step at which the pulse partially reflects and partially transmits. The joints and box are usually 0.5-2 m

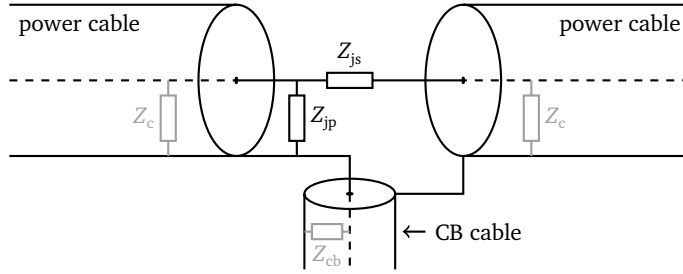**Figure 3.10** CB joint model. power and CB cables are represented by their characteristic impedances Z_c and Z_{cb}. Z_{js} is the series impedance of the joint itself and Z_{jp} is the parallel impedance of the joint and intersheath and ground modes.

long, much smaller than the wavelength associated with the frequency range of interest. Therefore, the joints and box are modeled as discrete components without involving transmission line effects inside the components.

Coaxial cross-bonding cables

In Figure 3.10 the proposed model for a single CB joint is depicted. Coaxial CB cables are modeled as a transmission line described by its characteristic impedance $Z_{cb}(\omega)$ and propagation coefficient $\gamma_{cb}(\omega)$. The joints and CB box are modeled as separate impedance steps. The joint itself is modeled by a series $Z_{js}(\omega)$ and parallel impedance $Z_{jp}(\omega)$. Owing to the loop formed by the joint $Z_{js}(\omega)$ is dominantly inductive. The parallel impedance $Z_{jp}(\omega)$ represents the capacitance between conductor and sheath in the joint. The parallel impedance also incorporates the effect that a part of the pulse will leave the power cable and continues between the earth sheaths of two cables and/or between a sheath and ground. See page 55 for a discussion on these modes.

    When a pulse arrives at a CB joint it will partially reflect and partially transmit. The voltage reflection coefficient for a pulse from the power cable arriving at the joint is given by Eq. 2.8. The load impedance Z_L in this equation is the impedance as seen by a pulse arriving at the joint. This impedance is $Z_{jp}(\omega)$ in parallel with $\left(Z_{js}(\omega) + Z_c(\omega) + Z_{cb}(\omega)\right)$:

$$Z_L = \frac{Z_{jp}\left(Z_{js} + Z_c + Z_{cb}\right)}{Z_{jp} + Z_{js} + Z_c + Z_{cb}} \tag{3.4}$$

The voltage transmitted from the cable to the joint $\tau_{cj}(\omega)$ is given by Eq. 2.9. The transmitted voltage divides over the characteristic impedance of the continuing power cable $Z_c(\omega)$, the characteristic impedance of the cross-bonding cable $Z_{cb}(\omega)$, and the series impedance of the joint $Z_{js}(\omega)$. The total voltage transmission coefficient from the left to the right power cable ($\tau_{cc,1}(\omega)$) is the combination of $\tau_{cj}(\omega)$ and this voltage

division:

$$\tau_{cc,1} = \tau_{cj} \frac{Z_c}{Z_{js} + Z_c + Z_{cb}} \tag{3.5}$$

Similarly, the voltage transmission coefficient from the power cable to the CB cable is:

$$\tau_{ccb} = \tau_{cj} \frac{Z_{cb}}{Z_{js} + Z_c + Z_{cb}} \tag{3.6}$$

The polarity of $\tau_{ccb}(\omega)$ depends on which side of the joint's earth sheath is connected to the conductor and sheath of the CB cable.

The pulse entering the CB cable propagates to the CB box. The propagation and distortion in the CB cable is determined by its propagation coefficient $\gamma_{cb}(\omega)$:

$$H_{cb} = e^{-\gamma_{cb} l_{cb}} \tag{3.7}$$

where $H_{cb}(\omega)$ is the transfer function from the beginning of the CB cable to the end of the CB cable and l_{cb} the length of the CB cable.

When the pulse arrives at the CB box, it will partly reflect and partly transmit. The model for the CB box is similar to the joint model shown in Figure 3.10. The PD signal transfers from a CB cable to the other CB cables. The parallel and series impedance of the CB box are denoted with $Z_{bp}(\omega)$ and $Z_{bs}(\omega)$ respectively. The pulses reflected on and transmitted through the CB box propagate back to the CB joints of all three phases. At the joints they again partly reflect and partly transmit. Every time a pulse, either a reflection or a transmitted pulse, arrives at a CB joint or CB box it results in three other pulses: one reflected and two transmitted. This goes on and on until all pulses are either quenched or have entered one of the power cables. The total transmission for a pulse from one power cable to all other power cables is the sum of all these reflected and transmitted pulses:

$$\tau_{cc} = \tau_{cc,1} + \tau_{ccb} H_{cb}^2 \Gamma_{cb} \tau_{cbc} + \ldots \tag{3.8}$$

where $\Gamma_{cb}(\omega)$ is the reflection coefficient for a pulse from the CB cable reflecting on the CB box and $\tau_{cbc}(\omega)$ is the transmission coefficient from the CB cable to the power cable. In the end a single pulse will be distributed over all three phases traveling in both directions.

Due to the exponentially growing number of reflected and transmitted pulses the resulting signals are most conveniently calculated using an iterative approach. During each step the signals traveling in each direction at each interface are calculated from the signals of the previous step. For example, the voltage for the current iteration step of the pulse traveling from a joint into the left power cable is given by:

$$V_{1-}^k = V_{1+}^{k-1} \Gamma_1 + V_{2+}^{k-1} \tau_{21} + V_{3+}^{k-1} \tau_{31} \tag{3.9}$$

where k indicates the iteration step, $V_{1+}(\omega)$ the voltage of the pulse traveling towards the joint from the left power cable, $\Gamma_1(\omega)$ the reflection coefficient from a pulse from the left cable, $V_{2+}(\omega)$ the voltage of the pulse traveling towards the joint from the right
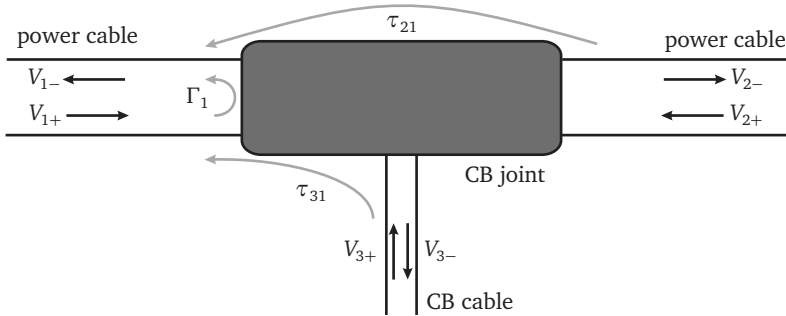
Figure 3.11 Definitation of pulses traveling towards and from a CB joint. The reflection coeffient Γ_1 and transmission coefficients τ_{21} and τ_{31} are also indicated.

power cable, $\tau_{21}(\omega)$ the total transmission coefficient for a pulse from the right cable to the left cable, V_{3+} the voltage of the pulse traveling towards the joint from the cross-bonding cable, and $\tau_{31}(\omega)$ the total transmission coefficient from the cross-bonding cable to the left cable. These voltages and coefficients are indicated in Figure 3.11. For every interface and direction such an equation is determined. After a number of iteration loops the signals converge to a stable solution. The main advantage of this procedure is that it is not necessary to keep track of every single reflected and transmitted pulse. Therefore, the computation time increase linearly with the number of calculated reflected and transmitted pulses instead of exponentially. If the CB cables are very short with respect to the wavelength this model leads to the same results as the simpler model for single-core CB cables described in the next section.

Short single-core and short cross-bonding cables

Some cross-bonding systems use per phase two single-core CB cables instead of a single coaxial CB cable. These two single-core CB cables do not form a proper transmission line like a coaxial CB cable. Therefore, the model of pulses propagating back and forth through the CB cables is not valid. Instead, a simpler model is presented in this section. If the length of the CB cables is short with respect to the wavelength the following model is applicable.

The three joints, CB cables and, if present, the CB box are treated as one discrete load impedance $Z_L(\omega)$. That means that the contribution of the other power cables to $Z_L(\omega)$ is a series impedance of five times $Z_c(\omega)$ (the continuing cable and the other two phases in both directions, Figure 3.12). Due to the larger dimensions of the loops formed by the CB cables there will also be a large inductive series impedance $Z_{1c,s}(\omega)$ representing the combined inductance of all loops. The capacity of the joint itself and intersheath and ground modes are modeled by a parallel impedance $Z_{1c,p}(\omega)$ placed in parallel to the
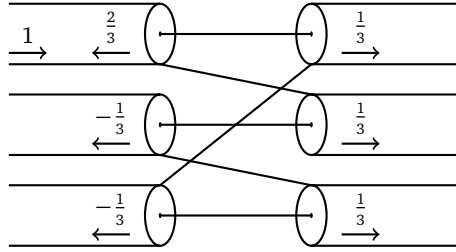
Figure 3.12 Reflected and transmitted pulses with short cross-bonding cables when $Z_{1c,s}$ and $Z_{1c,p}$ are neglected.

$Z_c(\omega)$ of every cable. This results in:

$$Z_L = \frac{Z_{1c,p}\left(Z_{1c,s} + 5Z_{c,p}\right)}{Z_{1c,p} + Z_{1c,s} + 5Z_{c,p}} \tag{3.10}$$

with $Z_{c,p}(\omega)$ is the impedance of $Z_c(\omega)$ and $Z_{1c,p}(\omega)$ in parallel:

$$Z_{c,p} = \frac{Z_c Z_{1c,p}}{Z_c + Z_{1c,p}} \tag{3.11}$$

The total transmission coefficient from power cable to power cable is:

$$\tau_{1c,cc} = \frac{2Z_L}{Z_L + Z_c}\frac{Z_{c,p}}{5Z_{c,p} + Z_{1c,s}} \tag{3.12}$$

This transmission coefficient is the same for all power cables, except that it has opposite polarity for the two parallel cables going back. If $Z_{1c,p}(\omega)$ and $Z_{1c,s}(\omega)$ are neglected the reflection coefficient is $\frac{2}{3}$ and the transmission coefficient is $\pm\frac{1}{3}$. These coefficients are also indicated in Figure 3.12.

Intersheath and ground modes

A pulse can exit the coaxial power cables and start traveling outside the cables. Assuming that the power cables are perfectly shielded, the pulses traveling inside the cable have no influence outside and vice versa. The earth screens of the three phases and the earth itself can be regarded as a multi-conductor transmission line with multiple propagation modes between the conductors. There are modes between the earth sheaths of two cables (intersheath mode), or between a sheath and ground (ground mode). With respect to the intersheath and ground modes two questions are relevant: 1) how much signal is "lost" at the CB joints (i.e. enters the intersheath/ground modes), and 2) will a pulse traveling in intersheath or ground mode couple back into the power cables at the next joint? The
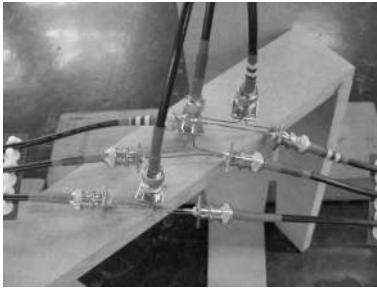
(a) Three CB joints. Coaxial cables at left and righ of picture are power cables; cables at top are CB cables.
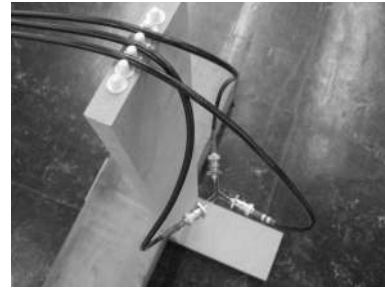
(b) CB box. Cables at top-left of picture are the CB cables going to the joints.

Figure 3.13   Photos of CB joints and CB box in laboratory test setup.

signal lost in the intersheath mode depends on the impedance of this mode. Because this impedance depends on the configuration of the cable system and its surroundings it has to be determined for each specific situation. The propagation of the intersheath and ground modes depends on the soil properties. The dielectric soil parameters reported in [11] result in an attenuation coefficient much higher than the attenuation in the power cable. Therefore, any pulse traveling in an intersheath mode is expected to be neglectable at the next joint. This corresponds with measurements in [21].

3.3.3   Test setup measurements

As a first verification of the proposed model for coaxial CB cables a laboratory test setup was constructed. The setup consists of $50\,\Omega$ RG58 coaxial cables that represent both the power and the CB cables. The joints and CB box are small (approx. 10 cm) copper wire models. At each side of the joint the RG58 "power" cables are 30 m long, which is longer than the injected pulses ($\approx 10\,\text{m}$), so that they can be separated in time domain. The CB cables are taken 10 m long, hence the CB model for long coaxial CB cables will be used to predict measured signals. The three phases are in flat formation with an axial distance of 1.5 cm so that the ratio (cable diameter)/(axial distance) is about the same as in a typical HV cable system. Figure 3.13 shows some details of the setup.

At position [A] (see Figure 3.9) a pulse (3 V, 50 ns) is injected. The reflected and transmitted pulses are measured at the ends of all six "power" cables (positions [A]–[F]). In Figure 3.14 the measured pulses at three positions are depicted. The pulses at [D], [E] and [F] are virtually the same as in [C], except that [D] and [F] have a positive polarity. In the same figure also voltage simulated using the iterative procedure are plotted. The simulation is performed using $Z_c = Z_{cb} = 50\,\Omega$ and $H_{cb}(\omega)$, which is calibrated beforehand by means of pulse injection and detection. The impedances $Z_{js}(\omega)$ and $Z_{bs}(\omega)$ are $0\,\Omega$ because the accessories are small and thus the inductance is neglectable compared to Z_c
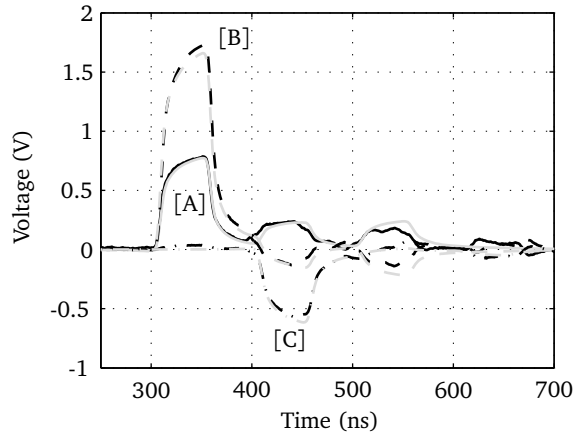
Figure 3.14   Measured and simulated reflected and transmitted pulses as the result of an incoming pulse from [A]. Black lines: measured and gray lines: simulated. Solid lines: reflected back into [A], dashed lines: transmitted to [B], and dashed lines: transmitted to [C].

and Z_{cb}. The values of the parallel impedances are optimized until the simulations match the measurements: $Z_{jp} = 1500\,\Omega$ and $Z_{bp} = 300\,\Omega$. The capacitance between conductor and earth in the joint and box is assumed to be neglectable. The fitted values for Z_{jp} and Z_{bp} indicate that in the CB box more signal is lost to the intersheath/ground modes than in the joints. An explanation for the difference could be that the HV cables and CB cables are mutually perpendicular at the joints, so that there is no neat channel between the cables connected to a single joint for exciting an intersheath mode. At the CB box all three CB cables return close to each other, creating a good intersheath mode channel between the CB cables. See Figure 3.13 for photos of the joints and CB box in the laboratory test setup.

3.3.4   Field measurements

A field measurement is conducted on a 150 kV cable circuit when it was still under construction. Therefore, it is possible to make a direct connection to the HV cable, without distortion by large cable terminations. The tested system consisted of a section of 2150 m (three single-core cables in trefoil formation), then a set of three CB joints, followed by a section of 1100 m (also in trefoil). The 2150 m section has a set of three straight joints at 1100 m. The applied CB cables are single-core cables. A schematic representation of the setup is shown in Figure 3.15.

A pulse is injected in the yellow phase at the end of the 2150 m cable section. The voltage of the injected pulse is measured, together with its reflections. In Figure 3.16 three measured signals are plotted. The pulse (square, 3.5 V, 120 ns) is injected using a
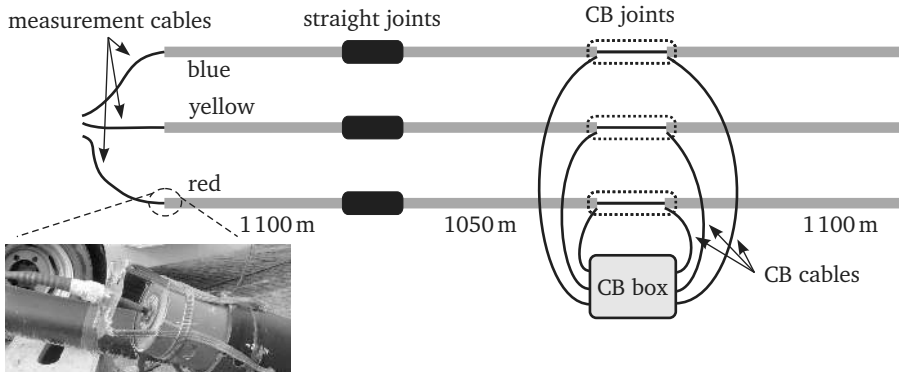
Figure 3.15   Schematic drawing of field measurement setup with CB joints with single-core CB cables.

47 m long injection cable so that the injected pulse and the reflection on the HV cable can be separated. At the same time the signals in the other two phases are recorded. The injected pulse is shortly followed by its reflection on the HV cable (both are truncated in Figure 3.16). From this reflection the characteristic cable impedance (26 Ω) can be determined using the method described in §2.5. At about 14 μs a very small reflection on the straight joint at 1.1 km is observed. The next pulse, at 26 μs, is the reflection on the CB joints. At the same time much smaller reflections can be seen in the blue and red phase. The pulse at 37 μs is the pulse transmitted through the CB joints, reflected on the far end, transmitted again through the CB joints and propagated back to the beginning of the cable. The transmitted pulse on the yellow phase (where the pulse was injected) is clearly much larger than the transmitted pulses in the other phases.

   The model for single-core CB cables predicts that the reflected pulse has twice the amplitude of the two pulses transmitted to and traveling back through the other two phases. These are the pulses arriving at $t = 26\,\mu s$ in Figure 3.16. The ratio between the amplitude of the reflected pulse (yellow phase) and the pulses transmitted to and returning through the blue and red phase is much larger than the predicted factor 2. The model also predicts that the pulses transmitted to continuing cables are equal for all three phases. In this measurement these pulses reflected on the far cable-end (which is open), propagated back through the cable (and again through the CB joints), and were detected at the beginning. The pulses measured at $t = 37\,\mu s$ in Figure 3.16 do not match the prediction. The pulse in the yellow phase (where the pulse was injected) is significantly larger that the pulses in the other two phases.

   At the same cable end also an intersheath mode signal is measured. The earth sheaths of two HV cables are short-circuited and a current probe is installed around the short-circuit. Any current measured by the probe is a signal traveling in an intersheath mode. In Figure 3.17 two signals are plotted. The black signal is the current in the normal mode
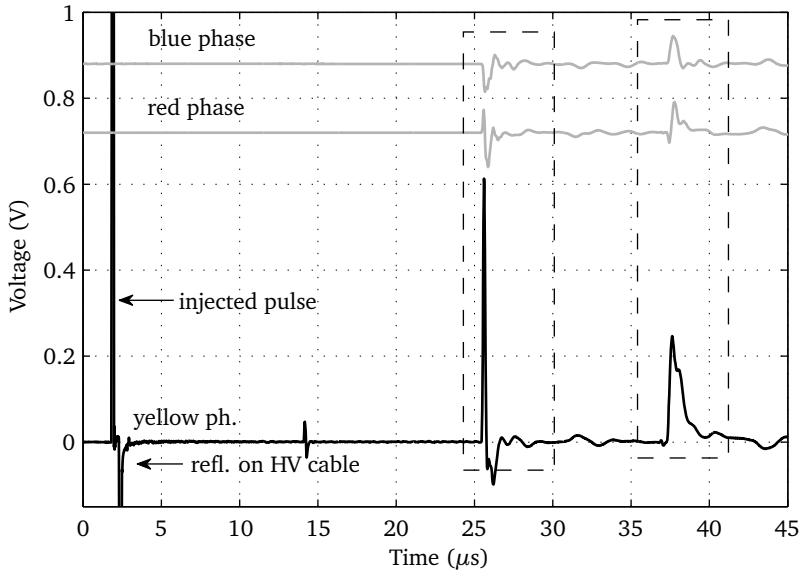
Figure 3.16 Measured signals after pulse injection in the yellow phase.
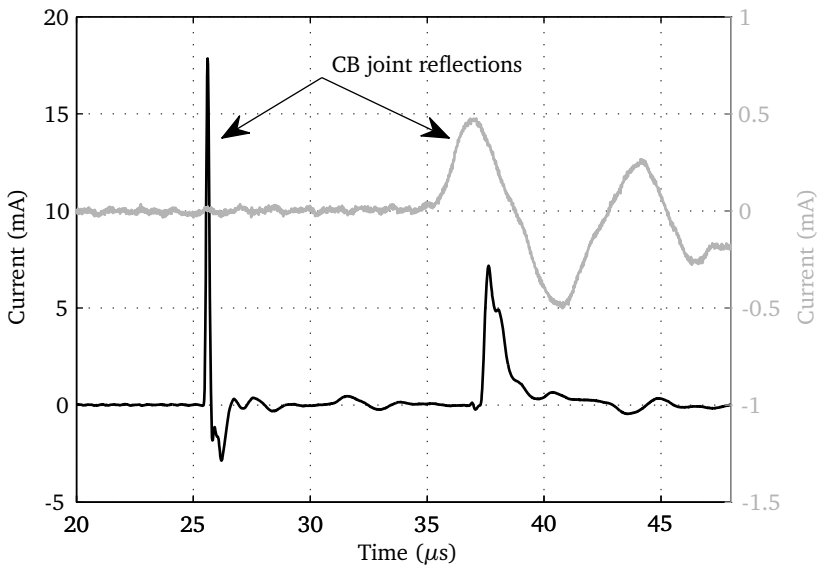
Figure 3.17 Measured signals (black line/left axis: normal cable mode, gray line/right axis: intersheath mode.
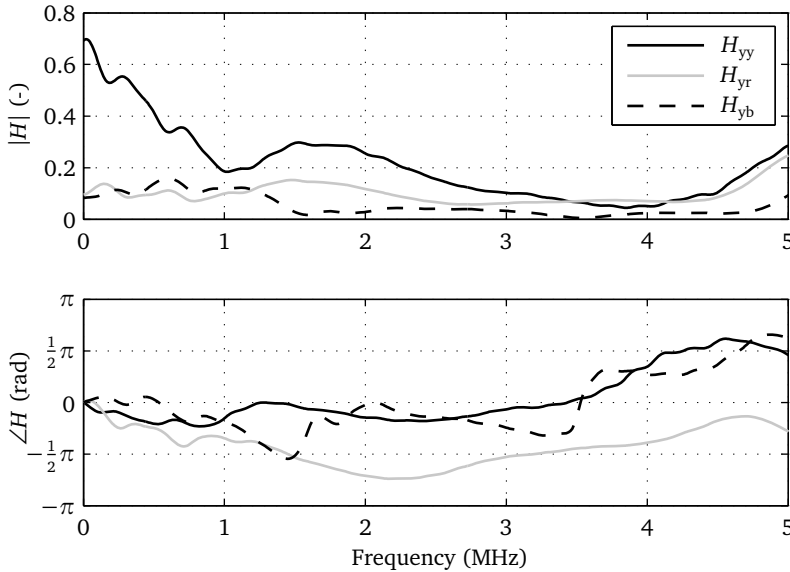
Figure 3.18 Transfer functions of propagating back and forth through a set of CB joints. The plotted transfer functions are for a pulse injected in the yellow phase, and detected in the yellow ($H_{yy}(\omega)$), red ($H_{yr}(\omega)$) and blue ($H_{yb}(\omega)$) phase. The transfer functions are corrected for the influence of the power cable and injection circuit.

propagating through the cable (same signal as depicted in Figure 3.16, except that now the current is plotted). The much smaller gray signal is the intersheath mode signal. Based on the time-of-arrival the propagation velocity of the intersheath mode is determined to be $102\,\text{m}/\mu s$, compared to $185\,\text{m}/\mu s$ for the normal cable mode.

The pulse that propagated back through the intersheath mode has a much smaller amplitude than the pulses that traveled back through the cable. The intersheath mode is not measured at the point where the pulse couples into the intersheath mode (near the CB joints). This measurement can therefore not be used to determine whether the signal loss is caused by the high attenuation of the intersheath mode, by the weak coupling to the intersheath mode at the CB joints, or a combination of both.

The measurement in Figure 3.16 is also used to determine the transfer function of the propagation back and forth through the CB joints. A major section of a circuit with cross-bonding has two sets of three (one in each phase) CB joints. Propagating back and forth through the same set of CB joints is expected to be similar to propagating through two sets of CB joints. The transfer functions from the pulse injected in the yellow phase to the pulses measured at $t = 37\,\mu s$ in the yellow, red and blue phase are calculated. These transfer functions are corrected for the influence of propagating through the power cable, propagating through the injection cable, transferring from the injection cable to the power

Manufacturer	Smit	Trench Electric
Rated impedance	$0.9\,\Omega$	$1.5\,\Omega$
Frequency	$50\,Hz$	$50\,Hz$
System voltage	$10\,kV$	$50\,kV$

Figure 3.19 Photo of air core reactor manufactured by Smit and technical information on the two tested reactor models.

cable, and vice versa. The propagation coefficient of the power cable was measured using a pulse response measurement (see §2.5.1) on an identical 1 km cable sample without any joints. The influence of the injection cable and the adapter connecting the injection cable to the power cable where calibrated in the same way as during a pulse response measurement. The resulting transfer functions are only affected by the CB joints. The transfer functions are plotted in Figure 3.18.

For frequencies below 2 MHz the transfer function to the yellow phase ($H_{yy}(\omega)$) is between 0.5 and 0.2. For the calculation of the transfer functions a time interval is selected around the measured pulses. Because this time interval is limited the transfer functions are not reliable below approximately 300 kHz. In the range 2 MHz to 4.5 MHz $H_{yy}(\omega)$ is mostly below 0.1. The transfer functions to the other two phases ($H_{yr}(\omega)$ and $H_{yb}(\omega)$) are approximately 0.1 for frequencies below 4.5 MHz. These transfer functions show that CB joints result in a significant signal loss. For online PD monitoring on a relativly short cable circuit with a single major CB section the signal loss is most likely acceptable (depending on noise level, attenuation and load impedance). For longer cable circuits with multiple major CB sections the signal loss increases and online PD monitoring becomes unfeasible. A PD occuring in one phase will result in pulses traveling in the other two phases as well. The amplitude of the pulse in the originating phase is much higher, making it possible to identify the correct phase.

3.4 Other components and issues

3.4.1 Air core reactors

Air core reactors, such as depicted in Figure 3.19, are installed in some substations to protect the equipment in case of a short-circuit in an outgoing feeder. The air core reactor is installed in the substation in series with the outgoing cable. In case of a short-circuit in the cable the impedance of the reactor limits the short-circuit current.

To monitor an outgoing cable for PD activity measurement units are installed in the

substation and the RMU at the other cable end. The fraction of the PD signal transmitted to the substation is determined by the substation impedance relative to the characteristic cable impedance. Since the reactor is placed in series and is possibly a high impedance for frequency range of interest, a PD arriving at the substation reflects back almost completely and the transmitted fraction may be too low to detect.

For 50 Hz the impedance of such an air core reactor is in the order of 1 Ω. This corresponds to an inductance of approximately 3 mH. For the frequency range of interest this is an impedance of 2–200 kΩ. An air core reactor is not designed for this frequency range. Above a certain frequency the capacitance between the turns will dominate the inductance and the impedance will decrease. The question is whether this impedance becomes sufficiently low to enable PD detection.

Impedances of three air core reactors of two different models have been measured while they were disconnected from the grid. One reactor is manufactured by Smit and the other two by Trench Electric. Figure 3.19 contains a photo of the Smit reactor and the technical information of both reactors. The impedance was measured using a pulse response measurement (§2.5). The reactor impedance follows from the reflection coefficient.

The measured impedances of the reactors are plotted in Figure 3.20. All three reactors have a similar impedance. The impedance is approximately 2.5 kΩ at 100 kHz, peaks at 6 kΩ near 300 kHz, and decreases to 200 Ω at 10 MHz. There are small variations in the individual reactors but these are not significant. The measured impedance can be approximated by an inductance of 3 mH in parallel with a capacitance of 80 pF.

The air-core reactor impedances are much higher that the characteristic cable impedance over the entire frequency range of interest. If such a reactor is installed in a substation in series with the cable under test, a PD at that substation will see a high load impedance. Only a small fraction of an incoming PD pulse will be transmitted to the substation. This makes a two-sided measurement with inductive sensors with sufficient detection sensitivity unfeasible for such a configuration.

3.4.2 Parallel impedance in last earth connection

There are different locations in an RMU where an inductive sensor can be installed for PD detection. The preferred location is around the cable Past the Last Earth Connection (PLEC). Alternatively, the sensor can be installed in the Last Earth Connection (LEC). As discussed in [63] the PLEC location is preferred above the LEC location because of the lower noise level. Due to space limitations installing the sensor in the PLEC location is not always possible and the sensor is installed in the LEC location instead. The potentially higher noise level is not the only disadvantage of the LEC location. The second disadvantage is that the sensor may see another impedance in parallel with the load impedance of the RMU $Z_{\text{load}}(\omega)$. Injected pulses will therefore also be injected in the parallel impedance, resulting in an incorrectly measured load impedance. The parallel impedance $Z_{\text{x}}(\omega)$ is the impedance of the common mode circuit between the cable's earth screen and the earth itself, or between the cable's earth screen and the earth screen of a
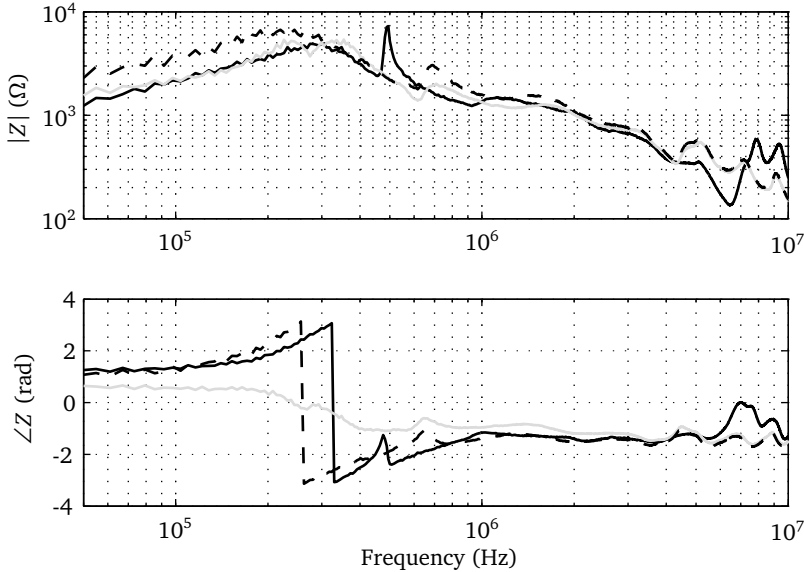
Figure 3.20 Measured impedance of three air core reactors. Black solid line: Smit; black dashed and gray solid lines: Trench electric reactors.
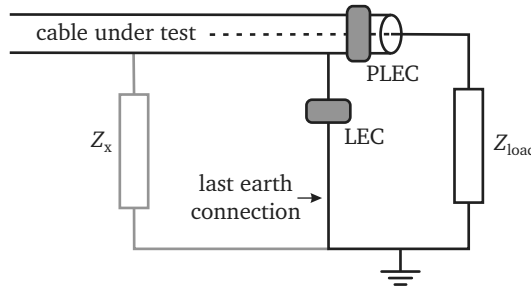
Figure 3.21 Location of parallel impedance with respect to the CBLUT and possible two sensor positions.

parallel cable. In Figure 3.21 the location of $Z_x(w)$ is shown with respect to the CBLUT. The two sensor positions PLEC and LEC are also indicated in this figure.

The parallel impedance has been measured in two large substations. The first substation has an open installation with air core reactors (§3.4.1). The impedance was measured online (see Appendix D for the measurement method) with the injection probe placed around the earth connection (LEC). Due to the high impedance of the air core reactors,
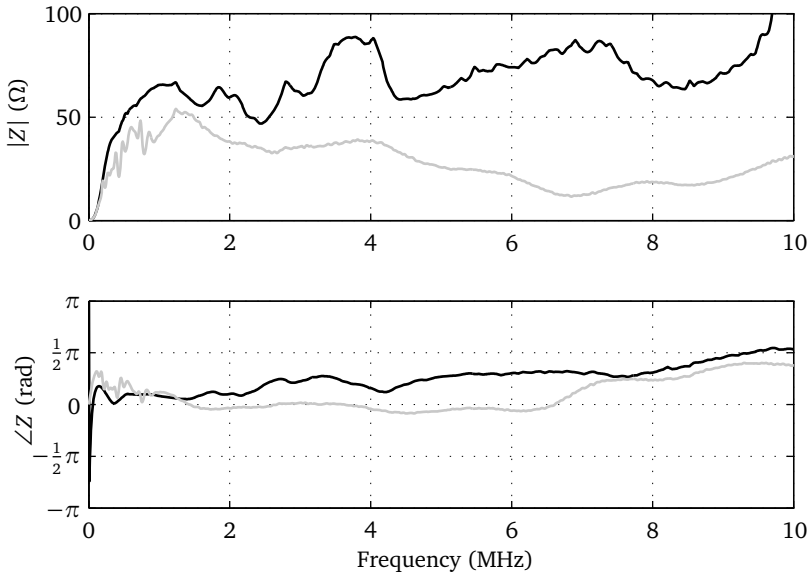
Figure 3.22 Parallel impedances $Z_x(\omega)$ measured in two large substations. Black line: open installation, gray line: installation depicted in right photo in Figure 3.1.

being part of $Z_{\text{load}}(\omega)$, the measured impedance is dominated by the parallel impedance $Z_x(\omega)$. The second substation is depicted in the right photo in Figure 3.1. The impedance was measured in the earth connection of a cable. The cable was disconnected from the busbar so that the load impedance $Z_{\text{load}}(\omega)$ is infinite. Therefore, the measured impedance is equal to $Z_x(\omega)$. Both measured parallel impedances are depicted in Figure 3.22.

The parallel impedance $Z_x(\omega)$ is also determined for the compact substation as used in the measurements on page 48. The impedance $Z_x(\omega)$ is determined by performing two online impedance measurements: one in the PLEC location and one in the LEC location of the same cable. The measured impedances are combined to find the parallel impedance:

$$Z_x = \frac{Z_{\text{PLEC}} \, Z_{\text{LEC}}}{Z_{\text{PLEC}} - Z_{\text{LEC}}} \tag{3.13}$$

where $Z_{\text{PLEC}}(\omega)$ is the impedance measured at the PLEC location ($Z_{\text{PLEC}} = Z_{\text{load}} + Z_c$) and $Z_{\text{LEC}}(\omega)$ is the impedance measured at the LEC location. The parallel impedances are determined for the compartments 3, 4 and 5. They are plotted in Figure 3.23.

If a PD measurement unit is installed in the LEC location instead of the PLEC location, the measured impedance will be lower than actual RMU impedance due to the parallel impedance $Z_x(\omega)$. The measured parallel impedances are larger than the typical RMU impedance, but their influence is not neglectable. For the tested compact substation this estimation error is in the order of 20%.
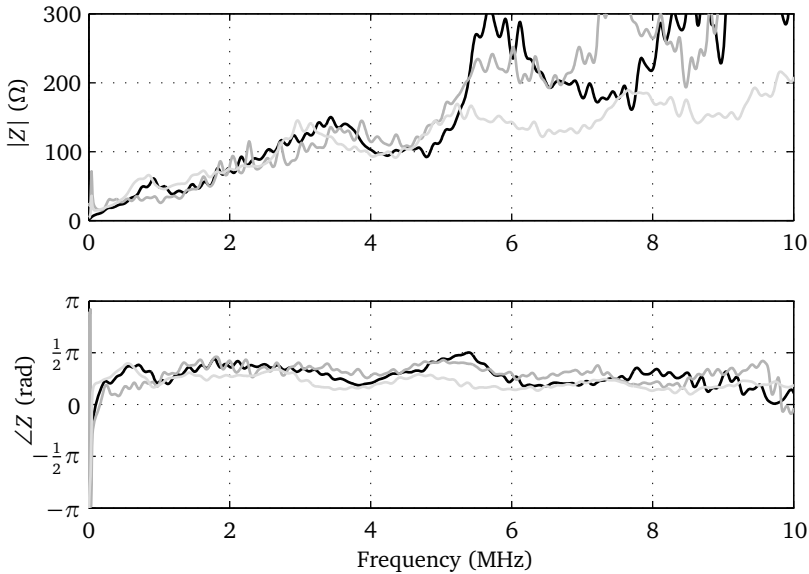
Figure 3.23   Parallel impedances of three compartments in a compact substation.

3.4.3   Semiconducting sleeve in termination

A measurement unit for online PD detection is preferably installed around the cable past the last earth connection, or alternatively around the last earth connection [59, 63]. The exact position of the last earth connection is not always obvious. The last earth connection for the frequency range of interest for PD detection is not always the same as the for 50 Hz intended earth connection. For example, a small capacitance between a cable's earth screen and the metal enclosure of the switchgear may be a high impedance at 50 Hz, but for higher frequencies it can act as a low impedance. Another problem encountered is a semiconducting heat shrinkable sleeve in the termination of an XLPE cable. In Figure 3.24 such a termination is depicted. The metal clamp, which is connected to the horizontal beam behind the cable, has a tight connection with the semiconducting sleeve over a relatively large area. The semiconducting sleeve on its turn is pressed against the earth screen of the cable. Together this forms an earth connection with a relatively low impedance past the actual earth connection of the cable.

Because the inner diameter of the measurement unit is too small it can not be installed above the metal clamp. The alternative position is in the cable's earth connection. Due to the parallel earth connection formed by the semiconducting sleeve and metal clamp the measurement unit will see the low sleeve impedance instead of the RMU/substation impedance. Therefore, it will be unable to inject pulses in the CBLUT or to detect pulses coming from the CBLUT. This problem can be solved by replacing the metal clamp by an
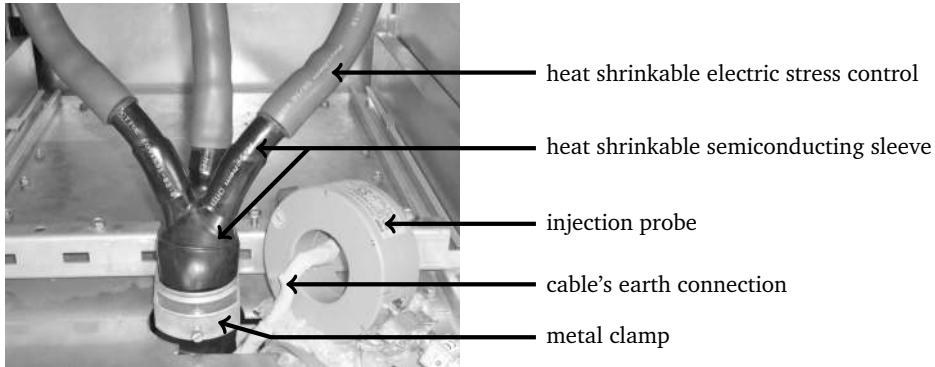
Figure 3.24   Termination of 10 kV cable with heat shrinkable semiconducting sleeve and metal clamp.

insulating plastic clamp. The effectiveness of this solution was verified by an impedance measurement in the cable's earth connection, as indicated by the injection probe in Figure 3.24, before and after replacing the clamp. The impedance was measured online using the method described in Appendix D. Both measured impedances are plotted in Figure 3.25. The measurement with the metal clamp corresponds to an inductance of approximately 200 nH. This corresponds to the expectation based on the size of the loop of the cable's earth connection and the metal clamp. After replacing the metal clamp the impedance increased from a 200 nH inductance to an impedance of approxiamtely 40 Ω, indicating that the semiconducting sleeve and metal clamp were indeed causing the short-circuit. However, the impedance is lower than the infinite impedance that would be expected for open switchgear. The measured impedance is most likely dominated by the common mode impedance as discussed in §3.4.2.

3.4.4   Break in earth continuity

For safety reasons the earth screen of a power cable must be continuous along the entire cable. Any break in the earth continuity somewhere along a cable is an undesirable situation and is therefore considered to be a defect. For a succesful PD measurement it is essential that PD pulses can propagate through the entire cable under test. A break in the earth continuity of a cable forms an approximately infinite impedance. A pulse reflects completely on the infinite impedance and no signal passes the break. The PD-OL system injects pulses to measure the cable propagation time, the local impedance, and to synchronize the measurement units at each cable end. These pulses will also reflect on a break in the earth continuity. Because the pulses injected by the measurement system do not reach the far end, the measurement system will notice immediately that there is a problem. If there is a break, there will be relatively large reflection in the signal recorded while injecting a pulse. The presence of such a reflection indicates that there
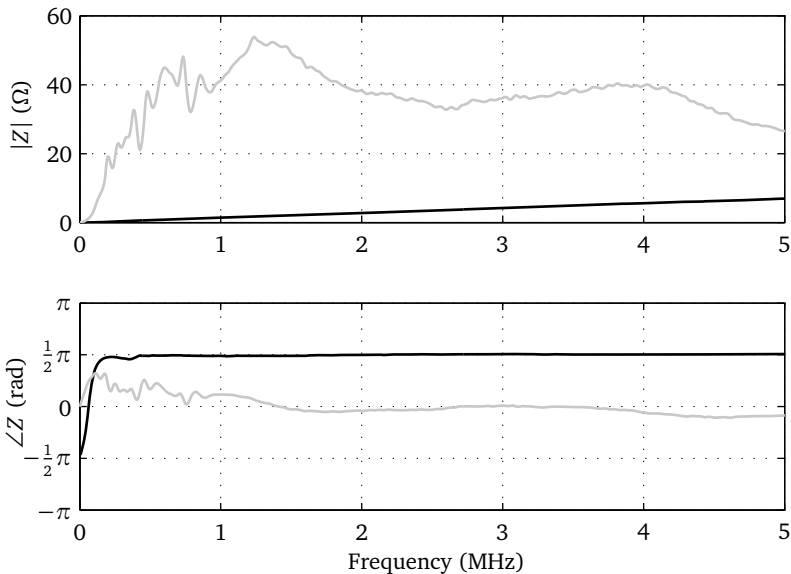
Figure 3.25 Measured impedance of termination with metal clamp (black line) and with plastic clamp (gray line).

is a significant discontinuity along the cable. If the pulses injected by the measurements units at both cable ends are not detected at the other cable end, and both measurement units detect a large reflection, there is likely a break in the earth continuity of the cable under test. The location of the break can be determined using the time between the injected pulse and the reflection. The ratio between this reflection time from one cable end and the reflection time from the other cable end gives the relative location of the break. Alternatively, a reflection time from one cable end can be combined with an estimated propagation velocity to determine the distance to the break. Even though a PD measurement system is not designed to detect and locating a break in the earth continuity of a cable, it is capable to do so.

A PD-OL system was installed on a PILC cable with a break in the earth continuity. Pulses injected by the measurement units were not detected by the measurement unit at the other cable end. The pattern measured upon injection of a pulse is plotted in Figure 3.26. The large reflection observed at $t = 30\,\mu s$ is the reflection on the break in the earth screen. Combining the reflection time with an estimated propagation velocity ($158\,\text{m}/\mu s$) and the knowledge that the break is most likely located in a joint, yields the defect location in a joint at 1407 m. Inspection of the joint revealed bad connection of the earth screen indeed. After repair the reflection was gone and the PD-OL system was able to monitor the cable.
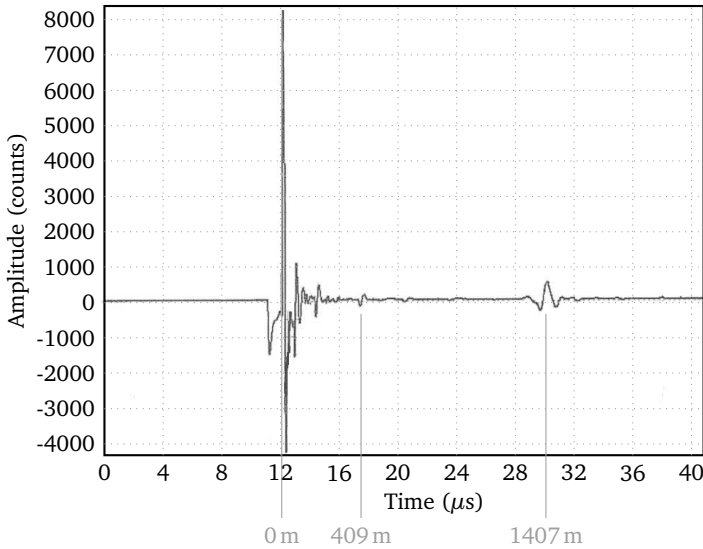
Figure 3.26 Reflection pattern measured in a cable circuit with a break in the earth continuity.

3.5 Discussion and conclusions

The proposed RMU/substation model can predict the behavior of RMUs and compact substation for frequencies up to 5 MHz with a mean accuracy of 10 – 30%. This covers the most important part of the frequency range of interest, especially in case of longer cable lengths. This accuracy is sufficient to allow prediction of the shape and amplitude of (PD) pulses propagating through and reflection on RMUs to preform qualitative and reasonable quantitative analyses, as done in Chapter 6. The model is expected to be also applicable to larger substations, although this is not verified. The only caveat is that for larger substations the upper frequency for which the model is valid will be reduced due to transmission line effects within the installation. Consider, for example, a large substation with a busbar of 15 m long. Assuming air as dielectric this corresponds to the wavelength of 20 MHz. To neglect transmission line effects the upper frequency must be much (a factor 10) lower than 20 MHz. That means that the model will only be valid up to a few megahertz, which is still sufficient for the analysis of PD waveforms coming from cables longer than a couple hundreds of meters. See Chapter 6 for the application of these models for the analysis of the influence of RMUs and substations on online PD measurements.

The cross-bonding (CB) model with coaxial CB cables can accurately predict the behavior of the test setup. The model for short single-core CB cables predicts that upon injection of a pulse in one phase the reflected pulses in the other two phases are equal. Also all three transmitted pulses should be equal. The field measurements in Figure 3.16

show that both predictions fail. In practice the CB cables from the joints to the CB box are laid out arbitrarily on top of each other. Therefore, the inductive coupling between phases is strong. The proposed single-core CB cable model does not take this coupling into account. For coaxial CB cables the influence of the environment and the exact configuration of the CB cables is smaller. Therefore, the proposed model may still be valid, but this was not verified.

However small, an intersheath mode signal is detected. Since it is unknown what fraction of the injected signal did couple to the intersheath mode at the CB joint it is not possible to determine the attenuation of the intersheath mode channel based on these measurements.

Based on the results of the field measurement, online PD monitoring on cable circuits with multiple major CB sections seems unfeasible due to the signal loss. If the cable circuit has only a single major CB section, the signal loss may be acceptable. These conclusions are based on a single measurement on a circuit with CB joints. The presented model was unable to predict the measurement results. Therefore, it is recommended to investigate this aspect further and to improve the model in order to verify whether these conclusions are generally applicable.

Air core reactors applied in MV grids have a high impedance for the frequency range of interest. If they are placed in series with the cable under test it is not possible to monitor that cable with a two-sided measurement with inductive sensors without modifying the installation. A solution is to install a capacitor between the conductor and earth before the reactor. This capacitor has a low impedance for high frequencies which makes it possible to detect PD pulses from the cable under test. Alternatively, a single-sided time-domain reflectometry can be performed from RMU at the other cable end. This has the disadvantage that the maximum cable length that can be monitored is halved and that it is more difficult to discriminate disturbing signals from PDs from the CBLUT.

A parallel impedance $Z_x(\omega)$ influences the PD measurements if the PD measurement unit is installed in the last earth connection of the cable under test. The measured parallel impedances are larger than the typical RMU impedance, but their influence is not always neglectable. Due to $Z_x(\omega)$ the measured impedance will be slightly lower than the actual PLEC impedance and therefore the predicted PD waveform and amplitude will be incorrect. For the tested compact substation this estimation error is in the order of 20%. For other RMUs and substation it depends on the dimensions of the installation and the number of connected cables and transformers. If, for example, only a transformer is connected and no other MV cables, the effect will be larger.

A semiconducting sleeve in the termination of an XLPE cable can form a low impedance path to the earth screen. If a metal clamp is applied around the semiconducting sleeve to hold the cable in place a parallel earth connection is created. This earth connection must be taken into account when installing the PD measurement unit. This problem can be mitigated by applying a clamp of insulating material.

CHAPTER 4

TIME-OF-ARRIVAL OF PD PULSES

4.1 Introduction

The accuracy of defect location depends on the accuracy of the time-of-arrival estimate of each pulse and on the precision the propagation time of the entire cable is known. Nowadays, continuous PD measurement, while the cable remains in service, has become a viable technique (see for example [30, 46, 72, 73]). Continuous partial discharge monitoring generates massive data streams and an automated algorithm is required to determine the time-of-arrival of PD pulses with high accuracy. The location methods analyzed in this chapter are generally applicable to different PD location systems. However, our main interest concerns online application because of its obvious advantages above offline techniques. An online technique inherently has technical complications. Ring Main Units (RMUs) or substations, at the cable ends or in between, distort the pulse shape of both PD signal and injected signal at the cable end. Furthermore, when a cable remains in service the measurements are impeded with higher noise and disturbance levels from the rest of the grid.

PD location in cable systems can be achieved with a single sensor if the far end is disconnected, or with two sensors (one at each cable end) if the cable is in normal operation (see [46]). Both methods need an estimate of the total propagation time of the cable (t_c) and the time-of-arrival (t_{oa}) of PD pulses in order to locate the origins of the PDs. The propagation time t_c is determined using the time-of-arrival of injected pulses and their responses.

In this chapter five algorithms are evaluated. The algorithms are based on:

- Trigger level

Published in slightly altered form in [54]

- Signal energy

- Akaike Information Criterion (AIC)

- Gabor centroid

- Phase in frequency domain

A set of evaluation criteria, including the sensitivity to noise level and spectrum, the pulse shape, and effect of RMU impedance is used for comparison. The methods are analyzed analytically and by simulations. The results are verified experimentally.

4.2   Evaluation criteria

In order to make a well-founded comparison of the strong and weak points of each method a set of evaluation criteria is defined on which the methods are judged. The following criteria are considered:

- Arrival time should be independent of noise level and spectrum. The stochastic variation in t_{oa} due to noise should be as small as possible.

- Arrival time should be independent of pulse shape and amplitude.

- Arrival time should be independent of length of recorded signal.

- Arrival time should be independent of the pulse location (in time) in the record.

- Arrival time should be insensitive to reflections of the main pulse on joints and RMUs. These reflections are often present in measured signals.

- Combination of arrival times of injected pulses and measured PD pulses should result in an accurate location of the PD origin.

A t_{oa}-method that meets all these criteria would be preferable. But even if not all criteria are met, the method can be useful in specific situations. For PD diagnostics on power cables a location uncertainty of 1% of the cable length is usually considered to be sufficient.

4.3   Time-of-arrival methods

Each method is analyzed analytically with respect to the criteria mentioned in the previous section. The recorded signal ($x[k] = s[k] + n[k]$), noise-free PD signal ($s[k]$), noise ($n[k]$) and their associated power (respectively P_x, P_s and P_n) and energy (respectively E_x, E_s and E_n) are defined in §A.3 in Appendix A. A PD signal has a finite duration and thus E_s is finite if the number of samples $B \to \infty$. The noise on the other hand is time-invariant and has constant power P_n, and thus $E_n \to \infty$ if $B \to \infty$. Finite-energy disturbances, such
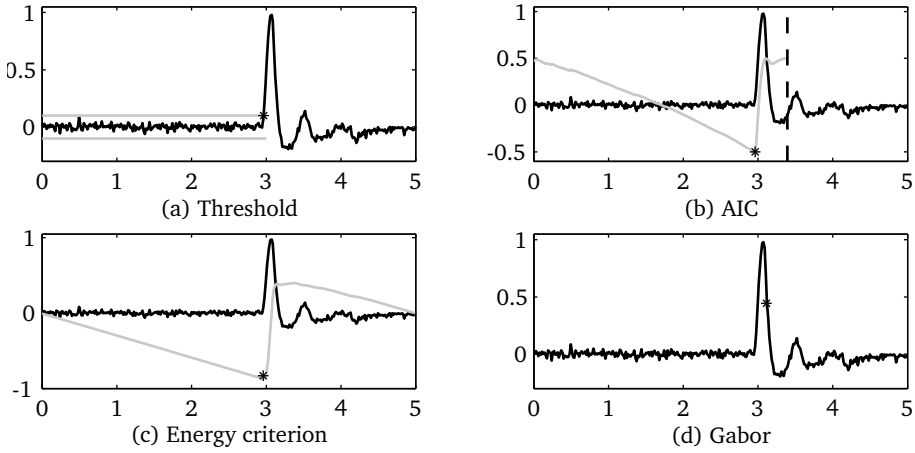
Figure 4.1 Example of recorded pulse with four t_{oa}-methods applied. Time axes are in μs. Black line: recorded PD signal, gray line: threshold[(a)], normalized & shifted AIC curve[(b)], normalized EC curve[(c)] , *: time-of-arrival, and dashed line: end of record used for AIC analysis.

as thyristor pulses, are not considered in this chapter. Two of the t_{oa}-methods use the noise power P_n in their evaluation. The noise power P_n can be estimated using a noise measurement prior to the PD measurement, or using a signal of a PD measurement and calculating P_n from a part of the signal that contains only noise.

4.3.1   Trigger level method

The trigger level method positions t_{oa} at the time at which the signal $x[k]$ exceeds a certain threshold level x_{thres}. This is a straightforward method that can easily be implemented [24] and is therefore used in many PD detection systems. The threshold level is chosen relative to the noise level, making it always as low as the noise permits without too many false triggers. First, the algorithm will determine the noise power P_n from a signal sample without PD pulse. Next, the threshold is chosen according to:

$$x_{\text{thres}} = m \cdot \sqrt{P_n} \tag{4.1}$$

where m is a parameter chosen by the user. In this chapter the value $m = 5$ is chosen for all simulations. In Figure 4.1a an example of a recorded pulse is plotted together with the threshold x_{thres}.

The t_{oa} determined by this method is noise-level dependent since the threshold x_{thres} is chosen relative to the noise level. The arrival time of steep pulses is not very sensitive to the noise level, while the arrival time of slow rising pulses is sensitive to both noise level and pulse amplitude.

4.3.2 Akaike Information Criterion method

The Akaike Information Criterion (AIC) is a measure of the goodness of fit of a statistical model to a set of observations [23]. It optimizes to a good trade-off between the complexity of the model and the goodness of fit. In seismology this criterion has been used in combination with two autoregressive (AR) fits to determine the onset of seismic waves (see for example [43]). Alternatively, the AIC can be calculated directly from the signal itself [71]. The direct AIC method has been applied to ultrasound signals in concrete [25] and PD detection in cable systems [18].

The direct AIC method used in this chapter defines an AIC value for each sample k of a signal:

$$\text{AIC}[k] = k \cdot \ln\left(\sigma_{0,k}^2\right) + (B - k - 1) \cdot \ln\left(\sigma_{k,B-1}^2\right) \tag{4.2}$$

with k an index ranging from 0 to $(B-1)$, B the total number of samples in signal $x[k]$ and $\sigma_{m,n}^2$ the variance of signal $x[k]$ from index m up to and including index n. The value AIC$[k]$ is calculated for each sample in the signal $x[k]$. The t_{oa} is the global minimum of all AIC$[k]$ values. Figure 4.1b shows a signal and its corresponding AIC curve.

Equation Eq. 4.2 is symmetric in the sense that the second term is equal to the first term, except that it starts at the end of the signal. Consider a signal containing a pulse shorter than half of the signal length. Applying this method to the total signal when the pulse is in the first half of the signal and the second half contains only noise, will yield a different t_{oa} (relative to the pulse), than when applied to a similar signal with the same pulse in the second half of the signal. Arranging that the onset of the pulse is always in the second half of the signal, as suggested in [25], avoids this potential pitfall. The tail of the pulse can be cropped at the end of the signal.

At the global minimum of AIC$[k]$ is the derivative with respect to k equal to zero.

$$\frac{\partial \text{AIC}[k]}{\partial k} = \ln\left(\sigma_{0,k}^2\right) + \frac{k}{\sigma_{0,k}^2} \cdot \frac{\partial \sigma_{0,k}^2}{\partial k} - \ln\left(\sigma_{k,B-1}^2\right) + \frac{B-k-1}{\sigma_{k,B-1}^2} \cdot \frac{\partial \sigma_{k,B-1}^2}{\partial k} \tag{4.3}$$

Since equation Eq. 4.3 contains $\sigma_{0,k}^2$, which strongly depends on the noise level, the t_{oa} will be influenced by the noise level. This sensitivity depends on the steepness of the pulse.

4.3.3 Energy criterion method

The energy criterion (EC) method is based on the energy content of the signal. This method combines the partial signal energy with a negative trend. It has been applied to ultrasound signals [25] and PD diagnostics [18]. The signal EC$[k]$ is defined as:

$$\text{EC}[k] = \frac{E_{\text{p},x}[k]}{\Delta t} - k \cdot P_x \tag{4.4}$$

with $E_{p,x}[k]$ the partial signal energy of signal $x[k]$ defined as:

$$E_{p,x}[k] = \Delta t \sum_{i=0}^{k} x^2[i] \tag{4.5}$$

The value EC$[k]$ is calculated for k ranging for 0 to $(B-1)$. The global minimum of all EC$[k]$ values coincides with the t_{oa}. In [25, 71] a factor α is introduced in the second term of Eq. 4.4 to move the t_{oa} closer towards the base of the pulse. In this chapter α is omitted since it introduced a noise-dependency and had no significant influence on the overall location accuracy. Figure 4.1c depicts a signal, its EC curve, and corresponding t_{oa}.

Substituting $x[k] = s[k] + n[k]$ in equation Eq. 4.4 and assuming the noise to be time-invariant yields:

$$EC[k] = \frac{E_{p,s}[k]}{\Delta t} + \frac{E_{p,n}[k]}{\Delta t} - k \cdot P_s - k \cdot P_n = \frac{E_{p,s}[k]}{\Delta t} - k \cdot P_s \tag{4.6}$$

At the global minimum in equation Eq. 4.6:

$$\frac{\partial EC[k]}{\partial k} = 0 = s^2[k] - P_s \tag{4.7}$$

The noise $n[k]$ does not arise in equation Eq. 4.7, indicating that t_{oa} is independent of the noise level. Since a PD pulse has a finite duration, the mean signal power P_s depends on the length of the signal. As a consequence t_{oa} depends on the signal length. All analyses are done using the same record length to prevent a record-length dependency in the results.

4.3.4 Gabor centroid method

Gabor defines the "epoch" of order 1 of a signal [12]. Assuming a real time-discrete signal with $x[k] = s[k] + n[k]$ this epoch is defined as:

$$t_g = \frac{\sum_{k=0}^{B-1} t[k]x^2[k]}{\sum_{k=0}^{B-1} x^2[k]} = \frac{\sum_{k=0}^{B-1} t[k]s^2[k] + P_n \sum_{k=0}^{B-1} t[k]}{\sum_{k=0}^{B-1} s^2[k] + P_n \cdot B} \tag{4.8}$$

where t_g is Gabor's epoch and $t[k]$ the time corresponding to sample k. This equation shows that t_g is dependent on the noise level. This error can be corrected by defining:

$$t_{oa,g} = \frac{\sum_{k=0}^{B-1} t[k]x^2[k] - P_n \sum_{k=0}^{B-1} t[k]}{\sum_{k=0}^{B-1} x^2[k] - P_n \cdot B} \tag{4.9}$$

The noise power P_n can be estimated based on a part of signal $x[k]$ that has no pulse, or on a separate noise measurement. Figure 4.1d shows a signal and its corresponding $t_{\mathrm{oa,g}}$.

4.3.5 Phase method

The phase method converts the recorded signal $x[k]$ to frequency domain and retrieves the phase for a chosen frequency. A time delay is represented in frequency domain as:

$$X_{\mathrm{delayed}} = X\,\mathrm{e}^{-j\omega\tau} \tag{4.10}$$

where τ is the delay time and $X_{\mathrm{delayed}}(\omega)$ is $X(\omega)$ delayed for τ. The phase method uses this relation and defines the arrival time as:

$$\tau = \frac{-\angle X(\omega_{\mathrm{c}})}{\omega_{\mathrm{c}}} \tag{4.11}$$

where $X(\omega)$ is the recorded signal converted to frequency domain, $\angle$ denotes the phase of a signal in frequency domain and ω_{c} is a chosen frequency. For all pulses the same ω_{c} must be used.

Due to the periodicity of 2π the phase is not unambiguously determined by equation Eq. 4.11:

$$\tau = \frac{-\angle X(\omega_{\mathrm{c}})}{\omega_{\mathrm{c}}} + \frac{m \cdot 2\pi}{\omega_{\mathrm{c}}} \tag{4.12}$$

with m an unknown integer. This problem can be solved by multiplying $X(\omega)$ with a (negative) time delay τ_{ch} (see Eq. 4.10) first. This time delay must be chosen such that the phase does no longer wraps around (jump from $-\pi$ to π, or vice versa). Since τ_{ch} is unknown a priori, an iteration loop is used to find the correct time delay. Once the correct τ_{ch} has been found the phase of the delayed $X(\omega)$ is converted to a time using equation Eq. 4.11 and added to τ_{ch}. The entire procedure is implemented by the following steps:

1. Convert recorded signal $x[k]$ to frequency domain $X(\omega)$.

2. Determine frequency range(s) over which $X(\omega)$ has a good signal-to-noise ratio. In these ranges the phase of $X(\omega)$ is most reliable.

3. Start iteration loop.

4. Add time delay τ_{ch} (an initial value or a value based on previous iteration step) to $X(\omega)$:

$$X_{\mathrm{ch}} = X\mathrm{e}^{j\omega\tau_{\mathrm{ch}}} \tag{4.13}$$

5. Check the phase of $X_{\mathrm{ch}}(\omega)$ for phase jumps of $\pm 2\pi$ in the frequency ranges determined in step 2. If there are jumps, go back to step 3 and choose a new τ_{ch}. If not, proceed with the next step.
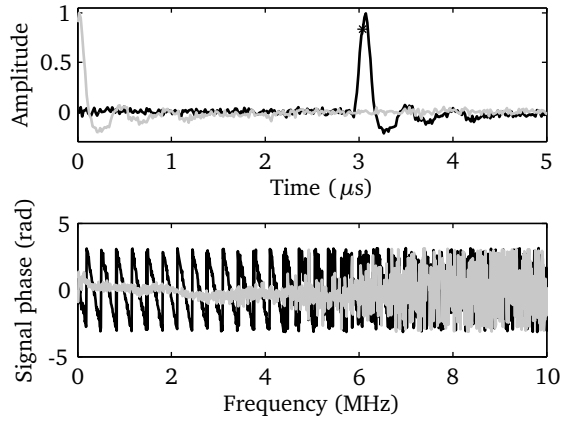
Figure 4.2 Signal before and after iteration loop. The signal is plotted in time domain and the phase in frequency domain. The iteration loop ended with $\tau_{\text{ch}} = 3.05\,\mu s$. Black line: signal before iteration, gray line: signal after iteration loop, and *: time-of-arrival.

6. Calculate the time-of-arrival using:

$$t_{\text{oa,p}} = \tau_{\text{ch}} - \frac{\angle X_{\text{ch}}(\omega_{\text{c}})}{\omega_{\text{c}}} \tag{4.14}$$

where ω_{c} is a frequency within the range determined in step 2. Choosing a higher frequency gives higher accuracy (see Appendix B), as long as the signal-to-noise ratio is sufficient. For consistency, ω_{c} must be the same for all measurements. Taking the average over a small frequency range around ω_{c} reduces the sensitivity to noise and reflections in the signal. In this chapter $\omega_{\text{c}} = 2\pi \cdot 1.5\,\text{MHz}$ is used together with a range of $\pm 500\,\text{kHz}$ for averaging to reduce noise sensitivity.

In Figure 4.2 a recorded PD signal is plotted in time domain together with the phase of the signal in frequency domain. After the iteration loop (steps 3–5) the signal is shifted in time domain towards $t = 0$. This shifted signal is also plotted in Figure 4.2. Due to the nature of the discrete Fourier transform the first part of the pulse is wrapped to the end of the signal, which is not shown.

The major advantage of this method is that it is not influenced by dispersion and attenuation of the cable. In the absence of complications due to a complex load impedance ($Z_{\text{load}}(\omega)$) at the cable ends the mean location error will be zero. Choosing a narrow but finite frequency range around ω_{c} introduced only an insignificant error. Unfortunately, for online diagnostics, signal transmission to the connected load impedances from RMUs introduces a phase shift. If the characteristic cable impedance (Z_{c}) and the load impedance are known, e.g. by using an impedance measurement as described in [59], the phase shift

can be estimated and can be corrected for:

$$t_{\mathrm{oa,p,corr}} = t_{\mathrm{oa,p}} + \frac{\angle T(\omega_{\mathrm{c}})}{\omega_{\mathrm{c}}} \tag{4.15}$$

where $t_{\mathrm{oa,p,corr}}$ is the corrected arrival time and T is the current transmission coefficient from cable to load, given by $T = 2Z_{\mathrm{c}}/(Z_{\mathrm{c}} + Z_{\mathrm{load}})$. However, the impedance estimate has limited accuracy depending on the RMU configuration. In the Appendix B the sensitivity of the location accuracy to errors in the impedance estimation is analyzed.

Since there is no correlation between the phase of the signal at ω_{c} and the phase of the noise, the noise has no influence on the expected value of $t_{\mathrm{oa,p}}$, but only on its standard deviation.

4.4 PD location

For the location of a PD two measurements are required: a cable propagation time (t_{c}) measurement and the actual PD measurement. Offline diagnostics often employs a single-sided system where the propagation time measurement and PD location are based on reflections from the far end [28]. The impedances of RMUs connected to the cable during online measurements can prevent visible reflections from the cable ends. Detection of the pulses at both ends is then preferred [59]. Although the analyses in this section are based on a two-sided system, the conclusions of the t_{oa}-method evaluation can equally well be applied to other PD-measurement configurations.

4.4.1 Cable propagation time measurement

The t_{c}-measurement using two, non-synchronized measurement systems (one at each cable end) is conducted as follows. A pulse is injected by measurement unit 1 (MU 1) at the near cable end ($s_{11}(t)$), which is detected by MU 2 at the far end ($s_{21}(t)$). After a short delay (t_{wait}, for example $10\,\mu$s) MU 2 injects a similar pulse ($s_{22}(t)$), which is detected by MU 1 ($s_{12}(t)$). The record taken by each unit must contain both pulses. Figure 4.3 illustrates schematically the signals recorded by MU 1 and MU 2.

In the t_{c}-measurement there are in total four pulses. The arrival time of each pulse is determined using a t_{oa}-method. The time difference between the two pulses recorded by MU 1 is given by $\tau_1 = 2t_{\mathrm{c}} + t_{\mathrm{wait}}$, and the between the pulses of MU 2 by $\tau_2 = t_{\mathrm{wait}}$. The cable propagation time t_{c} is equal to: $t_{\mathrm{c}} = \frac{1}{2}(\tau_1 - \tau_2)$. The advantage of this method is that the time bases of MU 1 and MU 2 do not need to be synchronized for the cable propagation time measurement.

4.4.2 PD measurement

During the PD measurement the measurement units at each cable end detects a PD pulse. The time bases of the units must be accurately synchronized (for example using pulse
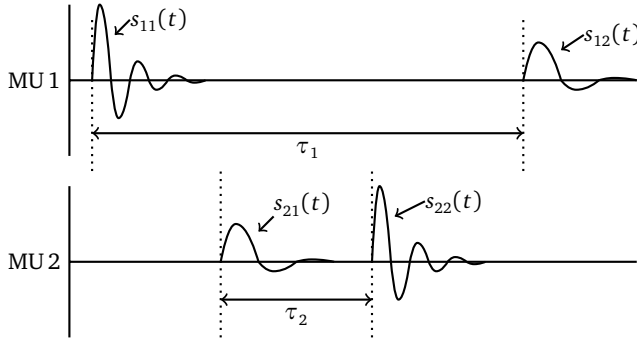
Figure 4.3 Signals arriving at both cable ends during a propagation time measurement.

injection [59] or GPS [45]). The arrival time of the PD pulses is determined using one of the t_{oa}-methods. The difference in time-of-arrival at both ends is taken, together with t_c, to calculate the PD origin:

$$z_{PD} = \tfrac{1}{2} l_c \left(1 - \frac{t_{oa,2} - t_{oa,1}}{t_c} \right) \qquad (4.16)$$

where z_{PD} is the distance from near cable end to the PD origin, l_c the cable length and $t_{oa,1}$, $t_{oa,2}$ the arrival times of the PD pulse at respectively MU 1 and MU 2.

4.5 Simulations

Several simulations have been conducted to evaluate the t_{oa}-methods using the criteria proposed in §4.2. For all simulations a model for a cable of 1 km is used. The characteristic impedance and propagation coefficient for this cable were measured on a field-aged 3-core MV PILC cable of 200 m to obtain realistic values in the simulations. At each end the cable is terminated with a load impedance ($Z_{load}(\omega)$), representing the effect of an RMU or substation, where the sensor is installed. The sensor is assumed to be an ideal current probe that measures the current through the load impedance. The choice for a current probe as sensor is related to the online application in which case usually it is the only sensor type allowed to be installed. Moreover, it is also the most challenging situation because the RMU-cable injection circuit will have a profound effect on the waveforms. The transmission coefficient from cable to load is calculated using the load impedance and the characteristic cable impedance. The load impedance can be varied to investigate its effect on the t_{oa}-methods. In the other simulations the load impedance is matched to the cable impedance (real-valued, frequency-independent impedance of 12 Ω).

The t_c-measurement is simulated using different pulse shapes for the injected pulse. Since PDs are short phenomena with respect to $1/f_d$ (f_d detection bandwidth) a PD signal is represented by a δ-pulse at the origin. All pulses in the simulated signal are normalized
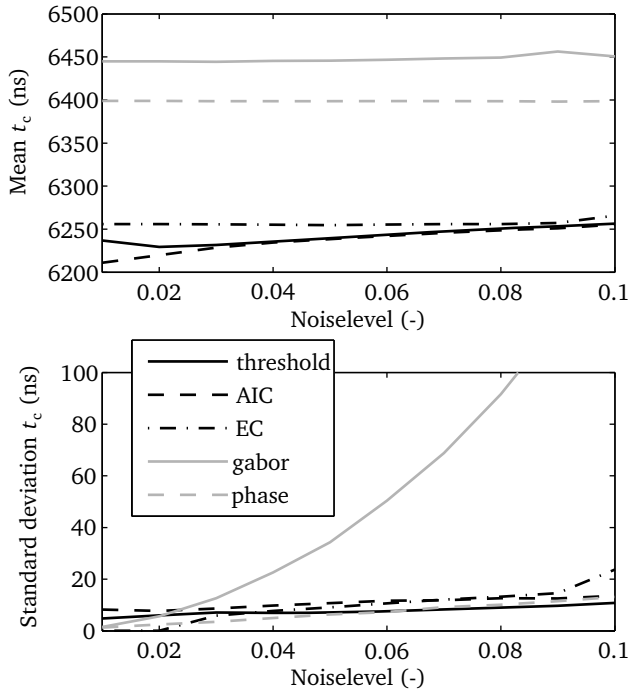
Figure 4.4 Mean and standard deviation of cable propagation time simulation. Unit of noise level is the ratio of the standard deviation of noise relative to maximum amplitude of pulses

to a maximum amplitude of one, so that the signal-to-noise ratio is about the same for all pulses. Uncorrelated Gaussian noise with a specified spectrum is added to the signal to simulate realistic noise conditions. Unless stated otherwise, the noise spectrum taken is white.

Each simulation is repeated 1000 times. The mean and standard deviation of those 1000 repetitions give a good estimate for the accuracy and precision of the methods. Due to the stochastic nature of noise the application of the t_{oa}-methods to a simulation returns occasionally an obviously incorrect value, especially with higher noise levels. These outliers are eliminated using the modified z-score method [20], which is based on the median deviation from the median of all 1000 repetitions of the simulation.

4.5.1 Sensitivity to noise level

The accuracy should be independent of the noise level. A t_c-measurement using PD-like pulses is simulated at different noise levels. The results are plotted in Figure 4.4.

The mean values of the EC, Gabor and phase method are virtually independent of the
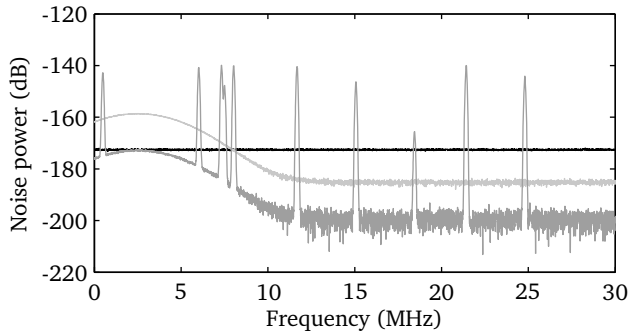
Figure 4.5   Noise spectra used in the noise-spectrum-sensitivity simulations. Black: situation 1, light gray: situation 2 and dark gray: situation 3.

noise level. The threshold and AIC method show a small noise-level dependency. The standard deviation of the Gabor method shows a quadratic relation with the noise level. For higher noise levels the standard deviation of the Gabor method is unacceptably high. The standard deviations of the other methods are within 0.5% of the mean t_c.

The methods estimate different cable propagation times. This is related to the distinct backgrounds of the methods. They yield different t_{oa}'s on the same pulse, as shown in Figure 4.1 and Figure 4.2. Since there exists no unambiguous definition for t_c the accuracy of the methods can not be judged on the propagation time. The differences cancel out when the t_{oa}'s are combined to obtain the PD origin. Therefore, the accuracy of the methods can only be tested using the PD location as tested in §4.5.4.

4.5.2   Sensitivity to noise spectrum

During a measurement the noise is rarely white. In this section a t_c-measurement is simulated using three different noise conditions shown in Figure 4.5. In all three situations the noise is Gaussian and has the same mean power. The only difference between the simulations is the noise spectrum. Spectrum 1 is white; spectrum 2 and 3 are computer-generated with a shape similar to spectra measured during field measurements. The difference between 2 and 3 is that spectrum 2 lacks narrow band sources.

The mean and standard deviation of the 1000 repetitions of the simulations are given in Table 4.1. These results show that the t_{oa}-methods are virtually insensitive to the noise spectrum. Only the standard deviation of the Gabor method shows a significant change.

4.5.3   Sensitivity to pulse shape

A simulated t_c-measurement is performed using pulses injected by the measurement system. There are different methods to couple a pulse into the cable system (capacitive, inductive or galvanic). Different coupling mechanism will inject different pulse shapes.

Table 4.1 Mean and standard deviation of t_c of the noise-spectrum-sensitivity simulations. All values are in ns.

Spec.	Threshold	AIC	EC	Gabor	Phase
1	6232 ± 7	6228 ± 9	6256 ± 5	6445 ± 13	6399 ± 4
2	6231 ± 7	6229 ± 10	6256 ± 6	6445 ± 21	6399 ± 8
3	6232 ± 7	6228 ± 9	6256 ± 6	6445 ± 32	6399 ± 4

Pulse 1: measured inductive coupled pulse
Pulse 2: measured inductive coupled pulse with low bump
Pulse 3: ideal PD-like pulse
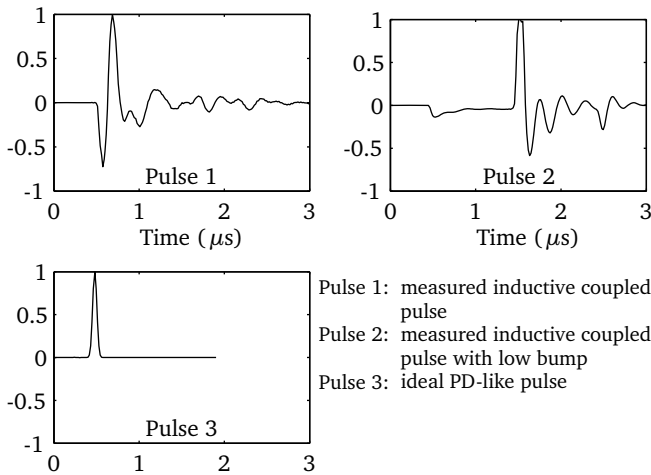
Figure 4.6 Pulse shapes used in injection in pulse-shape-sensitivity simulations.

Also, the design of the pulse source and the load impedance where the pulse is injected influence the pulse shape. The cable propagation time t_c is independent of the pulse shape. Therefore, a t_{oa}-method should yield the same t_c for different pulse shapes.

Figure 4.6 shows three different pulse shapes of injected pulses. Pulse 1 is an inductively coupled pulse that was measured during an online PD measurement in an MV cable system. Most energy of this pulse is concentrated in the beginning of the pulse. The second pulse is also an inductively coupled pulse, but with different pulse source design, different injection coil and different load impedance. This pulse starts with a long low bump (charging) and then a short steep pulse. Thus, most low frequency content is located in the first part of the pulse and most high frequency content comes about $1\,\mu s$ later. This kind of waveforms can arise not only due to the pulse source design as is the case with this pulse, but also due to distinct signal propagation modes, e.g. in belted cables [66]. The third pulse is a short pulse with a width of about $100\,\mathrm{ns}$. This pulse is similar to a real PD pulse that has propagated through a power cable over a short distance.

For each pulse 1000 simulations of t_c-measurements have been conducted. The mean and standard deviation of each simulation set is summarized in Table 4.2. Except

Table 4.2 Mean and standard deviation of t_c of the pulse-shape-sensitivity simulations. All values are in ns.

Pulse	Threshold	AIC	EC	Gabor	Phase
1	6230 ± 6	6209 ± 8	6241 ± 3	6355 ± 7	6399 ± 5
2	5333 ± 10	5272 ± 12	5391 ± 10	6318 ± 11	6399 ± 3
3	6231 ± 7	6228 ± 8	6256 ± 6	6445 ± 12	6399 ± 4

for the phase method, all methods are sensitive to the pulse shape. Especially pulse 2 yields unacceptable results. There, most high and low frequency content of the pulse are concentrated at different times. At injection the start of the high-frequency part is chosen as time-of-arrival, because it contains most energy. After propagating through the cable most high-frequency content is attenuated, and the low-frequency becomes dominant. Therefore, at the far end the time-of-arrival is determined by the low-frequency part. The only method that is not influenced by the pulse shape is the phase method, because it analyzes the pulse in frequency domain and uses a fixed frequency for all analyses. The change in t_c of the Gabor method less than 2%, which is twice the target accuracy of 1%. The differences of the other methods are unacceptable.

An option to reduce the sensitivity to the pulse shape is to calculate the transfer function from the near end pulse to the far end pulse. Converting a transfer function in frequency domain to time domain gives the impulse response of the channel. It can be regarded as the far-end pulse from an injected δ-pulse. The arrival time of the impulse response is t_c. The calculated transfer functions are:

$$H_{12} = \frac{S_{21}}{S_{11}} \qquad \text{and} \qquad H_{21} = \frac{S_{12}}{S_{22}} \qquad (4.17)$$

with $H_{12}(\omega)$ the transfer function from near end to far end, and $S_{ij}(\omega)$ the frequency-domain representation of $s_{ij}(t)$ (see Figure 4.3). If time bases of the near and far end are not synchronized the average of the arrival times of $h_{12}(t)$ and $h_{21}(t)$ is equal to the propagation time.

The simulations of the t_c-measurements with different pulse shapes have been repeated. The t_{oa} is now determined using the channels impulse response. The results are listed in Table 4.3. The results for pulse 1 are clearly unusable for all methods, except for the phase method. The results for pulse 2 and 3 are satisfactory. The reason that the results for pulse 1 are far off is the lack of low frequency content. Therefore, the constructed transfer function becomes unreliable at low frequencies and the impulse response is impeded by noise.

4.5.4 Sensitivity to load impedance

This section deals with the location accuracy in general and the influence of the load impedance on the accuracy. To be able to locate PDs both a t_c-measurement simulation

Table 4.3 Mean and standard deviation of t_c of the pulse-shape-sensitivity simulations using the channel's impulse response. All values are in ns.

Pulse	Threshold	AIC	EC	Gabor	Phase
1	3442 ± 1653	5321 ± 688	5896 ± 135	6521 ± 138	6398 ± 2
2	6190 ± 5	6153 ± 9	6192 ± 0	6451 ± 9	6399 ± 1
3	6183 ± 6	6143 ± 6	6192 ± 0	6446 ± 4	6399 ± 1

and the actual PD measurement simulation are required. Since the load impedance at each cable end has a significant influence on the pulse shape the location simulations are conducted with different load impedances. Four different impedances are used: a real impedance matching the cable impedance, a capacitive load, an inductive load and a load impedance measured online in a ring-main-unit (RMU) (see [59] for the online impedance measurement method). The last impedance is a typical load impedance encountered in a medium-voltage distribution grid. The t_c-measurement was simulated using the short PD-like pulse (pulse 3 in Figure 4.6). The noise is white and has a constant level for all simulations.

In the first simulation the load impedance at both cable ends is equal to the characteristic cable impedance. Therefore the pulse shape will not be distorted at the transition from cable to load impedance. This simulates the location accuracy of the t_{oa}-methods when a PD pulse shape is influenced by the dispersion and attenuation of the cable. The mean and standard deviation of the location error of the simulations are plotted in Figure 4.7. This figure shows that all methods provide an accurate location ($< 0.1\%$ of cable length). Note that the location error of the phase method is virtually zero. The standard deviation of the Gabor method is larger than the other methods, which are similar to each other.

In the second simulation the near end is terminated with an inductance of $1\,\mu H$ and the far end is terminated with a capacitance of $2\,nF$. These impedances do not represent field conditions, but are meant to test the methods for different loads with opposite phase shift at both ends. This is a worst-case scenario for the phase method because the errors introduced due to the phase shift at the transitions to the load impedances at both ends accumulate. The results of the simulations are plotted in Figure 4.8. As expected the phase method performs poorly for this configuration. But if the load impedance at the test frequency ω_c would be known, the phase shift at the transmission to the load impedance can be corrected. The performance of the Gabor method is not within the 1% target accuracy limit and has a relatively large standard deviation. The other three methods have a mean error less than 0.5% of the cable length.

The third simulation consists of a matched impedance at the near end and at the far end a realistic load impedance that was actually measured in the field. The results are depicted in Figure 4.9. The AIC method has both the largest mean and standard deviation. The phase method without correction and Gabor method have both a maximum mean error of approximately $10\,m$ (1% of the cable length). Note that due to the frequency-dependency of $Z_{load}(\omega)$ the accuracy of the phase method is influenced by the choice of

Figure 4.7   Mean and standard deviation of the location error for PDs from different locations in the cable. Load impedances at both cable ends are matched to the characteristic impedance of the cable.

ω_c. The energy criterion method has both a low mean error and a low standard deviation.

4.6   Experiment

In order to test the methods experimentally measurements on a test setup have been conducted. The test setup consists of two RMUs with MV/LV transformer and three-core MV Paper Insulated Lead Covered (PILC) cables. A schematic drawing of the test setup is depicted in Figure 4.10. The MV cable between RMU 1 and RMU 2 consists of two different field-aged cable sections. The propagation velocity of the first section (96 m) is about 5% higher than the other section (201 m). RMU 1 has a second MV cable that can be disconnected. RMU 1 has an MV/LV transformer of 1 MVA, and RMU 2 has a transformer of 100 kVA. The joint can be opened to inject PD-like pulses with a pulse source. Current probes and injection coils are installed in both RMUs as indicated in Figure 4.10 (see [59] for details on the installation options).

Two configurations are tested. In the first experiment the parallel cable in RMU 1

Figure 4.8 Mean and standard deviation of the location error for PDs from different locations in the cable. Load impedance at near end is and inductance of $1\,\mu$H and the load impedance at the far end is a capacitance of $2\,$nF.

is disconnected. In both RMUs the load impedance is formed by the transformer and the cables connecting the transformer. In the second experiment the parallel cable in RMU 1 is connected to the rail. The load impedance is now the transformer impedance parallel to the cable impedance. For both measurements first a t_c-measurement is conducted, followed by a PD measurement where PD-like pulses are injected in the joint. All measurements are repeated 100 times.

The results of both experiments are listed in Table 4.4. Eq. 4.16 yields a distance of 93 m instead of 96 m due to the difference in propagation speed in the 96 m section and the 201 m section. The different propagation velocities can be incorporated in the analysis (see [59]), but for convenience we assume the joint to be at 93 m and both cable segments to have equal propagation velocities.

The threshold, AIC and EC methods have an accuracy better than 1% of the cable length in both experiments. The accuracy of the Gabor and (uncorrected) phase methods is insufficient. The accuracy of the phase method can be improved significantly if the load impedances are known around the test frequency ω_c, but the analysis in Table 4.4

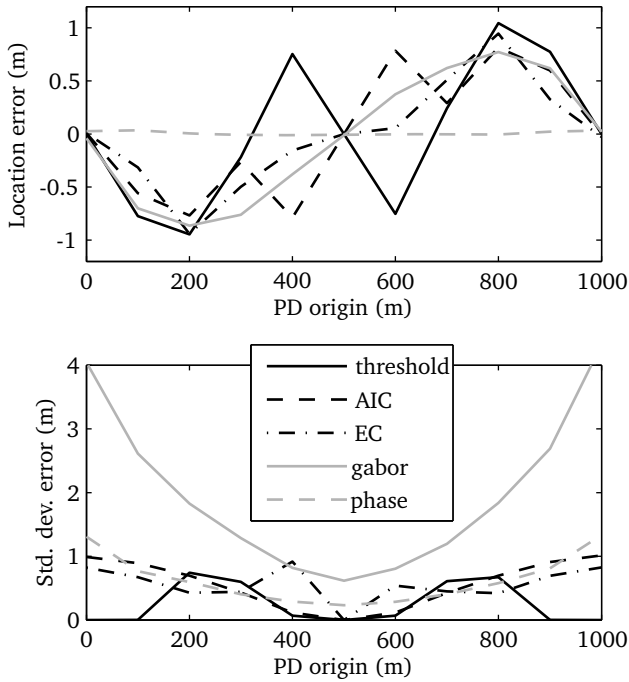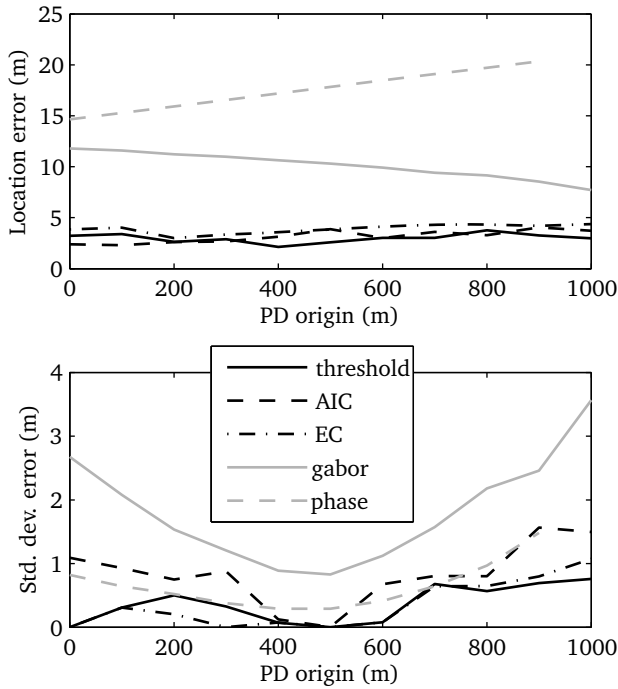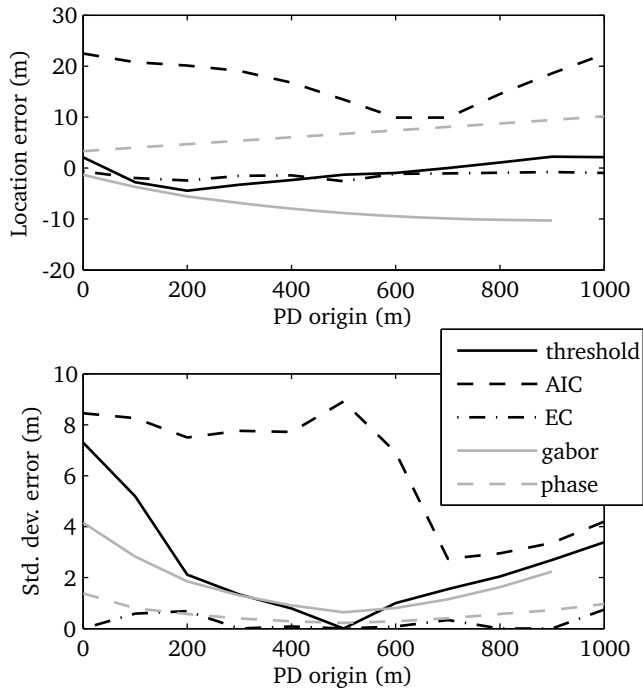**Figure 4.9** Mean and standard deviation of the location error for location of PDs from different locations in the cable. Load impedance at near end is matched to the cable and load impedance at far end is the load impedance measured in an RMU.
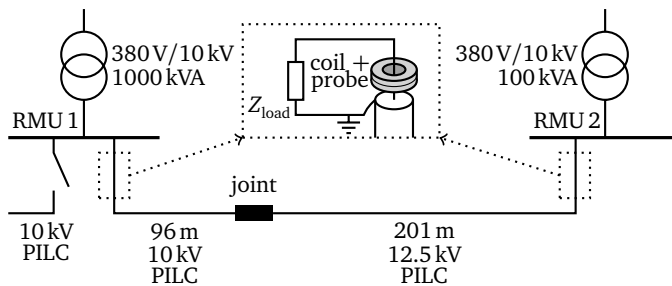
Figure 4.10 Schematic drawing of test setup. The inset shows the position of the current probe and injection coil in the RMU

Table 4.4 Mean and standard deviation of location of experiments. All values are in meters.

	Threshold	AIC	EC	Gabor	Phase
Experiment 1	93.3 ± 0.8	93.5 ± 0.6	94.4 ± 0.6	87.3 ± 0.3	96.7 ± 0.3
Experiment 2	94.3 ± 0.7	94.1 ± 0.9	93.6 ± 0.3	121.9 ± 0.4	82.7 ± 0.5

Table 4.5 Summary of strong and weak points of t_{oa}-methods. See §4.2 for a description of the criteria.

	Threshold	AIC	EC	Gabor	Phase
Noise	$-$	$-$	$+$	0	$+$
Pulse shape	$-/0^a$	$-/0^a$	$-/0^a$	$-/0^a$	$+/+^a$
Record length	$+$	$+$	0	$+$	$+$
Pulse location in record	$+$	0	$+$	$+$	$+$
Reflections in signal	$+$	$+$	$+$	$-$	$+$
Location accuracy	$+$	$+$	$+$	$-$	$-/+^b$

a) by incorporating channel's impulse response
b) if load impedances are known accurately

does not take this into account. It intends to simulate the worst-case scenario in which this measurement is not performed accurately or not done at all. During experiment 1 the accuracy of the phase method is reasonable, but during the second experiment the accuracy is definitely insufficient. During the first experiment the load impedances in RMU 1 and RMU 2 were similar, so the phase shifts cancel, while during experiment 2 the load impedance of RMU 1 is changed significantly due to the parallel MV cable. A second cause for the relatively large error is that the cable in the experiment is shorter than in the simulations. Therefore, any phase shift at the cable ends introduces in the experiment results a larger relative error than in the simulations. The inaccuracy of the Gabor method is probably caused by reflections present in the signal. The term $t[k]x^2[k]$ in Eq. 4.9 causes reflections coming after the main pulses to have a significant effect on the $t_{oa,g}$.

4.7 Conclusions

The t_{oa}-methods discussed in this chapter have been evaluated analytically and with simulations to investigate the strong and weak points of the methods. As far as practically possible these have been verified experimentally. The strong and weak points are summarized in Table 4.5.

Altogether, no single method performs superior on all criteria. Depending on the situation either the EC method or the phase method will provide the most reliable overall performance. The EC method has good accuracy in most situations. The only point where it failed is on its sensitivity to particular pulse shapes. Incorporating the channels impulse

response improved the pulse shape sensitivity for some pulse shapes. The strongest point of the phase method is its complete insensitivity to the pulse shape. The second advantage is the high accuracy, provided that the load impedance and characteristic cable impedance can be measured or estimated. If the load impedance is unknown, or if there are other locations in the cable circuit where the phase changes suddenly the accuracy of the phase method is poor for most situations.

ADAPTIVE MATCHED FILTER BANK

5.1 Introduction

Partial discharge (PD) measurements, especially under online conditions, are impeded with noise and interference caused by numerous natural and artificial sources. The three main disturbance classes that can be distinguished are: i) broadband background noise, ii) finite-energy interference, and iii) continuous periodic interference. PD detection is hampered by the noise and disturbances. The PD detection sensitivity can be improved by applying signal processing techniques, such as matched filters [49–51]. A matched filter is the optimal linear filter for maximizing the signal-to-noise (SNR) in the presence of additive noise, provided that the signal (PD) waveform and noise spectrum are known. The noise spectrum can be estimated from the measured signal itself before the matched filter is applied. Estimating the PD signal waveform is more complicated. The PD signal waveform is determined by the cable system under test. This includes the cable itself, any RMU along the cable under test (CBLUT) and the RMUs at both ends of the CBLUT (where the PD measurement units are installed). The transfer function of the measurement unit itself also influences the detected waveform. The measurement unit needs to construct PD templates that are specific to each situation because most of these parameters differ per cable system. The impedance of the RMU where the measurement unit is installed is measured through injection and detection of reference pulses [59]. The PD waveform is predicted using the measured local impedance combined with a cable model that simulates the effect of the PD pulse propagation through the cable. Because the PD waveform depends on the distance it traveled through the cable a set of matched filters, the matched filter bank (MFB), is constructed. Each filter corresponds to a specific traveled distance.

The level of detail of the cable system that a measurement unit installed at the end of the cable under test can detect is limited. Even though the unit measures the most

prominent parameters, the templates are suboptimal. In certain situations a significant factor is not taken into account. For example, an RMU along the CBLUT can have a strong influence on the pulse shape. A suboptimal template results in a decreased detection sensitivity and location accuracy. The sensitivity can be improved by creating templates that match better with measured PD pulses. Obviously, templates that have the best match with measured pulses are the measured pulses themselves. A cable defect produces discharges with the same shape but a range of amplitudes. Large PDs will be detected, even though the template does not perfectly match the PD. These large PDs can be used to either create a new or to update an existing template. This effectively increases the detection sensitivity and improves the estimation of arrival time and amplitude for that location.

This chapter describes an algorithm that improves the templates in the MFB based on detected pulse signals. In §5.2 an overview of the MFB as it is applied for PD detection is given. The adaptation algorithm for creating new templates from detected PDs is described in §5.3. In §5.4 the presented algorithm is applied to data sets acquired during online PD measurements on a cable systems. Conclusions are in §5.6.

5.2   Matched filter bank for PD detection

5.2.1   Introduction

Matched filtering is a technique to detect known signals in the presence of noise. It maximizes the average signal-to-noise ratio (SNR) at the output, provided that the signal waveform and the noise power spectrum density function are known. Basic theory can be found in literature, such as [9, 49]. This section summarizes the application of matched filters to PD detection as described in [50].

The transfer function of the mth matched filter for colored noise in the MFB is defined as:

$$H_m = \frac{S_m^*}{P_N} \tag{5.1}$$

where $H_m(\omega)$ is the transfer function of the mth matched filter, $P_N(\omega)$ the power spectral density function (PSDF) of the noise and $S_m(\omega)$ the mth predicted PD waveform (template), m and index ranging from 1 to M, with M the number of the filters in the MFB. In Figure 5.1 a schematic overview of the filtering process is depicted. First, the PSDF is estimated from recorded signal $x[k]$. Next, signal $x[k]$ is filtered by the common filter, which contains the part in Eq. 5.1 that is independent of the templates. The templates are applied to the signal after the common filter, giving M different signals. In the next block a threshold is applied to each signal to detect the occurrence of PD signals. A single PD may be detected by multiple templates. If multiple templates detect the same pulse they are combined into a cluster. The maximum-likelihood (ML) detector determines for each cluster which template has the best match. The amplitude and arrival time estimated by
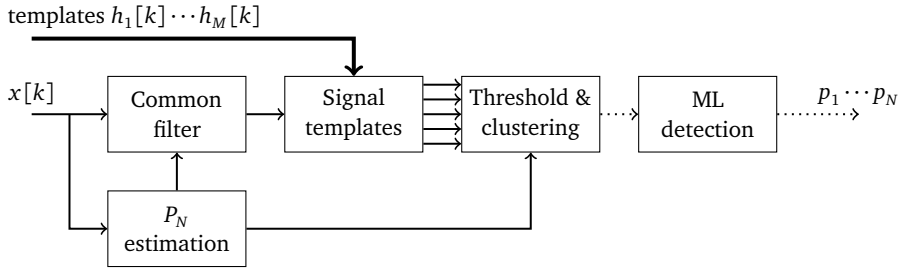
Figure 5.1   Schematic overview of matched filter bank

that template are recorded in the detected pulses $p_1 \cdots p_N$. In the following subsections these steps are discussed in detail.

5.2.2   Common filter

The PD waveform depends on the distance the PD signal traveled through the cable. The part common to all templates can be separated. The noise $P_N(\omega)$ is the same for all filters. Because the noise spectrum often contains narrow peaks caused by radio broadcasts a relatively long filter is required. The filters for the signal templates $S_m(\omega)$ are generally much shorter. Therefore, it is more efficient to preprocess the signal with a common filter and apply the shorter signal templates to the output of this common filter. The transfer function of the common filter is:

$$H_{\text{cf}} = \frac{1}{P_N} \tag{5.2}$$

The noise spectrum $P_N(\omega)$ is required for constructing the common filter. It is estimated using an averaged periodogram of measured signal $x[k]$, see appendix §A.4.

5.2.3   Signal templates

The signal templates $S_m(\omega)$ are initially based on system identification measurements combined with a standard model. The standard model is based on separate measurements of the typical behavior of components in cable connections and is used for the parameters that can not be measured locally by the PD measurement unit. The mth template is given by:

$$S_m = e^{-\gamma z_m} \cdot \tau_I \cdot H_{\text{sens}} \tag{5.3}$$

$$= e^{-\gamma z_m} \cdot \frac{2Z_c}{Z_c + Z_{\text{load}}} \cdot H_{\text{sens}} \tag{5.4}$$

where $\gamma(\omega)$ is the cable propagation coefficient, z_m the traveled distance, $\tau_I(\omega)$ the current transmission coefficient from the cable to the load impedance (RMU), Z_c the

characteristic cable impedance, $Z_{\text{load}}(\omega)$ the RMU impedance as seen by a PD from the CBLUT arriving at the RMU, and $H_{\text{sens}}(\omega)$ the transfer function relating the enclosed sensor current to the sensor output voltage.

The sensor transfer function $H_{\text{sens}}(\omega)$ is calibrated before installation. The total impedance ($= Z_{\text{c}}(\omega) + Z_{\text{load}}(\omega)$) is measured by injection and detection of reference pulses [59] during the system identification procedure. For the cable model parameters ($Z_{\text{c}}(\omega)$ and $\gamma(\omega)$) standard values are used that were measured on a typical MV cable. The distances z_m are chosen such that for the current noise conditions the probability that a PD matches an incorrect template is below an acceptable value [50]. Because the PD signal is an exponential function of the propagated distance the distances z_m are distributed approximately logarithmically. The distribution is not exactly logarithmic due to the frequency dependent propagation velocity $v_{\text{p}}(\omega)$, attenuation $\alpha(\omega)$ and current transmission coefficient $\tau_I(\omega)$.

5.2.4 Threshold and clustering

A pulse is detected by a matched filter if the (absolute) matched filter output exceeds a certain threshold. This threshold is defined in terms of the average noise power in the output of the matched filter. The average noise power at the output of the mth filter is given by:

$$\sigma_{n,m}^2 = \Delta f \sum_{i=0}^{B-1} P_N[i] \left| H_m[i] \right|^2 \tag{5.5}$$

where $P_N[i]$ and $H_m[i]$ are the discrete representations of $P_N(\omega)$ and $H_m(\omega)$ (see Eq. A.2 for the relation between ω and i).

Under the assumption that the noise is Gaussian a threshold can be defined that corresponds to the false positive probability. For example, for a Gaussian distribution approximately one in a million noise samples will exceed a threshold of $5\sigma_{n,m}$. Since the threshold depends on the filter's transfer function each filter has its own threshold value. If a signal exceeds the threshold the maximum amplitude of the output signal in the region exceeding the threshold is determined. The amplitude and time (t_{max}) corresponding to the maximum gives the amplitude of the detected PD and time at which the template is exactly aligned with the raw signal (i.e. t_{max} corresponds to the time of the first sample of the template). The time-of-arrival (t_{oa}) of the PD is given by t_{max} plus the arrival time within the template. See Figure 5.2 for demonstration of the estimation of t_{max} and t_{oa}. The amplitude of the output signal at t_{max} is converted to the PD charge Q. This is achieved by sending the predicted PD waveform of the corresponding template through the same filtering procedure. Because the predicted PD waveform has a charge of 1 C, the charge of the detected PD is given by:

$$Q = 2 \frac{y_{\text{max}}}{y_{\text{max,tmpl}}} \tag{5.6}$$
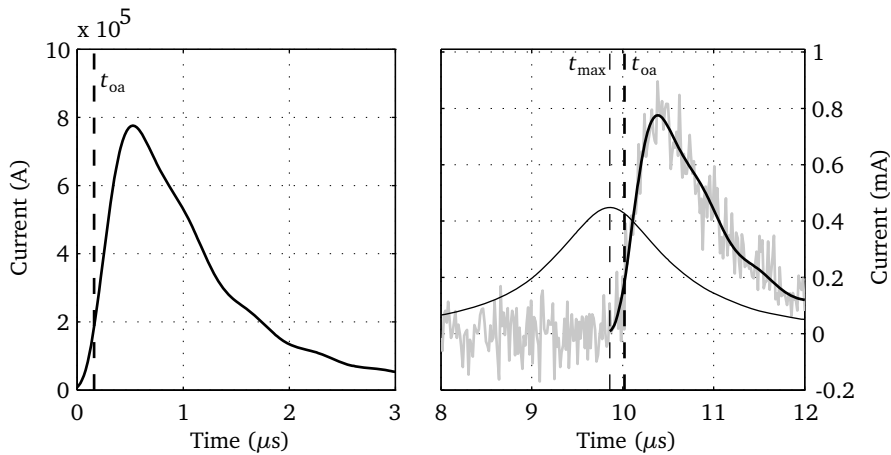
Figure 5.2 Detection of 1000 pC PD by matched filter. Left figure: template with a charge of 1 C, including the time-of-arrival estimated by the energy criterion. Right figure: gray line: (part of) raw signal with PD, thin solid black line: output of matched filter (scaled for figure), thick solid black line: template aligned with raw signal, thin dashed vertical line: time of maximum in filter output and time of the start of template, thick dashed vertical line: estimated time-of-arrival of detected PD.

where y_{max} is the amplitude of the output signal at t_{max} and $y_{max,tmpl}$ the maximum amplitude of the output signal if the PD template is send through the same filters. A PD in a cable results in two equal pulses, each with half the charge, traveling in both directions, hence the factor 2 in Eq. 5.6.

The same pulse may be detected by multiple templates. If pulses detected by different templates are "close together in time" they are assumed to refer to the same pulse and are combined into a single cluster. The definition of "close together in time" is chosen as no further apart than the length of the templates. A smaller margin can be determined by sending a template through the matched filters corresponding to the same template and to another template. The time difference between the maxima in the outputs can also be used as margin for the combination of these two filters. For simplicity and because PD activity in most cables is relatively low, the safe margin of the template length is used.

5.2.5 Maximum-likelihood detection

If a cluster contains multiple pulses, it means that the same pulse was detected by multiple templates. Different templates detecting the same pulse will most likely yield different arrival times and amplitudes. The maximum likelihood detector determines which template has the best match with the signal. The arrival time and amplitude corresponding to that template are assumed to be the best values. The likelihood for the

m^{th} filter is given by [50]:

$$L(S_m) = \Delta f \sum_{i=0}^{B-1} -\frac{\left| X[i] - S'_m[i] \right|^2}{2 P_N[i]} \tag{5.7}$$

where $X[i]$ is the section of the recorded signal $x[k]$ that contains the detected pulse converted to frequency domain, $S'_m[i]$ the signal template $S_m[i]$ after it has been scaled and aligned to match the amplitude and arrival time of the pulse in the recorded signal. The likelihood $L(S_m)$ is calculated for every template in a cluster. The arrival time t_{oa} and magnitude Q estimated by the template with the maximum likelihood are recorded in pulse p_n. The t_{oa} and Q estimated by the other templates are discarded. The detected pulses are send to the central server for combination with the pulses detected by the measurement unit at the other end of the CBLUT [50, 59]. The combined pulses are used for the condition assessment.

5.3   Adaptation algorithm

The MFB described in the previous section uses a calibrated sensor transfer function, system identification measurements and a standard cable model to predict the PD waveforms from which a set of templates is created. These predicted waveforms do not always have a good match with the actual waveforms. This section describes an extension to the MFB that improves the set of templates based on detected (PD) pulses, thus improving sensitivity and location accuracy for subsequent PD measurements.

The PD measurement unit at each end of the CBLUT communicates the characteristics of detected pulses to a central server. The central server combines the pulses detected at both cable ends. The PD origin is located based on the difference in time-of-arrival at both measurement units (see Eq. 1.1). The communication between measurement unit and server usually takes place over a mobile data connection. Because of the slow connection and the costs involved with data transport an adaptive algorithm should not require any additional communication with the central server or the measurement unit at the other end of the cable. A stand-alone adaptation algorithm also saves computation time on the central server. Even if the adaptation algorithm requires only a few computations for every measurement unit, it would add up to a significant work load for a central server that performs the computation for a large number of measurement systems.

5.3.1   Adaptation algorithm overview

A PD measurement starts with recording a time-discrete signal $x[k]$. The recorded signal is filtered using an MFB as described in the previous section. Pulses detected by the MFB are not only used for the condition assessment of the CBLUT, but can potentially also be applied to improve the set of templates. The systems maintains two different types of templates: fixed and adaptive. Fixed templates are created as described in §5.2.3 at the start of a PD measurement session. Adaptive templates are templates created by the
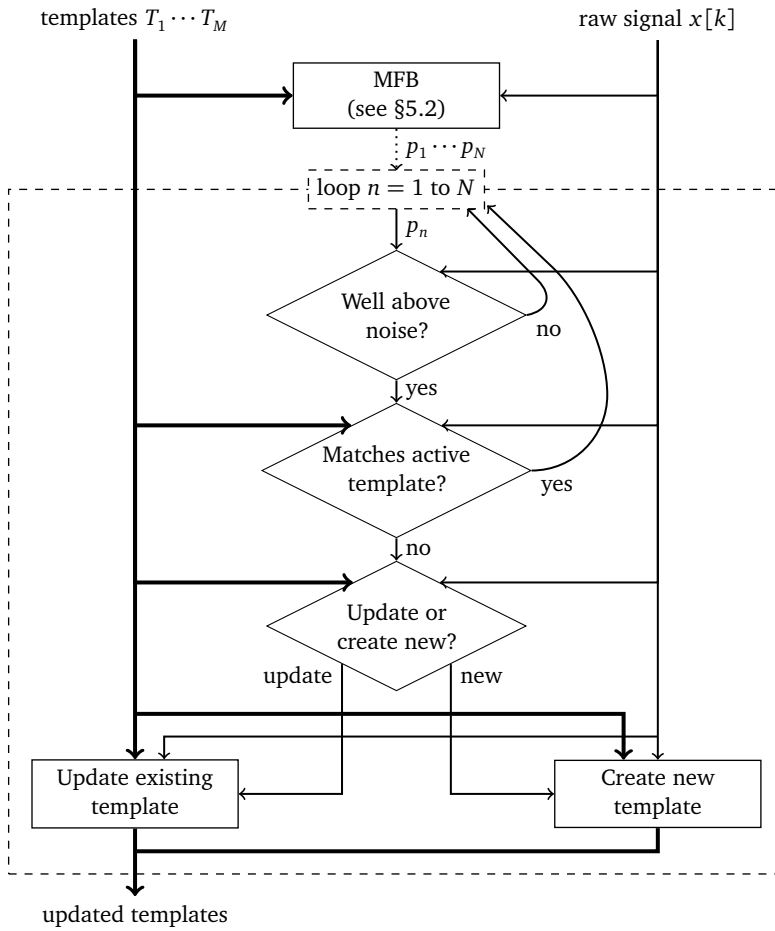
Figure 5.3   Overview of adaptation algorithm

adaptation algorithm based on detected pulses. An adaptive template can be either active or passive. Active means that it is being used to create a matched filter that is added to the MFB. Passive templates are not (yet) used for creating matched filters in the MFB.

In Figure 5.3 a flow diagram of the adaptation algorithm is depicted. The input data required by the algorithm are the pulses detected by the MFB (p_1 to p_N), the raw signal ($x[k]$), and all templates (both fixed and adaptive) (T_1 to T_M). Each pulse (p_n) is characterized by the arrival time t_{oa} and magnitude Q. Each template T_m contains the filter coefficients $h_m[k]$ formed by the significant samples in the predicted or measured waveform. Adaptive templates also keep track of all measured waveforms $x_n[k]$ associated with it, the standard deviation of the noise in each waveform $\sigma_{x,n}[k]$, an averaged signal $x_{\text{tp},m}[k]$ of the measured waveforms, and the standard deviation $\sigma_{\text{tp},m}$ of the noise in $x_{\text{tp},m}[k]$. For an adaptive template the filter coefficients $h_m[k]$ are extracted from the averaged signal $x_{\text{tp},m}[k]$. The pulses are handled one by one as indicated by the dashed line in Figure 5.3. The steps taken for each pulse are described in detail in the following subsections.

5.3.2 Well above noise?

Only signals that are well above the noise are used by the adaptation algorithm. The signal-to-noise ratio (SNR) is used to quantify how far a detected pulse is above the noise. For pulse p_n the SNR is defined as:

$$
\text{SNR}_n = 10 \log \left(\frac{\Delta t}{t_{\text{SNR}}} \frac{\sum\limits_{k=0}^{K-1} \left| x_n[k] \right|^2 - K\sigma_x^2}{\sigma_x^2} \right) \tag{5.8}
$$

where Δt is the sample time, t_{SNR} is an observation interval, $x_n[k]$ a restricted time interval of K samples in $x[k]$ around detected pulse p_n, and σ_x^2 the variance of the noise in $x[k]$. Eq. A.8 can be used to determine σ_x from the PSDF estimated for the construction of the common filter of the MFB. Because a pulse signal has finite energy and the noise is continuous the observation interval t_{SNR} is introduced to create a proper dimensionless signal-to-noise ratio. Following [50] this interval is defined as $t_{\text{SNR}} = 1\,\mu\text{s}$.

A detected pulse is considered to be well above the noise if the SNR is above threshold T_{wan}. In §5.3.7 the value of this threshold is discussed.

5.3.3 Good match with active template?

If a detected pulse, well above the noise, has a good match with a fixed template or with an *active* adaptive template there is no need to use the detected pulse to further improve the set of templates. A similarity measure is required to define a "good match". This measure should be independent of noise level and spectrum so that a generally applicable threshold can be defined. The measure should also take into account the signal before

and after the template. The signal-to-error ratio (SER) meets these requirements. It is defined as the ratio between the template's mean power and the mean squared distance between signal and template. The value is corrected for the noise present in the signal and in the template. The SER between the mth template and the nth pulse is defined as:

$$\text{SER}_{m,n} = 10 \log \left(\frac{\frac{1}{K} \sum_{k=0}^{K-1} \left| x_{\text{tp},m}[k] \right|^2 - \sigma_{\text{tp},m}^2}{\frac{1}{K} \sum_{k=0}^{K-1} \left| A_{\text{sc},n} x_n[k] - x_{\text{tp},m}[k] \right|^2 - \sigma_{\text{tp},m}^2 - (A_{\text{sc},n} \sigma_x)^2} \right) \qquad (5.9)$$

where K is the number of samples in the selected part of the signal $x_n[k]$, $x_{\text{tp},m}[k]$ is the averaged signal of an adaptive template or the predicted waveform of the fixed template, $\sigma_{\text{tp},m}$ the standard deviation of the noise in $x_{\text{tp},m}[k]$, and $A_{\text{sc},n}$ a scaling factor to match the signal amplitude to the template. For a fixed template $\sigma_{\text{tp},m} = 0$ because the template is based on a model and the noise is therefore neglectable.

For the calculation of SER the signal $x[k]$ must be aligned in time with template $h_m[k]$ and scaled to match its amplitude. The arrival time and amplitude for p_n determined by the MFB are not the best options for this because all templates have different shapes and will therefore result in different arrival times and amplitudes. Therefore, the arrival time and scaling factor $A_{\text{sc},n}$ are determined for each template separately in the same way as the MFB does. This involves calculating the cross correlation between signal and template, after the common filter has been applied to the signal (see §5.2 for details). Note, that the MFB already did this for all fixed and active adaptive templates and the results can be reused.

Next, a region from $x[k]$ is selected. This region must be longer than the template $h_m[k]$ because the SER must also take into account the expected signal before and after the template $h_m[k]$. For the experiments in this paper a region of $\frac{1}{2}N_{\text{tp},m}$ is included before and after the template, where $N_{\text{tp},m}$ is the number of samples in $h_m[k]$. Thus the total length of $x_n[k]$ is $2N_{\text{tp},m}$ samples. To match this length, any fixed template $h_m[k]$ is padded with zeros. Adaptive templates keep $2N_{\text{tp},m}$ measured signal samples so that for the SER calculation reflections that come after the template are taken into account.

If a template has a SER above threshold T_{SER}, that template is considered to have good match with the signal; §5.3.7 discusses the selection of this threshold. If pulse p_n has a good match with a fixed template or with an active adaptive template, the adaptation algorithm moves on to the next pulse p_{n+1}. If not, the pulse will be used to improve the set of templates.

5.3.4 Update existing or create new template?

Once it has been established that a detected pulse will be used to improve the set of templates it must be decided how it is implemented. It can be used to either update/improve an existing *inactive* adaptive template or to create a new adaptive template. For this decision the SER values between the signal and all inactive adaptive templates are cal-

culated. If any of the SER values is above threshold T_{SER} the detected pulse is used to update the corresponding template (§5.3.6). If there are multiple SER values above the threshold only the oldest template is updated. This ensures that a single template will be made active as soon as possible and it prevents two similar templates being improved simultaneously. The detected pulse is used to start a new template (§5.3.5) if none of the SER values is above the threshold.

5.3.5 Creating new template

For the creation of the new template from a detected pulse first the pulse is cut out from the signal $x[k]$. Because at this moment it is unknown where the pulse starts or ends a large region ($x_n[k]$) is selected far enough around the arrival time determined by the MFB (e.g. from $5\,\mu$s before t_{oa} to $10\,\mu$s after t_{oa}). Besides the signal $x_n[k]$ also the estimate of the noise's standard deviation $\sigma_{x,n}$ is stored.

For the calculation of the SER between this template and future detected pulses the start and end of the pulse need to be estimated. The selected pulse should include the significant samples, but not reflections or disturbing pulses that are often present in measured signals. The criterion which samples are significant is based on whether the samples contribute significantly to the maximum filter output if the selected pulse would be used as filter and applied to the same pulse. The maximal output in such a situation is given by the total signal energy of the selected pulse:

$$y_{\text{max}} = \sum_{k=k_{\text{start}}}^{k_{\text{end}}} x_n^2[k] \tag{5.10}$$

where k_{start} and k_{end} are the indices of respectively the first and the last sample of the selected pulse. The goal of the pulse selection is to make k_{start} as high and k_{end} as low as possible without significantly decreasing y_{max}. The presence of disturbing pulses, reflections and noise complicates the selection of the pulse. For the selection of the pulse the normalized cumulative energy of the entire signal $x_n[k]$ is calculated:

$$E_{\text{cum}}[k] = \frac{\displaystyle\sum_{i=0}^{k-1} x_n^2[i] - (k+1)\sigma_x^2}{E_{\text{cum}}[K-1]} \tag{5.11}$$

where k is an index ranging from 0 to $(K-1)$ and K the total number of samples in $x_n[k]$. Basically, the process is to first calculate $E_{\text{cum}}[k]$ without the denominator, and then the entire curve is normalized to the last value. In Figure 5.4 a pulse $x_n[k]$ recorded during an online PD measurement is plotted together with the corresponding normalized cumulative energy curve $E_{\text{cum}}[k]$. The next step is to identify pulses by detecting horizontal areas in $E_{\text{cum}}[k]$. If there are multiple pulses in the signal there will be multiple horizontal areas. The difference in $E_{\text{cum}}[k]$ between two consecutive horizontal areas is the total signal energy of the corresponding pulse (E_{pulse}). The pulse with most energy, i.e. the
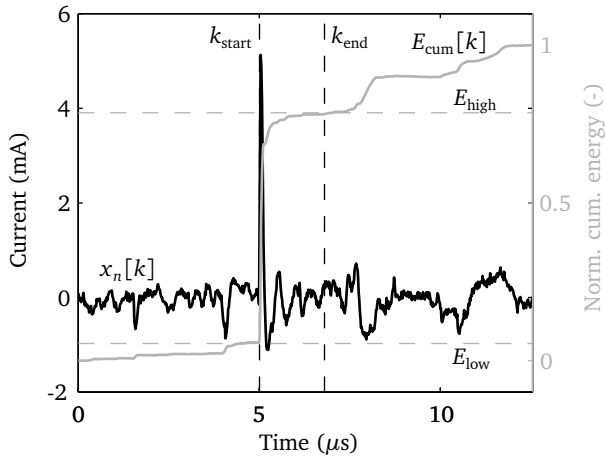
Figure 5.4 Demonstration of pulse selection algorithm. Black solid: measured signal ($x_n[k]$), dashed vertical lines: beginning (k_{start}) and end (k_{end}) of selected pulse, solid gray: normalized cumulative energy ($E_{\text{cum}}[k]$), and dashed horizontal lines: cumulative energy levels before (E_{low}) and after (E_{high}) pulse.

largest vertical distance between horizontal areas, is assumed to be the correct pulse. Once this pulse has been identified the beginning and end can be determined. The difference between the horizontal levels before (E_{low}) and after (E_{high}) the correct pulse is the maximum output y_{max} if the complete pulse would be used as coefficient of a FIR filter. To reduce the length of the pulse only the significant samples are selected. The first and last sample (k_{start} and k_{end}) of the pulse are the samples for which the following conditions are true:

$$E_{\text{cum}}[k] > \left(E_{\text{low}} + a E_{\text{pulse}} \right) \quad \forall \quad k \geq k_{\text{start}} \tag{5.12}$$

$$E_{\text{cum}}[k] < \left(E_{\text{high}} - a E_{\text{pulse}} \right) \quad \forall \quad k \leq k_{\text{end}} \tag{5.13}$$

where E_{pulse} is the pulse energy ($= E_{\text{high}} - E_{\text{low}}$) and a is a threshold. If $a = 0.01$ the maximum error in the maximum filter output y_{max} is 2% (1% due to potential discarding of samples at the beginning of the pulse and 1% due to potential discarding of samples at the end of the pulse). The levels E_{low} and E_{high} and the pulse start k_{start} and end k_{end} are also indicated in Figure 5.4.

A reflection in the signal, such as the pulse at $t \approx 7 \, \mu s$ in Figure 5.4, could be included in the template. Including such a reflection slightly improves the PD detection sensitivity for PDs from the same location. But it also increases the filter length and decreases the extraction performance for PDs from other locations. If a PD originates from a location nearby the origin of the template, the first pulse will be virtually identical, but the reflection will move in time with respect to the first pulse. If the template does not include

the reflection, the PD detection sensitivity and location accuracy will be unaffected by the moved reflection. However, if the reflection is too close to the first pulse there is no way to separate them and the reflection must be included in the template.

To prevent creating active templates for disturbing pulses that occur rarely a new template is not yet made active. Similar pulses will have to be detected multiple times and the SNR of the averaged signal must be sufficient before the new template will be used in the MFB. If after a long period still no similar pulse has been detected the template is discarded.

5.3.6   Updating existing template

If a pulse is detected that has a good match with an existing *inactive* adaptive template that pulse is added to the template. Adding a new detected signal to an existing template starts with aligning the signal with the template in time and amplitude. Note that this was already done for calculating the SER. After scaling and aligning the signal $(A_{\text{sc},n} x_n[k])$ and corresponding standard deviation of the noise $(A_{\text{sc},n} \sigma_{x,n})$ are added to the template. The template keeps track of all previously added signals and corresponding noise levels.

Averaging signals

All signals added to template T_m are combined into an averaged signal $x_{\text{tp},m}[k]$. To maximize the signal-to-noise ratio in the average signal each signal is multiplied by a weight factor:

$$x_{\text{tp},m}[k] = \sum_{\substack{n=1 \\ n \in T_m}}^{N} w_n \cdot A_{\text{sc},n} \cdot x_n[k] \qquad \text{with constraint}: \quad \sum_{\substack{n=1 \\ n \in T_m}}^{N} w_n = 1 \qquad (5.14)$$

where w_n a weight-factor for measured pulse n. The standard deviation of the noise in the resulting average is given by:

$$\sigma_{\text{tp},m} = \sqrt{\sum_{\substack{n=1 \\ n \in T_m}}^{N} w_n^2 \left(A_{\text{sc},n} \sigma_{x,n}\right)^2} \qquad (5.15)$$

Minimizing $\sigma_{\text{tp},m}$ with respect to w_n, using the method of Lagrange multipliers, yields:

$$w_n = \frac{1}{\left(A_{\text{sc},n} \sigma_{x,n}\right)^2} \frac{1}{\sum_{\substack{n=1 \\ n \in T_m}}^{N} \frac{1}{\left(A_{\text{sc},n} \sigma_{x,n}\right)^2}} \qquad (5.16)$$

Recorded signals may contain disturbing pulses. These pulses invalidate part of the signal while the rest of the signal is fine. Samples that are outliers are detected and

discarded before averaging the signal to prevent the disturbances from influencing the averaged signal. This outlier detection takes place on a sample by sample basis because disturbing pulses only invalidate part of the signal. The outlier detection is based on a modified z-score method [20]. A disturbing pulse usually introduces a number of samples with a huge deviation from the expected value. Therefore, this method applies the median instead of the mean. First, distance of every sample from the median is calculated:

$$d_n[k] = \left| x_n[k] - \mu_{1/2}^n \left(x_n[k] \right) \right| \quad \forall\, n \in T_m \tag{5.17}$$

where $\mu_{1/2}^n \left(f(n) \right)$ denotes the median value over all applicable values of n. The median distance is calculated:

$$\sigma_{\frac{1}{2}}[k] = \mu_{1/2}^n \left(d_n[k] \right) \quad \forall\, n \in T_m \tag{5.18}$$

If the distance of a sample ($d_n[k]$) is larger than $T_{\text{out}} \sigma_{\frac{1}{2}}[k]$ it is considered an outlier and not used for calculating the average signal. This process is repeated for all k indices. T_{out} is chosen by assuming a Gaussian noise distribution and accepting 1% of the correct samples to be discarded. This gives $T_{\text{out}} = 4$.

Activating template

Averaging multiple signals increases the SNR of the averaged signal. Each time a signal is added to a template the average and corresponding SNR are calculated. If the SNR of the averaged signal is above threshold T_{activ} the template is made active. Before a template is made active a number of quantities need to be estimated from the averaged signal:

- Start and end of the pulse within the averaged signal $x_{\text{tp},m}[k]$ using the method from §5.3.5.

- Time-of-arrival of the selected pulse using the energy criterion from Chapter 4.

- Charge Q of the pulse as described in Appendix C. The selected pulse must be scaled so that the charge is 1 C.

Once the template is active it will be used to create an additional matched filter in the MFB.

5.3.7 Thresholds

The adaptation algorithm defines several thresholds. The functioning of the algorithm and the accuracy of the created templates depends on the selections of their values.

SER threshold T_{SER} — good match with template

The most important threshold is T_{SER}. It defines the level of similarity between two pulses that is considered to be a good match. The higher this threshold the more templates will

be created. Choosing this value too high creates an impractical (i.e. too computationally intensive) number of templates. With a value too low many different pulses will match the same template, decreasing the location accuracy and sensitivity. The threshold T_{SER} should be chosen as low as possible while keeping sufficient accuracy in the estimated location and amplitude.

The optimal value for T_{SER} is determined by simulation. The simulation starts with the creation of a number of PD waveforms that correspond to actual PD shapes that occur in practice. The PD pulses are simulated using Eq. 5.3. The propagation coefficient and characteristic impedance of the cable used in this equation are taken from a pulse reflection measurement (§2.5) on a 300 m MV PILC cable sample. The chosen traveled distances z range up to 4 km. The RMU load impedances Z_{load} are based on the RMU model presented in §3.2.2. For each pulse the model parameters are chosen at random within the ranges encountered in practice that are mentioned in the same chapter. The arrival time of each pulse is estimated using the energy criterion (§4.3.3) and the amplitude is based on the model.

After the creation of the PD pulses, each pulse is used as template in a matched filter and applied to all other pulse signals. This yields for every pulse signal an estimated time-of-arrival t_{oa} and charge Q. These values are compared to the reference values of the corresponding pulse signal. The SER between the template and each pulse signal is also calculated. This is done for every pulse so that all pulses have been applied as template to filter every other pulse. In Figure 5.5 for every combination the relative error in t_{oa} and Q is plotted as function of the SER. Each dot represents a combination of two PD pulses, one as template and the other as signal. These graphs show the relation between the SER and relative t_{oa} and Q estimation errors. The Q estimation error corresponds to the reduction in detection sensitivity. Each graph shows two clearly separated bands of dots. Each pair of pulses generates two dots, i.e. one pulse is used as template and the other as signal, and the other way around. These two dots have the same absolute error in t_{oa} and Q, but because of the difference the relative error is different.

The target location accuracy is 1% of the cable length. Owing to the factor $^1/_2$ in the equation (Eq. 1.1) to calculate the PD origin from the t_{oa} at both ends, the required t_{oa} accuracy is 2%. As can be seen in Figure 5.5 a SER threshold of 10 dB gives a maximum t_{oa} error of 2%. Taking into account that there are also other causes for location errors the threshold T_{SER} used in this chapter is $T_{SER} = 12$ dB. For this threshold the maximum error in Q estimation is approximately 25%. This is acceptable as the trend of PD activity over time is a more important indicator of an upcoming failure than the absolute level.

SNR threshold T_{wan} — well above noise

Once the threshold T_{SER} has been chosen the SNR threshold T_{wan} can be determined. The criterion for choosing this threshold is whether the SER of the pulse and a template can be determined with acceptable precision. This precision not only depends on the SNR but also on the SER value. For example, a high SER value means that the distance between the two pulses is small. For a precise estimation of the SER value the noise needs to be
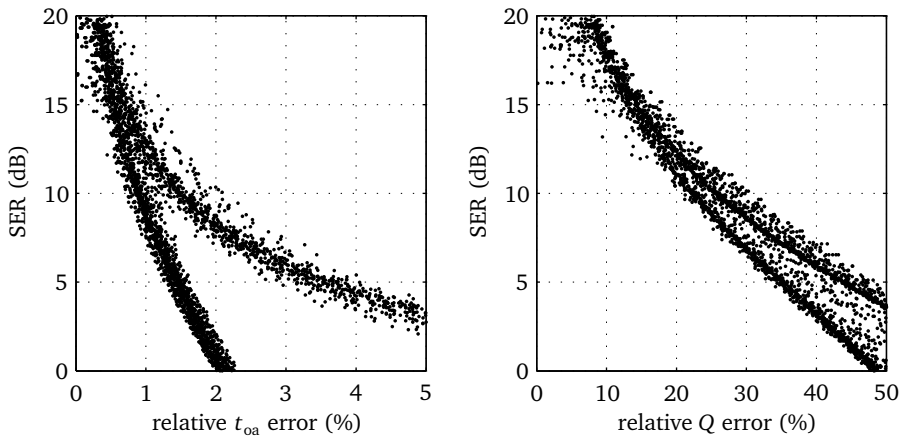
Figure 5.5 Signal-to-error ratio as function of relative error in estimation of arrival time and charge. Every dot represents a combination of two PD pulses (one as template and the other as signal).

small compared to this error. Therefore, this threshold is defined relative to T_{SER}.

The relation between the precision of the SER and the SNR (relative to the expected SER value) is determined on basis of simulation results. Random PD pulses are simulated using the same procedure as previously. First, the SER between two random pulses is determined. Only pulses with a SER around T_{SER} are considered. Therefore, pairs with a SER too low or too high are discarded. For this simulation only pulses with $10 < \text{SER} < 15$ are used. Next, a SNR is chosen at random and the precision of the SER estimation under that noise level is determined. This precision is determined by adding uncorrelated Gaussian white noise with the selected SNR to both pulses and calculating the SER value. To simulated the fact that both an adaptive template and the signal contain noise, noise is added to both pulses. This is a worst-case scenario because most templates will have a lower noise level. Fixed templates do not have noise because they are based on a model and most adaptive templates will have multiple signals averaged. The process of adding noise and calculating the SER is repeated 1000× for each pair of pulses. The standard deviation σ_{SER} of all SER values gives the precision. This entire process is repeated for 1000 pairs of random pulses. The results are plotted in Figure 5.6. Choosing an acceptable $\sigma_{\text{SER}} = 2\,\text{dB}$ (derived from the SER variations observed in Figure 5.5 for t_{oa} error $= 1\%$) corresponds to $\text{SNR} - \text{SER} = 8\,\text{dB}$ and thus the SNR threshold is $T_{\text{wan}} = 8 + T_{\text{SER}} = 20\,\text{dB}$.

SNR threshold T_{activ} — activating template

The last threshold that needs to be determined is the SNR threshold T_{activ}. This threshold determines whether an inactive adaptive template will be made active. To ensure a proper
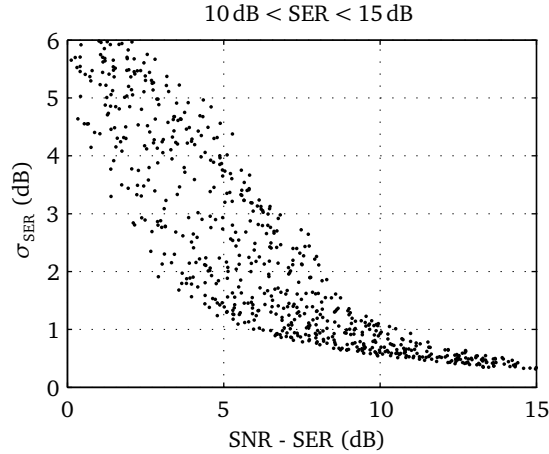
Figure 5.6   Standard deviation of SER estimation as function of SNR (relative to expected value of SER).

selection of the actual pulse within the complete signal, this decision is based on the accuracy estimation of the beginning and end of the pulse as described in §5.3.5. The beginning and end of the pulse is based on the cumulative signal energy E_{cum} (Eq. 5.11) of the averaged signal. As a measure for the accuracy the maximum distance between the E_{cum} of a pulse with noise and a reference E_{cum} curve of the same pulse without noise is used:

$$d_{\max} = \max \left| E_{\text{cum}}[k] - E_{\text{cum,ref}}[k] \right| \tag{5.19}$$

where $E_{\text{cum}}[k]$ is the cumulative energy curve of a PD signal with noise, and $E_{\text{cum,ref}}[k]$ the reference cumulative energy curve of the same PD signal without noise. The maximum distance $d_{\max}$ is calculated for 1000 random PD signals and noise levels. The result is plotted in Figure 5.7. A $d_{\max}$ of $0.5 \times a$ (factor 0.5 because an error is made at both the beginning and the end of the pulse and for $a = 0.01$ see §5.3.5) is assumed to allow proper selection of the beginning and end of the pulse. From the figure the maximum $d_{\max}$ is 0.5% for a threshold of $T_{\text{activ}} = 33\,\text{dB}$.

5.4   Experiments

The adaptation algorithm has been applied to several sets of field test data acquired during online PD measurements. Three different cases are studied. The first case consist of signals with a large number of discharges. The second case has a few small discharges and some large disturbing pulses. The third case has many disturbing pulses caused by industry in the neighbourhood. An example of a raw signal from each of these cases is plotted in Figure 5.8.
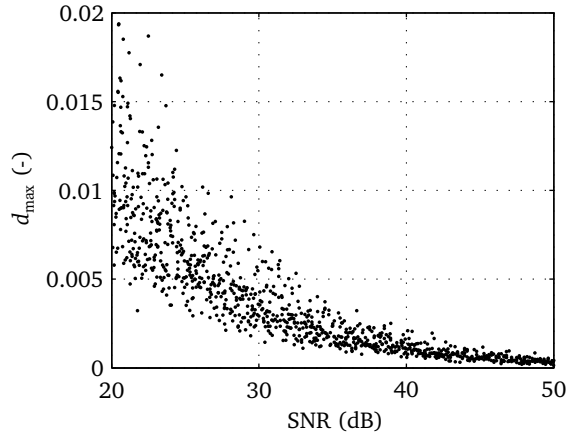
Figure 5.7 Maximum distance between E_{cum} of PD signal with noise and reference E_{cum} of the same PD signal without noise for random PD pulses with different signal-to-noise ratios.

5.4.1 Case 1

The first set of data is obtained on a measurement setup consisting of a 300 m field-aged PILC MV cable with a joint at 100 m. Both the cable and the joint are known to be heavily discharging. At both ends the cable is connected to an RMU. A 50 Hz 6 kV voltage is applied so that joint and cable start discharging. In both RMUs an inductive current sensor is installed that records signals of 20 ms, see Figure 5.8a. The raw data acquired by one of the sensors is analyzed twice: once using an MFB *without* adaptation algorithm and once using the same MFB *with* adaptation algorithm. The MFB is constructed using generic templates that do not take into account the local impedance, see left graph in Figure 5.9. Normally, the local impedance is taken into account, but for testing the adaptation algorithm the effect of the local impedance on the PD waveform is ignored. This represent the situation where e.g. an RMU along the cable under test causes a similar distortion of the PD waveform. RMUs along the cable are not taken into account constructing the fixed templates.

Analysis of 10 measurement records of 20 ms using the MFB with adaptation algorithm resulted in 12698 detected pulses and one new active adaptive template was created from 14 detected pulses. The new adaptive template $(h_m[k])$ is plotted in Figure 5.9 along with the fixed templates. The figure also depicts all detected pulses $(x_n[k])$ that were used to construct the template and the average of these detected pulses $(x_{tp,m}[k])$. The template consist of a typical PD pulse. The damped oscillation in the tail of the pulse is caused by resonances in the transformer and the cables connecting the transformer. The pulse at 2.5 μs is the reflection of the PD pulse on the far end of the cable under test. This time corresponds to the propagation time back and forth from the joint to the far end of the
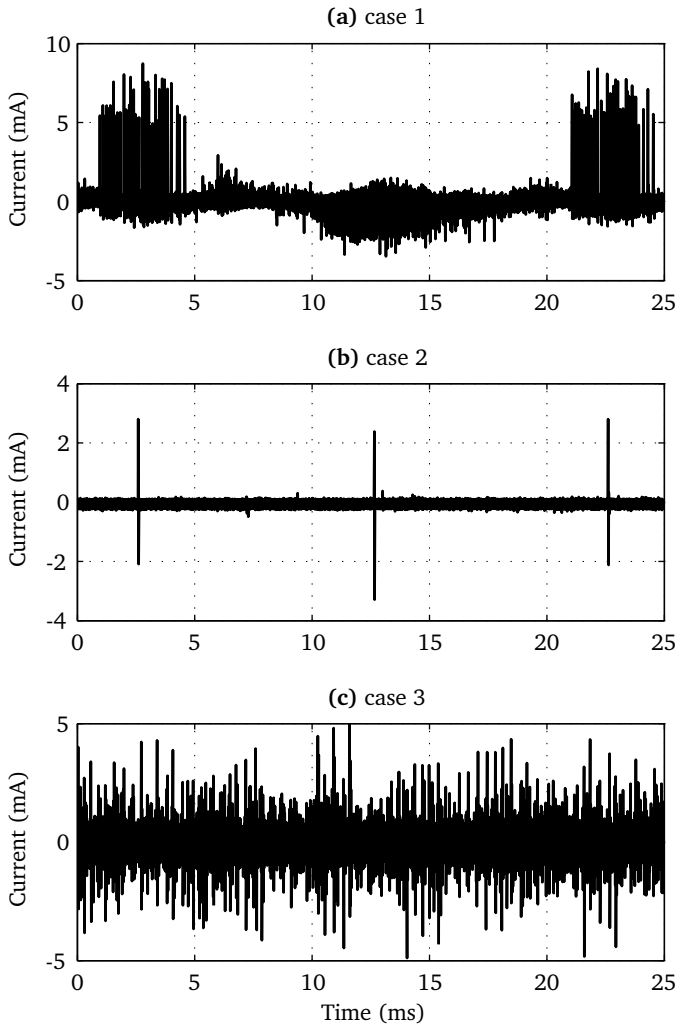
Figure 5.8 Examples of raw signals recorded during online PD measurements.
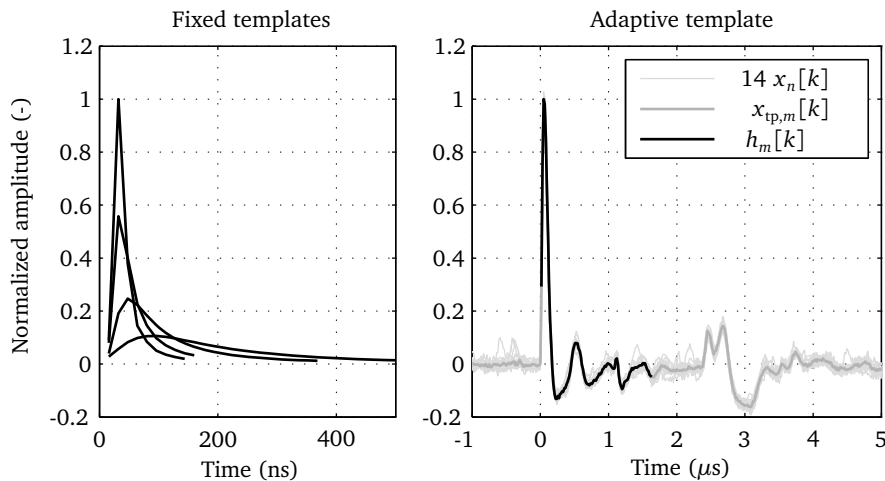
Figure 5.9 Case 1: fixed generic templates and adaptive template constructed using measured signals.

cable. These pulses therefore must originate from the joint. Out of all 12698 detected PDs, 9058 are detected by this new adaptive template.

Next, the same data is analyzed by the same MFB, but without the adaptation algorihm. Out of the 9058 pulses detected previously by the new adaptive template only 7913 are detected without adaptation algorithm. This demonstrates that detection sensitivity is increased by the adaptive template. This is demonstrated in Figure 5.10. This figure depicts the historgram of the 9058 pulses detected by the new adaptive template and the 7913 corresponding pulses detected without adaptation algorithm. Since different templates give different charge estimates, the pulses detected without adaptation algorithm were scaled to match the charge of the pulses detected by the adaptive template. At 120 pC the MFB without adaptation misses a few PDs and at 80 pC it misses the majority of the PDs. Because of the high number of discharges many pulses overlap in each record. If multiple pulses overlap or are close together the largest pulse is selected. Consequently, many small PDs are not detected, even though they are above the detection threshold. Therefore it is difficult to judge the increase in detection sensitivity based on these numbers only, in reality the increase may be higher.

5.4.2 Case 2

The second case is an online measurement on a 2 km long MV PILC cable with measurement units at both ends. The measurement records contains only a few small PDs. Every 10 ms there is a large disturbing pulse. In Figure 5.8b a measured raw signal is plotted.

An MFB is created with the same fixed generic templates as applied for case 1 (left
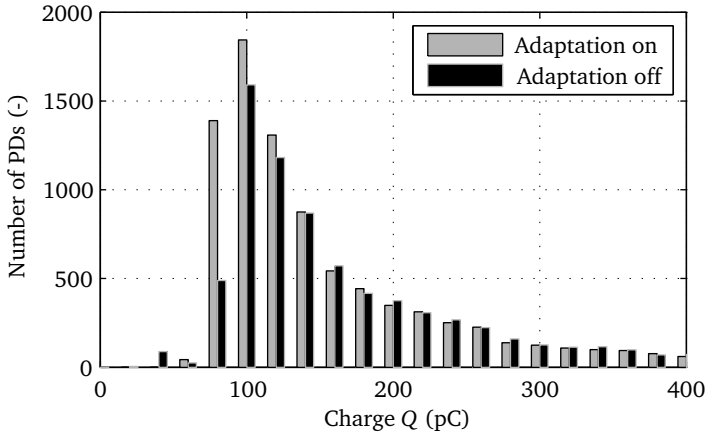
Figure 5.10   Case 1: histogram of detected PDs with and without adaptation algorithm.

graph in Figure 5.9). Ten records of 20 ms are analyzed by this MFB, both with and without the adaptation algorithm. The disturbing pulses do not resemble a typical PD pulse, but because of its amplitude it is detected anyway. Because it does not match any of the fixed templates the adaptation algorithm creates a new template based on three detected pulses. The new template is plotted in Figure 5.11 along with the pulses and averaged signal. Without the adaptation algorithm 1131 pulses are detected and with the adaptation algorithm 1155 pulses are detected. The new template collects the disturbing pulses, which would otherwise be detected by a template associated with real PDs. This demonstrates that templates can be used to classify different types of pulses. A new pulse type will automatically gets its own matching template.

5.4.3   Case 3

The third set of data is recorded during an online measurement on a 340 m long MV PILC cable in an industrial area. The measured signals contain an extraordinary large number of various disturbing pulses, see Figure 5.8c. An MFB is created with the same generic fixed templates as in case 1 (left graph in Figure 5.9). One hunderd records of 20 ms are filtered using this MFB, both with and without adaptation algorithm. Without the adaptation algorithm 22133 pulses are detected, and with the adapation algorithm 59688 pulses are detected. Due to the large number of different disturbing pulses, 751 new adaptive templates are created by the adaptation algorithm. Most of these templates are discarded before they become active because they contain only a single signal $x_n[k]$ and no second pulse is detected that matches it. Twelve adaptive templates collect enough matching signals (approx. 18 pulses) to have a SNR above T_{activ} and be activated. Six of those are depicted in Figure 5.12. Most of these templates are similar, but differ slightly in
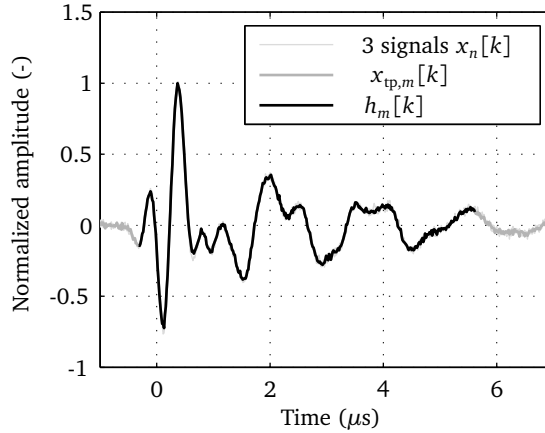
Figure 5.11 Case 2: adaptive template constructed using measured signals.

Template	F1	F2	F3	F4	A1	A2	A3	A4	A5	A6	A7	A8	A9	A10	A11	A12
Without:	6	7	14	137	-	-	-	-	-	-	-	-	-	-	-	-
With:	5	5	6	50	44	32	11	28	130	28	25	55	25	38	23	50

Table 5.1 Case 3: number of pulses detected by each template in a single 20 ms record. The same record was filtered twice by the MFB: once with and once without adaptation algorithm. Templates F1–F4 are the fixed templates and templates A1–A12 are the created active adaptive templates.

the oscillations in the tail. Judging them on their shape they are most likely not discharges, but disturbing pulses.

The number of pulses detected by each template is analyzed in more detail for a single 20 ms record. The number of detected pulses per template for this record are listed in Table 5.1. Without the adaptation algorithm most of the pulses are detected by fixed template F4. But if the adaptation algorithm is turned on, it turns out that most of these pulses match one of the new adaptive templates. Also the total number of detected pulses is much higher (555 compared to 164). This demonstrates that for each pulse type a template is created. After the adaptation algorithm has had sufficient time to create new templates, the template with which a detected pulse is associated is an identifier for the type of that pulse.

5.5 Discussion

The adaptation algorithm creates new templates for every pulse type that does not match an existing template. Adaptive templates that match PDs from the cable under test can
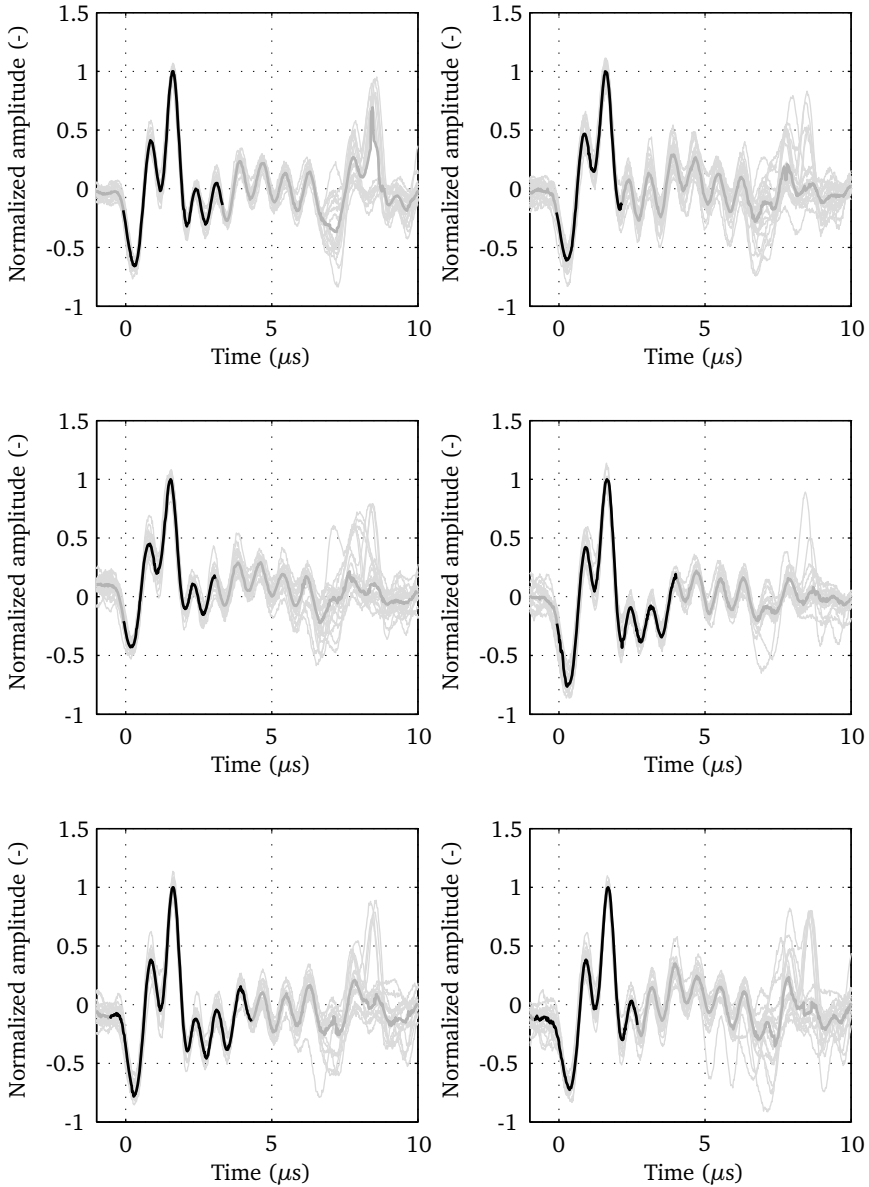
Figure 5.12 Case 3: six of the active adaptive templates. Light gray: measured signals ($x_n[k]$), dark gray: averaged signal ($x_{\text{tp},m}[k]$), black: filter coefficients ($h_m[k]$)

improve the system model. The new template created in case 1 can improve the current transmission coefficient $\tau_I[i]$ from cable to RMU to include the resonances in the tail of the PD waveform. The improved system model can then be used to improve the predictions of the PD waveforms for other locations in the cable under test.

As online PD measurements can be impeded with disturbing pulses not all the detected pulses are caused by PDs. Therefore, the system will also create templates for these disturbing pulses, as demonstrated in case 2 (§5.4.2). At first, this may seem undesirable, but it can be very useful. The measurement unit sends detected pulses to a central server where they are combined with the pulses detected at the other end of the cable. Based on the difference in arrival time at each cable end, amplitude and polarity the server determines whether a detected pulse comes from the cable under test or from elsewhere. If the measurement unit includes a unique template identification number with which a pulse is detected the server can determine whether certain templates always match PDs from a certain location in the cable under test, or pulses from outside the cable. This information can be communicated back to the measurement unit. The measurement unit can use this information to discard pulses immediately without communicating them to the server.

In case 3 (§5.4.3) fixed template F4 detects many pulses when the adaptation algorithm is turned off. When the adaptation algorithm is turned on it becomes clear that most of these pulses have a better match with one of the adaptive templates. These adaptive templates have a completely different shape. Based on the pulse shape and the fact that the cable is located in an industrial area it is likely that these pulses are not PDs, but disturbing pulses caused by heavy equipment in the neighbourhood. Due to the shape of these pulses the arrival times and amplitudes are estimated incorrectly by template F4. Depending on the pulse shape at the other end of the cable this could lead to a concentration of "PDs" that seem to come from the cable under test.

If too many adaptive templates are created the time required to process a measured signal may become impractically long. In case 3 (§5.4.3) a large number of adaptive templates is created. Whether this is too many depends on the hardware of the measurement unit and maximum allowable time between two consecutive measurements. For a proper condition assessment of the cable under test a minimum number of measurements per hour is required. Current experience shows that the minimum is in the order of ten measurements per hour. The threshold T_{SER} can be decreased to reduce the number of adaptive templates. The currently active adaptive templates should be compared amongst each other to see whether they have a SER below this new threshold. If two templates have a SER below the new threshold one of them can be discarded. Decreasing the threshold T_{SER} has the disadvantage that the location accuracy and detection sensitivity will decrease. Alternatively, if it is known that some of the adaptive templates correspond to disturbing pulses they might be left out from the MFB. Instead, they are only applied to each detected pulse to check whether it is a disturbing pulse.

5.6 Conclusions

An MFB for PD detection requires predictions of the waveforms of PDs from the cable under test. There are cable circuit configurations where system identification measurements combined with a standard cable model does not predict the PD waveform with sufficient accuracy. The adaptation algorithm proposed in this chapter creates new templates based on detected pulses that do not have a good match with the predicted waveforms. The sensitivity and location accuracy are improved when these new active adaptive templates are used to construct additional matched filters for the MFB. By choosing the thresholds used by the algorithm it can be tuned to the desired location accuracy and detection sensitivity.

Adaptive templates that can be related to a certain location or small region in the cable under test can be used to improve the model of the cable system. This improved model can then be used to create improved templates for other locations from which no large PDs have been measured yet.

The adaptation algorithm will create new templates for any pulse type that is detected multiple times. Therefore, it will also create templates for recurring disturbing pulses. If a certain template always matches disturbing pulses from outside the cable under test the measurement unit can safely discard pulses detected by this template. This saves processing time in the PD measurement unit and reduces the amount of communication with the central server.

CHAPTER 6

IMPLICATIONS FOR ONLINE PD MEASUREMENTS

6.1 Introduction

There are many different MV cable circuit configurations. For large scale implementation of online PD monitoring in MV cable networks it is critical to know the options for installing a PD measurement system in different network configurations. In this chapter the options for and the limits of online PD monitoring in different cable network configurations are analyzed.

There is a large variety of cable lengths installed in MV cable networks. As a PD pulse propagates through the cable under test (CBLUT) the pulse attenuates. This decreases the PD detection sensitivity of PDs that travel through the cable over longer distances. The cable length that can be monitored with sufficient sensitivity is therefore limited. The detection sensitivity as a function of the distance is analyzed in §6.2 for three different cable types.

The original proof-of-concept online PD monitoring system [50, 59] was designed to monitor a single cable between two consecutive RMUs. It would save money and effort to monitor two or more consecutive cables, with RMUs in between, using a single monitoring system (consisting of two measurement units). Moreover, practical experience with the PD-OL system [61], shows that in some large substations, and sometimes also in RMUs, installation is hampered or even impossible. Some installations, for example, do not provide sufficient space for the measurement unit at the desired location. Monitoring two consecutive cables, with the problematic RMU/substation in between, would solve this problem. The influence of RMUs and substations of different sizes on the propagation of PD pulses is studied in §6.3.

Some RMU/substation types along the CBLUT result in unacceptable signal loss.
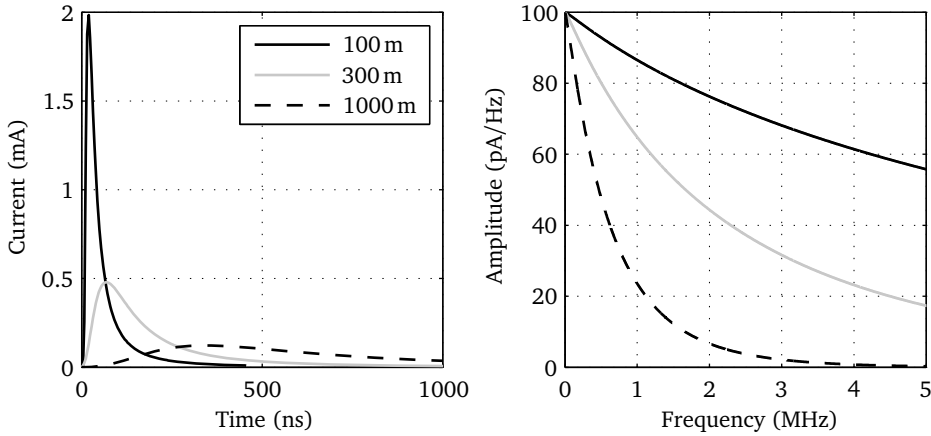
Figure 6.1   Time-domain and frequency-domain representation of a 100 pC PD after having traveled through a PILC cable for 100 m, 300 m and 1000 m.

An alternative is to monitor the cables to these RMUs/substations using a single-sided measurement from the other cable end. The origin of PDs is determined using time-domain-reflectometry (TDR), as used in on-site offline PD diagnostics. For this to work the PD pulses must reflect on the problematic RMU/substation. The reflection coefficient of RMUs and substations is studied in §6.4.

6.2   Effect of cable length

The attenuation of a cable is frequency-dependent, i.e. higher frequencies attenuate stronger than lower frequencies. At its origin a PD is a very narrow pulse with energy content over a wide frequency range, from DC up to hundreds of megahertz. As a PD signal propagates through the cable it attenuates, typically as represented in Figure 6.1. Consequently, the signal-to-noise ratio and thus also the PD detection sensitivity depends on the distance between the defect that produced the PD and the measurement unit.

    The PD detection sensitivity as function of the distance is estimated for three different cable types, both without any noise reduction and with matched filtering. The detection sensitivity is determined using the following steps:

1. **Predict PD waveform** The PD waveform $s[k]$ is predicted for a particular distance z using Eq. 5.3. The required propagation coefficients $\gamma(\omega)$ and characteristic impedances Z_c were measured on cable samples using pulse response measurements §2.5. As load impedance $Z_{\text{load}}(\omega)$ a compact RMU with two connected MV cables and no distribution transformer ($L_c = 360$ nH, $L_{bb} = 80$ nH and $Z_c = 11\,\Omega$) is used.

See §3.2.2 for the RMU model. The sensor transfer function $H_{\mathrm{sens}}(\omega)$ is assumed to be frequency-independent.

2. **Generate noise** Gaussian noise $n[k]$ is generated with a power spectral density function $P_N(\omega)$ as observed in an RMU during an online PD measurement. The spectrum is shown in Figure 6.2.

3. **Apply matched filter** The noise spectrum $P_N(\omega)$ and predicted PD waveform $s[k]$ are used to construct a matched filter (see §5.2). This matched filter is applied separately to the generated noise $n[k]$ and to $s[k]$, resulting in respectively $n_{\mathrm{f}}[k]$ and $s_{\mathrm{f}}[k]$.

4. **Estimate PD detection sensitivity** To estimate the PD detection sensitivity the standard deviation of the original noise $n[k]$ and the noise at the output of the filter $n_{\mathrm{f}}[k]$ are determined and divided by the amplitude of respectively the PD signal $s[k]$ and the filtered PD signal $s_{\mathrm{f}}[k]$. Because the predicted PD waveform $s[k]$ represents a PD with a charge of $1\,\mathrm{C}$, the amplitude of the normalized noise signals represents the charge. The PD detection sensitivity is given by:

$$\mathrm{DS} = T_{\mathrm{detect}} \frac{\sigma_n}{\frac{1}{2}\max|s|} \qquad \text{and} \qquad \mathrm{DS_f} = T_{\mathrm{detect}} \frac{\sigma_{n,\mathrm{f}}}{\frac{1}{2}\max\left|s_{\mathrm{f}}\right|} \qquad (6.1)$$

where DS is the PD detection sensitivity without noise reduction, $\mathrm{DS_f}$ the detection sensitivity with matched filtering applied, σ_n the standard deviation of $n[k]$, $\sigma_{n,\mathrm{f}}$ the standard deviation of $n_{\mathrm{f}}[k]$, and T_{detect} the threshold for detection. Following §5.2.4 the threshold $T_{\mathrm{detect}} = 5$ is used. The factor $\frac{1}{2}$ in the denominator corrects for the fact that a PD in a cable results in two equal pulses with half the charge traveling in each direction. The charge of a detected pulse is therefore half the apparent charge displaced in the original PD.

These steps are used to estimate the detection sensitivity for distances ranging from $10\,\mathrm{m}$ to $10\,\mathrm{km}$ for three different cables types: a belted PILC cable, a three-core XLPE cable with common earth screen (cable 3 in §2.6.2), and a single-core XLPE cable (cable 2 in §2.6.1). The results are plotted in Figure 6.3. The plotted sensitivities are based on typical parameters. For every situation the input parameters are different and the plotted sensitivities should therefore mainly be used qualitatively.

As expected, the sensitivity is best for short distances. For distances shorter than a few tens of meters all three cable types have the same sensitivity because the influence of the cable of the PD waveform is neglectable and the sensitivity is only determined by the noise spectrum and noise reduction algorithm. For distances larger than a few tens of meters the PD shape and amplitude is dominated by the propagation coefficient and the traveled distance.

The figure shows that the maximum length that can be monitored is larger for the XLPE cables than for the PILC cable. For example, if a sensitivity of $600\,\mathrm{pC}$ is required for proper condition assessment and matched filtering is applied, the maximum length
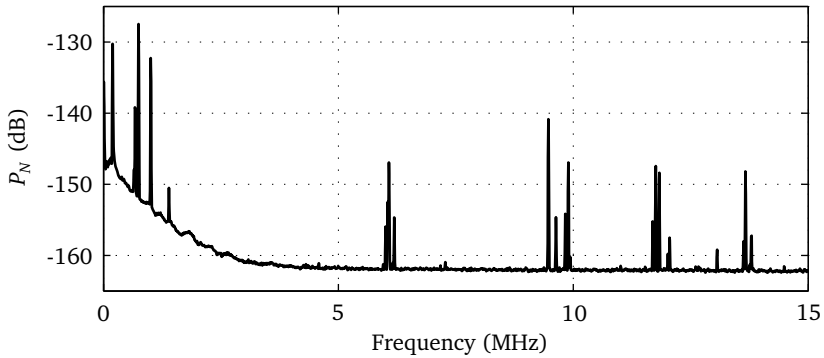
Figure 6.2   Measured noise spectrum $P_N(\omega)$; used in simulations on the effect of cable length on the PD detection sensitivity.

for the XLPE cables is 8 km, while the maximum length for the PILC cable is 4 km. The matched filter can improve the detection sensitivity significantly. For example, a sensitivity of 600 pC corresponds to a maximum length of 1.3 km for the PILC cable if no noise reduction is applied. Applying matched filters increase the maximum length to 4 km. For most distances, matched filtering improves the detection sensitivity by a factor 2–3. This factor depends on the noise spectrum, but is more or less the same for all three cable types.

6.3   RMUs or substations along cable under test

It has significant advantages to monitor two or more consecutive cables using only a single monitoring system (consisting of two measurement units). See Figure 6.4 for a schematic drawing of a setup monitoring two consecutive cables. An RMU/substation along the CBLUT affects PD pulses propagating through it. It acts as a complex impedance formed by the combination of the influence of switchgear, transformer, MV cables, and other components such as line reactors. The load impedance $Z_{\mathrm{load}}(\omega)$ as seen by a PD pulse arriving from a cable is therefore not matched to the cable's characteristic impedance Z_{c}. The pulse will partly reflect and partly transfer to other connected MV cables, resulting in a distortion of the pulse shape and amplitude.

     The effect of an RMU (or substation) can be expressed in the total transfer function $H_{\mathrm{rmu}}(\omega)$. It is a combination of the current transmission coefficient $\tau_{\mathrm{c1}}(\omega)$ from the CBLUT to the load impedance $Z_{\mathrm{load}}(\omega)$ and transfer function $H_{\mathrm{c}n}(\omega)$ that describes the distribution of the current (inside the RMU) from the incoming cable to the other connected components:

$$H_{\mathrm{rmu}} = \tau_{\mathrm{c1}} \cdot H_{\mathrm{c}n} = \frac{2Z_{\mathrm{c}}}{Z_{\mathrm{c}} + Z_{\mathrm{load}}} \cdot H_{\mathrm{c}n} \qquad (6.2)$$
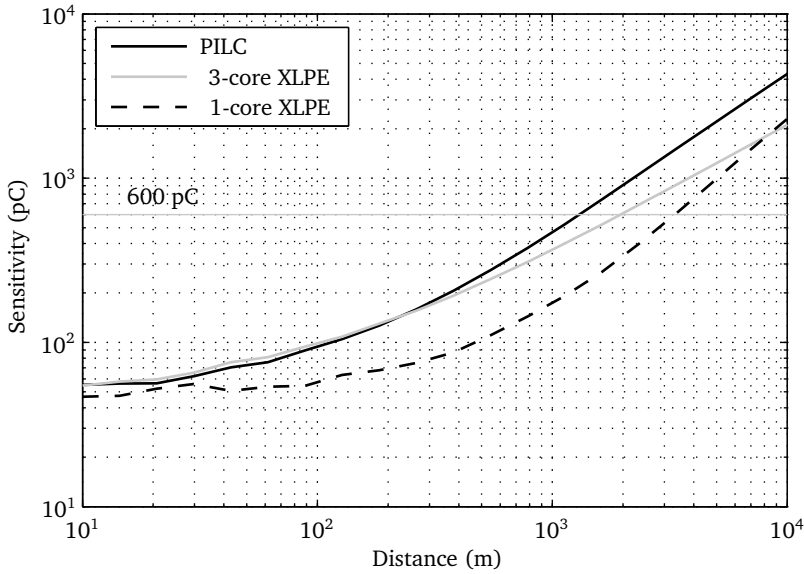
(a) Without noise reduction
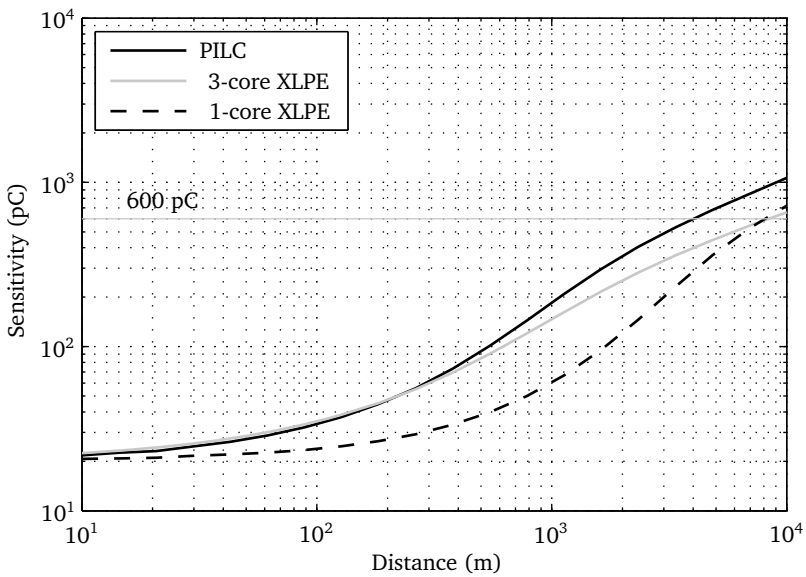
(b) With matched filters

Figure 6.3   PD detection sensitivity as function of traveled distance.
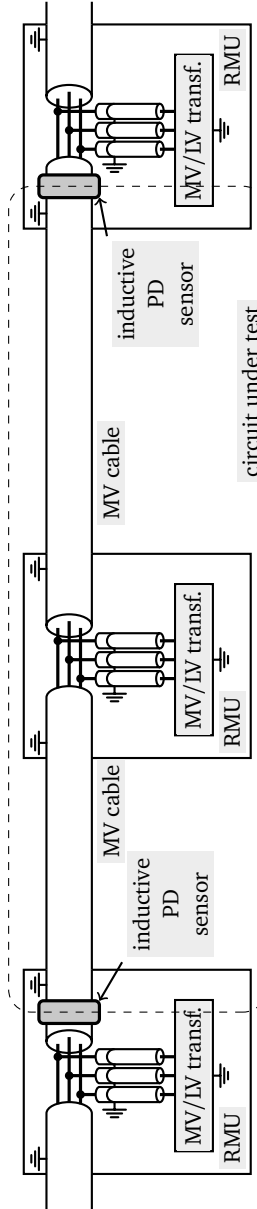
Figure 6.4 Setup monitoring two consecutive cables with one RMU along the CBLUT.
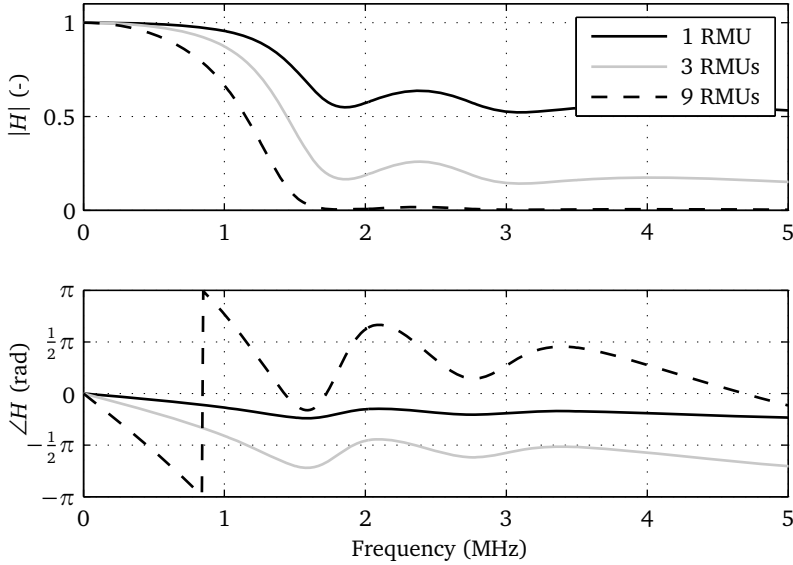
Figure 6.5   Total transfer function $H_{\text{rmu}}(\omega)$ of a typical RMU. The combined transfer functions $H_{\text{tot}}(\omega)$ of three and nine consecutive RMUs are also plotted.

where $Z_{\text{load}}(\omega)$ is the RMU impedance as seen by a pulse arriving from a cable. Both the transfer function $H_{cn}(\omega)$ and the load impedance $Z_{\text{load}}(\omega)$ can be derived from the model described in §3.2.2.

6.3.1   RMUs with two connected cables

Most RMUs in a distribution grid with a ring structure have two connected MV cables. The effect of an RMU with two connected cables on the propagation of PD pulses can be studied using the model presented in §3.2.2. The total transfer function $H_{\text{rmu}}(\omega)$ is calculated using this model and Eq. 6.2 for a typical compact RMU with two connected MV cables and an MV/LV transformer. The typical model parameters are derived from Table 3.1: $L_{\text{c}} = 340\,\text{nH}$, $L_{\text{bb}} = 120\,\text{nH}$, $L_{\text{tr}} = 2.6\,\mu\text{H}$, $C_{\text{tr}} = 2.5\,\text{nF}$, $R_{\text{tr}} = 12\,\Omega$, $L_{\text{tcc}} = 1.2\,\mu\text{H}$, $C_{\text{tcc}} = 1.9\,\text{nF}$, $R_{\text{tcc}} = 8.6\,\Omega$, $Z_{\text{c}} = 11\,\Omega$. The total transfer function $H_{\text{rmu}}(\omega)$ corresponding to these parameters is plotted in Figure 6.5. If there are multiple (identical) RMUs along the CBLUT the combined transfer function $H_{\text{tot}}(\omega)$ RMUs is given by:

$$H_{\text{tot}} = \left(H_{\text{rmu}}\right)^{L} \tag{6.3}$$

where L is the number of RMUs. The total transfer functions for three and nine RMUs are also plotted in Figure 6.5.

Table 6.1 Relative signal energy loss $F_{\mathrm{lr}}(L, l_{\mathrm{c}})$ due to L typical RMUs along a CBLUT of length l_{c}.

	$l_{\mathrm{c}} = 100\,\mathrm{m}$	$l_{\mathrm{c}} = 500\,\mathrm{m}$	$l_{\mathrm{c}} = 1000\,\mathrm{m}$	$l_{\mathrm{c}} = 2000\,\mathrm{m}$	$l_{\mathrm{c}} = 4000\,\mathrm{m}$
$L = 1$	50%	25%	10%	2%	0%
$L = 3$	72%	41%	19%	4%	1%
$L = 9$	81%	53%	28%	9%	2%

Signal loss

As shown in Figure 6.5 the transfer function of a compact RMU with two connected cables is close to one for frequencies below 1 MHz. Figure 6.1 shows that most of the energy of a PD pulse that propagated through a cable for 1 km is below 1 MHz. Consequently, the influence of one or more RMUs with two connected cables along the CBLUT is limited if the combined cable length is more 1 km. The PD signal energy of a PD that propagated through a cable of length l_{c} with L RMUs is given by:

$$E_{\mathrm{pd}}(L, l_{\mathrm{c}}) = \Delta f \sum_{i=0}^{B-1} \left| \tau_{\mathrm{c1}}[i] \left(H_{\mathrm{rmu}}[i] \right)^L \mathrm{e}^{-\gamma[i]l_{\mathrm{c}}} \right|^2 \tag{6.4}$$

The fraction of the PD signal energy that is lost due to L RMUs along the CBLUT is given by:

$$F_{\mathrm{lr}}(L, l_{\mathrm{c}}) = \left(1 - \frac{E_{\mathrm{pd}}(L, l_{\mathrm{c}})}{E_{\mathrm{pd}}(0, l_{\mathrm{c}})} \right) \cdot 100\% \tag{6.5}$$

The relative signal energy loss $F_{\mathrm{lr}}(L, l_{\mathrm{c}})$ is listed in Table 6.1 for different number of RMUs L and combined cable lengths l_{c}. An RMU along a 1 km cable introduces a 10% signal loss. This is a small reduction in sensitivity, but not significant. For longer cables the relative signal loss is less, e.g. for a 2 km cable with 9 RMUs the signal loss is below 10%.

Location and charge estimation accuracy

An RMU along the CBLUT does not only result in a signal loss, but also a location error. The location error is estimated for different configurations using a simulation of a cable propagation time measurement followed by PD measurements for different PD origins. The location accuracy and charge estimation accuracy is determined for each PD origin. Three different simulations are performed for a particular circuit configuration:

1. Reference simulation. The circuit does not yet include the RMUs along the CBLUT. This is the same simulation performed to evaluate the location accuracy of the time-of-arrival methods in §4.5.4, except that here only a single time-of-arrival method, the energy criterion (EC) is applied. The charge Q is estimated by integrating the current over time.
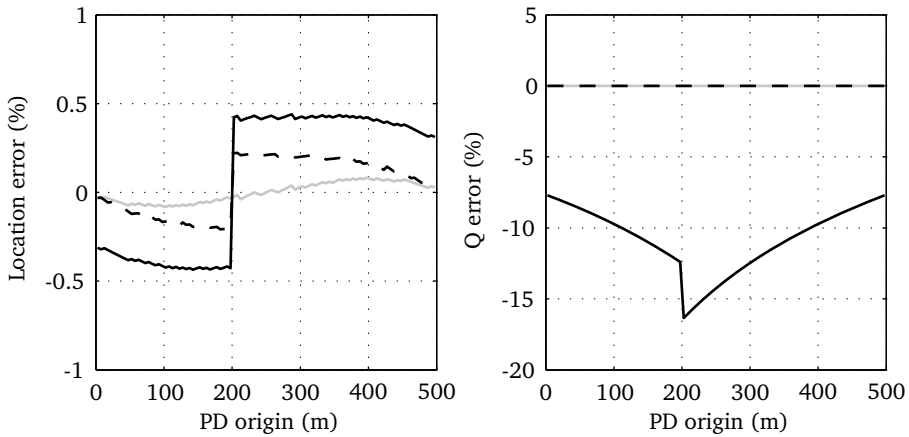
Figure 6.6 PD location and amplitude error for different PD origins. The cable is a 500 m long PILC cable with one typical RMU at 200 m. The RMUs at the beginning and end of the cable are matched to the characteristic cable impedance. Black solid line: original matched filter that does not take into account RMU along CBLUT, black dashed line: adaptive matched filter, and gray solid line: without RMU along CBLUT and correct matched filters.

2. Original matched filters. The RMU(s) are introduced along the CBLUT. The arrival time and amplitude of the PDs are determined using matched filters that do not take into account the RMUs along the CBLUT. This represents the original matched filter bank as described in §5.2 and [50].

3. Adaptive matched filters. Similar to the previous simulation, except that the matched filters do take into account the RMUs along the CBLUT. This represents a situation where the adaptation algorithm described in §5.3 is used to create new matched filters based on detected signals.

In Figure 6.6 the location accuracy and charge estimation accuracy is plotted for a 500 m PILC cable with one typical compact RMU at 200 m. The maximum location error increases from 0.1% to almost 0.5% of the cable length for the filters that do no take it into account the RMU. If the filters do take into account the RMU, as is the case for an adaptive filter, the maximum location error is 0.2%. This demonstrates that an RMU introduced to a PILC cable of 500 m increases the location error, but it stays well within an acceptable error of 1%.

In Figure 6.7 the simulation results are plotted for a 2 km PILC cable with 9 RMUs (one RMU every 200 m). The maximum location error increase from 0.1% to 0.75% for the filters that do not take into account the RMUs. With adaptive filters the maximum location error is 0.5% of the cable length.
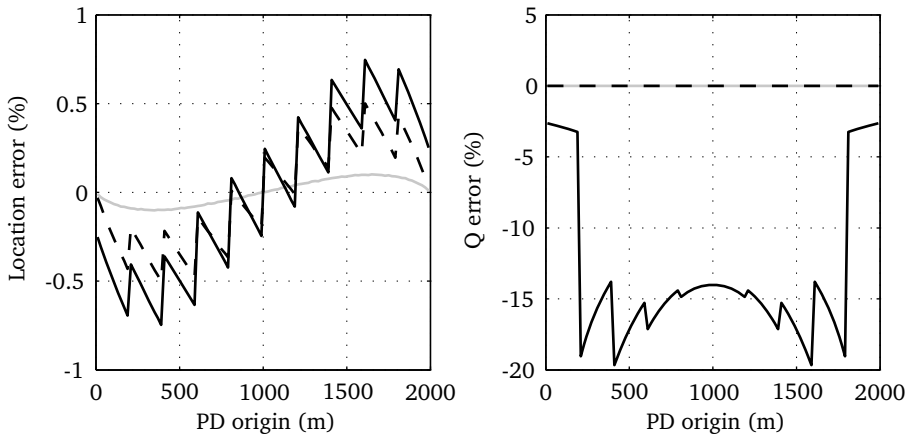
Figure 6.7   PD location and amplitude error for different PD origins. The cable is a 2 km long PILC cable with a typical RMU every 200 m. The RMUs at the beginning and end of the cable are matched to the characteristic cable impedance. Black solid line: original matched filter that does not take into account RMUs along CBLUT, black dashed line: adaptive matched filter, and gray solid line: without RMU along CBLUT and correct matched filters.

Introducing RMUs along the cable under test not only increases the PD location error, it also introduces an error in the charge Q estimate. For the two simulations the maximum charge estimation error is 15 – 20%. This is acceptable as the trend of PD activity over time is more important indicator of an upcoming failure than the absolute level.

These simulations demonstrate that one or more RMUs with two connected MV cables along the CBLUT is acceptable for most practical situations. Only in case of relatively short cables with several RMUs the location accuracy is above 1%. However, for short cables a location accuracy just above 1% is not a real problem, because the absolute error is only a few meters. This is sufficient for locating the physical defect location along the cable route. Creating new matched filters based on detected PDs can significantly improve the PD location accuracy in case of RMUs along the CBLUT.

6.3.2   RMUs and substations with more than two connected cables

A (PD) pulse arriving at a substation or RMU with more than two connected MV cables distributes its energy over multiple outgoing cables. This results in a significant signal loss and therefore a lower PD detection sensitivity. In this section the transfer function of RMUs and substation with more than two connected MV cables is analyzed.

Low-frequency approximation

For distances longer than approximately 1 km most of the energy of the PD pulse is contained in the frequency range 0–1 MHz. For longer distances this frequency range decreases. For low frequencies the influence of the inductances and capacitances in compact RMUs on the shape and amplitude of the PD waveform becomes neglectable. If the capacitances and inductances are neglected the equivalent circuit of an RMU/substation with N connected MV cables reduces to N parallel connections of characteristic cable impedances Z_c. The load impedance $Z_{load}(\omega)$ as seen by a PD arriving at an RMU/substation is for low frequencies:

$$Z_{load} \approx \frac{Z_c}{N-1} \tag{6.6}$$

Once inside the RMU/substation a PD pulse distributes equally over all outgoing cables:

$$H_{cn} \approx \frac{1}{N-1} \tag{6.7}$$

where H_{cn} is the transfer function from the current through the incoming cable (inside the RMU) to an outgoing cable. Substituting in Eq. 6.2 gives for the total RMU transfer function:

$$H_{rmu} \approx \frac{2Z_c}{Z_c + \frac{Z_c}{N-1}} \frac{1}{N-1} = \frac{2}{N} \tag{6.8}$$

If there are L RMUs along the CBLUT the total transfer function at low frequencies is:

$$H_{tot} \approx \prod_{i=1}^{L} \frac{2}{N_i} \tag{6.9}$$

where N_i is the number of cables in the ith RMU. If all L RMUs have the same number of cables, H_{tot} reduces to:

$$H_{tot} \approx \left(\frac{2}{N}\right)^L \tag{6.10}$$

Values for H_{tot} for several N and L values are listed in Table 6.2. For RMUs with two connected cables ($N = 2$) the total transfer function H_{tot} is equal to one. This is in agreement with the low frequency range in Figure 6.5. For $L > 1$ and $N > 2$ the transfer function H_{tot} decreases rapidly.

Note H_{tot} is the fraction of the signal that reaches the far cable end if it propagates through the RMUs. The detection sensitivity is therefore deteriorated by a factor that is the inverse of this fraction ($= 1/H_{tot}$). The charge estimation error by the PD measurement unit at one cable end will be the same factor as the total transfer function H_{tot}. After recombination of the PD pulses measured at both cable ends, the charge estimation error will be smaller because the charge estimated by both measurement units is averaged.

Table 6.2   Low-frequency total transfer function $H_{\text{tot}}(\omega)$ of L consecutive RMUs with N connected cables (see Eq. 6.10).

	$L=1$	$L=2$	$L=3$	$L=4$	$L=5$
$N=2$	1.00	1.00	1.00	1.00	1.00
$N=3$	0.67	0.44	0.30	0.20	0.13
$N=4$	0.50	0.25	0.13	0.06	0.03
$N=5$	0.40	0.16	0.06	0.03	0.01
$N=8$	0.25	0.06	0.02	0.00	0.00
$N=15$	0.13	0.02	0.00	0.00	0.00

Complete RMU/substation model

The installation found in most substations has larger dimensions than the compact RMU considered in §6.3.1. As the dimensions increase the assumption that the inductances are neglected for the frequency range 0–1 MHz no longer holds. The model described in §3.2.2 is used to study the distribution of an incoming pulse over multiple outgoing cables in a large substation. A substation with 15 connected MV cables is modeled using $L_{\text{c}} = 750\,\text{nH}$, $L_{\text{bb}} = 200\,\text{nH}$ and $Z_{\text{c}} = 11\,\Omega$. The inductances are larger than given in Table 3.2 because the compartments found in substations are larger than the compartments of that particular substation. A pulse arrives from cable connected in compartment 5 and distributes over the other cables. The total transfer functions (see Eq. 6.2) from cable 5 to four outgoing cables are plotted in Figure 6.8.

For low frequencies the transfer function to all cables is equal to $\frac{2}{15}$, agreeing with Eq. 6.8. For higher frequencies the influence of the inductances becomes significant, resulting in a decrease of the transfer function for cables further away and an increase for the cables close to the cable from which the pulse arrives. Depending on distance (within substation) between cables, the total cable length and the noise spectrum a substation with 15 connected cables will result in a deterioration of the detection sensitivity by a factor 5 – 15. A phase that decreases linearly with increasing frequency can be interpreted as a time delay and causes a PD location error. The phase of the substation transfer functions decreases only a little with increasing frequency (compared to those in Figure 6.5). The PD location accuracy is therefore not significantly influenced by such a large substation along the CBLUT.

6.4   Reflections on RMUs and substations

The total transfer function $H_{\text{rmu}}(\omega)$ of RMUs and substations with many parallel MV cables is small. It is therefore unfeasible to monitor a cable with such an RMU or substation along the CBLUT. Many parallel cables form a low load impedance $Z_{\text{load}}(\omega)$ for low frequencies. For high frequencies the inductances in the load impedance will be large compared to the characteristic cable impedance Z_{c}. In case of both a small and a large load impedance
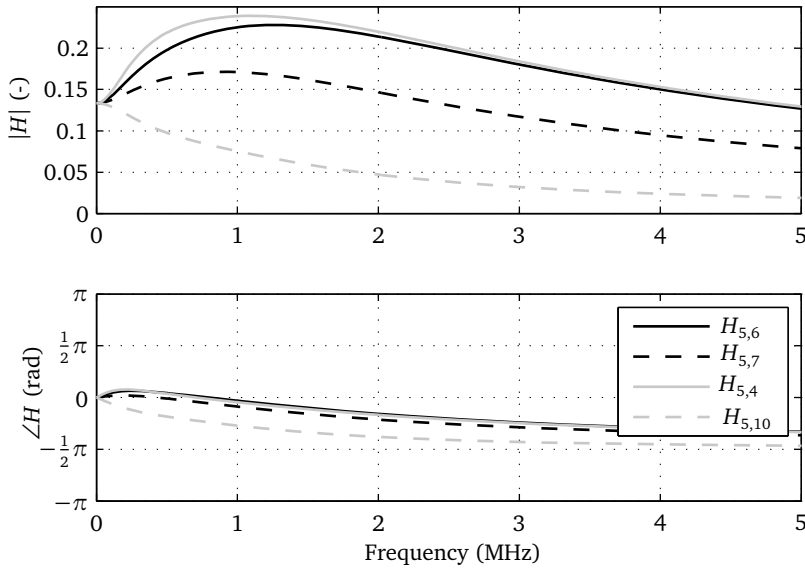
Figure 6.8 Total transfer function for a pulse arriving at the substation from the cable in compartment 5 to other cables. The substation has 15 connected MV cables. $H_{m,n}(\omega)$ denotes the total transfer function $H_{\mathrm{rmu}}(\omega)$ for a pulse arriving from cable m and going to cable n.

$Z_{\mathrm{load}}(\omega)$ the reflection coefficient $\Gamma_{\mathrm{RMU}}(\omega)$ is relatively high, meaning that a (PD) pulse arriving at that RMU/substation will largely reflect back into the cable. A good reflection on one cable end enables a single-sided PD from the other cable end. The reflection at the far cable end makes time-domain reflectometry (TDR) [29, 44, 47] for PD location feasible. In this section the reflection coefficient of RMUs and substation is analyzed.

Low-frequency approximation

For low frequencies the impedances of the inductances and capacitances are neglectable compared to the characteristic cable impedance Z_{c}. Neglecting the inductances and capacitances the RMU reflection coefficient is given by:

$$\Gamma_{\mathrm{RMU}} = \frac{Z_{\mathrm{load}} - Z_{\mathrm{c}}}{Z_{\mathrm{load}} + Z_{\mathrm{c}}} \approx \frac{2 - N}{N} \tag{6.11}$$

In Table 6.3 the low-frequency Γ_{RMU} is listed for different number of connected cables. If there is only one connected cable ($N = 1$) there is no outgoing cable and the load impedance is infinite, resulting in a reflection coefficient of 1. If there are two connected cables ($N = 2$) the load impedance is formed by a single power cable and is therefore matched to the characteristic cable impedance Z_{c}. For more than two connected cables the

Table 6.3 Low-frequency reflection coefficient on RMU/substation for different numbers N of connected cables (see Eq. 6.11).

	$N = 1$	$N = 2$	$N = 3$	$N = 4$	$N = 5$	$N = 10$	$N = 15$	$N = 30$
Γ_{RMU}	1	0	-0.33	-0.50	-0.60	-0.80	-0.87	-0.93

load impedance is lower than Z_c and therefore the reflection coefficient is negative. The more cables are connected the lower the load impedance and the closer Γ_{RMU} approaches -1. Reflection coefficients that are close to ± 1 indicate a good reflection point. Analogue to the total transmission coefficient (see Eq. 6.10), the detection sensitivity deteriorates by a factor that is the inverse of the reflection coefficient ($= 1/|\Gamma_{\text{RMU}}|$).

Complete RMU/substation model

In Figure 6.9 the reflection coefficients are given for a compact RMU with an MV/LV transformer and N connected MV cables. The plotted reflection coefficients are based on the model presented in §3.2.2, with the same typical parameters as used in §6.3.1. For low frequencies these reflection coefficients correspond to the values listed in Table 6.3. For frequencies above approximately 4 MHz the inductances L_c and L_{bb} become dominant, resulting in a high load impedance and a reflection coefficient close to 1.

The reflection coefficients are also estimated for larger substations using the same model. The modeled substation consists of N MV cables and has no transformer. The model parameters are: $L_c = 750$ nH, $L_{\text{bb}} = 200$ nH and $Z_c = 11\,\Omega$. The reflection coefficient for different number of cables is plotted in Figure 6.10. The plotted reflection coefficients are for a pulse arriving from the cable connected in the middle of the busbar. For the other cables the reflection coefficients do not differ significantly. For low frequencies the reflection coefficients correspond to Table 6.3. For higher frequencies the inductances L_c and L_{bb} are dominant and the load impedance $Z_{\text{load}}(\omega)$ is a high impedance. Because the load impedance is inductive and the characteristic cable impedance is real-valued there is no frequency for which the load impedance is matched to the characteristic cable impedance Z_c. The amplitude of the reflection coefficient is therefore relatively large over the entire frequency range, providing a good reflection point. The decrease in phase with increasing frequency is similar to that of 3 RMUs (see Figure 6.5). As discussed before 3 RMUs, and therefore also the reflection coefficients in this section, do introduce an acceptable PD location error.

The upper limit of the horizontal axis in Figure 6.10 is taken 5 MHz. For small substations the lumped impedance approach is valid for this frequency range, but for large substations transmission line effects along the busbar become significant, see §3.2.3. Based on the dimensions of large substations and the wave length in air the plotted reflection coefficients are valid up to at least 1 MHz. For cable lengths above 1 km most of the PD signal energy is within this range, see §6.2.
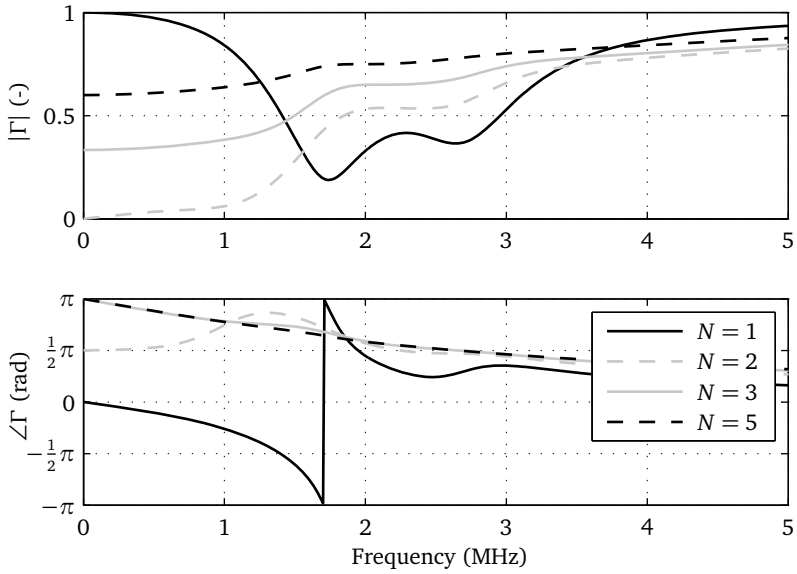
Figure 6.9 Simulated reflection coefficients on RMUs with N connected MV cables and an MV/LV transformer.
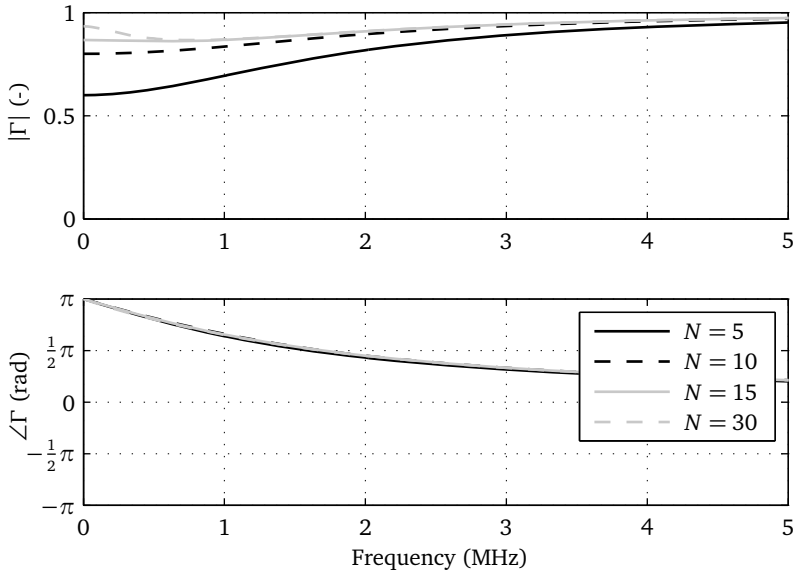
Figure 6.10 Simulated reflection coefficients on substations with N connected MV cables.

Discussion

A single-sided PD measurement, using TDR for PD location, has compared to a two-sided measurement the advantage that it requires only a single measurement unit. But it also has disadvantages:

- It relies on the reflection of the PD on the far end. This pulse has to travel back and forth through the cable under test. The maximum distance that a PD pulse has to travel is therefore twice the cable length. Consequently, the maximum cable length that can be monitored using a single-sided measurement is half the maximum cable length that can be monitored using a two-sided measurement.

- Reflections on joints along the CBLUT complicate the signal processing because they have to be distinguished from reflections on the far cable end. Some joints, e.g. joints that connect a PILC and an XLPE cable, cause large reflections. This makes it difficult to distinguish reflections on these joints from reflections on the far end, especially if the signal processing is fully automated. Automated signal processing is a requirement for large scale implementation of online PD monitoring in cable networks.

- Reflections on joints and RMUs in other connected cables. A PD pulse from the CBLUT will continue to other connected cables. If these cables contain joints or RMUs that cause a significant reflection, the measurement unit must distinguish these from the reflection on the far end of the CBLUT. This problem can be solved using directional sensing as described in [53, 59].

- More difficult to distinguish between PDs from the CBLUT and disturbing signals (or other PDs) from other connected cables. This problem can also be solved using directional sensing as described in [53, 59].

6.5   Experiments

6.5.1   Compact RMU along cable under test

To verify the feasibility of monitoring two consecutive cables with an RMU along a cable under test a PD-OL PD monitoring system is installed on such a circuit. The two cables are 10 kV belted PILC cables with a combined length of 1801 m and an RMU at 753 m. The PD-OL system was able to monitor the circuit without any problem. During the period the circuit was monitored one spot in the circuit started discharging. There were several periods of PD activity with increasing intensity, see Figure 6.11. The joints at 993 m and 995 m were replaced and examined. The grease in the joints contained traces of electrical treeing and signs of potential moisture ingress. After replacing the joint the PD activity stopped.

   The apparent location of the discharges is approximately 50 m away from the replaced joints. Based on the PD pattern and past experience the nearby joints were judged to be
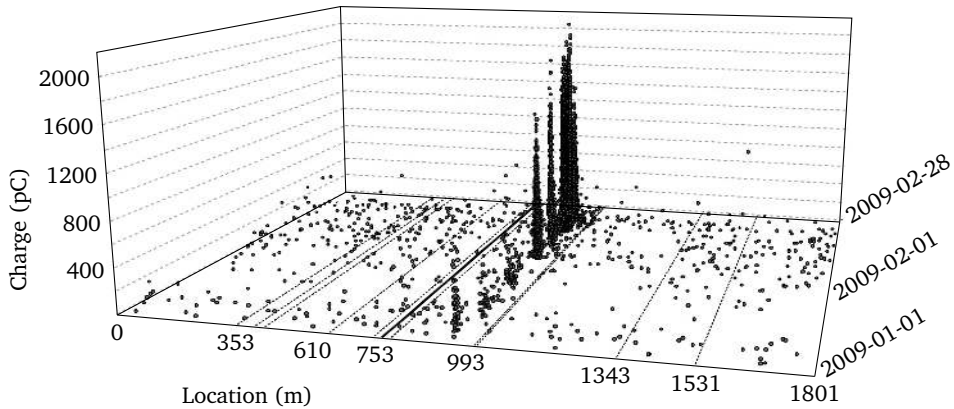
Figure 6.11 Detected partial discharges during a period of two months. The circuit consists of two consecutive PILC cables with a total length of 1801 m and an RMU at 753 m. Dashed lines in bottom plane indicate joint locations. Solid lines in bottom plane indicate RMU locations.

the most likely source and not the cable itself. This location error is larger than expected to be caused by the RMU along the CBLUT. Moreover, the discharges appear at the left side of the joints, while the model predicts them to be at the right side. The source of this location error is therefore most likely not the presence of the RMU, but inaccuracies in the cable circuit information. Different sections of the cable may have different propagation velocities. Because the exact velocities of the sections are unknown the propagation velocity is assumed to be the same for the entire cable. Another source of error might be the cable circuit information supplied by the utility. Past experiences learns that the lengths of the cable sections supplied by the utilities are not always accurate.

The PD-OL system is also installed on a circuit consisting of 4 consecutive XLPE cables with a total length 5661 m and three RMUs along the CBLUT at 4694 m, 5033 m and 5106 m. On July 31 PD activity started on one location. Over a couple of days the discharge activity intensified. The utility replaced the joint at the location of the discharge activity. Investigation of the joint showed that it was partially burned due to excessive heating caused by a bad crimp connector. After repair the discharge activity had disappeared. For this circuit the location accuracy is much better. According to the circuit data from the utility the joint is at 3526 m, while the PD-OL system located the PDs at 3520 m. This is a deviation of 0.1% of the cable length.

The PD-OL system is also successfully installed on several other circuits with one or more RMUs along the CBLUT. These circuits include cable circuits with PILC cable and circuits with XLPE cable. The number of RMUs along the CBLUT in these circuits vary from one to five.
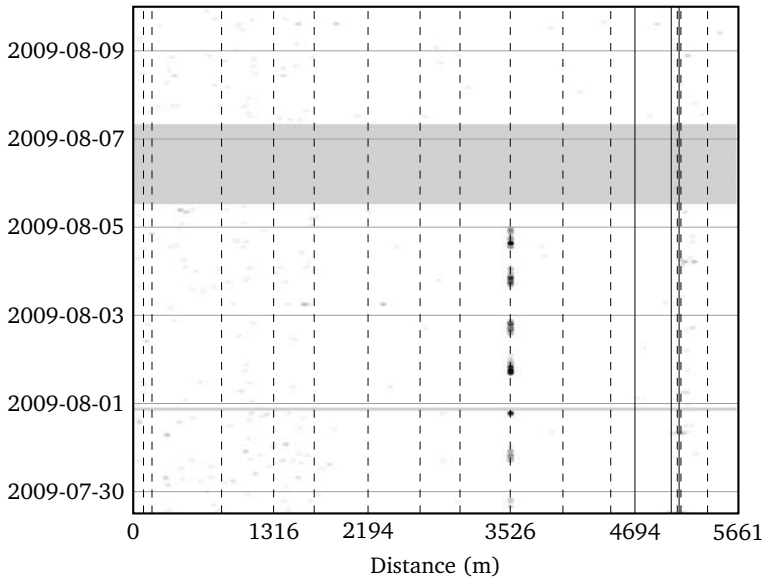
Figure 6.12   Detected partial discharge density (darker means higher density). The circuit consists of four consecutive XLPE cables with a total length of 5661 m and RMUs at 4694 m, 5033 m and 5106 m. Dashed vertical lines indicate joint locations. Solid vertical lines indicate RMU locations. The solid gray areas indicate periods during which there was no PD measurement, e.g. during the period that the joint was being replaced.

6.5.2   Large substation

The propagation through and reflection on a large substation is tested on a substation with 22 connected MV cables and two HV/MV transformers. A pulse is injected in the first RMU of the 7th MV cable. The cable circuit between this RMU and the substation consists of single-core XLPE cables with a length of approximately 800 m. The injected pulse is detected in the first RMU of the 12th MV cable. The length of the cable between this RMU and the substation is approximately 700 m. The injected and detected pulses are plotted in Figure 6.13.

   The pulse that is transmitted through the substation and detected in the first RMU of the 12th cable is much smaller than the injected pulse; the peak amplitude is approximately 200× smaller. The pulse is much smaller than what would be expected from propagating through 1500 m of a similar XLPE cable (with substation). This indicates that most signal is lost due to the substation. Because the propagation coefficient of this particular cable is unknown, it is impossible to determine the exact transfer function of the substation from this measurement. The signal of the injected pulse also shows the reflection of the injected pulse on the substation. This reflection is much larger than the pulse that
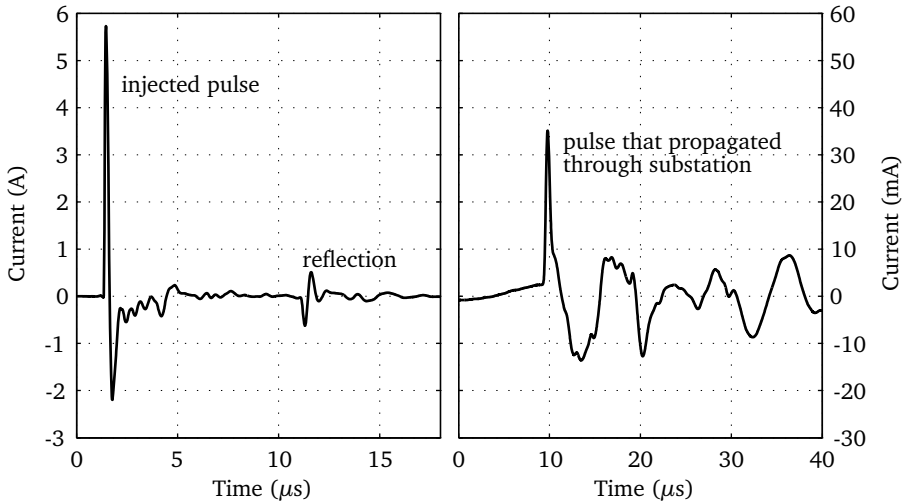
Figure 6.13 Measured signal after pulse injection in the first RMU of a cable connected in a large substation (left figure). The injected pulse is detected in the first RMU of another cable connected to the same substation (right figure). The time axes of both measurements are not synchronized. Notice that the horizontal and vertical scaling is different for both figures.

propagated through the substation; about 20× larger. The distance that both pulses propagated through a cable is similar, the main difference is reflection on and propagation through the substation. The low-frequency approximation (Eq. 6.11 and Eq. 6.8) of the substation model predicts a reflection coefficient of $\Gamma_{\mathrm{RMU}} = -0.9$ and a total transfer function of $H_{\mathrm{rmu}} = 0.09$. The ratio between these two is larger than the measured ratio. If the full model is used, this ratio could be a factor two larger. See, for example, $H_{5,10}(\omega)$ in Figure 6.8, at 1 MHz its amplitude is only halve the amplitude at 0 Hz. This experiment shows that a single-sided TDR measurement with the substation at the far cable end is likely more feasible than a two-sided measurement with the substation along the CBLUT.

6.6 Conclusions

The signal energy of a detected PD signal decreases for increasing distance between the PD origin and the detection point due to attenuation in the cable. The maximum cable length that can be monitored is therefore limited. Because the attenuation of most XLPE cables is lower than the attenuation of PILC cables, the maximal XLPE cable length that can be monitored is higher than the maximal PILC cable length. Depending on the noise spectrum a matched filter can significantly increase the maximum cable length that can be monitored. For example, for a desired sensitivity of 600 pC, a noise spectrum as in

Figure 6.2, and adaptive filtering for reduction, the maximum PILC cable length is 4 km, while the maximum XLPE cable length is 8 km.

An RMU along the CBLUT introduces a signal loss and a PD location error. The influence of a compact RMU with two connected cables is neglectable if the total cable length is longer than approximately 1 km. The longer the total cable length, the smaller the influence of an RMU along the CBLUT. For a 4 km PILC cable the signal loss caused by 9 RMUs (all with two connected cables) is neglectable and the location accuracy is well within 1% of the cable length. If the RMU(s) along the CBLUT have more than two connected cables a significant part of the signal is lost, decreasing the detection sensitivity significantly. The influence of an RMU along the CBLUT on the charge estimation and location accuracy can be reduced by creating new adaptive templates based on measured PD signals.

A large substation along the CBLUT introduces a large signal loss, which may be unacceptable in some situations with a two-sided measurement system. However, a major part of an incoming pulse reflects on a large substation with many connected cables. This reflection enables a single-sided PD measurement from the other cable end. The PD origin can be determined using TDR with the reflection on the substation at the far cable end. A single-sided measurement has the disadvantage that the maximum cable length that can be monitored is halved, that it is sensitive to reflections on joints in the CBLUT and other connected cables, and that it is more difficult to discriminate between PDs and disturbing signals.

CONCLUSIONS AND RECOMMENDATIONS

7.1 Conclusions

The main goal of the work presented in this thesis is to improve the applicability of the online PD monitoring system for MV cable networks that was developed during a previous project. This is achieved by investigating several aspects of the cable network and the measurement system itself. Each of these aspects contribute to the improvement of the monitoring system and its applicability in MV cable networks.

Power cable model

Single-core cables and three-core power cables that have a metallic earth screen around each core can be interpreted as (uncoupled) two-conductor transmission lines with a single propagation mode. A three-core cable with common earth screen has multiple propagation modes. These modes can be interpreted as an SP mode traveling between the three conductors and earth screen and two PP modes traveling between two conductors. The transmission line parameters of a single-core cable can be measured by a pulse response measurement. The transmission line parameters of the two different propagation channels of a three-core cable with common earth screen can be assessed by two pulse response measurements. Detailed prediction of multiple reflections was achieved, including the mixing of propagation modes having distinct propagation velocities, validating both the model and the measurement method for three-core cables with common earth screen.

   The characteristic impedance Z_c and propagation velocity v_p of single-core and three-core XLPE cables can be estimated using data that is found in a cable datasheet. For single-core cables Z_c and v_p are estimated with an accuracy within 5%. For three-core cables with common earth screen the accuracy of the estimation of Z_c of both the BEM and the conformal mapping method is 5 to 10%. For the estimation of the PD pulse shape

and amplitude this accuracy is sufficient. The accuracy required for PD location (1%) is not achieved. Therefore, the estimated velocity can not be used for accurate PD location. But accurate PD location can be achieved nonetheless by measurement of the propagation time of the cable. Practical experience has shown that occasionally mistakes are made in the cable circuit information provided by utilities. The accuracy of the estimated v_p is sufficient for judging whether, for example, the combination of a measured cable propagation time and the cable length supplied by the utility can be correct.

Cable system model

The proposed RMU/substation model can predict the behavior of RMUs and compact substation for frequencies up to 5 MHz with a mean accuracy of 10 – 30%. This covers the most important part of the frequency range of interest, especially in case of longer cable lengths. The model is expected to be also applicable to larger substations, although this is not verified. The only caveat is that for large substations the upper frequency for which the model is valid will be limited due to transmission line effects within the installation.

The cross-bonding model with coaxial CB cables can accurately predict the behavior of a small test setup. The model for short single-core CB cables is unable to predict the signals measured during a field measurement on an HV cable system. The inductive coupling between phases is strong because the CB cables are laid out arbitrarily on top of each other. This effect can not be taken into account in a general model. For coaxial CB cables the influence of the environment and the exact configuration of the CB cables is smaller. Therefore, the proposed model for coaxial CB cables may still hold, but this was not verified with a field measurement.

During the deployment of PD-OL systems in MV grids complications were encountered in a few cable circuits. These problems include: air core reactors placed in substations in series with the CBLUT, a parallel impedance $Z_x(\omega)$ if the measurement unit is installed around the last earth connection itself, and a semiconducting sleeve in the termination of an XLPE cable. These problems were identified and analyzed to find appropriate solutions.

Time-of-arrival

Several methods to estimate the time-of-arrival t_{oa} of a pulse were evaluated analytically, using simulations, and experimentally to investigate the strong and weak points of the methods. Altogether, no single method performs superior on all criteria. Depending on the situation either the energy criterion (EC) method or the phase method will provide the most reliable overall performance. The EC method is based on the global minimum in curve of the cumulative pulse signal energy combined with a negative trend. The phase method is based on the phase of the pulse signal in frequency domain. The EC method has good accuracy in most situations. The only point where it failed is on its sensitivity to particular pulse shapes. Incorporating the impulse response of the propagation channel between both measurement units improved the pulse shape sensitivity for some pulse shapes. The strongest point of the phase method is its complete insensitivity to the pulse

shape. The second advantage is the high accuracy, provided that the load impedance and characteristic cable impedance can be measured or estimated reliably. If the load impedance is unknown, or if there are other locations in the cable circuit where the phase changes suddenly, the accuracy of the phase method is poor.

Adaptive matched filter bank

A matched filter bank (MFB) for PD detection requires predictions of the waveforms of PDs from the CBLUT. There are cable circuit configurations where system identification measurements combined with a standard cable model do not predict the PD waveform with sufficient accuracy. The adaptation algorithm proposed in this thesis creates new templates based on detected pulses that do not have a good match with the predicted waveforms. The sensitivity and location accuracy is improved when these new active adaptive templates are used to construct additional matched filters for the MFB. By choosing the thresholds used by the algorithm it can be tuned to the desired location accuracy and detection sensitivity.

The adaptation algorithm will create new templates for any pulse type that is detected multiple times. Therefore, it will also create templates for recurring disturbing pulses. If a certain template always matches disturbing pulses from outside the cable under test, the measurement unit can safely discard pulses detected by this template in an early stage. This saves processing time in the PD measurement unit and reduces the amount of communication with the central server.

Implications for application in cable networks

The maximum cable length that can be monitored is limited because the signal energy of a detected PD signal decreases for increasing distance. Because the attenuation of most XLPE cables is lower than the attenuation of PILC cables, the maximum cable length that can be monitored is larger for an XLPE cable than for a PILC cable. Depending on the noise spectrum a matched filter can significantly increase the maximum cable length that can be monitored.

An RMU along the CBLUT introduces a signal loss and a PD location error. The influence of a compact RMU with two connected cables is neglectable if the total cable length is longer than approximately 1 km. The longer the total cable length, the smaller the relative influence of an RMU along the CBLUT. For a 4 km PILC cable the signal loss caused by 9 RMUs (all with two connected cables) is neglectable and the location accuracy remains well within 1% of the cable length. If the RMU(s) along the CBLUT have more than two connected cables a significant part of the signal is lost, decreasing the detection sensitivity significantly. The influence of an RMU along the CBLUT on the charge estimation and location accuracy can be reduced by creating new adaptive templates based on detected PD signals.

A large substation along the CBLUT introduces a significant signal loss, which is unacceptable in most situations. A major part of an incoming pulse reflects back on a large

substation with many connected cables. This reflection, however, enables a single-sided PD measurement from the other cable end. The PD origin can be determined using TDR with the reflection on the substation at the far cable end. A single-sided measurement has the disadvantage that the maximum cable length that can be monitored is halved, that it is sensitive to reflections on joints in the CBLUT and other connected cables, and that it is more sensitive to disturbing signals from the rest of the grid.

7.2 Recommendations for future work

Single-sided PD measurements

The cables to a large substation could be monitored using a single-sided PD measurement from the other cable end. Because the substation provides a good reflection TDR can be used to locate the origin of detected PDs. TDR is an already proven technique for on-site offline PD measurements. Before the same technique can be applied to online PD measurements a few issues have to be resolved:

- During offline measurements the far cable end is disconnected, providing a perfect reflection point. A substation provides a good reflection, but not perfect. Due to the complex impedance formed by a substation the pulse shape of a reflected pulse is distorted. Pulse injection, which is already integrated in PD-OL measurement units for synchronization and impedance measurement, can be used to measure the far-end reflection. Research on methods to correctly analyze and process these signals is required.

- The direct PD pulse and the pulse reflected on the far end overlap if the PD origins is close to the far end. Correct automated analysis of overlapping (reflected) pulses is not straightforward. Pulse injection and detection of the reflection pattern may be used to characterize the overlapping (reflected) pulses and provide a solution for the analysis.

- During an online measurement the CBLUT is connected to the rest of the grid. Pulses and reflection from other connected cables will also be detected, complicating the identification of the pulses from the CBLUT. This problem can be solved using directional sensing. Although this technique is explored on a test setup, it has not yet been applied during field measurements in different cable circuits.

Cross-bonding

The model proposed for circuits with CB joints with coaxial CB cables is not yet tested on a full-scale test setup. For circuits with single-core CB cables the model was shown to be unable to predict the signals measured during a field measurement. More work is required to verify the model for coaxial CB cables and to improve the model for single-core CB cables. The work presented in [15] might be useful in this process. Because currently the

research and development is focused on MV cable networks, where CB joints are scarce, this is likely not a high priority topic. If in the future research focuses on HV cable circuits, where cross-bonding is much more common, it is critical for correct signal interpretation to have correct CB models.

Adaptive matched filter bank

The adaptation algorithm that improves the MFB based on detected (PD) signals has been tested on a relatively small set of measurement data. The next step is to apply the algorithm to more circuits and for longer periods of time. Two main goals for a large scale test are:

- Test and, if necessary, improve the robustness of the algorithm in difficult situations, such as: many different types of disturbing pulses and many partially overlapping pulses (both PDs and disturbances).

- Estimate the gain in PD detection sensitivity and location accuracy that can be achieved in practice in different situations.

The adaptation algorithm and its application can be improved by identifying PD templates and disturbing pulse templates. Pulses matching disturbing pulse templates can be discarded immediately and PD templates can be used to improve the system model. To achieve this identification the server that recombines the pulses detected at each cable end must determine whether a newly created template belongs to a disturbing pulse or to a PD. Based on the origin of detected pulses their corresponding templates can be classified as a disturbing pulse or a PD from a certain location. Due to the presence of noise and disturbances the templates will occasionally be classified incorrectly. Therefore, a statistical analysis is required to determine the likelihood that a template belongs to a PD signal or to a disturbing pulse. The best method to achieve this remains to be investigated.

Once a new adaptive template has been identified as PD template, corresponding to a particular origin, it is possible to improve the cable system model. The cable system model used to create the original MFB templates is a relatively simple model consisting of a homogeneous cable terminated by an RMU at each end. In reality, there are more factors that influence the PD waveform. For example, an RMU or joint along the CBLUT can significantly influence the PD waveform. Because the PD waveform is influenced by many factors it is not straightforward to determine which part of the model to improve. It requires more research to find the best method to update the cable circuit model based on new detected PD templates.

SIGNAL PROCESSING DEFINITIONS

This appendix summarizes the definitions of time-discrete signals that are used throughout this thesis, both in time and frequency domain. The calculations of energy, mean power, power spectral density function are also given.

A.1 Time and frequency domain signals

The signal $y[k]$ is acquired by sampling the continuous signal $y(t)$ at fixed time interval Δt:

$$y[k] = y(t_k) = y(k\Delta t); \tag{A.1}$$

The index k ranges from 0 to $B-1$ and B is the total number of samples in the signal. The frequency domain signal $Y[i]$ is the discrete equivalent of $Y(\omega)$. It is calculated from time-domain signal $y[k]$ following:

$$Y[i] = Y(\omega_i) = Y(2\pi i\Delta f) = \Delta t \underbrace{\sum_{k=0}^{B-1} y[k]\mathrm{e}^{-j2\pi i\Delta f k\Delta t}}_{\mathrm{DFT}\left(y[k]\right)} \tag{A.2}$$

where i is an integer ranging from 0 to $B-1$ and Δf the frequency domain resolution in Hz, i.e. the difference in frequency between two consecutive samples. It is given by:

$$\Delta f = \frac{1}{\Delta t\, B} \tag{A.3}$$

The summation in Eq. A.2 is the discrete Fourier transform (DFT). If B is a power of two a fast Fourier transform (FFT) can be used to improve computational performance. The

frequency domain signal $Y[i]$ contains frequencies from $0\,\text{Hz}$ (index $i = 0$) to the Nyquist frequency $f_{\text{nyq}} = 1/(2\Delta t)$ (at index $\lfloor i = B/2 \rfloor$). The indices above the Nyquist frequency can be interpreted as negative frequencies in reverse order. Recorded time-domain signals $y[k]$ are real-valued. Therefore, the values of $Y[i]$ for the negative frequencies are given by $Y[B - i] = Y^*[i]$ for $1 \leq i \leq (B - 1)$.

The inverse transform of $Y[i]$ is:

$$y[k] = \frac{1}{\Delta t} \underbrace{\frac{1}{B} \sum_{i=0}^{B-1} Y[i] e^{j2\pi i \Delta f k \Delta t}}_{\text{IDFT}(Y[i])} \tag{A.4}$$

The second part of this equation (summation and $1/B$) is the inverse discrete Fourier transform (IDFT).

The unit of the frequency-domain signal $Y[i]$ is V/Hz if the time-domain signal $y[k]$ has unit V. Multiply $|Y[i]|$ by $\sqrt{2}\Delta f$ to get the RMS value of a sine wave in $y[k]$. For example, assume $\Delta t = 1\,\text{ns}$, $B = 10000$ and a sine wave of $10\,\text{MHz}$ (i.e. $y[k] = \sin(2\pi\, 10^7\, k\Delta t)$). The frequency domain resolution is $\Delta f = 1/(B\Delta t) = 100\,\text{kHz}$. The index of the sine wave frequency is $i = 10^7/\Delta f = 100$. The amplitude of the frequency domain signal at that index is $|Y[100]| = 5 \times 10^{-6}\,\text{V/Hz}$. The RMS value is $\sqrt{2}\Delta f\,|Y[100]| \approx 0.707\,\text{V}$, which is indeed the RMS value of a sine wave with amplitude $1\,\text{V}$.

A.2   Signal energy and power

The signal energy of signal $y[k]$ is given by the integral of the momentary signal power. According to Parseval's theorem this is equal to the integral of the frequency domain representation $Y[i]$:

$$E_y = \Delta t \sum_{k=0}^{B-1} \left| y[k] \right|^2 = \Delta f \sum_{i=0}^{B-1} |Y[i]|^2 \tag{A.5}$$

If the unit of signal $y[k]$ is V, the unit of the signal energy is $\text{V}^2\,\text{s}$.

The mean signal power of signal $y[k]$ is given by:

$$P_y = \frac{E_y}{\Delta t\, B} = \frac{1}{B} \sum_{k=0}^{B-1} \left| y[k] \right|^2 = \Delta f^2 \sum_{i=0}^{B-1} |Y[i]|^2 \tag{A.6}$$

If the unit of $y[k]$ is V, the unit of the power is V^2. Note that if the signal is continuous and has no offset the power is equal to the variance σ_y^2 of signal $y[k]$.

The power spectral density function (PSDF) of $y[k]$ is:

$$P_Y[i] = \Delta f\, |Y[i]|^2 \tag{A.7}$$

The unit of $P_Y[i]$ is V^2/Hz. The PSDF can be converted to the mean signal power P_y by integrating over frequency:

$$P_y = \sigma_y^2 = \Delta f \sum_{i=0}^{B-1} P_Y[i] \tag{A.8}$$

A.3 Signals and noise

A recorded pulse signal is a combination of the actual signal and additive noise:

$$x[k] = s[k] + n[k] \tag{A.9}$$

where $x[k]$ is the recorded time-discrete signal, $s[k]$ is the noise free PD-pulse signal. For $n[k]$ we assume additive, uncorrelated Gaussian noise with zero mean, with k an integer ranging from 0 to $(B-1)$ and B the total number of samples in the signal. The signal energy in this signal is:

$$E_x = \Delta t \sum_{k=0}^{B-1} x^2[k] = \Delta t \sum_{k=0}^{B-1} s^2[k] + \Delta t \sum_{k=0}^{B-1} n^2[k] = E_s + E_n \tag{A.10}$$

with E_x the total energy in the recorded signal, E_s the energy of the actual signal and E_n the noise energy.

The mean signal power in a recorded signal is:

$$P_x = \frac{E_x}{\Delta t\, B} = \frac{E_s}{\Delta t\, B} + \frac{E_n}{\Delta t\, B} = P_s + P_n \tag{A.11}$$

where P_x is the total signal power, P_s the actual signal power and P_n the noise power. Note that P_n is equal to the variance of the noise σ_n^2.

A.4 Noise spectrum estimation

The averaged periodogram of a recorded noise signal $n[k]$ is an estimate of the PSDF of the noise [22, 58]. The signal is split into blocks of B samples, giving a total of R blocks. The PSDF (Eq. A.7) of the rth block (with r ranging from 1 to R) is calculated following:

$$P_{N,r}[i] = \frac{\Delta t}{B\,U} \left| \sum_{k=0}^{B-1} n[k+(r-1)B]w[k]e^{-j2\pi i \Delta f k \Delta t} \right|^2 \tag{A.12}$$

where $w[k]$ is a window, e.g. a Blackman window, to reduce spectral leakage, and

$$U = \frac{1}{B} \sum_{k=0}^{B-1} w^2[k] \tag{A.13}$$

The PSDF is estimated by averaging the blocks:

$$\hat{P}_N[i] = \frac{1}{R} \sum_{r=1}^{R} P_{N,r}[i] \tag{A.14}$$

During online PD measurements it is unlikely that a recorded noise signal is completely free of PDs and finite-energy disturbances. Especially, in industrial areas there are often many disturbances caused by heavy equipment. If a number of blocks contain disturbances the estimated noise spectrum may be overestimated. A few blocks containing disturbances can already significantly affect the averaged spectrum.

Assuming that the noise in the recorded signal has a Gaussian distribution then the variable $P_{N,r}[i]$ has an exponential distribution [8, 27] and is determined by one parameter. The probability density function is:

$$f(x) = \lambda e^{-\lambda x} \tag{A.15}$$

The expected mean $\mu(X)$ and median $\mu_{1/2}(X)$ of a random variable X with exponential distribution are [16]:

$$\mu(X) = \frac{1}{\lambda}$$
$$\mu_{1/2}(X) = \frac{\ln 2}{\lambda} \tag{A.16}$$

The λ parameter can be estimated for each frequency bin by calculating the median value of $P_{N,r}[i]$ of all blocks. The median is used instead of the mean because it is much less sensitive to occasionally occurring high outliers. Even though the influence of a few outliers on the median is limited, there still is a small effect. Therefore, all outliers are discarded and the mean is calculated from the remaining values. A value of $P_{N,r}[i]$ is considered an outlier if:

$$\frac{P_{N,r}[i]}{\mu_{1/2}^r \left(P_{N,r}[i] \right)} > T_{\text{out}} \tag{A.17}$$

where $\mu_{1/2}^r \left(P_{N,r}[i] \right)$ denotes the median value of the $P_{N,r}[i]$ value over all blocks and T_{out} is the threshold. The mean calculated this way is biased because a few good large values will be discarded as well. The threshold must be chosen high enough the reduce the bias to an acceptable level. The bias in the mean, if there are no disturbances, is 1% for a threshold of $T_{\text{out}} = 9.6$. If there are disturbances the error depends on the number of disturbances and their distribution.

SENSITIVITY OF PHASE METHOD TO ERRORS IN IMPEDANCE ESTIMATION

The major disadvantage of the phase method for time-of-arrival estimation (§4.3.5) is that a phase shift in the transmission coefficient from cable to load impedance introduces a location error. This error can be corrected using Eq. 4.15 provided that the transmission coefficient is known accurately. The transmission coefficient is calculated using the characteristic cable impedance Z_c and load impedance $Z_{load}(\omega)$. Unfortunately, estimates of these quantities have limited accuracy. The sensitivity of the location accuracy to errors in the estimation of Z_c and $Z_{load}(\omega)$ can be derived as follows. Assuming that Z_c is real and frequency-independent the phase of the transmission coefficient $T(\omega)$ is given by:

$$\angle T = -\arctan\left(\frac{\sin\left(\alpha_{load}\right)\left|Z_{load}\right|}{Z_c + \cos\left(\alpha_{load}\right)\left|Z_{load}\right|}\right) \tag{B.1}$$

with $\alpha_{load}(\omega)$ the phase of $Z_{load}(\omega)$. In order to estimate the error due to the limited knowledge of $\alpha_{load}(\omega)$, $Z_{load}(\omega)$ and Z_c we analyze the derivatives of Eq. B.1 with respect to these parameters. The absolute value of the derivative of this equation to $\alpha_{load}(\omega)$ is always less than one. The absolute value of the derivative of this equation to either $|Z_{load}|$ or Z_c is less than 0.1 for practical values ($-90° \leq \alpha_{load} \leq 90°$, $2 \leq |Z_{load}| \leq 200$, and $10 \leq Z_c \leq 30$). The next step is to use Eq. 4.11 to convert the phase to a time shift t_e introduced at the transmission from cable to load impedance. The derivative of this time shift to $\angle T$ is:

$$\frac{\partial t_e}{\partial\left(\angle T(\omega_c)\right)} = \frac{-1}{\omega_c} \tag{B.2}$$

with t_e the time shift/error introduced at the transmission from cable to load impedance. This indicates that ω_c should be chosen as high as the signal-to-noise ratio permits. The

last step is to convert the time shifts at both ends ($t_{e,1}$ and $t_{e,2}$) to a location error. Taking the PD location procedure described in §4.4 this error is given by:

$$e_{PD} = v_p t_c \frac{t_{e,1} - t_{e,2} - (x - \frac{1}{2})(t_{e,1} + t_{e,2})}{2t_c + t_{e,1} + t_{e,2}} \tag{B.3}$$

where v_p the propagation velocity, t_c the total propagation time of the cable, $t_{e,1}/t_{e,2}$ the time shift introduced due to the phase shift in T at respectively the near end and the far end, and x the PD origin in fraction of the cable length. Normally, for cable systems $t_c \gg (t_{e,1} + t_{e,2})$. Using this assumption and calculating the derivatives to $t_{e,1}$ and $t_{e,2}$ yields:

$$\frac{\partial e_{PD}}{\partial t_{e,1}} = \frac{1}{2}v_p \left(1 - \left(x - \frac{1}{2}\right)\right) \tag{B.4}$$

$$\frac{\partial e_{PD}}{\partial t_{e,2}} = \frac{1}{2}v_p \left(-1 - \left(x - \frac{1}{2}\right)\right) \tag{B.5}$$

$$\tag{B.6}$$

Since $0 \le x \le 1$ the maximum of Eq. B.4 is $^3/_4 v_p$. The result of an inaccurate estimation of $Z_{load}(\omega)$ can now be estimated according:

$$\Delta e_{PD} = \frac{\partial e_{PD}}{\partial t_e} \frac{\partial t_e}{\partial (\angle T)} \Delta(\angle T) \tag{B.7}$$

If, for example, the estimation in the phase of $Z_{load}(\omega)$ is 10°, the error in $\angle T(\omega)$ is less than 10°. If $\omega_c/2\pi$ is 2 MHz the error in t_e is less than 14 ns. Assuming $v_p = 165$ m/μs yields a location error less than 1.7 m.

CHARGE ESTIMATION PULSE SIGNALS MEASURED WITH INDUCTIVE SENSOR

The charge Q of a pulse is given by the time integral of the pulse current. In frequency domain charge Q is equal to the DC component of the current:

$$Q = \int_{-\infty}^{\infty} i(t)\,dt = \int_{-\infty}^{\infty} \mathfrak{F}^{-1}\{I(\omega)\}\,dt = \int_{-\infty}^{\infty}\int_{-\infty}^{\infty} I(\omega)\,e^{j\omega t}\,d\omega\,dt = I(0) \qquad \text{(C.1)}$$

where $i(t)$ is the current of the PD pulse in time domain, $I(\omega)$ the current in frequency domain, and $\mathfrak{F}^{-1}\{\cdot\}$ denotes the inverse Fourier transform. The PD current $i(t)$ is a causal signal with the time axis such that the pulse starts at $t = 0$. Therefore, the lower limit of the time integral over the current can be $t = 0$ instead of $t = -\infty$. Because there are always losses in the system the PD pulse has a finite duration, i.e. $\lim_{t\to\infty} i(t) = 0$. Therefore, the time integral can use $t = t_{\text{end,i}}$ as upper limit (with $i(t) \approx 0$ for $t > t_{\text{end,i}}$) without significantly affecting the calculated charge Q. Practical PD measurements can be impeded with an additional offset and low-frequency noise, most notably the 50/60 Hz power frequency. The knowledge that a PD signal is causal and should be zero just before the start of the pulse can be used to correct any offset in $i(t)$ before calculating the time integral.

Online impedance measurements are most conveniently performed using inductive sensors. An inductive sensor does not have a flat (i.e. frequency independent) transfer impedance over the entire frequency range. For low frequencies the output of an inductive sensor is the time derivative of the current, while for higher frequencies the the transfer impedance is usually more or less flat. The transfer impedance $Z_{\text{t}}(\omega)$ of an inductive
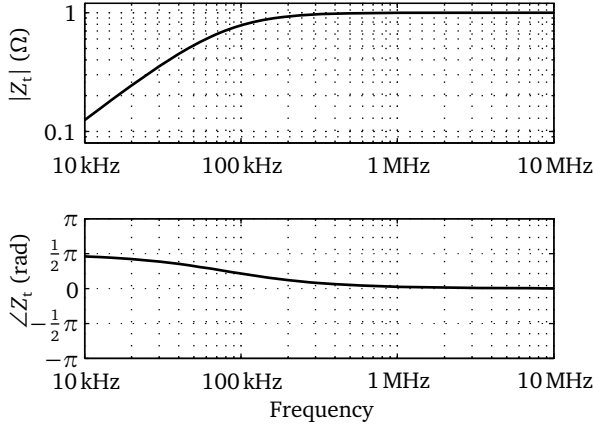
Figure C.1   Typical transfer impedance of inductive sensor with ferrite core

sensor is given by [59]:

$$Z_\mathrm{t} = \frac{V_\mathrm{ind}}{I} = j\omega M \frac{Z_\mathrm{load}}{Z_\mathrm{load} + j\omega L} \tag{C.2}$$

where M is the mutual inductance, L the self inductance of the sensor, $Z_\mathrm{load}(\omega)$ the load impedance with which the sensor is terminated, and $V_\mathrm{ind}(\omega)$ is the induced voltage at the output terminals. A typical transfer function is plotted in Figure C.1.

For the calculation of the charge only the low-frequency behavior is relevant. The transfer impedance can more generally be rewritten as:

$$Z_\mathrm{t} = j\omega M \, H_\mathrm{hf} \tag{C.3}$$

where the $H_\mathrm{hf}(\omega)$ is the transfer function for high frequencies. $H_\mathrm{hf}(\omega)$ has the properties $H_\mathrm{hf}(0) = 1$ and $\lim_{\omega \to \pm\infty} H_\mathrm{hf}(\omega) = 0$.

By integrating the measured voltage $v_\mathrm{ind}(t)$ over time and correcting for M the low-frequency components of the original pulse current $i(t)$ can be reconstructed. This does not correctly reconstruct the high-frequency components of the signal, but for estimating the charge Q only the low-frequency part of the signal is relevant. By integrating the reconstructed current the charge Q can be determined:

$$Q = \int\limits_{-\infty}^{\infty} \frac{1}{M} \int\limits_{-\infty}^{\tau} v_\mathrm{ind}(t)\,dt\,d\tau \tag{C.4}$$

This equation can be verified by substituting $v_\mathrm{ind}(t)$ for $\mathfrak{F}^{-1}\{V_\mathrm{ind}(\omega)\}$ with $V_\mathrm{ind}(\omega) =$

$I(\omega)\, Z_t(\omega)$:

$$Q = \int\limits_{-\infty}^{\infty} \frac{1}{M} \int\limits_{-\infty}^{\tau} v_{\text{ind}}(t)\, dt\, d\tau = \int\limits_{-\infty}^{\infty} \frac{1}{M} \int\limits_{-\infty}^{\tau} \int\limits_{-\infty}^{\infty} V_{\text{ind}}(\omega)\, e^{j\omega t}\, d\omega\, dt\, d\tau$$

$$= \int\limits_{-\infty}^{\infty} \frac{1}{M} \int\limits_{-\infty}^{\tau} \int\limits_{-\infty}^{\infty} j\omega M\, H_{\text{hf}}(\omega)\, I(\omega)\, e^{j\omega t}\, d\omega\, dt\, d\tau \tag{C.5}$$

In the next step two M symbols have canceled and the order of the $d\omega$ and dt integrals is changed:

$$Q = \int\limits_{-\infty}^{\infty} \int\limits_{-\infty}^{\infty} j\omega\, H_{\text{hf}}(\omega)\, I(\omega) \int\limits_{-\infty}^{\tau} e^{j\omega t}\, dt\, d\omega\, d\tau$$

$$= \lim_{\tau_1 \to -\infty} \int\limits_{-\infty}^{\infty} \int\limits_{-\infty}^{\infty} j\omega\, H_{\text{hf}}(\omega)\, I(\omega) \frac{1}{j\omega} \left[e^{j\omega\tau} - e^{j\omega\tau_1} \right] d\omega\, d\tau \tag{C.6}$$

Rearranging the terms in the square brackets gives:

$$Q = \int\limits_{-\infty}^{\infty} \int\limits_{-\infty}^{\infty} I(\omega)\, H_{\text{hf}}(\omega)\, e^{j\omega\tau}\, d\omega\, d\tau - \int\limits_{-\infty}^{\infty} \lim_{\tau_1 \to -\infty} \int\limits_{-\infty}^{\infty} I(\omega)\, H_{\text{hf}}(\omega)\, e^{j\omega\tau_1}\, d\omega\, d\tau \tag{C.7}$$

According to Eq. C.1 the first term is the charge Q since $H_{\text{hf}}(0) = 1$. In the second term the inverse Fourier transform (integral $d\omega$) of $I(\omega)\, H_{\text{hf}}(\omega)$ is replaced a convolution between $i(t)$ and $\mathfrak{F}^{-1}\{H_{\text{hf}}(\omega)\} = h_{\text{hf}}(t)$).

$$\int\limits_{-\infty}^{\infty} \lim_{\tau_1 \to -\infty} \left(i * h_{\text{hf}} \right)(\tau_1)\, d\tau = \int\limits_{-\infty}^{\infty} \lim_{\tau_1 \to -\infty} \int\limits_{-\infty}^{\infty} i(t')h_{\text{hf}}(\tau_1 - t')\, dt'\, d\tau \tag{C.8}$$

Both $i(t)$ and $h_{\text{hf}}(t)$ are causal so that the range of the convolution changes to $0 - \tau_1$. Because τ_1 is negative the signal $i(t)$ is zero over the whole integration range. The range of the integral $d\tau$ can also be limited because both $i(t)$ and $h_{\text{hf}}(t)$ are causal and have a finite duration, $t_{\text{end,i}}$ and $t_{\text{end,h}}$ respectively.

$$\int\limits_{0}^{t_{\text{end,i}}+t_{\text{end,h}}} \lim_{\tau_1 \to -\infty} \int\limits_{0}^{\tau_1} i(t')h_{\text{hf}}(\tau_1 - t')\, dt'\, d\tau = \int\limits_{0}^{t_{\text{end,i}}+t_{\text{end,h}}} 0 \ d\tau = 0 \tag{C.9}$$

With the first term of Eq. C.7 equal to the charge Q and the second term equal to zero it is verified that Eq. C.4 correctly represents the PD charge.

The time integrals in Eq. C.4 are taken from $-\infty$ to ∞. Because both current $i(t)$ of a PD pulse and the impulse response of an inductive sensor are causal and have a finite duration the integration range can be finite in practical applications. PD measurements can be impeded with low-frequency noise, most notably the 50/60 Hz power frequency. For the duration of a measured PD pulse (up to several microseconds) this low-frequency noise will appear to be an offset in $v_{\text{ind}}(t)$. Calculating charge Q using Eq. C.4 with this offset will introduce an error. This offset can be corrected using:

$$v_{\text{ind}}^{\text{c}}(t) = v_{\text{ind}}(t) - \frac{\int\limits_{t_1}^{t_2} v_{\text{ind}}(t)\,dt}{t_2 - t_1} \tag{C.10}$$

where $v_{\text{ind}}^{\text{c}}(t)$ is the corrected signal and t_1/t_2 indicates a short time interval (e.g. $1\,\mu s$) before the start of the detected pulse. The average over a small time interval is used instead of a single time instant to limit the influence of noise.

ONLINE IMPEDANCE MEASUREMENT

The impedance of an RMU or substation can be measured using an online impedance measurement method without interrupting the power delivery. The impedance of an RMU or substation is an important parameter for the prediction of the propagation of PD pulses through a cable system. In [59] an online impedance measurement method is described that combines an injection coil and a current probe. It is based on injection and detection of a reference a reference pulse. In this appendix another online impedance measurement method is proposed that requires only a single coil. The single coil must have a strong coupling between its terminals and the secondary load impedance. A bulk current injection probe meets this requirement in the frequency range of interest. The input impedance of a such probe when installed in e.g. an RMU or substation, is affected by the load formed by the RMU or substation. This appendix describes how this effect can be exploited to perform an online impedance measurement.

D.1 Model

In literature several transformer/probe models are described, e.g. [13]. We use a T-network as depicted in Figure D.1. The injection circuit represent whatever is connected to the coaxial connector of the probe. The load impedance $Z_{\text{load}}(\omega)$ at the other side of the probe represents the impedance of the installation where the probe is applied, e.g. the RMU impedance when it is installed around an MV cable in an RMU. In the T-network the impedance $Z_{\text{m}}(\omega)$ represents the mutual inductance. The impedances $Z_1(\omega)$ and $Z_2(\omega)$ represent the series impedance at respectively the primary side and secondary side. The ideal n:1 transformer included in transformer models is omitted since the probe can be considered as a 1:1 transformer.

The injection circuit (e.g. a vector network analyzer or a pulse response measurement setup such as described in §2.5.1) measures the input impedance $Z_{\text{in}}(\omega)$ of the probe
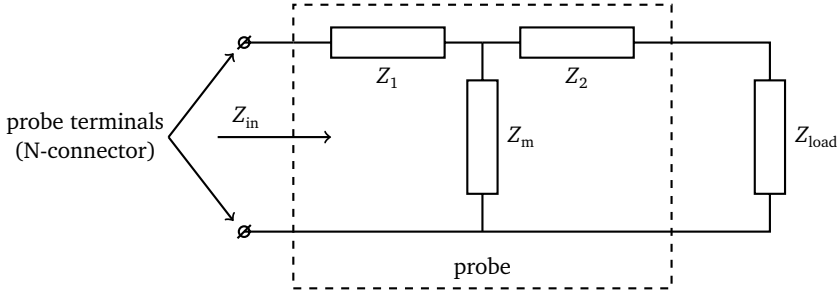
Figure D.1 Equivalent circuit of bulk current injection probe. Left-hand side is whatever is connected to the terminals of the probe. The right-hand side is the load impedance in which the probe is installed.

from the left-hand side while looking into the probe. If the model parameters $Z_1(\omega)$, $Z_2(\omega)$ and $Z_m(\omega)$ are known the load impedance $Z_{load}(\omega)$ can be determined from:

$$Z_{load} = \frac{Z_m Z_2 + (Z_2 + Z_m)(Z_1 - Z_{in})}{Z_{in} - Z_1 - Z_m} \tag{D.1}$$

D.2   Calibration

The model parameters $Z_1(\omega)$, $Z_2(\omega)$ and $Z_m(\omega)$ must to be known before a measured input impedance $Z_{in}(\omega)$ can be converted to the load impedance $Z_{load}(\omega)$. These parameters are determined using a calibration procedure. The probe is calibrated in a calibration fixture such as depicted in Figure D.2. A vector network analyzer is connected to one side of the calibration fixture while the other side of the calibration fixture is terminated by $50\,\Omega$. First, the calibration fixture itself must be calibrated, i.e. the impedance of the fixture $Z_{fix}(\omega)$ is measured by the network analyzer without the probe installed. Next, the probe is installed around the central conductor of the calibration fixture. The connector of the probe is terminated with a known impedance and the network analyzer measures the impedance $Z_{meas}(\omega)$ of the calibration fixture including the probe. Note that in this setup the injection circuit is connected to the right-hand side in Figure D.1 and a known load impedance to the left-hand side. The fixture impedance $Z_{fix}(w)$ is subtracted from the measured impedance so that only the impedance contributed by the probe remains. This process is repeated for three known impedances: $\infty\,\Omega$, $50\,\Omega$ and $0\,\Omega$ yielding three measured impedances: $Z_{meas,\infty}(\omega)$, $Z_{meas,50}(\omega)$ and $Z_{meas,0}(\omega)$. The measured impedances
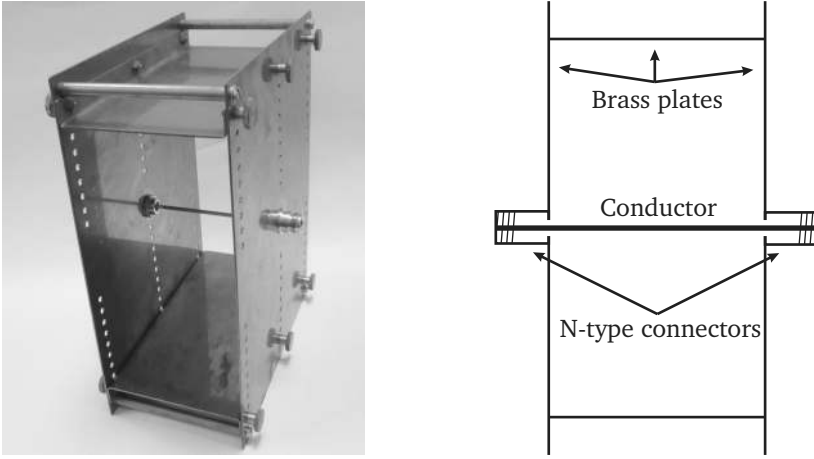
Figure D.2 Photo and schematic drawing of calibration fixture

can be expressed in terms of the model parameters and fixture impedance:

$$Z_{\text{cal1}} = Z_{\text{meas},\infty} - Z_{\text{fix}} = Z_2 + Z_{\text{m}}$$

$$Z_{\text{cal2}} = Z_{\text{meas},50} - Z_{\text{fix}} = Z_2 + \frac{Z_{\text{m}}\left(Z_1 + 50\,\Omega\right)}{Z_{\text{m}} + Z_1 + 50\,\Omega}$$

$$Z_{\text{cal3}} = Z_{\text{meas},0} - Z_{\text{fix}} = Z_2 + \frac{Z_1\,Z_{\text{m}}}{Z_1 + Z_{\text{m}}}$$

(D.2)

The model parameters are obtained from $Z_{\text{cal1}}(\omega)$, $Z_{\text{cal2}}(\omega)$ and $Z_{\text{cal3}}(\omega)$:

$$Z_{\text{m}} = \frac{\sqrt{50(Z_{\text{cal2}} - Z_{\text{cal3}})(Z_{\text{cal1}} - Z_{\text{cal3}})(Z_{\text{cal1}} - Z_{\text{cal2}})}}{Z_{\text{cal2}} - Z_{\text{cal3}}}$$

$$Z_1 = \frac{Z_{\text{m}}\left(Z_{\text{cal1}} - Z_{\text{cal3}} - Z_{\text{m}}\right)}{Z_{\text{cal3}} - Z_{\text{cal1}}}$$

(D.3)

$$Z_2 = Z_{\text{cal1}} - Z_{\text{m}}$$

The bulk current injection probe used for the experiments in this thesis is a F-120-5 manufactured by Fischer Custom Communications (FCC). The model parameters of this probe are determined using the calibration fixture depicted in Figure D.2 and a HP 8753C network analyzer with HP 85047A S-parameter set. The derived model parameters are depicted in Figure D.3. The mutual impedance $Z_{\text{m}}(\omega)$ is dominantly inductive below 500 kHz. Above that frequency core losses [65] become significant. Above 10 MHz $Z_1(\omega)$ and $Z_2(\omega)$ are almost perfect inductances. For lower frequencies they are noisy and their behavior is no longer inductive. This deviation is a measurement error. The model
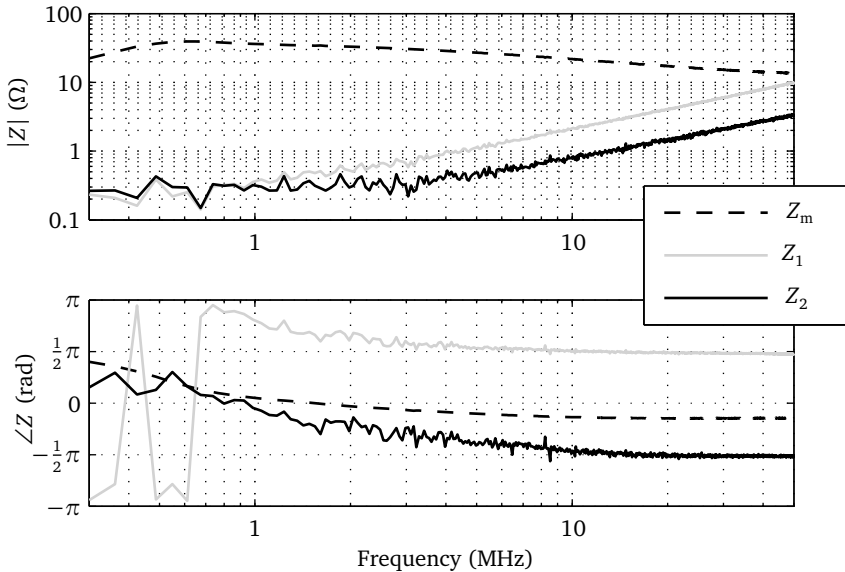
Figure D.3 Measured bulk current injection probe parameters.

parameters are not directly measured but calculated using Eq. D.3. In these equations relatively large impedances are subtracted to get the much smaller $Z_1(\omega)$ and $Z_2(\omega)$. Therefore, the deviation of $Z_1(\omega)$ and $Z_2(\omega)$ from an ideal inductance is caused by the limited accuracy of the impedance measurements. In reality they should behave dominantly inductive down to much lower frequencies. The impedance $Z_2(\omega)$ has a negative phase/inductance. By installing the probe in a circuit with a load impedance the area of the loop of the load impedance is slightly decreased because the presence of the probe decreases the area of that loop. That part is accounted for in the mutual impedance $Z_m(\omega)$. The decrease in area of the loop of the load impedance results in a decrease of the inductance of that loop. This decrease is compensated as a negative inductance for $Z_2(\omega)$.

D.3 Validation measurements

D.3.1 Test loop measurement

The first validation of the online impedance measurement method is performed by an impedance measurement in a loop with known impedance. The calibration fixture in Figure D.2 is used as test loop. For the validation measurement the probe is installed in the fixture. The fixture is terminated with a resistance. The input impedance $Z_{in}(\omega)$ of the probe is measured using a pulse response measurement as described in see §2.5.1.
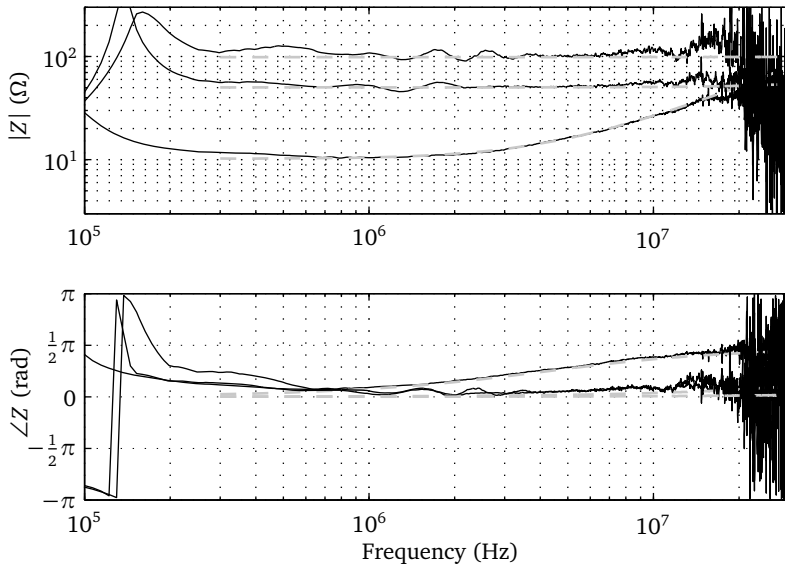
Figure D.4   Validation of impedance measurement with load impedances of $10\,\Omega$, $50\,\Omega$ and $100\,\Omega$ in test loop. Black line: online impedance measurement, dashed gray line: reference measurement with vector network analyzer.

The measured $Z_{\text{in}}(\omega)$ is converted to the load impedance $Z_{\text{load}}(\omega)$ using Eq. D.1. As a reference the impedance of the fixture, without the probe installed, is measured using a vector network analyzer. The measured load impedance $Z_{\text{load}}(\omega)$ is compared to the reference impedance. This procedure is repeated for resistances of $10\,\Omega$, $50\,\Omega$ and $100\,\Omega$ terminating the fixture. The results are plotted in Figure D.4.

Below approximately $500\,\text{kHz}$ the impedance measurement is unreliable due to the limitations of the pulse response measurement and the steep slope and low impedance of $Z_{\text{m}}(\omega)$ at lower frequencies. Between $500\,\text{kHz}$ and $12\,\text{MHz}$ the maximum error is 10% for all three impedances. Above $12\,\text{MHz}$ the measurement is unreliable due to the lack of energy for those frequencies of the injected pulse and because the mutual impedance $Z_{\text{m}}(\omega)$ become too low.

D.3.2   Field measurement

The online impedance measurement method is also tested in an RMU with two connected MV cables and compared to the impedance measured at the same location with the two coil method from [59]. The impedance is measured with the coil(s) installed around one of the MV cables in the RMU. The measured impedances are plotted in Figure D.5. The peaks and valleys observed below $3\,\text{MHz}$ are caused by reflections on joints along the
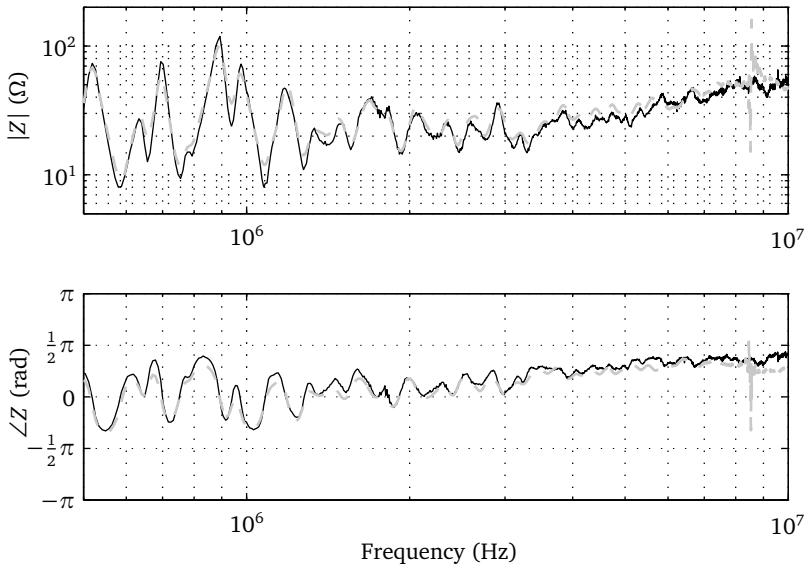
Figure D.5 Two different online impedance measurement methods applied in an RMU with two connected MV cables. Black line: single coil method described in this appendix, dashed gray line: two coil method described in [59].

cables and the RMUs at the far end of both cables. The artifact observed near 8.5 MHz is caused by the lack of energy in the injected pulse for that frequency. The injected pulse is a square pulse with a width of approximately 120 ns. Below 3 MHz the impedance varies between 8 Ω and 100 Ω. Above 3 MHz the impedance becomes dominantly inductive, going from 20 Ω at 3 MHz up to 50 Ω at 10 MHz. The mean difference between both methods over the frequency range 500 kHz – 8 MHz is approximately 18%.

Bibliography

[1] N. Ahmed and N. Srinivas. On-line partial discharge diagnostic system in power cable system. In *2001 IEEE/PES Transm. Distrib. Conf. Exp.*, volume 2, pages 853–858, Atlanta, GA, USA, Nov. 2001. doi: 10.1109/TDC.2001.971350.

[2] J. Bajorek. Admittance and impedance matrices of multiconductor power cables: Application of poynting's theorem. *Int. J. Electr. Power & Energy Systems*, 7(2): 120–126, Apr. 1985. doi: 10.1016/0142-0615(85)90017-1.

[3] R. Bartnikas. Partial discharges — their mechanism, detection and measurement. *IEEE Trans. Dielectr. Electr. Insul.*, 9(5):763 – 808, Oct. 2002. doi: 10.1109/TDEI. 2002.1038663.

[4] R. Bartnikas and K. D. Srivastava. *Power and communication cables: theory and applications*. McGraw-Hill, London, UK, 2000.

[5] BICC Cables Ltd. *Electric Cables Handbook*. Blackwell Science Ltd, London, UK, 1997.

[6] S. Boggs, A. Pathak, and P. Walker. Partial discharge xxii: High frequency attenuation in shielded solid dielectric power cable and implications thereof for pd location. *IEEE Electr. Insul. Mag.*, 12(1):9–16, 1996. doi: 10.1109/57.484104.

[7] O. Breien and I. Johansen. Attenuation of travelling waves in single-phase high-voltage cables. *Proc. IEE*, 118(6):787–793, Jun. 1971.

[8] D. R. Brillinger. *Time series: data analysis and theory*. Holt, Rinehart and Winston, London, 1975.

[9] L. W. Couch II. *Digital and analog communication systems*. Prentice-Hall, Upper Saddle River, 7th edition, 2007.

[10] A. Cuppen, E. F. Steennis, and P. C. J. M. van der Wielen. Partial discharge trends in medium voltage cables measured while in service with pd-ol. In *Accepted for IEEE PES Transm. Distrib. Conf. Exp.*, New Orleans, LA, USA, Apr. 2010.

[11] W. G. Fano and V. Trainotti. Dielectric properties of soils. In *2001 Ann. Rep. Conf. Electr. Insul. Dielectric Phenomena*, pages 75–78, 2001. doi: 10.1109/CEIDP.2001. 963492.

[12] D. Gabor. Theory of communication. *Journal of the Institute of Electrical Engineering, Part III: Radio and Communication Engineering*, 93:429–457, Nov. 1946.

[13] F. Grassi, F. Marliani, and S. A. Pignari. Circuit modeling of injection probes for bulk current injection. *IEEE Trans. Electromagn. Compat.*, Vol. 49(3):563–576, Aug. 2007. doi: 10.1109/TEMC.2007.902385.

[14] E. Gulski, J. J. Smit, P. N. Seitz, and J. C. Smit. Pd measurement on site using oscillating wave test system. In *Conf. Rec. IEEE Int. Symp. Electr. Insul. (ISEI)*, pages 420 – 423, Arlington, VA, USA, Jun. 1998. doi: 10.1109/ELINSL.1998.694823.

[15] E. Gulski, B. S. Munir, J. J. Smit, B. Quak, and P. P. Seitz. Partial discharge signal analysis in cross-bonding joints. In *Proc. 16th Int. Symp. High Voltage Eng. (ISH)*, pages D–39, Cape Town, South Africa, Aug. 2009.

[16] G. J. Hahn and S. S. Shapiro. *Statistical models in engineering*. Wiley, London, UK, 1967.

[17] C. G. Henningsen, K. Polster, B. A. Fruth, and D. W. Gross. Experience with an on-line monitoring system for 400 kv xlpe cables. In *Proc. 1996 IEEE Transm. Distrib. Conf.*, pages 515–520, Los Angeles, CA, USA, Sep. 1996. doi: 10.1109/TDC.1996.547564.

[18] C. Herold, T. Leibfried, S. Markalous, and I. Quint. Algorithms for automated arrival time estimation of partial discharge signals in power cables. In *XVth International Symposium on High Voltage Engineering (ISH)*, pages T7–332, Ljubljana, Slovenia, Aug. 2007.

[19] D. A. Hill and J. R. Wait. Propagation along a coaxial cable with a helical shield. *IEEE Trans. Microw. Theory Tech.*, 28(2):84–89, 1980.

[20] B. Iglewicz and D. C. Hoaglin. *How to detect and handle outliers*. ASQC Quality Press, Milwaukee, USA, 1993.

[21] R. J. Jackson, A. Wilson, and D. B. Giesner. Partial discharges in power cable joints: their propagation along a crossbonded circuit and methods for their detection. *IEE Proc. C Generation, Transmission and Distribution*, 127(6):420–429, Nov 1980.

[22] S. M. Kay. *Modern spectral estimation: theory and application*. Prentice Hall, 1988.

[23] G. Kitagawa and H. Akaike. A procedure for the modeling of non-stationary time series. *Annals of the Institute of Statistical Mathematics*, 30(1):351–363, Dec. 1978. doi: 10.1007/BF02480225.

[24] F. H. Kreuger, M. G. Wezelenburg, A. G. Wiemer, and W. A. Sonneveld. Partial discharge xviii: Errors in the location of partial discharges in high voltage solid dielectric cables. *IEEE Electr. Insul. Mag.*, 9(6):15–24, Nov/Dec. 1993. doi: 10.1109/57.245980.

[25] J. H. Kurz, C. U. Grosse, and H.-W. Reinhardt. Strategies for reliable automatic onset time picking of acoustic emissions and of ultrasound signals in concrete. *Ultrasonics*, 43(7):538–546, Jun 2005. doi: 10.1016/j.ultras.2004.12.005.

[26] E. Lemke, P. Schmiegel, H. Elze, and D. Russwurm. Procedure for evaluation of dielectric properties based on complex discharge analyzing (cda). In *Conf. Rec. 1996 IEEE Int. Symp. Electr. Insul. (ISEI)*, volume 1, pages 385–388, Montreal, Canada, Jun. 1996. doi: 10.1109/ELINSL.1996.549362.

[27] R. Martin. Bias compensation methods for minimum statistics noise power spectral density estimation. *Signal Processing*, 86(6):1215–1229, Jun. 2006. doi: 10.1016/j.sigpro.2005.07.037.

[28] M. S. Mashikian. Partial discharge location as a diagnostic tool for power cables. In *IEEE Power Engineering Society Winter Meeting*, volume 3, pages 1604–1608, 2000. doi: 10.1109/PESW.2000.847582.

[29] M. S. Mashikian, R. Bansal, and R. B. Northrop. Location and characterization of partial discharge sites in shielded power cables. *IEEE Trans. Power Delivery*, 5:833 – 839, Apr. 1990. doi: 10.1109/61.53090.

[30] M. Michel. Innovative asset management and targeted investments using on-line partial discharge monitoring & mapping techniques. In *19th Int. Conf. Electricity Distrib. (CIRED)*, page 0551, Vienna, Austria, May 2007.

[31] G. Mugala, R. Eriksson, U. Gäfvert, and P. Pettersson. Measurement technique for high frequency characterization of semi-conducting materials in extruded cables. *IEEE Trans. Dielectr. Electr. Insul.*, 11(3):471–480, 2004. doi: 10.1109/TDEI.2004.1306725.

[32] G. Mugala, R. Eriksson, and P. Pettersson. Comparing two measurement techniques for high frequency characterization of power cable semiconducting and insulating materials. *IEEE Trans. Dielectr. Electr. Insul.*, 13(4):712–716, 2006. doi: 10.1109/TDEI.2006.1667728.

[33] G. Mugala, R. Eriksson, and P. Pettersson. Dependence of xlpe insulated power cable wave propagation characteristics on design parameters. *IEEE Trans. Dielectr. Electr. Insul.*, 14(2):393–399, 2007. doi: 10.1109/TDEI.2007.344619.

[34] R. Papazyan and R. Eriksson. Calibration for time domain propagation constant measurements on power cables. *IEEE Trans. Instrum. Meas.*, 52(2):415–418, 2003. doi: 10.1109/TIM.2003.811657.

[35] R. Papazyan, P. Pettersson, H. Edin, R. Eriksson, and U. Gafvert. Extraction of high frequency power cable characteristics from s-parameter measurements. *IEEE Trans. Dielectr. Electr. Insul.*, 11(3):461–470, 2004. doi: 10.1109/TDEI.2004.1306724.

[36] R. Papazyan, P. Pettersson, and D. Pommerenke. Wave propagation on power cables with special regard to metallic screen design. *IEEE Trans. Dielectr. Electr. Insul.*, 14 (2):409–416, 2007. doi: 10.1109/TDEI.2007.344621.

[37] C. R. Paul. *Analysis of Multiconductor Transmission Lines*. Wiley, Chichester, 1994.

[38] C. R. Paul. Decoupling the multiconductor transmission line equations. *IEEE Trans. Microw. Theory Tech.*, 44(8):1429–1440, 1996. doi: 10.1109/22.536026.

[39] M. N. O. Sadiku. *Elements of Electromagnetics*. Oxford University Press, New York, 3rd edition, 2001.

[40] R. Schinzinger and A. Ametani. Surge propagation characteristics of pipe enclosed underground cables. *IEEE Trans. Power App. Syst.*, PAS-97(5):1680–1688, Sep./Oct. 1978. doi: 10.1109/TPAS.1978.354660.

[41] A. Semlyen and D. Kiguel. Phase parameters of pipe type cables. In *IEEE PES Winter Meeting*, pages A 78 001–0, New York, USA, 1978.

[42] S. R. Seshadri. *Fundamentals of transmission lines and electromagnetic fields*. Addison-Wesley, London, 1971.

[43] R. Sleeman and T. van Eck. Robust automatic p-phase picking: an on-line implementation in the analysis of broadband seismogram recordings. *Physics of the Earth and Planetary Interiors*, 113(1-4):265–275, June 1999. doi: 10.1016/S0031-9201(99) 00007-2.

[44] E. F. Steennis, E. Hetzel, and C. W. J. Verhoeven. Diagnostic medium voltage cable test at 0.1hz. In *Proc. 3rd Int. Conf. Insul. Power Cables (JICABLE)*, pages 408 – 414, Versailles, France, Jun. 1991.

[45] E. F. Steennis, R. Ross, N. van Schaik, W. Boone, and D. M. Van Aartrijk. Partial discharge diagnostics of long and branched medium-voltage cables. In *Proc. 2001 7th Int. Conf. Solid Dielectrics (ICSD)*, pages 27–30, Jun. 2001. doi: 10.1109/ICSD. 2001.955502.

[46] E. F. Steennis, P. C. J. M. van der Wielen, B. Kaptein, D. Harmsen, M. Kruithof, and A. Postma. Permanent on-line monitoring of mv power cables based on partial discharge detection and localisation - an update. In *7th Int. Conf. Insul. Power Cables (Jicable)*, page A.4.1, Paris, France, 2007.

[47] J. P. Steiner, P. H. Reynolds, and W. L. Weeks. Estimating the location of partial discharges in cables. *IEEE Trans. Electr. Insul.*, 27(1):44–59, 1992. doi: 10.1109/14. 123440.

[48] G. C. Stone and S. A. Boggs. Propagation of partial discharge pulses in shielded power cable. In *Annu. Rep. Conf. Electr. Insul. Dielectr. Phenom. (CEIDP)*, pages 275–280, Amherst, MA, USA, Oct. 1982. National Academy of Science.

[49] G. L. Turin. An introduction to matched filters. *IEEE Trans. Inf. Theory*, 6(3):311–329, 1960. doi: 10.1109/TIT.1960.1057571.

[50] J. Veen. *On-line Signal Analysis of Partial Discharges in Medium-Voltage Power Cables*. PhD thesis, Eindhoven University of Technology, Eindhoven, the Netherlands, 2005.

[51] J. Veen and P. C. J. M. van der Wielen. The application of matched filters to pd detection and localization. *IEEE Electr. Insul. Mag.*, 19(5):20–26, 2003. doi: 10.1109/MEI.2003.1238714.

[52] R. Villefrance, J. T. Holbøll, and M. Henriksen. Estimation of medium voltage cable parameters for pd-detection. In *Conf. Rec. 1998 IEEE Int. Symp. Electr. Insul. (ISEI)*, pages 109–112, 1998. doi: 10.1109/ELINSL.1998.704660.

[53] P. Wagenaars, P. C. J. M. van der Wielen, P. A. A. F. Wouters, and E. F. Steennis. Directional sensing for online pd monitoring of mv cables. In *Proc. 19th Nordic Insul. Symp. (NORD-IS)*, pages 79–82, Trondheim, Norway, Jun 2005.

[54] P. Wagenaars, P. A. A. F. Wouters, P. C. J. M. van der Wielen, and E. F. Steennis. Accurate estimation of the time-of-arrival of partial discharge pulses in cable systems in service. *IEEE Trans. Dielectr. Electr. Insul.*, 15(4):1190–1199, Aug. 2008. doi: 10.1109/TDEI.2008.4591242.

[55] P. Wagenaars, P. A. A. F. Wouters, P. C. J. M. van der Wielen, and E. F. Steennis. Approximation of transmission line parameters of single-core and three-core xlpe cables. Accepted on 18 August 2009 for publication in IEEE Trans. Dielectr. Electr. Insul., 2010.

[56] P. Wagenaars, P. A. A. F. Wouters, P. C. J. M. van der Wielen, and E. F. Steennis. Measurement of transmission line parameters of three-core power cables with common earth screen. Accepted on 5 Jan. 2010 for publication in IET Sci. Meas. Technol., 2010.

[57] W. L. Weeks and Y. M. Diao. Wave propagation characteristics in underground power cable. *IEEE Trans. Power App. Syst.*, PAS-103(10):2816–2826, Oct 1984. doi: 10.1109/TPAS.1984.318279.

[58] P. D. Welch. The use of fast fourier transform for the estimation of power spectra: A method based on time averaging over short, modified periodograms. *IEEE Trans. Audio Electroacoust.*, 15(2):70–73, 1967.

[59] P. C. J. M. van der Wielen. *On-line Detection and Location of Partial Discharges in Medium-Voltage Power Cables*. PhD thesis, Eindhoven University of Technology, Eindhoven, The Netherlands, 2005.

[60] P. C. J. M. van der Wielen and E. F. Steennis. First field experience of on-line partial discharge monitoring of mv cable systems with location. In *Proc. 20th Int. Conf. Electricity Distribution (CIRED) 2009*, page paper no. 0070, Jun. 2009.

[61] P. C. J. M. van der Wielen and E. F. Steennis. Experiences with continuous condition monitoring of in-service mv cable connections. In *Proc. Power Engineering Society (PES) Power Systems Conf. & Exp. (PSCE)*, Seattle, WA, USA, Mar. 2009. doi: 10. 1109/PSCE.2009.4840266.

[62] P. C. J. M. van der Wielen, J. Veen, and P. A. A. F. Wouters. Evaluation of different types of sensors and their positioning for on-line pd detection and localisation in distribution cables. In *Proc. Nordic Insulation Symp. (Nord-IS)*, Tampere, Finland, Jun. 2003.

[63] P. C. J. M. van der Wielen, J. Veen, P. A. A. F. Wouters, and E. F. Steennis. Sensors for on-line pd detection in mv power cables and their locations in substations. In *Proc. 7th Int. Conf. Prop. Appl. Dielectr. Materials (ICPADM)*, volume 1, pages 215–219, 2003. doi: 10.1109/ICPADM.2003.1218391.

[64] P. C. J. M. van der Wielen, J. Veen, P. A. A. F. Wouters, and E. F. Steennis. On-line partial discharge detection of mv cables with defect localisation (pdol) based on two time synchronised sensors. In *18th Int. Conf. Electricity Distribution (CIRED)*, Turin, Italy, Jun 2005.

[65] P. R. Wilson, J. N. Ross, and A. D. Brown. Modeling frequency-dependent losses in ferrite cores. *IEEE Trans. Magn.*, Vol. 40(3):1537–1541, May 2004. doi: 10.1109/ TMAG.2004.826910.

[66] P. A. A. F. Wouters. Online calibration of high-frequency partial discharge signals in three-phase belted power cables. *IEE Proc. Sci., Meas. & Tech.*, 152(2):79–86, 2005. doi: 10.1049/ip-smt:20051268.

[67] P. A. A. F. Wouters, P. C. T. van der Laan, and E. F. Steennis. Inductive ultra-wide band detection and location of partial discharges in high-voltage cables. *European Trans. on Electrical Power*, 4(3):223–229, May/Jun. 1994. doi: 10.1002/etep.4450040307.

[68] C. Xu and S. A. Boggs. High frequency properties of shielded power cable part 2: sources of error in measuring shield dielectric properties. *IEEE Electr. Insul. Mag.*, 22 (1):7–13, 2006. doi: 10.1109/MEI.2006.1618966.

[69] J. Yang, R. Huang, and D. Zhang. A field-circuit coupled method to accurately determine intrinsic complex permittivity of xlpe insulation material. *IEEE Trans. Dielectr. Electr. Insul.*, 15(2):334–341, Apr. 2008. doi: 10.1109/TDEI.2008.4483450.

[70] Y. Yildir and B. Klimpke. Calculation of transmission line parameters with the boundary element method. In *Symp. Antenna Technology and Applied Electromagnetics (ANTEM)*, Winnipeg, Canada, Aug. 1988.

[71] H. Zhang, C. Thurber, and C. Rowe. Automatic p-wave arrival detection and picking with multiscale wavelet analysis for single-component recordings. *Bulletin Seism. Soc. America*, 93(5):1904–1912, Oct. 2003. doi: 10.1785/0120020241.

[72] H. Zhang, T. R. Blackburn, B. T. Phung, and D. Sen. A novel wavelet transform technique for on-line partial discharge measurements part 1: Wt denoising algorithm. *IEEE Trans. Dielectr. Electr. Insul.*, 14(1):3–14, 2007. doi: 10.1109/TDEI.2007.302864.

[73] Y. Zhou, Y. Qin, and P. Chappell. Cost-effective on-line partial discharge of measurements for cables. *IEEE Electr. Insul. Mag.*, 22(2):31–38, 2006. doi: 10.1109/MEI.2006.1619000.

Nomenclature

Abbreviations

Abbreviation	Description
AIC	Akaike Information Criterion
BEM	Boundary Element Method
CB	Cross-Bonding
CBM	Condition Based Maintenance
CBLUT	CaBLe Under Test
DFT	Discrete Fourier Transform
DS	(see list of symbols)
EC	Energy Criterion
FFT	Fast Fourier Transform (efficient algorithm to compute the DFT)
FIR	Finite Impulse Response (FIR filter is a type of digital filter)
HV	High Voltage ($> 36\,\text{kV}$)
IDFT	Inverse Discrete Fourier Transform
LEC	Last Earth Connection (of power cable in RMU or substation)
LV	Low Voltage ($< 1\,\text{kV}$)
MFB	Matched Filter Bank (set of multiple matched filters)
ML	Maximum Likelihood
MU	Measurement Unit (unit that is installed at one cable end to detect PDs. Forms a measurement system in combination with an identical unit installed at the other cable end.)
MV	Medium Voltage ($1\text{–}36\,\text{kV}$)
PD	Partial Discharge
PD-OL	PD monitoring On-line with Location (commercial online PD monitoring system for MV cable networks)

PE	Polyethylene
PILC	Paper-Insulated Lead-Covered (type of power cable with paper insulation and lead earth screen)
PLEC	Past Last Earth Connection (preferred location to install MU in RMU)
PP	Phase-to-Phase (propagation mode in power cable)
PSDF	Power Spectral Density Function
PVC	Polyvinyl Chloride
RMS	Root-Mean-Square
RMU	Ring-Main-Unit
SNR	Signal-to-Noise Ratio
SP	Shield-to-Phase (propagation mode in power cable)
TCC	Transformer Connecting Cables (cables that connect MV/LV transformer in RMU to switchgear)
TDR	Time-Domain Reflectometry (method to locate PDs and defects in power cables)
XLPE	Cross-Linked Polyethylene (type of insulation used is most modern MV and HV power cables)

Symbols

Symbol	Description	Unit
α_G	per-unit-length attenuation due to losses in insulation and semiconducting layers	Np/m
α_R	per-unit-length attenuation due to losses in conductor(s) and earth screen	Np/m
Γ_{cb}	voltage reflection coefficient on CB box	–
γ_{cb}	propagation coefficient of cross-bonding cables	Np/m
Γ_I	current reflection coefficient	–
$\boldsymbol{\gamma}_m$	modal propagation coefficient matrix	Np/m
γ_{meas}	measured propagation coefficient	Np/m
γ_{pp}	PP mode propagation coefficient	Np/m
Γ_{RMU}	voltage/current reflection coefficient on RMU	–
γ_{sp}	SP mode propagation coefficient	Np/m
Γ_V	voltage reflection coefficient	–
$\boldsymbol{\Gamma}_V$	voltage reflection coefficient matrix	–
Δf	frequency domain resolution, i.e. distance between two consecutive samples of frequency axis	Hz

Δt	sample time, i.e. time between two consecutive samples	s
ϵ_{r}	relative permittivity	–
ϵ_{r}'	real part of relative permittivity	–
ϵ_{r}''	imaginary part of relative permittivity	–
$\epsilon_{\mathrm{r,cs}}$	relative permittivity of conductor screen	–
$\epsilon_{\mathrm{r,eff}}$	effective relative permittivity	–
$\epsilon_{\mathrm{r,insu}}$	relative permittivity of insulation	–
$\epsilon_{\mathrm{r,is}}$	relative permittivity of insulation screen	–
$\sigma_{\mathrm{tp},m}$	standard deviation of noise in averaged signal of mth template	V
σ_n	standard deviation of noise	V
$\sigma_{n,\mathrm{f}}$	standard deviation of noise after filtering	V
σ_{SER}	standard deviation of SER calculations	dB
σ_x	standard deviation of noise in measured signal $x[k]$	V
$\sigma_{x,n}$	standard deviation of noise in n^{th} detected pulse	V
τ_{cc}	total transmission coefficient in CB joint (power cable to power cable)	–
τ_{cbc}	voltage transmission coefficient in CB joint (CB cable to power cable)	–
τ_{ccb}	voltage transmission coefficient in CB joint (power cable to CB cable)	–
$\tau_{\mathrm{1c,cc}}$	total transmission coefficient in CB joint (power cable to power cable) in case of short CB cables	–
τ_{ch}	time delay used in phase t_{oa} method	s
τ_{cj}	voltage transmission coefficient from cable to CB joint	–
τ_{c1}	transmission coefficient from cable 1 to RMU	–
τ_I	current transmission coefficient	–
τ_V	voltage transmission coefficient	–
$\boldsymbol{\tau}_V$	voltage transmission coefficient matrix	–
ω	angular velocity	rad/s
ω_{c}	center angular velocity	rad/s
$\omega_{\min}$	minimum angular velocity	rad/s
$\omega_{\max}$	maximum angular velocity	rad/s
$A_{\mathrm{sc},n}$	scaling factor to match n^{th} signal to template	–
$\mathbf{C}$	per-unit-length capacitance matrix	F/m
C_{cs}	per-unit-length capacitance of conductor screen	F/m
C_{eff}	per-unit-length effective capacitance (combination of C_{cs}, C_{insu} and C_{is})	F/m
c_1	parameter used for conformal transformation	–
c_2	parameter used for conformal transformation	–

C_{insu}	per-unit-length capacitance of insulation	F/m
C_{is}	per-unit-length capacitance of insulation screen and swelling tapes	F/m
C_{m}	per-unit-length mutual capacitance	F/m
C_{s}	per-unit-length self capacitance	F/m
C_{tr}	transformer capacitance (between windings and earth)	F
C_{tcc}	capacitance of transformer connecting cables	F
d_{max}	maximum distance between two E_{cum} curves	−
DS	PD detection sensitivity without noise reduction	C
$\mathrm{DS_f}$	PD detection sensitivity with noise reduction	C
E_{cum}	normalized cumulative signal energy curve	−
$E_{\mathrm{cum,ref}}$	reference E_{cum} curve	−
E_{high}	normalized cumulative signal energy after pulse	−
E_{low}	normalized cumulative signal energy before pulse	−
E_n	energy of $n[k]$ (noise)	$\mathrm{V^2 s}$
E_{pulse}	normalized signal energy of pulse	−
E_{pd}	energy of a PD signal	$\mathrm{V^2 s}$
e_{PD}	PD location error	−
E_s	energy of $s[k]$ (signal)	$\mathrm{V^2 s}$
E_x	energy of $x[k]$ (signal + noise)	$\mathrm{V^2 s}$
f	frequency	Hz
f_{d}	detection bandwidth	Hz
F_{hl}	factor for velocity due to helical lay of wire screen	−
F_{lr}	fraction of PD energy lost due to RMUs along CBLUT	%
f_{nyq}	Nyquist frequency	Hz
H_{cb}	transfer function of propagation through CB cable	−
$H_{\mathrm{c}n}$	transfer function (inside RMU) from current through incoming cable to current through cable n	−
H_{cf}	transfer function of common filter	−
H_{hf}	transfer function at high frequencies	−
h_{hf}	impulse response of H_{hf}, i.e. H_{hf} converted to time domain	−
H_m	transfer function of mth matched filter	−
h_m	taps of mth matched filter, i.e. H_m converted to time domain	−
$H_{m,n}$	transfer function from compartment m to compartment n	−
H_{rmu}	total transfer function of RMU or substation	−
H_{sens}	transfer function of sensor	
$H_{\mathrm{subs},56}$	total transfer function of substation from cable 5 to 6	−

H_{tcc}	transfer function (inside RMU) from current through incoming cable to current through earth of transformer connecting cables	–
H_{tot}	combined total transfer transfer function of multiple RMUs along CBLUT	–
H_{yb}	transfer function of two sets of CB joints from yellow to blue phase	–
H_{yr}	transfer function of two sets of CB joints from yellow to red phase	–
H_{yy}	transfer function of two sets of CB joints from yellow to yellow phase	–
$\mathbf{I}$	current vector $\mathbf{I} = \left(I_1,\ I_2,\ I_3 \right)^T$	A
I_{c1}	current through cable 1	A
I_{c2}	current through cable 2	A
I^{i}	current of incident wave	A
$\mathbf{I}_{\text{m}}$	modal current vector $\mathbf{I}_{\text{m}} = \left(I_{\text{sp}},\ I_{\text{pp},1},\ I_{\text{pp},2} \right)^T$	A
$\mathbf{I}_{\text{m}}^{+}$	modal current vector of forward traveling wave	A
$\mathbf{I}_{\text{m}}^{-}$	modal current vector of backward traveling wave	A
$I_{\text{pp},k}$	current of kth PP mode	A
$I_{\text{pp},k}^{+}$	current of forward traveling wave in k^{th} PP mode	A
$I_{\text{pp},k}^{-}$	current of backward traveling wave in k^{th} PP mode	A
I_{sp}	current of SP mode	A
I_{sp}^{+}	current of forward traveling wave in SP mode	A
I_{sp}^{-}	current of backward traveling wave in SP mode	A
I^{r}	current of reflected wave	A
I^{t}	current of transmitted wave	A
I_{tcc}	current through earth connection of transformer connecting cables	A
k_{end}	index of last sample of pulse in signal	–
k_{start}	index of first sample of pulse in signal	–
$\mathbf{L}$	per-unit-length inductance matrix	H/m
L_{bb}	busbar inductance over width of one compartment	H
L_{c}	compartment inductance	H
l_{c}	cable length	m
l_{cb}	cross-bonding cable length	m
l_{l}	lay length, i.e. the axial distance for a single turn of a helical wire screen	m
L_{m}	per-unit-length mutual inductance	H/m
L_{s}	per-unit-length self inductance	H/m

L_{tcc}	inductance of transformer connecting cables	H
L_{tr}	transformer inductance	H
$n[k]$	time-discrete noise signal	V
$N_{tp,m}$	number of samples in n^{th} template in MFB	–
p_n	n^{th} pulse detected by MFB	
P_n	power of $n[k]$ (noise)	V^2
P_N	power spectral density function	V^2/Hz
$\hat{P}_N$	estimated power spectral density function	V^2/Hz
P_s	power of $s[k]$ (signal excluding noise)	V^2
P_x	power of $x[k]$ (signal + noise)	V^2
Q	PD charge	C
r_c	conductor radius	m
R_c	conductor radius after conformal transformation	m
r_{insu}	outer radius of insulation	m
R_{rmu}	reflection coefficient on RMU or substation	–
r_s	inner radius of metallic earth screen	m
R_s	inner radius of metallic earth screen after conformal transformation	m
$R_{subs,5}$	reflection coefficient on substation for a pulse from cable 5	–
R_{tcc}	resistance (losses) of transformer connecting cables	Ω
R_{tr}	transformer resistance (losses)	Ω
r_x	distance between cable center and conductor center in a three-core cable	m
R_x	distance between cable center and conductor center in a three-core cable after conformal transformation	m
$s[k]$	time-discrete signal, excluding noise	V
S_m	frequency domain representation of predicted PD signal of mth filter	V/Hz
T_{activ}	SNR threshold for making template active	dB
t_c	cable propagation time	s
t_{cs}	thickness of semiconducting conductor screen	m
T_{detect}	PD detection threshold (relative to standard deviation of noise)	–
$\mathbf{T}_I$	current transformation matrix	–
t_{is}	thickness of semiconducting insulation screen (including swelling tapes)	m
T_m	m^{th} template in MFB	
t_{max}	time of maximum	s
t_{oa}	time-of-arrival	s
$t_{oa,1}$	time-of-arrival at RMU 1	s

$t_{\text{oa,2}}$	time-of-arrival at RMU 2	s
$t_{\text{oa,g}}$	time-of-arrival determined by Gabor method	s
$t_{\text{oa,p}}$	time-of-arrival determined by phase method	s
$t_{\text{oa,p,corr}}$	corrected time-of-arrival determined by phase method	s
T_{out}	threshold that determines whether a sample is an outlier	−
T_{SER}	SER threshold for adaptive MFB decision "has good match"	dB
t_{SNR}	observation interval for SNR calculation	s
$\mathbf{T}_V$	voltage transformation matrix	−
t_{wait}	waiting time between arrival of a pulse and injection of a reply pulse	s
T_{wan}	SNR threshold for adaptive MFB decision "well above noise"	dB
$\mathbf{V}$	voltage vector $\mathbf{V} = \left(V_1,\ V_2,\ V_3\right)^T$	V
V^{i}	voltage of incident wave	V
$\mathbf{V}^{\text{i}}$	voltage vector of incident wave	V
v_{ind}	induced voltage (in time domain)	V
V_{ind}	induced voltage (in frequency domain)	V
$\mathbf{V}_{\text{m}}$	modal voltage vector $\mathbf{V}_{\text{m}} = \left(V_{\text{sp}},\ V_{\text{pp},1},\ V_{\text{pp},2}\right)^T$	V
$\mathbf{V}_{\text{m}}^{+}$	modal voltage vector of forward traveling wave	V
$\mathbf{V}_{\text{m}}^{-}$	modal voltage vector of backward traveling wave	V
v_{p}	propagation velocity	m/s
V_{sp}	voltage of SP mode	V
V_{sp}^{+}	voltage of forward traveling wave in SP mode	V
V_{sp}^{-}	voltage of backward traveling wave in SP mode	V
$V_{\text{pp},k}$	voltage of kth PP mode	V
$V_{\text{pp},k}^{+}$	voltage of forward traveling wave in k^{th} PP mode	V
$V_{\text{pp},k}^{-}$	voltage of backward traveling wave in k^{th} PP mode	V
V^{r}	voltage of reflected wave	V
$\mathbf{V}^{\text{r}}$	voltage vector of reflected wave	V
V^{r1}	voltage of first reflected pulse	V
$\mathbf{V}^{\text{r1}}$	voltage vector of first reflected pulse	V
V^{r2}	voltage of second reflected pulse	V
$\mathbf{V}^{\text{r2}}$	voltage vector of second reflected pulse	V
V^{t}	voltage of transmitted wave	V
$\mathbf{V}^{\text{t}}$	voltage vector of transmitted wave	V
w_n	weight factor for n^{th} pulse	−
$x[k]$	time-discrete signal, including noise $x[k] = s[k] + n[k]$	V
$x_{\text{tp},m}$	average signal of mth template	V
x_n	measured signal of nth detected pulse	V

$\mathbf{Y}$	per-unit-length admittance matrix	$(\Omega m)^{-1}$
Y_m	per-unit-length mutual admittance	$(\Omega m)^{-1}$
$\mathbf{Y}_m$	per-unit-length modal admittance matrix	$(\Omega m)^{-1}$
y_{max}	maximum filter output	V
$y_{max,tmpl}$	maximum filter output when filtering predicted PD waveform	V
Y_s	per-unit-length self admittance	$(\Omega m)^{-1}$
$\mathbf{Z}$	per-unit-length impedance matrix	Ω/m
Z_0	characteristic impedance of measurement cables, typically $50\,\Omega$	Ω
Z_{adpt}	adapter impedance	Ω
Z_{bp}	parallel impedance of cross-bonding box	Ω
Z_{bs}	series impedance of cross-bonding box	Ω
Z_c	characteristic cable impedance	Ω
$\mathbf{Z}_c$	characteristic impedance matrix	Ω
$Z_{c,1}$	characteristic cable impedance of cable in first compartment	Ω
$Z_{c,2}$	characteristic cable impedance of cable in second compartment	Ω
Z_{cb}	characteristic impedance of CB cables	Ω
$Z_{c,inj}$	characteristic impedance of injection cable	Ω
$\mathbf{Z}_{c,inj}$	characteristic impedance matrix of injection circuit	Ω
$\mathbf{Z}_{c,m}$	modal characteristic impedance matrix	Ω
$Z_{c,meas}$	measure characteristic impedance	Ω
Z_{fix}	impedance of calibration fixture	Ω
Z_∞	infinite impedance (from floating conductor to earth)	Ω
Z_{in}	input impedance	Ω
Z_{jp}	parallel impedance of joint	Ω
Z_{js}	series impedance of joint	Ω
z_{PD}	location of PD origin or distance to PD origin	m
Z_{pp}	characteristic impedance of PP mode	Ω
z_m	distance to PD origin for m^{th} template	m
Z_m	per-unit-length mutual impedance	Ω/m
$\mathbf{Z}_m$	per-unit-length modal impedance matrix	Ω/m
Z_{meas}	measured impedance	Ω
Z_{LEC}	impedance at LEC location in RMU	Ω
Z_{load}	load impedance	Ω
Z_L	load impedance (at end of transmission line)	Ω
$\mathbf{Z}_L$	load impedance matrix	Ω
Z_{PLEC}	impedance at PLEC location in RMU	Ω
Z_s	per-unit-length self impedance	Ω/m
Z_t	transfer impedance	Ω

Z_{sp}	characteristic impedance of SP mode	Ω
Z_{tot}	total RMU impedance ($Z_{\text{load}} + Z_{\text{c}}$)	Ω
$Z_{\text{tot,6}}$	total RMU impedance in 6th compartment	Ω
Z_{x}	parallel impedance encountered when measuring in LEC location	Ω

Acknowledgement

First of all, I would like to thank my professor and promotor Fred Steennis. He is the initiator of the PD-online project, without him this project would not have existed. His huge knowledge of underground power cables has been invaluable for the completion of this work. I also owe many thanks to my supervisor and co-promotor Peter Wouters for his more fundamental knowledge on the subject. I especially would like to thank him for his quick response when I requested comments on draft versions of papers and this thesis. Next, I would like to thank my predecessors as PhD students on the PD-online project: Peter van der Wielen and Jeroen Veen. Together, they laid a solid foundation on which I could base my work. Additionally, during the past years Peter was available for valuable discussions and suggestions on my work.

Essential factors for a pleasant and productive work atmosphere are the office mates. At the university in Eindhoven my office mates were Arjan van Schijndel and Shima Mousavi Gargari. I would like to thank them for all the helpful discussions, and all other conversations on topics of "great importance". Over the years at KEMA Dick van Aartrijk, Auke van der Weij, Ad Kerstens, Jihane Nasseh, Bart Simons, Asido Patar Nainggolan and André Cuppen shared the office with me. I also thank them for the nice work atmosphere. Besides the office mates there are of course many other colleagues at both the university and KEMA. They are too many to list all of them, but nonetheless I would like to thank them all for making working at both the university and KEMA a pleasant experience.

Over the past years, I supervised several students during their graduation projects and internships within the PD-online project. They helped me with several topics presented in this thesis. These student are: Inge Tigchelaar, Guus Muisers, Joep Schreurs and Bart Simons. I would like to thank them for their contributions.

Research such as presented in this thesis is not possible without support from the industry. I would like to thank KEMA, Alliander, Enexis and Stedin for their support. Their support was not only financial, but they also made available a test setup and a number of cable circuits for measurements.

Curriculum vitae

February 1, 1981	Born in Schaijk, The Netherlands.
1999–2004	M.Sc. (cum laude) in Electrical Engineering at Eindhoven University of Technology
	Master thesis project at the Electrical Power Systems (EPS) group of the Eindhoven University of Technology and at the Transmission and Distribution Testing Services department of KEMA. Subject: Inductive sensors and directional sensing for PD monitoring in RMUs. Supervisors: prof.dr.ir. E. F. Steennis, ir. P. C. J. M. van der Wielen, and dr. P. A. A. F. Wouters.
2004–2005	Research and Development Engineer at the Transmission and Distribution Testing Services department of KEMA. Task: development of new methods and software to calculate the ampacity (current carrying capacity) of complex underground cable circuit configurations. This included both static and dynamic calculations using the finite-element method (FEM) on configurations with multiple circuits with an arbitrary configuration, multiple layers of soil and external heat sources.
2006–2010	Ph.D. student at the Electrical Power Systems (EPS) group of the Eindhoven University of Technology. Subject: Integration of Online Partial Discharge Monitoring and Defect Location in Medium-Voltage Cable Networks. Supervisors: prof.dr.ir. E. F. Steennis and dr. P. A. A. F. Wouters

List of publications

Journal papers

P. Wagenaars, P. A. A. F. Wouters, P. C. J. M. van der Wielen, and E. F. Steennis. Accurate estimation of the time-of-arrival of partial discharge pulses in cable systems in service. *IEEE Trans. Dielectr. Electr. Insul.*, 15(4):1190–1199, Aug. 2008.

P. Wagenaars, P. A. A. F. Wouters, P. C. J. M. van der Wielen, and E. F. Steennis. Approximation of transmission line parameters of single-core and three-core xlpe cables. Accepted on 18 August 2009 for publication in *IEEE Trans. Dielectr. Electr. Insul.*

P. Wagenaars, P. A. A. F. Wouters, P. C. J. M. van der Wielen, and E. F. Steennis. Measurement of transmission line parameters of three-core power cables with common earth screen. Accepted on 5 January 2010 for publication in *IET Sci. Meas. Technol.*

Conference papers

P. Wagenaars, I. J. Tigchelaar, P. A. A. F. Wouters, P. C. J. M. van der Wielen, and E. F. Steennis. Partial discharge propagation through cable systems with cross-bonding joints. In *Proc. 20th Nordic Insulation Symp. (Nord-IS)*, pages 119–122, Lyngby, Denmark, Jun. 2007.

P. Wagenaars, P. C. J. M. van der Wielen, P. A. A. F. Wouters, and E. F. Steennis. Pd detection and localization on hv cable systems lacking integrated sensors. In *Proc. 15th Int. Symp. High Voltage Eng. (ISH)*, Ljubljana, Slovenia, Aug. 2007.

P. Wagenaars, P. A. A. F. Wouters, P. C. J. M. van der Wielen, and E. F. Steennis. Estimation of transmission line parameters for single-core xlpe cables. In *Proc. 2008 Int. Conf. Condition Monitoring Diag. (CMD)*, pages 1132–1135, Beijing, China, Apr. 2008.

Paul Wagenaars, Peter A.A.F. Wouters, Peter C.J.M. van der Wielen, and E. Fred Steennis. Comparison of arrival time estimate methods for partial discharge pulses in power cables. In *Proc. 2008 Int. Conf. Condition Monitoring Diag. (CMD)*, pages 1162–1165, Beijing, China, Apr. 2008.

P. Wagenaars, P. A. A. F. Wouters, P. C. J. M. van der Wielen, and E. F. Steennis. Algorithms for arrival time estimation of partial discharge pulses in cable systems. In *Conf. Rec. 2008 IEEE Int. Symp. Electr. Insul. (ISEI)*, pages 694–697, Vancouver, Canada, Jun. 2008.

P. Wagenaars, P. A. A. F. Wouters, P. C. J. M. van der Wielen, and E. F. Steennis. Approximation of transmission line parameters of single-core xlpe cables. In *Conf. Rec. 2008 IEEE Int. Symp. Electr. Insul. (ISEI)*, pages 20–23, Vancouver, Canada, Jun. 2008.

Bart Simons, Paul Wagenaars, Peter Wouters, and Fred Steennis. Online impedance measurement method for rmus and substations. In *Proc. Nordic Insul. Symp. (Nord-IS)*, pages 259–262, Gothenburg, Sweden, Jun. 2009.

Paul Wagenaars, Peter A.A.F. Wouters, Peter C. J. M. van der Wielen, and E.Fred Steennis. Partial discharge propagation in three-core cables with common earth screen. In *Proc. 9th Int. Conf. Prop. Applicat. Dielectr. Materials (ICPADM)*, pages 433–436, Harbin, China, Jul. 2009.

Paul Wagenaars, Peter A.A.F. Wouters, Peter C. J. M. van der Wielen, and E. Fred Steennis. Propagation of pd pulses through ring-main-units and substations. In *Proc. 9th Int. Conf. Prop. Applicat. Dielectr. Materials (ICPADM)*, pages 441–444, Harbin, China, Jul. 2009.

Peter A.A.F. Wouters, Shima Mousavi Gargari, Paul Wagenaars, Peter C. J. M. van der Wielen, and E. Fred Steennis. Practical experiences and technical challenges in large scale introduction of on-line pd diagnosis for power cables. In *Proc. 9th Int. Conf. Prop. Applicat. Dielectr. Materials (ICPADM)*, pages 976–979, Harbin, China, Jul. 2009.

P. A. A. F. Wouters, S. Mousavi Gargari, P. Wagenaars, I. J. Tigchelaar, B. H. M. M. Simons, P. C. J. M. van der Wielen, and E. F. Steennis. Technical developments and practical experience in large scale introduction of on-line pd diagnosis. In *Int. Symp. High Voltage Eng. (ISH)*, Capetown, South Africa, Aug. 2009.

P. Wagenaars, P. A. A. F. Wouters, P. C. J. M. van der Wielen, and E. F. Steennis. Technical advancements in the integration of online partial discharge monitoring in distribution cable networks. In *2009 Annu. Rep. Conf. Electr. Insul. Dielectr. Phenom. (CEIDP)*, Virginia Beach, VA, USA, Oct. 2009.

P. Wagenaars, P. A. A. F. Wouters, P. C. J. M. van der Wielen, and E. F. Steennis. Adaptive matched filter bank for noise reduction in online partial discharge monitoring. In *2009 Annu. Rep. Conf. Electr. Insul. Dielectr. Phenom. (CEIDP)*, Virginia Beach, VA, USA, Oct. 2009.